Experimental Dielectric Spectroscopic Investigation of Room Temperature Biodegradable Eutectic Solvents and Related Chemical Systems

Thesis Submitted for the Degree of

Doctor of Philosophy (Science)

of

Jadavpur University

By

Jayanta Mondal

Department of Chemical, Biological and Macromolecular Sieneses

S. N. Bose National Centre for Basic Sciences

Block-JD, Sector-III, Salt Lake

Kolkata-700106, India

May 2024

S.N. Bose National Centre for Basic Sciences
Sector - III, Block - JD, Salt Lake, Kolkata - 700098

Dr. Ranjit Biswas
Senior Professor
Chemical and Biological Sciences

Phone: 033 2335 5706-08 (O)
email: *ranjit@bose.res.in*
Fax: 033 2335 3477

CERTIFICATE FROM THE SUPERVISOR

This is to certify that the thesis entitled "**Experimental Dielectric Spectroscopic Investigation of Room Temperature Biodegradable Eutectic Solvents and Related Chemical Systems**" submitted by Sri Jayanta Mondal (Index no.: 127/19/Phys./26) who got his name registered on 11/11/2019 for the award of Ph. D. (Science) degree of Jadavpur University, is absolutely based upon his own work under the supervision of Prof. Ranjit Biswas and that neither this thesis nor any part of it has been submitted for either any degree / diploma or any other academic award anywhere before.

Ranjit Biswas
(Dr. Ranjit Biswas)
16.05.24

DR. RANJIT BISWAS
Senior Professor
Dept. of Chemical, Biological & Macromolecular Sciences
S. N. Bose National Centre for Basic Sciences
Block - JD, Sector-III, Salt Lake, Kolkata - 700 106, India

Dedicated to my parents

Bhabasindhu Mondal and Chaina Mondal

And to my beloved wife Prathama Ghosh

Acknowledgement

I am deeply grateful and honoured to convey my sincere regards and heartfelt thanks to Professor Ranjit Biswas, my supervisor, for his unwavering support and encouragement throughout my academic journey. Working under his guidance has been an enriching and invaluable experience, and I consider myself incredibly fortunate to have had him as my mentor. His supervision has not only allowed me to enhance my critical thinking skills and work independently but has also taught me the importance of approaching challenges from multiple perspectives. Professor Biswas's extensive knowledge, dedication to his work, and enthusiasm for exploring new ideas have been a constant source of inspiration for me. Furthermore, his kind and supportive demeanour has provided me with both comfort and motivation. I am profoundly grateful for his mentorship, which has not only enriched my academic pursuits but has also left a lasting impact on me.

I wish to express my gratitude to DST INSPIRE, Govt. of India, for their financial support throughout my PhD journey.

I am immensely thankful to the members of my thesis committee and research advisory committee (RAC), Prof. Manik Pradhan, SNBNCBS, Dr. Suman Chakrabarty, SNBNCBS, Prof. Anjan Barman, SNBNCBS and Prof. Nabin Baran Banik, Jadavpur University for their insightful comments, suggestions, and scholarly contributions, which have enriched the quality of this work.

I am deeply grateful to Professor Samir Kumar Pal from SNBNCBS Kolkata for collaborative work with me. Furthermore, I would like to extend my heartfelt appreciation to the faculty members of the Centre, whose contributions have been pivotal in shaping my personal and academic journey.

I wish to extend my heartfelt appreciation to all the individuals who have been involved in procuring and maintaining the experimental and computational facilities at SNBNCBS. Their tireless dedication and hard work have ensured that I had access to the necessary resources to conduct my research effectively, and for this, I am truly grateful. Additionally, I would like to express my gratitude to the Dean (Academic Programme) office for their unwavering support during my tenure at SNBNCBS. Their assistance has been invaluable, and I am thankful for their guidance and help throughout the years.

I want to extend my sincere appreciation to my labmates Dhrubajyoti, Narayan, Amrita, Sudipta, Rik, and Aziz, as well as to Dr. Tonima Nandy and Dr. Jayeta Banerjee from the PCCP Lab. Their presence has been like having an extended family here, providing a supportive atmosphere that has been invaluable to me. They have stood by me through thick and thin, and I am deeply grateful for their unwavering companionship. I also want to thank Dr. Ejaj Tarif, Dr. Kajal Kumbhakar, Dr. Atanu Baksi, and Dr. Juriti Rajbangshi for their invaluable contributions to my personal and academic growth. Their guidance and support have helped me acquire a range of academic and non-academic skills, and I truly appreciate their efforts.

I express my heartfelt gratitude to both the academic and non-academic personnel at SNBNCBS for their invaluable support and assistance.

I convey my sincere regards to Dr. Parijat Das for her kind and nurturing attitude during my visit to her home. The loving memories created with the cute duo Rik and Sam will remain close to my heart.

I would like to extend my sincere regards to the educators who have guided me at different stages of my academic journey. Their support and motivation have been invaluable to me.

Finally, this journey has been possible due to the constant support of my family. I want to express my gratitude from the bottom of my heart to the best person of my life My parents Bhabasindhu Mondal and Chaina Mondal for their love, blessing and lessons for the life. I thank my brother Subrata Mondal who has been source of love, support and motivation all the time. To my beloved wife, Prathama Ghosh, words cannot express the depth of my gratitude for everything you are and everything you do. You have stood by my side through thick and thin, celebrating my successes and comforting me in times of need. Your unwavering faith in me has given me the courage to chase my dreams and the confidence to overcome any obstacle.

I want to express my heartfelt regards to my maternal grandfather Late Ananda Garai and grandmother Kalpana Garai. Their blessings have been invaluable for me. I want to acknowledge all my family members: Gour Chandra Ghosh (father-in-law), Rupali Ghosh (mother-in-law), Purnata Ghosh (sister-in-law), Anwesha Mondal (sister-in-law), Shib Da, Dablu Da (cousin's brothers) and cute duo Soumyadip (nephew) and Shreya (niece) for their love and support.

Abstract

The main focus of this Thesis is the study of interaction and relaxation dynamics of room temperature biodegradable eutectic solvents and other complex systems via experimental dielectric relaxation (DR) spectroscopy, time-resolved fluorescence (TRF) spectroscopy and other measurement methods, and molecular dynamics simulations. A significant part of the work in this thesis is dedicated to deep eutectic solvents (DES), which includes ionic DES, naturally abundant DES (NADES), therapeutic DES (THEDES) and low viscosity green solvent. The selection of DESs components have been inspired by certain industrial needs and aims to minimize the ecological footprint through suitable replacement of common organic solvents. The need to explore new solvents also arises from the solubility aspects of drugs and therapeutic administration. In this Thesis we have extensively explored the interaction and dynamics of these DESs via DR, TRF and complemented the findings, wherever possible, with results from molecular dynamics simulations.

A combined experimental and simulation study of DR in a naturally abundant DES composed of betaine, urea and water was carried out to explore the interaction and dynamics of the system by separating out the constituent contributions arising from the self and the cross interactions via molecular dynamics simulations. Simulation results suggested that the collective single molecule reorientational relaxation and the structural hydrogen bond fluctuation dynamics, not the hydrodynamic single molecular rotations, hold the key to understand the multiple relaxation timescales measured DR experiments.

We next studied ionic acetamide DESs containing NaSCN and KSCN salts where focus was on to explore and understand the impact of successive replacement of K^+ by Na^+ on the measured DR. Both experimental and simulated DR showed multi-Debye relaxations and a decrease in the static dielectric constant (ε_S) upon Na^+ substitution. Na^+-DES exhibited stronger viscosity decoupling, higher glass transition temperature (~220 K), and increased fragility compared to K^+-DES. Simulations suggested significant rupture of the acetamide-acetamide H-bond network structure in this DES and a linear decrease of the ε_s with the average number of H-bonds per acetamide molecule. Cation-dependent cross interactions had negligible impact on ε_S.

The poor water solubility of aspirin, a nonsteroidal anti-inflammatory drug, led to the engineering of a THEDES containing aspirin and menthol at 1:4 molar ratio which significantly enhanced the solubility of aspirin. Preliminary investigation of its structure and dynamics was carried out by combining TRF with computer simulations. TRF revealed a strong temporal heterogeneity in the medium and a significant decoupling between medium viscosity and solute dynamics. Computer simulations revealed extensive inter-molecular H-bond formation.

To counter the adverse effects of high viscosity on important chemical reactions, we have developed a low-viscosity, transparent, multi-component molten mixture using biocompatible sorbitol, urea, and water. The ε_s of this molten mixture is similar to that of water ($\varepsilon_s \sim 80$) and makes it an excellent solvent, even though its dynamics are much slower than water. Frequency-dependent DR measurements within the range $0.2 \leq \nu/GHz \leq 50$ unveil multi-Debye relaxation steps in this medium, with the average relaxation time spanning from ~400 ps to 100 ps. Fluorescence emission studies using fluorescent dyes, namely coumarin 153 (C153) and coumarin 343 (C343), suggest the medium being spatially homogeneous, although the study of rotational dynamics indicates presence of weak temporal heterogeneity.

Apart from preparing designer solvents, this Thesis deals with capturing ultrafast solvation of glycerol and ethylene glycol (EG) using a streak camera providing a temporal resolution ~2 ps. We combined streak camera and time-correlated single photon counting (TCSPC) data which captured nearly 90% of the total solvation of EG and suggested that solute lifetime may play an important role in capturing sub-picosecond solvent response.

Addressing organ dysfunction stemming from hyaluronic acid (HA) aggregation in aqueous environments necessitates a thorough investigation of concentration-dependent HA aggregation. This is pivotal as the minimum concentration threshold for HA aggregation $\left(c_{\mathrm{HA}}^{\mathrm{Aggre}}\right)$ governs structural transitions, leading to slower relaxation dynamics in bulk water. Analysis of various parameters in DR and conductivity measurements indicates approximately 0.5 - 0.66 wt% HA in water as the critical concentration for HA aggregation. DR measurements reveal the emergence of biphasic water dynamics with 'slow' and bulk-like relaxations having time constants around 0.3-4 ns and ~10 ps, respectively, as $c_{\mathrm{HA}}^{\mathrm{Aggre}}$ was approached. Differential scanning calorimetric measurements further supported the existence of two types of water.

সারাংশ

এই থিসিসের মূল লক্ষ্য হল পরীক্ষামূলক ডাইলেকট্রিক রিলাক্সেশন স্পেকট্রোস্কোপি, টাইম রিসলভড ফ্লুরোসেন্স স্পেকট্রোস্কোপি এবং অন্যান্য পরিমাপ পদ্ধতি, এবং আণবিক গতিবিদ্যা সিমুলেশনের মাধ্যমে বায়োডিগ্রেডেবল ইউটেটিক দ্রাবক এবং অন্যান্য জটিল সিস্টেমের মিথস্ক্রিয়া এবং গতিবিদ্যার অধ্যয়ন। এই থিসিসের কাজের একটি উল্লেখযোগ্য অংশ ডীপ ইউটেটিক দ্রাবক, যার মধ্যে রয়েছে আয়নিক, প্রাকৃতিক, থেরাপিউটিক ডীপ ইউটেটিক দ্রাবক এবং কম সান্দ্রতাযুক্ত প্রাকৃতিক দ্রাবক। উপাদানগুলির নির্বাচন নির্দিষ্ট শিল্প চাহিদা দ্বারা অনুপ্রাণিত হয়েছে এবং সাধারণ জৈব দ্রাবকগুলির উপযুক্ত প্রতিস্থাপনের মাধ্যমে পরিবেশগত বিরূপ প্রভাব কমিয়ে আনার লক্ষ্য। এই থিসিসে আমরা উপরিউক্ত পদ্ধতিগুলো ব্যবহর করে মিথস্ক্রিয়া এবং গতিশীলতাকে ব্যাপকভাবে অন্বেষণ করেছি এবং আণবিক গতিবিদ্যা সিমুলেশনের ফলাফলের সাথে পরিপূরক করেছি।

আণবিক গতিবিদ্যা সিমুলেশন এবং পরীক্ষামূলক ডাইলেকট্রিক রিলাক্সেশন স্পেকট্রোস্কোপির মাধ্যমে বিটেইন, ইউরিয়া এবং জলের সমন্বয়ে গঠিত প্রাকৃতিক ডীপ ইউটেটিক দ্রাবকের নিজস্ব এবং সংমিশ্রিত মিথস্ক্রিয়া থেকে উদ্ভূত উপাদান অবদানগুলিকে আলাদা করে সিস্টেমের মিথস্ক্রিয়া এবং গতিশীলতা অধ্যয়ন করা হয়েছিল। সিমুলেশন ফলাফলগুলি দেখিয়েছে যে হাইড্রোডাইনামিক একক আণবিক ঘূর্ণন নয়, বরং সমষ্টিগত একক অণুর ঘূর্ণন এবং কাঠামোগত হাইড্রোজেন বন্ডের গতিবিদ্যা, পরীক্ষামুলক ভাবে প্রাপ্ত একাধিক টাইমস্কেল গুলো বোঝার চাবিকাঠি ধরে রাখে।

আমরা পরবর্তীতে সোডিয়ম এবং পটাশিয়াম থায়োসায়ানেট লবণের সাথে অ্যাসিটামাইড ডীপ ইউটেটিক দ্রাবকের সোডিয়ম আয়ন দ্বারা পটাশিয়াম আয়নের ধারাবাহিক প্রতিস্থাপনের প্রভাব অন্বেষণ এবং বোঝার চেষ্টা করেছি। পরীক্ষামূলক এবং সিমুলেটেড ডাইলেকট্রিক রিলাক্সেশন উভয়ই মাল্টি-ডিবাই শিথিলতা এবং সোডিয়ম আয়ন প্রতিস্থাপনের উপর স্থির অস্তরক ধ্রুবক হ্রাস দেখিয়েছে। সোডিয়ম আয়ন যুক্ত দ্রাবক শক্তিশালী সান্দ্রতা ডিকাপলিং, উচ্চ গ্লাস ট্রানজিশন তাপমাত্রা, এবং বর্ধিত ভঙ্গুরতা প্রদর্শন করেছে। সিমুলেশন এই মাধ্যমের অ্যাসিটামাইড-অ্যাসিটামাইড হাইড্রোজেন বন্ড নেটওয়ার্ক কাঠামোর উল্লেখযোগ্য ফাটল এবং প্রতি অ্যাসিটামাইড অণুতে হাইড্রোজেন বন্ডের গড় সংখ্যা সহ স্থির অস্তরক ধ্রুবক-এর রৈখিক হ্রাস প্রদর্শন করেছে ।

অ্যাসপিরিনের অতিমাত্রায় কম জল দ্রবণীয়তা উল্লেখযোগ্যভাবে বাড়িয়ে তোলার জন্য ১:৪ মোলার অনুপাতে অ্যাসপিরিন এবং মেন্থল স্বমনয়ে একটি নতুন থেরাপিউটিক ডীপ ইউটেটিক দ্রাবক তৈরি করা হয়েছিল। কম্পিউটার সিমুলেশনের সাথে টাইম রিসলভড ফ্লুরোসেন্স স্পেকট্রোস্কোপি একত্রিত করে এর

গঠন এবং গতিবিদ্যার প্রাথমিক তদন্ত করা হয়েছিল। ফ্লুরোসেন্স স্পেকট্রোস্কোপি-এর মাধ্যমের একটি শক্তিশালী অস্থায়ী বৈচিত্র্য প্রকাশ করেছে এবং মাঝারি সান্দ্রতা এবং দ্রবণীয় গতিবিদ্যার মধ্যে একটি উল্লেখযোগ্য ডিকাপলিং লক্ষ্য করা গেছে। কম্পিউটার সিমুলেশন এই সিস্টেম এর ব্যাপক আন্তঃ-আণবিক হাইড্রোজেন -বন্ড গঠন প্রকাশ করেছে।

গুরুত্বপূর্ণ রাসায়নিক বিক্রিয়ায় উচ্চ সান্দ্রতার বিরূপ প্রভাব মোকাবেলা করার জন্য, আমরা জৈব সামঞ্জস্যপূর্ণ সরবিটল, ইউরিয়া এবং জল ব্যবহার করে একটি কম-সান্দ্রতা, স্বচ্ছ, বহু-উপাদান গলিত মিশ্রণ তৈরি করেছি। এই গলিত মিশ্রণের স্থির অস্তরক ধ্রুবক জলের অনুরূপ যেটি এটিকে একটি চমৎকার দ্রাবক করে তোলে, যদিও এর গতিশীলতা জলের চেয়ে অনেক ধীর। কম্পাঙ্ক-নির্ভর ডাইলেকট্রিক রিলাক্সেশন পরিমাপ এই মাধ্যমের মাল্টি-ডিবাই শিথিলকরণ পদক্ষেপগুলি উন্মোচন করে। ফ্লুরোসেন্ট রঞ্জক ব্যবহার করে ফ্লুরোসেন্স নির্গমন অধ্যয়ন, মাধ্যমটিকে স্থানিকভাবে সমজাতীয় প্রদর্শন করে , যদিও ঘূর্ণন গতিবিদ্যার অধ্যয়ন দুর্বল সাময়িক ভিন্নতার উপস্থিতি নির্দেশ করে।

ডিজাইনার দ্রাবক প্রস্তুত করা ছাড়াও, এই থিসিসটি একটি পিকোসেকেন্ড রিসলভড স্ট্রিক ক্যামেরা ব্যবহার করে গ্লিসারল এবং ইথিলিন গ্লাইকোল এর অতি দ্রুত সলভেশন গতিবিদ্যা ক্যাপচার করেছে । আমরা স্ট্রিক ক্যামেরা এবং টাইম-সম্পর্কিত একক ফোটন কাউন্টিং ডেটা একত্রিত করেছি যা ইথিলিন গ্লাইকোল এর মোট সলভেশনের প্রায় ৯০% ক্যাপচার করেছে।

জলীয় পরিবেশে হায়ালুরোনিক অ্যাসিড একত্রিতকরণ থেকে উদ্ভূত অঙ্গের কর্মহীনতার সমাধান করার জন্য ঘনত্ব-নির্ভর হায়ালুরোনিক অ্যাসিড সমষ্টির একটি পুঙ্খানুপুঙ্খ তদন্ত প্রয়োজন। এটি গুরুত্বপূর্ণ কারণ হায়ালুরোনিক অ্যাসিড সমষ্টির জন্য ন্যূনতম ঘনত্বের প্রান্তিক মান কাঠামোগত পরিবর্তনগুলিকে নিয়ন্ত্রণ করে, যা বিশুদ্ধ জলকে ধীর শিথিলকরণ গতিশীলতার দিকে পরিচালিত করে। ডাইলেকট্রিক রিলাক্সেশন এবং পরিবাহিতা পরিমাপের বিভিন্ন প্যারামিটারের বিশ্লেষণ এর মাধ্যমে দেখা গেছে এই ন্যূনতম ঘনত্বের প্রান্তিক মান জলে আনুমানিক ০.৫% হায়ালুরোনিক অ্যাসিড। ডাইলেকট্রিক রিলাক্সেশন পরিমাপ ধীর এবং বিশুদ্ধ জলের বাইফেসিক গতিবিদ্যার উত্থান প্রকাশ করে। ডিফারেনশিয়াল স্ক্যানিং ক্যালোরিমেট্রিক পরিমাপ এই দুই ধরনের জলের রিলাক্সেশন এর অস্তিত্বকে সমর্থন করে।

List of Publications

1. "Temperature Dependent Dielectric Relaxation Measurements of (Acetamide + K/Na SCN) Deep Eutectic Solvents: Decoding the Impact of Cation Identity via Computer Simulations" **Jayanta Mondal**, Dhrubajyoti Maji and Ranjit Biswas* *J. Chem. Phys.*, 2024**, 160**, 084506.

2. "Detection of ultrafast solvent dynamics employing a streak camera" **Jayanta Mondal**†, Narayan Chandra Maity† and Ranjit Biswas*, *J. Chem. Sci.*, 2023, **135**, 84. († equal contribution).

3. "Temperature Dependent Dielectric Relaxation Measurements of (Betaine+Urea+Water) Deep Eutectic Solvent in Hz-GHz Frequency Window: Microscopic Insights into Constituent Contributions and Relaxation Mechanisms" **Jayanta Mondal**, Dhrubajyoti Maji and Ranjit Biswas*, *J. Phys. Chem. B* (under review).

4. "Interaction and Dynamics in an Aspirin-Based Therapeutic Deep Eutectic Solvent: Temperature-Dependent Time Resolved Fluorescence Measurements and Computer Simulations" **Jayanta Mondal,** Dhrubajyoti Maji and Ranjit Biswas*, *Phys. Chem. Chem. Phys.* (to be submitted).

5. "Interaction and Dynamics of a Newly Prepared Multi-Component Molten Mixture: A Combined Dielectric Relaxation and Time-resolved Fluorescence Study" **Jayanta Mondal**, Ejaj Tarif and Ranjit Biswas* (to be submitted).

6. "Dynamical Transformation of Water During Sol-Gel Transition in Aqueous Solutions of Hyaluronic Acid" Narayan Chandra Maity†, **Jayanta Mondal**†, and Ranjit Biswas*, *J. Phys. Chem. Lett.* (to be submitted) [† equal contribution].

7. ***"Interaction and Dynamics in a Fully Biodegradable Glucose Containing Naturally Abundant Deep Eutectic Solvent: Temperature-Dependent Time-Resolved Fluorescence Measurements" Ejaj Tarif, **Jayanta Mondal** and Ranjit Biswas*, *J. Phys. Chem. B*, 2019, **123**, 9378 – 9387.

8. ***"How Frictional Response During Solute Solvation Controls Solute Rotation in Naturally Abundant Deep Eutectic Solvent (NADES)? A Case Study with Amino Acid Derivative Containing DES" Ejaj Tarif, **Jayanta Mondal** and Ranjit Biswas*, *J. Mol. Liq.*, 2020, **303**, 112451.

9. ***"Structurally Dynamic Monocyte-Liposome Hybrid Vesicles as an Anticancer Drug Delivery Vehicle: A Crucial Correlation of Microscopic Elasticity and Ultrafast Dynamics" Ria Ghosh, Lopamudra Roy, Dipanjan Mukherjee, Sushmita Sarker, **Jayanta Mondal**, Nivedita Pan, Md. Nur Hasan, Subhajit Ghosh, Arpita Chattopadhyay, Arghya Adhikary, Maitree Bhattacharyya, Asim Kumar Mallick, Ranjit Biswas*, Ranjan Das*, Samir Kumar Pal*, *J. Phys. Chem. Lett.*, 2024, **15**, 3078–3088.

10. ***"Interaction and Dynamics of a Glucose Based Biodegradable Naturally Abundant Deep Eutectic Solvent (NADES): Temperature Dependent Dielectric Measurement and Molecular Dynamics Study" **Jayanta Mondal,** Dhrubajyoti Maji and Ranjit Biswas*. (manuscript in preparation)

***Not included in this thesis.

Contents

Chapter 5: Interaction and Dynamics in an Aspirin-Based Therapeutic Deep Eutectic Solvent: Temperature-Dependent Time Resolved Fluorescence Measurements and Computer Simulations………………………………...125

Chapter 6: Interaction and Dynamics of a Newly Prepared Multi-Component Molten Mixture: A Combined Dielectric Relaxation and Time-resolved Fluorescence Study………………………………………………...162

Chapter 7: Detection of Ultrafast Solvent Dynamics Employing a Streak Camera……………………………………………………………..190

Chapter 8: Concluding Remarks and Future Problems…………………...211

Addendum I: Dynamical Transformation of Water During Sol-Gel Transition in Aqueous Solutions of Hyaluronic Acid: Probed via Dielectric Relaxation Spectroscopy……………………………………………………215

Chapter 1

Introduction

Solvents constitute an essential part in our daily life serving diverse purposes across various fields. Its use spans from laboratory to industry, food processing to drug delivery, cosmetic to battery and so on.[1–8] In laboratories, solvents are used for dissolving, diluting, and reacting with substances, as well as for carrying out desired chemical reactions, extraction, chromatography, crystallization and other essential tasks. In industry, solvents find applications in cleaning surfaces, dissolving substances, extracting desired compounds, purifying materials, facilitating chemical synthesis, and powering various other essential processes across diverse industries.[9,10] Additionally, solvents play a vital role in food processing,[8,11] by extracting flavours, colours, and essential oils from natural sources while in drug delivery, they serve as crucial vehicles for insoluble drugs, facilitate the dissolution of these drugs, enhancing their bioavailability and therapeutic efficacy.[12,13]

Various designer solvents are used for these purposes, and their efficacy and applicability in these fields depend on the primary properties of the solvent, which include polarity, viscosity, volatility, inflammability, and especially ecological footprints. Unfortunately, a large portion of the solvents used are tagged with hazardous and toxic label.[14–17] Developing new green media will facilitate less impact on environment as well as mankind caused by toxic media. This green media will promote the use of bio-solvents to reduce the harmful effects on environment.[18–21] Searching for an alternate to such toxic and environmentally harmful organic solvents are being continued with utmost desire. Room temperature ionic liquids (IL),[22–26] gas expanded liquids,[27,28] room temperature super critical fluids[29–31] and their aqueous mixtures, deep eutectic solvents (DESs)[32–39] have been introduced in past decades which are comparatively less toxic and have minimum effects on environment. Among these solvents ionic liquids and DESs are the two potential groups of solvents that can replace the traditional organic solvents in many applications. There exists a belief that DESs are sometimes superior to ILs.[11,40–42] ILs are highly expensive and difficult to synthesize in large scale. On the other hand, DESs have their own advantage because of easily availability of raw materials, easy synthesis route, convenient transportation, low cost, less toxicity, non-inflammability, and nonvolatility. Moreover, DESs can be made more bio-degradable by choosing right components.[40,42–47]

DESs are multicomponent mixtures of hydrogen bond donor (HBD) and hydrogen bond acceptor (HBA) that melt or solidify at a unique temperature which is much lower than the individual melting points of the components.[33,42,45,48–51] Therefore, temperature and the components ratio are the key factors in forming a DES. Intermolecular interaction such as hydrogen bonding interaction is one of the main interactions in DESs.[52,53] Also, the depression of melting point takes place due to presence of other component molecules which frustrates the lattice structure.[48] DESs have gain immense attention in recently as it exhibits remarkable versatility across a multitude of disciplines. They serve as effective reaction media for chemical transformations, facilitate controlled drug release in pharmaceutical formulations,[54–59] and contribute to the formulation of low-VOC paints and coatings.[60] DESs also play pivotal roles in various sectors such as food and beverage,[5,11,39,61] textile processing, and biorefining, where they enable selective extraction of natural compounds, improved dye uptake in fabrics, and sustainable production of bio-based chemicals.[62,63] Additionally, DESs are utilized as battery electrolytes, where their high ionic conductivity and compatibility with electrode materials enhance the performance and sustainability of energy storage devices.[64–68]. While DESs hold great promise in diverse fields of application, the interaction and dynamics of such systems are not fully understood. Extensive research is still needed to delve deeper into the unique characteristics of DESs and their smarter applications in diverse domains.

The DESs are classified into different categories depending upon the nature of the components. These are naturally abundant deep eutectic solvents (NADES), ionic deep eutectic solvents (IDES), therapeutic deep eutectic solvents (THEDES), non-ionic deep eutectic solvents and so on. NADESs,[34,37,38,44,69–71] a recently discovered category of DESs, are gaining attention for being environmentally friendly, safe, and sustainable. Despite being prepared at higher temperatures, they remain liquid at or near room temperature due to the intricate interplay of their components, primarily derived from plant metabolites such as amino acids, organic acids, urea, and sugars etc. These versatile solvents are increasingly utilized across diverse domains including chemical dissolution,[72] serving as reaction media,[73] pharmaceutical applications,[57] agricultural sector,[74] cosmetics formulations,[75] food processing,[5,39,76] extractions of natural compounds[77–80] etc. Notably, they play a crucial role in enhancing the solubility of metabolites within lipids and facilitate the permeability of cell membranes, thus aiding biological processes within living organisms.[81,82]

Although NADESs are increasingly recognized as promising alternatives to hazardous organic solvents, the exploration of the connection between the structure and dynamics in the medium has received little attention. Though several attempts were made to explore the structure and dynamics of a few NADESs via utilizing X-ray scattering,[83] quasi elastic neutron scattering[84] and molecular dynamics simulations.[85] These measurements revealed that NADESs are extremely complex systems with extensive formation of H-bonds which gives stability to their liquid structures. Few Raman spectroscopic and FTIR measurements were carried out to uncover the dynamics and structure of NADESs.[86] Time-resolved anisotropy and dynamic Stokes shift measurements conducted on NADESs containing (glucose+urea+water)[87] and (betaine+urea+water)[88] unveiled a notable correlation between solute rotation and solvation times and the fractional viscosity dependence. Until now, there has been a lack of research examining the inherent dynamics of this significant system and establishing connections between the measured or computed dynamics and the microscopic solution structure. Dielectric relaxation spectroscopy (DRS) has emerged as a powerful tool which directly probes the fluctuations in the collective dipole moment of a given system when subjected to a time-dependent electric field, providing insights into the inherent dynamics of medium. Due to the complexity of multi-component interactions in these systems, experimental methods cannot isolate individual contributions. Molecular dynamics simulations play a crucial role in addressing this challenge. Simulated dielectric relaxation (DR) spectra can be compared one-to-one with experimental spectra. Subsequently, the contributions from self-interactions of individual species and cross-interactions among species can be discerned separately, providing valuable molecular insights into NADES interactions.

Ionic deep eutectic solvents[89–94] (IDESs) represent an important class of solvents composed of a host solvent and guest ionic salts. These systems have garnered considerable attention across various domains, including battery electrolytes,[64,95] reaction media,[96] extraction and separation of natural products[97] and beyond. Upon incorporation of ionic salts into the host solvent, IDESs exhibit intriguing properties, such as a reduction in the dielectric constant of the host solvent. To elucidate the dynamics and structure of these IDESs, numerous studies employing techniques like DR spectroscopy,[51,90] NMR,[98] time-resolved fluorescence (TRF),[99,100] Raman induced Kerr effect spectroscopy,[101,102] FTIR, and molecular dynamics simulations[49,92] have been conducted. However, certain questions regarding the molecular-level aspects underlying the decrease in the static dielectric constant remain unanswered. In this context, a comprehensive investigation, combining experimental DR measurements with molecular dynamics simulations, holds promise to shed light on these unresolved queries. Our study aims to bridge this gap by directly connecting experimental static dielectric constant measurements to the average number of H-bonds per molecule. Through this approach, we unveil that the reduction in dielectric constant primarily arises from randomization in dipolar reorientation induced by the rupture of hydrogen bonds due to ion induction. Moreover, we demonstrate that dynamic dielectric decrement contributes negligibly via current-current and dipole-current interaction terms. This integrated approach provides valuable insights into the fundamental mechanisms governing the behaviour of IDESs and paves the way for their enhanced understanding and applications.

Therapeutic deep eutectic solvents[57,103–105] (THEDES) are a promising category of DESs that show potential for improving the solubility, permeability, and absorption of active pharmaceutical ingredients (APIs), thereby enhancing their bioactivity and therapeutic efficacy. THEDES, comprising diverse APIs like lidocaine, arginine, ibuprofen, and others, along with excipients like thymol and menthol, have been explored for pharmaceutical applications, including drug delivery enhancement,[56,57,106,107] improved permeability and solubility,[108,109] and exhibiting antiseptic and antibacterial properties.[110,111] Analytical techniques such as H-NMR, differential scanning calorimetry (DSC), microscopy, FTIR, Raman spectroscopy, and SEM have been employed to understand their properties thoroughly.

Despite their potential, there remains a gap in our understanding of the interaction, dynamics, and structure of these systems. Our objective is to address this gap by investigating these aspects through probe-specific measurements. Additionally, we will analyse the stability of such metastable DESs using computer simulations. The outcomes of this research may offer valuable insights into utilizing DESs as solvents for drug delivery and formulation, thereby potentially impacting the development of novel and improved pharmaceutical products.

Ultrafast solvation dynamics of significant solvents such as ethylene glycol (EG) and glycerol were investigated using picosecond-resolved streak camera systems.[112,113] With upconversion measurements[114] offering a resolution of ~180 fs and TCSPC[87,100] providing temporal resolution of ~90 ps, these experiments effectively bridged the gap between ultrafast upconversion and TCSPC methods, which typically have a temporal resolution of about 2 ps. Consequently, these measurements enable the capture of molecular solvation dynamics occurring within these timescales.

This Thesis comprises a total of 7 chapters, along with an addendum at the end. The first chapter is the introduction followed by the second chapter outlined the experimental techniques and procedures employed throughout the Thesis.

In chapter 3, we investigated the impact of substituting K^+ by Na^+ on the polarization response of $0.25[f\mathrm{KSCN} + (1-f)\mathrm{NaSCN}] + 0.75\mathrm{CH_3CONH_2}$ DESs. Through temperature-dependent $(303 \leq T/K \leq 343)$ DR measurements $(0.2 \leq \nu/GHz \leq 50)$ and simulations, it uncovers multi-Debye relaxations accompanied by a decrease of the solution static dielectric constant (ε_s) upon replacement of K^+ by Na^+. Temperature dependent measurements revealed much stronger viscosity decoupling of DR times for Na^+ containing DES than K^+ system. DSC measurements indicated a higher glass transition temperature for Na^+-DES (~220 K) than K^+-DES (~200 K), implying more fragility and cooperativity for the former (Na^+-DES) than the latter. Computer simulations revealed gradual decrease of the average number of H-bonds $(\langle n_\mathrm{HB} \rangle)$ per acetamide molecule and increased frustrations in the average orientational order upon replacement of K^+ by Na^+. Both measured and simulated ε_s values were found to decrease linearly with $\langle n_\mathrm{HB} \rangle$. Decompositions of the simulated DR spectra revealed that the cation-dependent cross interaction (dipole-ion) term contributes negligibly to ε_s, and appears in the terahertz regime. Finally, the simulated collective single-particle reorientational relaxations $(C_1(t))$ and the structural H-bond fluctuation dynamics $(C_{HB}(t))$ revealed the microscopic origin of the cation identity dependence shown by the measured DR relaxation times.

In Chapter 4, a combined experimental and simulated DR study of a NADES composed of betaine urea and water with the composition (in weight ratio 11.7: 12: 1) was performed to explore the interaction and dynamics through multi-step relaxation behaviour. Temperature dependent $(303 \leq T/K \leq 343)$ measurements were performed over 9 decades of frequency covering a frequency range of 20Hz to 50 GHz. Measured DR, comprised of four distinct steps with relaxation times spreading over a few picoseconds to several nanoseconds, was found to agree well with simulations. The simulated total DR spectra, upon dissection into three self (intra-species) and three cross (inter-species) interaction contributions, revealed that the betaine-betaine self-term dominated (~65%) the relaxation, while the urea-urea and the water-water interactions contributed only ~7% and ~1%, respectively. The cross-terms (betaine-urea, betaine-water and urea-water) together accounted for < 30% of the total DR. The slowest DR component with time constant of $\sim 1-10$ ns derived dominant contribution from betaine-betaine interactions, where betaine-water and urea-water interactions also contributed. The sub-nanosecond (0.1 - 0.6 ns) timescale originated from all interactions except betaine-water interaction. An extensive interaction of water with betaine and urea induced a dramatic reduction in the average number of water-water H-bond (~0.7) and consequently the ε_s of water in this DES (ε_s ~ 2). Furthermore, the origin of the experimental timescales was explained via simulated $C_1(t)$ and $C_{HB}(t)$, which showed well agreement between the two.

In chapter 5, interaction and dynamics of a new THEDES, developed by combining aspirin and menthol at 1:4 molar ratio, were investigated by performing temperature dependent time-resolved fluorescence measurements and computer simulations. For fluorescence measurements, two fluorescent probe molecules of different chemical nature, coumarin 153 (C153) and coumarin 343 (C343), were employed. Computer simulations were carried out to provide insight into the microscopic structure of the system and assistance to the interpretation of the experimental data. Measured viscosities (η) ranged from ~3 – 50 cP in the temperature range $(303 \leq T/K \leq 343)$, while differential scanning calorimetry (DSC) measurements indicated a glass transition temperature, T_g ~220 K. The magnitude of the Stokes shift measured using C153 in this medium (relative to that in hexane) was ~700 cm^{-1} and indicated chloroform-like medium polarity. Both steady state and time-resolved fluorescence measurements revealed presence of substantial spatio-temporal heterogeneity in this THEDES. Activation energy associated with the rotation of the probes used $(\sim 33\ kJ\ mol^{-1})$ was found to be nearly half of that from temperature-dependent viscosity measurements $(\sim 60\ kJ\ mol^{-1})$, suggesting a strong viscosity decoupling of solute rotational dynamics. Measured solvation correlation function via dynamic Stokes shift experiments exhibited biphasic decay with two well-separated timescales, ~0.2 ns and ~2 ns. Simulations of solution H-bond structure indicated that aspirin forms fewer H-bonds internally but exhibits a stronger propensity to form H-bonds with menthol.

In Chapter 6, to overcome the hindrance of high viscosity on important chemical reactions, we have prepared a low viscous transparent multi-component molten mixture from biocompatible sorbitol, urea and water. Our investigation explored the physical properties, interactions, dynamics, and heterogeneity of this prepared molten mixture. The measured viscosity coefficient (η) of the molten mixture varies from ~73 cP to 8 cP within the temperature range 288 K $\leq T \leq$ 338 K. Temperature dependent (303 K $\leq T \leq$ 343 K) dielectric relaxation (DR) measurements in the frequency window $0.2 \leq \nu/GHz \leq 50$ reveal multi-Debye relaxation dynamics in this medium with the average relaxation time, $\langle\tau_{DR}\rangle$, varying from ~400 ps to 100 ps within this temperature range. The static dielectric constant of this molten mixture is similar to that of water ($\varepsilon_s \sim 80$) and makes it an excellent solvent, even though its dynamics are much slower than water. Steady-state fluorescence emission studies by employing fluorescent dyes, coumarin 153 (C153) and coumarin 343 (C343), highlights spatial medium homogeneity, although mild dynamic heterogeneity signatures are evident from the fractional viscosity dependency of the rotational dynamics of the dye molecules ($\tau_r \propto \left[\frac{\eta}{T}\right]^p with\, p \approx 0.7$). Interestingly, experimental DR dynamics captures even milder dynamical heterogeneity of the system, with $p \approx 0.87$.Activation energies estimated from Arrhenius type temperature dependence of $\langle \tau_{DR} \rangle$ and $\langle \tau_r \rangle$ supports the above findings.

In Chapter 7, the ultrafast solvent dynamics of glycerol and EG in response to a sudden charge jump in two different solute probes, coumarin 153 (C153) and trans-2-[4-(dimethylamino)styryl] benzothiazole (DMASBT), were measured by employing streak camera based detection system (temporal resolution ~2ps). Subsequently, the detection of time dependent solvation of the excited solute was measured by appropriately combining the streak camera data with those from the time-correlated single photon counting (TCSPC) measurements (resolution ~90 ps). Interestingly, combined data for C153 provided dynamic Stokes shift magnitudes approximately double of the magnitudes accessed via the streak camera alone for these two solute probes in glycerol and EG. The initial phase of solvation in EG was found to be too fast to be measured by the present streak camera-based detection set-up and missed nearly half of the total response. The relatively shorter average excited state fluorescence lifetime of DMASBT ($\langle \tau_{fl} \rangle < 0.5$ ns) prohibited the detection of the ≥0.5 ns solvation component reported by C153 in glycerol, highlighting the importance of $\langle \tau_{fl} \rangle$ for complete measurements of polar solvation response via dynamic Stokes shift measurements. Inappropriate choice of fluorescent probe solute with shorter $\langle \tau_{fl} \rangle$ may therefore give rise to an unexpected solute dependence of polar solvation dynamics even when detection of the rapid initial decay is ensured through ultrafast measurements.

The remediation of organ dysfunction resulting from hyaluronic acid (HA) aggregation in aqueous media requires a comprehensive examination of concentration dependent HA aggregation. This is critical because the minimum concentration threshold for HA aggregation ($c_{\mathrm{HA}}^{\mathrm{Aggre}}$) dictates structural transition and transforms bulk water dynamics to produce slower relaxation features. In addendum I, we have carried out preliminary study of HA aggregation via concentration dependent study of HA in aqueous medium employing DR measurements and DSC study. DR measurements demonstrate a clear emergence of biphasic water dynamics with ‘slow’ and bulk-like relaxations with time constants ~ 0.3-4 ns and ~10 ps, respectively, as $c_{\mathrm{HA}}^{\mathrm{Aggre}}$ was approached. DSC measurements further supported the existence of two types of water.

Finally in chapter 8, we presented a general concluding remarks of the findings of this Thesis. This chapter also includes some future research problems.

References

1 D. J. C. Constable, C. Jimenez-Gonzalez and R. K. Henderson, *Org. Process Res. Dev.*, 2007, **11**, 133–137.

2 K. Grodowska and A. Parczewski, *Acta Poloniae Pharmaceutica - Drug Research*, 2010, **67**, 3–12.

3 J. R. Kelsey, in *Directory of Solvents*, ed. P. G. Whim B. P. and Johnson, Springer Netherlands, Dordrecht, 1996, pp. 158–180.

4 A. Saini and P. S. Panesar, *LWT*, 2020, **134**, 110263.

5 W. Prasad, A. D. Wani, K. Khamrui, S. A. Hussain and Y. Khetra, *Cleaner Chemical Engineering*, 2022, **3**, 100052.

6 M. Wang, X. Dong, I. C. Escobar and Y.-T. Cheng, *ACS Sustain Chem Eng*, 2020, **8**, 11046–11051.

7 R. Petibon, C. P. Aiken, L. Ma, D. Xiong and J. R. Dahn, *Electrochim Acta*, 2015, **154**, 287–293.

8 N. Izyan, W. Azelee, A. Nor, M. Ramli, N. Hasmaliana, A. Manas, N. Salamun, R. C. Man and H. El Enshasy, *Int. J. Sci. Technol. Res.*, 2019, **8**, 553–558.

9 L. SEEDORFF and E. OLSEN, *Ann Occup Hyg*, 1990, **34**, 371–378.

10 L. Cseri, M. Razali, P. Pogany and G. Szekely, *Green Chemistry*, Elsevier, 2018, pp. 513–553.

11 L. Benvenutti, A. A. F. Zielinski and S. R. S. Ferreira, *Trends Food Sci Technol*, 2019, **90**, 133–146.

12 P. J. Ginty, M. J. Whitaker, K. M. Shakesheff and S. M. Howdle, *Materials Today*, 2005, **8**, 42–48.

13 H. FUNG and T. NEALON, *Chem Pharm Bull (Tokyo)*, 1974, **22**, 454–458.

14 M. Ikeda, *Toxicol. Lett.*, 1992, **64–65**, 191–201.

15 P. Agarwal, A. Goyal and R. Vaishnav, *Asian Journal of Pharmaceutical and Clinical Research*, 2018, **11**, 27–35.

16 A. A. E. H. Hassan, S. A. E. M. Elnagar, I. M. El Tayeb, S. A. E. H. Bolbol, *Open Journal of Safety Science and Technology*, 2013, **3**, 87–95.

17 D. Raj Joshi, N. Adhikari and J. Cruz-Olivares, *J Pharm Res Int*, 2019, **28**, 1–18.

18 M. Lancaster, *Green Chemistry: An Introductory Text*, The Royal Society of Chemistry, 2016.

19 K. C. Williams, R. A. Page and A. R. Petrosky, *Journal of Strategic Innovation & Sustainability*, 2014, **9**, 11-33.

20 D. Krewski, D. Acosta, M. Andersen, H. Anderson, J. C. Bailar, K. Boekelheide, R. Brent, G. Charnley, V. G. Cheung, S. Green, K. T. Kelsey, N. I. Kerkvliet, A. A. Li, L. McCray, O. Meyer, R. D. Patterson, W. Pennie, R. A. Scala, G. M. Solomon, M. Stephens, J. Yager and L. Zeise, *J. Toxicol. Environ. Health, Part B*, 2010, **13**, 51–138.

21 M. Espino, M. de los Ángeles Fernández, F. J. V. Gomez and M. F. Silva, *TrAC, Trends Anal. Chem.*, 2016, **76**, 126–136.

22 T. Welton, *Chem. Rev.*, 1999, **99**, 2071–2083.

23 M. J. Earle and K. R. Seddon, *Pure Appl. Chem.*, 2000, **72**, 1391–1398.

24 M. T. Clough, C. R. Crick, J. Gräsvik, P. A. Hunt, H. Niedermeyer, T. Welton and O. P. Whitaker, *Chem. Sci.*, 2015, **6**, 1101–1114.

25 A. Samanta, *J. Phys. Chem. B.*, 2006, **110**, 13704–13716.

26 A. Stoppa, J. Hunger, R. Buchner, G. Hefter, A. Thoman and H. Helm, *J. Phys. Chem. B.*, 2008, **112**, 4854–4858.

27 A. M. Scurto, K. Hutchenson and B. Subramaniam, *ACS Symposium Series*, 2009, **1006**, 3–37.

28 J. P. Hallett, C. L. Kitchens, R. Hernandez, C. L. Liotta and C. A. Eckert, *Acc. Chem. Res.*, 2006, **39**, 531–538.

29 A. Das, R. Biswas and J. Chakrabarti, *J. Phys. Chem. A.*, 2011, **115**, 973–978.

30 J. E. Lewis, R. Biswas, A. G. Robinson and M. Maroncelli, *J. Phys. Chem. B.*, 2001, **105**, 3306–3318.

31 S. V Dzyuba and R. A. Bartsch, *Angew. Chem. Int. Ed.*, 2003, **42**, 148–150.

32 E. L. Smith, A. P. Abbott and K. S. Ryder, *Chem. Rev.*, 2014, **114**, 11060–11082.

33 Q. Zhang, K. De Oliveira Vigier, S. Royer and F. Jérôme, *Chem. Soc. Rev.*, 2012, **41**, 7108–7146.

34 Y. Liu, J. B. Friesen, J. B. McAlpine, D. C. Lankin, S. N. Chen and G. F. Pauli, *J. Nat. Prod.*, 2018, **81**, 679–690.

35 T. El Achkar, H. Greige-Gerges and S. Fourmentin, *Environ. Chem. Lett.*, 2021, **19**, 3397–3408.

36 B. B. Hansen, S. Spittle, B. Chen, D. Poe, Y. Zhang, J. M. Klein, A. Horton, L. Adhikari, T. Zelovich, B. W. Doherty, B. Gurkan, E. J. Maginn, A. Ragauskas, M. Dadmun, T. A. Zawodzinski, G. A. Baker, M. E. Tuckerman, R. F. Savinell and J. R. Sangoro, *Chem. Rev.*, 2021, **121**, 1232–1285.

37 R. Craveiro, I. Aroso, V. Flammia, T. Carvalho, M. T. Viciosa, M. Dionísio, S. Barreiros, R. L. Reis, A. R. C. Duarte and A. Paiva, *J. Mol. Liq.*, 2016, **215**, 534–540.

38 Y. Dai, J. van Spronsen, G. J. Witkamp, R. Verpoorte and Y. H. Choi, *Anal. Chim. Acta*, 2013, **766**, 61–68.

39 S. Kaoui, B. Chebli, safa Zaidouni, K. Basaid and Y. Mir, *Sustain. Chem. Pharm.*, 2023, **31**, 100937.

40 J. Płotka-Wasylka, M. de la Guardia, V. Andruch and M. Vilková, *Microchem. J.*, 2020, **159**, 105539.

41 H. Vanda, Y. Dai, E. G. Wilson, R. Verpoorte and Y. H. Choi, *Comptes Rendus Chimie*, 2018, **21**, 628–638.

42 A. P. Abbott, D. Boothby, G. Capper, D. L. Davies and R. K. Rasheed, *J. Am. Chem. Soc.*, 2004, **126**, 9142–9147.

43 M. Francisco, A. Van Den Bruinhorst and M. C. Kroon, *Angew. Chem., Int. Ed.*, 2013, **52**, 3074–3085.

44 A. Paiva, R. Craveiro, I. Aroso, M. Martins, R. L. Reis and A. R. C. Duarte, *ACS Sustain. Chem. Eng.*, 2014, **2**, 1063–1071.

45 D. V. Wagle, H. Zhao and G. A. Baker, *Acc. Chem. Res.*, 2014, **47**, 2299–2308.

46 J. H. Clark and S. J. Tavener, *Org. Process Res. Dev.*, 2007, **11**, 149–155.

47 P. Domínguez de María and Z. Maugeri, *Curr. Opin. Chem. Biol.*, 2011, **15**, 220–225.

48 A. P. Abbott, G. Capper, D. L. Davies, R. K. Rasheed and V. Tambyrajah, *Chem. Comm.*, 2003, 70–71.

49 J. Mondal, D. Maji and R. Biswas, *J. Chem. Phys.*, 2024, **160**, 084506.

50 J. Rajbangshi, K. Mukherjee and R. Biswas, *J. Phys. Chem. B.*, 2021, **125**, 5920–5936.

51 K. Mukherjee, A. Das, S. Choudhury, A. Barman and R. Biswas, *J. Phys. Chem. B.*, 2015, **119**, 8063–8071.

52 A. Pandey, Bhawna, D. Dhingra and S. Pandey, *J. Phys. Chem. B.*, 2017, **121**, 4202–4212.

53 Y. H. Choi, J. van Spronsen, Y. Dai, M. Verberne, F. Hollmann, I. W. C. E. Arends, G.-J. Witkamp and R. Verpoorte, *Plant Physiol.*, 2011, **156**, 1701–1705.

54 S. Emami and A. Shayanfar, *Pharm. Dev. Technol.*, 2020, **25**, 779–796.

55 I. M. Aroso, J. C. Silva, F. Mano, A. S. D. Ferreira, M. Dionísio, I. Sá-Nogueira, S. Barreiros, R. L. Reis, A. Paiva and A. R. C. Duarte, *Eur. J. Pharm. Biopharm.*, 2016, **98**, 57–66.

56 S. N. Pedro, M. G. Freire, C. S. R. Freire and A. J. D. Silvestre, *Expert Opin. Drug. Deliv.*, 2019, **16**, 497–506.

57 I. M. Aroso, R. Craveiro, Â. Rocha, M. Dionísio, S. Barreiros, R. L. Reis, A. Paiva and A. R. C. Duarte, *Int. J. Pharm.*, 2015, **492**, 73–79.

58 I. B. Qader and K. Prasad, *Pharm. Res.*, 2022, **39**, 2367–2377.

59 M. M. Abdelquader, S. Li, G. P. Andrews and D. S. Jones, *Eur. J. Pharm. Biopharm.*, 2023, **186**, 85–104.

60 K. D. Weiss, *Prog. Polym. Sci.*, 1997, **22**, 203–245.

61 I. Zahrina, M. Nasikin, E. Krisanti and K. Mulia, *Food Chem.*, 2018, **240**, 490–495.

62 M. Zheng, Y. Sun, C. Li, Y. Lu, Y. Dai and Z. Wang, *Coloration Technology*, 2023, **139**, 552–564.

63 Z. Jiang, Y. Cui, G. Zheng, Y. Wei, Q. Wang, M. Zhou, P. Wang and Y. Yu, *Green Chem.*, 2022, **24**, 5904–5917.

64 W. Chu, X. Zhang, J. Wang, S. Zhao, S. Liu and H. Yu, *Energy Stor. Mater.*, 2019, **22**, 418–423.

65 C. Zhang, L. Zhang and G. Yu, *Acc. Chem. Res.*, 2020, **53**, 1648–1659.

66 L. Geng, X. Wang, K. Han, P. Hu, L. Zhou, Y. Zhao, W. Luo and L. Mai, *ACS Energy Lett.*, 2022, **7**, 247–260.

67 M. E. Di Pietro and A. Mele, *J. Mol. Liq.*, 2021, **338**, 116597.

68 J. Wu, Q. Liang, X. Yu, Q.-F. Lü, L. Ma, X. Qin, G. Chen, B. Li, J. Wu, X. Yu, G. Chen, Q. Liang, -F Q Lü, L. Ma, X. Qin and B. Li, *Adv. Funct. Mater*, 2021, **31**, 2011102.

69 P. L. Pisano, M. Espino, M. de los Á. Fernández, M. F. Silva and A. C. Olivieri, *Microchem. J.*, 2018, **143**, 252–258.

70 A. P. R. Santana, J. A. Mora-Vargas, T. G. S. Guimarães, C. D. B. Amaral, A. Oliveira and M. H. Gonzalez, *J. Mol. Liq.*, 2019, **293**, 111452.

71 S. Khodaverdian, B. Dabirmanesh, A. Heydari, E. Dashtban-moghadam, K. Khajeh and F. Ghazi, *Int. J. Biol. Macromol.*, 2018, **107**, 2574–2579.

72 Y. L. Chen, X. Zhang, T. T. You and F. Xu, *Cellulose*, 2019, **26**, 205–213.

73 E. Durand, J. Lecomte, B. Baréa, G. Piombo, E. Dubreucq and P. Villeneuve, *Process Biochem.*, 2012, **47**, 2081–2089.

74 B. Socas-Rodríguez, M. V. Torres-Cornejo, G. Álvarez-Rivera and J. A. Mendiola, *Appl. Sci.* 2021 **11** 4897.

75 K. M. Jeong, J. Ko, J. Zhao, Y. Jin, D. E. Yoo, S. Y. Han and J. Lee, *J. Clean. Prod.*, 2017, **151**, 87–95.

76 W. C. Huang, D. Zhao, N. Guo, C. Xue and X. Mao, *J. Agric. Food Chem.*, 2018, **66**, 11897–11901.

77 Y. Dai and K. H. Row, *Molecules*, 2019, **24**, 2300.

78 C. G. González, N. R. Mustafa, E. G. Wilson, R. Verpoorte and Y. H. Choi, *Flavour Fragr. J.*, 2018, **33**, 91–96.

79 N. P. E. Hikmawanti, D. Ramadon, I. Jantan and A. Mun'im, *Plants*, 2021, **10**, 2091.

80 N. Tsvetov, O. Paukshta, N. Fokina, N. Volodina and A. Samarov, *Molecules*, 2023, **28**, 912.

81 M. J. Yang Nicole J. and Hinner, *Site-Specific Protein Labeling: Methods and Protocols*, Springer New York, 2015, pp. 29–53.

82 N. F. Hadley, *Prog. Lipid Res.*, 1989, **28**, 1–33.

83 L. Gontrani, N. V. Plechkova and M. Bonomo, *ACS Sustain. Chem. Eng.*, 2019, **7**, 12536–12543.

84 O. S. Hammond, D. T. Bowron, A. J. Jackson, T. Arnold, A. Sanchez-Fernandez, N. Tsapatsaris, V. Garcia Sakai and K. J. Edler, *J. Phys. Chem. B*, 2017, **121**, 7473–7483.

85 A. Baksi, J. Rajbangshi and R. Biswas, *Phys. Chem. Chem. Phys.*, 2021, **23**, 12191–12203.

86 S. Cao, W. Zheng, Z. Chen, F. Zhang, W. Jiang, Y. Qiu, M. Gu, Z. Chen, T. Zheng, H. Zhang, S. Wang and L. Liao, *J. Agric. Food Chem.*, 2021, **69**, 3452–3465.

87 E. Tarif, J. Mondal and R. Biswas, *J. Phys. Chem. B.*, 2019, **123**, 9378–9387.

88 E. Tarif, J. Mondal and R. Biswas, *J. Mol. Liq.*, 2020, **303**, 112451.

89 S. Das, R. Biswas and B. Mukherjee, *J. Chem. Phys.*, 2016, **145**, 84504.

90 K. Mukherjee, S. Das, J. Rajbangshi, E. Tarif, A. Barman and R. Biswas, *J. Phys. Chem. B.*, 2021, **125**, 12552–12567.

91 S. S. Hossain and A. Samanta, *J. Phys. Chem. B.*, 2017, **121**, 10556–10565.

92 D. Maji and R. Biswas, *J. Chem. Phys.*, 2023, **158**, 174503.

93 N. Subba, E. Tarif, P. Sen and R. Biswas, *J. Phys. Chem. B.*, 2020, **124**, 1995–2005.

94 A. Das and R. Biswas, *J. Phys. Chem. B.*, 2015, **119**, 10102–10113.

95 A. Boisset, S. Menne, J. Jacquemin, A. Balducci and M. Anouti, *Phys. Chem. Chem. Phys.*, 2013, **15**, 20054–20063.

96 T. Palomba, G. Ciancaleoni, T. Del Giacco, R. Germani, F. Ianni and M. Tiecco, *J. Mol. Liq.*, 2018, **262**, 285–294.

97 J. Huang, X. Guo, T. Xu, L. Fan, X. Zhou and S. Wu, *J Chromatogr. A*, 2019, **1598**, 1–19.

98 A. Sil, Sangeeta, R. Bhati, S. Das and B. Guchhait, *J. Mol. Liq.*, 2023, **388**, 122761.

99 B. Guchhait, S. Daschakraborty and R. Biswas, *J. Chem. Phys.*, 2012, **136**, 174503.

100 B. Guchhait, S. Das, S. Daschakraborty and R. Biswas, *J. Chem. Phys.*, 2014, **140**, 104514.

101 R. Biswas, A. Das and H. Shirota, *J. Chem. Phys.*, 2014, **141**, 134506.

102 H. Shirota, J. Rajbangshi, M. Koyakkat, A. Baksi, M. Cao and R. Biswas, *J. Photochem. Photobiol. A: Chem.*, 2023, **437**, 114504.

103 M. Saha, M. Saha, M. S. Rahman, M. N. Hossain, D. E. Raynie and M. A. Halim, *J. Phys. Chem. A*, 2020, **124**, 4690–4699.

104 F. Al-Akayleh, H. H. Mohammed Ali, M. M. Ghareeb and M. Al-Remawi, *J. Drug Deliv. Sci. Technol.*, 2019, **53**, 101159.

105 J. M. Silva, R. L. Reis, A. Paiva and A. R. C. Duarte, *ACS Sustain. Chem. Eng.*, 2018, **6**, 10355–10363.

106 M. H. Zainal-Abidin, M. Hayyan, G. C. Ngoh, W. F. Wong and C. Y. Looi, *J. Control. Release*, 2019, **316**, 168–195.

107 A. Roda, F. Santos, A. A. Matias, A. Paiva and A. R. C. Duarte, *J. Supercrit. Fluids*, 2020, **161**, 104826.

108 A. Gutiérrez, S. Aparicio and M. Atilhan, *Phys. Chem. Chem. Phys.*, 2019, **21**, 10621–10634.

109 A. R. C. Duarte, A. S. D. Ferreira, S. Barreiros, E. Cabrita, R. L. Reis and A. Paiva, *Eur. J. of Pharma. Biopharm.*, 2017, **114**, 296–304.

110 M. Zakrewsky, A. Banerjee, S. Apte, T. L. Kern, M. R. Jones, R. E. D. Sesto, A. T. Koppisch, D. T. Fox and S. Mitragotri, *Adv. Healthc. Mater*, 2016, **5**, 1282–1289.

111 J. M. Silva, E. Silva, R. L. Reis and A. R. C. Duarte, *Sustain Chem Pharm*, 2019, **14**, 100192.

112 J. Mondal, N. C. Maity and R. Biswas, *J. Chem. Sci.*, 2023, **135**, 1–12.

113 S. Saha, P. K. Mandal and A. Samanta, *Phys. Chem. Chem.*, 2004, **6**, 3106–3110.

114 M. Kondo, X. Li and M. Maroncelli, *J. Phys. Chem. B*, 2013, **117**, 12224–12233.

Chapter 2

Experimental Methods and Procedures for Data Analysis

The primary experimental techniques utilized for investigating various complex systems in this thesis encompass broadband dielectric relaxation spectroscopy, steady-state UV-Vis absorption, fluorescence, time-resolved fluorescence employing the time-correlated single photon counting (TCSPC) principle, and ultrafast streak camera. This chapter provides a succinct overview of these experimental methods and outlines the protocols for data analysis.

2.1 Dielectric Relaxation Spectroscopy (DRS)

Dielectric relaxation spectroscopy (DRS) is a powerful technique utilized to study the relaxation of macroscopic electric polarization within a liquid under the influence of a frequency-dependent external electric field. This relaxation phenomenon reflects the ensemble average of dipole-dipole correlations within the liquid. Specifically, DRS enables the investigation of the collective orientational motion of molecular dipoles, which significantly contributes to the macroscopic electric polarization. By analyzing the frequency-dependent behaviour of the electric polarization, DRS provides valuable insights into the dynamics and behaviour of dipolar liquids at a molecular level.

2.1.1 General Overview about DRS

The polarization induced in dielectric materials by an external electric field typically arises from two mechanisms: the distortion of the electron cloud distribution and the reorientation of molecular dipoles within the system. In the context of a liquid at room temperature, achieving a specific polarization level necessitates rapid motion of microscopic particles such as molecules, ions, atoms, and electrons, typically within a timeframe of approximately 1 μs or less. Rapid changes in electric field strength relative to particle motion cause macroscopic polarization to lag behind equilibrium, while gradual variations allow the system to achieve its equilibrium polarization state[1]. The dielectric properties of the systems under studies are measured at the equilibrium state.

The interaction of electromagnetic field with matter can be expressed by Maxwell's equation[2] as follows:

$$rot\,\boldsymbol{E} = -\frac{\partial}{\partial t}\boldsymbol{B} \tag{2.1}$$

$$rot\,\boldsymbol{H} = \boldsymbol{j} + \frac{\partial}{\partial t}\boldsymbol{D} \tag{2.2}$$

$$div\,\boldsymbol{D} = \rho_e \tag{2.3}$$

and

$$div\,\boldsymbol{B} = 0 \tag{2.4}$$

In the above Eq. (2.1-2.4), $\boldsymbol{E}$ and $\boldsymbol{H}$ symbolize the electric and magnetic fields, respectively, while $\boldsymbol{D}$ represents the dielectric displacement and $\boldsymbol{B}$ denotes the magnetic induction. The current density is denoted by $\boldsymbol{j}$, and the charge density is defined as ρ_e. In case of homogeneous, non-dispersive, isotropic material under a weak electric field, the expression for $\boldsymbol{D}$ can be formulated as,

$$\boldsymbol{D} = \varepsilon^* \varepsilon_0 \boldsymbol{E} \tag{2.5}$$

Where ε_0 (8.85×10^{-12} Fm^{-1}) is the free space permittivity and ε^* is defined as complex dielectric function. Maxwell's equations elucidate that the complex dielectric function (ε^*) of a material becomes time or frequency-dependent when dynamic phenomena occur within the sample. For a periodic electric field $E(t) = E\,exp(-i\omega t)$, where ω denotes the angular frequency and $i = \sqrt{-1}$, the complex permittivity $\varepsilon^*(\omega)$ is formulated as $\varepsilon^*(\omega) = \varepsilon'(\omega) - i\varepsilon''(\omega)$, where ε' and ε'' represent the real and imaginary parts of the complex dielectric function, respectively.

2.1.2 DRS Measurements

Dielectric relaxation measurements presented in this thesis integrated three distinct setups to measure the broadband dielectric spectra on the frequency region from 20 Hz to 50 GHz.

(i) A low frequency impedance analyzer (E4990A) equipped with liquid test fixture (15452A), covering a frequency range from 20 Hz to 10 MHz. The instrument with the the liquid test fixture has been shown in **Figure 2.1**. This impedance analyzer accessed the relatively of the sample by recording the capacitance and conductance of the material placed between two parallel plates. The instrument was calibrated by conducting measurements on a 50-ohm resistance, performing short compensation, and measuring air capacitance.

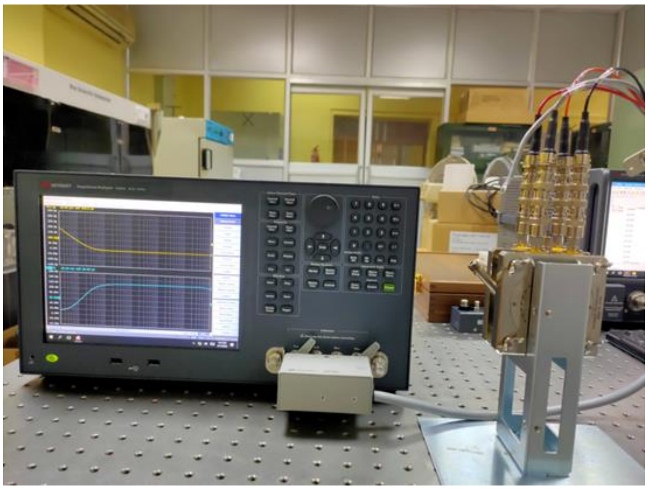

Figure 2.1 Impedance analyzer (E4990A) with the liquid test fixture

(ii) A middle-frequency impedance analyzer (E4991B) coupled with an open-ended coaxial line probe, featuring a dielectric probe kit (Keysight 85070E), and a high-temperature coaxial cable with high temperature probe, encompassing a frequency range from 10 MHz to 500 MHz. Calibration procedures involved measurements on air, shorting block, and water serving open, short, and load reference, respectively.

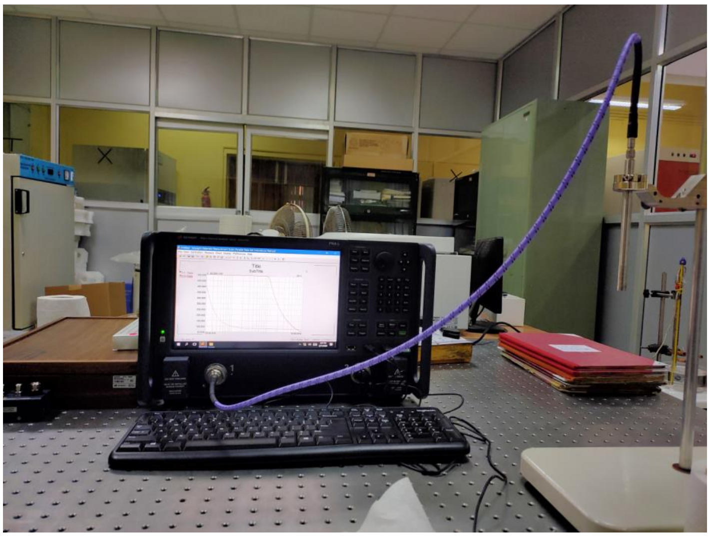

Figure 2.2 PNA-L network analyzer with open ended coaxial probe.

(iii) A PNA-L network analyzer (N5235B) complemented by an open-ended coaxial probe kit (N1501A), facilitating measurements across the frequency spectrum from 500MHz – 50GHz. Calibration of the instruments were performed by measuring air, shorting block and water open, short and load respectively. The instrument with the open-ended coaxial cable has been shown in **Figure 2.2**.

2.1.3 Mathematical Models and Data Analysis Procedures

The experimentally collected data from all three experimental setups were combined and finally set to analyse with the help of different mathematical models in order to gain comprehensive understanding about the dipolar rearrangements of the systems studied in this thesis. The models are described below

2.1.3.1 Debye Model

In order to analyse experimental DR data, the Debye model is the simplest one to describe complex dielectric response (ε^*). The functional form of Debye model[3] is given by,

$$\varepsilon^* = \varepsilon_\infty + \frac{\Delta\varepsilon}{1+i\omega\tau_D} \tag{2.6}$$

where ω is the angular frequency which is connected to linear frequency via the relation $\omega = 2\pi\nu$. $\Delta\varepsilon$ is termed as the dielectric strength which is defined by $\Delta\varepsilon = \varepsilon_s - \varepsilon_\infty$, where ε_s $(\omega \to 0)$ is the static dielectric constant at zero limiting frequency and ε_∞ $(\omega \to \infty)$ is the high frequency dielectric constant. τ_D represents the characteristic relaxation time.

2.1.3.2 Non-Debye Model

Dielectric relaxation with symmetric broadening is subject to treated with the Cole-Cole[4] relaxation model which is given by

$$\varepsilon^* = \varepsilon_\infty + \frac{\Delta\varepsilon}{1+(i\omega\tau_{CC})^{1-\alpha}} \tag{2.7}$$

The parameter α represents a symmetric broadening of the dielectric function. It can take any value within the range $0 \leq \alpha < 1$. τ_{CC} denotes the characteristic Cole-Cole relaxation time.

Alternatively, asymmetric broadening of the dielectric relaxation is taken care by the Cole-Davidson model[5,6]. This model is mathematically expressed as

$$\varepsilon^* = \varepsilon_\infty + \frac{\Delta\varepsilon}{(1+i\omega\tau_{CD})^{\beta}} \tag{2.8}$$

Here the parameter β represents an asymmetric broadening of the dielectric function. It may take any value within the range $0 < \beta \leq 1$. τ_{CD} denotes the characteristic Cole-Davidson relaxation time.

Havriliak-Negami[7] (HN) model is more standard and general model used to analyse complex dielectric function. The functional form of this model can be expressed as

$$\varepsilon^* = \varepsilon_\infty + \frac{\Delta\varepsilon}{(1+(i\omega\tau_{HN})^{1-\alpha})^{\beta}} \tag{2.9}$$

Here τ_{HN} is the relaxation time.

Dielectric relaxation in complex chemical systems may arise from the superposition of multiple relaxation modes, reflecting the diverse molecular interactions and dynamics within the system. This interplay of relaxation modes contributes to the overall dielectric behaviour observed. In practical for those system the HN function is expressed as a summation form:

$$\varepsilon^* = \varepsilon_\infty + \sum_j \frac{\Delta\varepsilon}{(1+(i\omega\tau_j)^{1-\alpha})^{\beta}} \tag{2.10}$$

2.1.3.3 Data Processing

Selecting appropriate mathematical models is essential for extracting physically meaningful insights from complex dielectric responses. The efficacy of the fit is evaluated by examining both goodness of fit (χ^2) parameters and the residual of the fittings. χ^2 is defined as[8],

$$\chi^2 = \frac{1}{2m-l}\sum_{i=1}^{m}\left[\left(\frac{\delta\varepsilon_i'}{\sigma(\varepsilon_i')}\right)^2 + \left(\frac{\delta\varepsilon_i''}{\sigma(\varepsilon_i'')}\right)^2\right] \tag{2.11}$$

where *m* denotes the number of data triples $(\nu, \varepsilon', \varepsilon'')$, *l* is the number of adjustable parameters, and $\delta\varepsilon_i$ and $\sigma(\varepsilon_i)$ are the residuals and standard deviation of the individual data points, respectively.

2.1.3.4 Conductivity Correction

DC conductivity significantly contribute to the dielectric loss part that is, imaginary part of the total dielectric spectra. The dipolar contribution of the liquid systems often submerged into the conductivity contribution. To get rid of this conductivity correction of the imaginary part of the dielectric spectra is crucial. The conductivity corrected DR spectra have been presented below[1],

$$\varepsilon^*(\nu) = \varepsilon'(\nu) - \left[i\varepsilon''(\nu) + \frac{ik}{2\pi\varepsilon_0\nu}\right] \tag{2.12}$$

where ε_0 denotes the free space permittivity and k denotes the conductivity of the medium. ε' and ε'' are the real and imaginary part of the complex permittivity.

2.2 Steady State UV-Vis Absorption Spectroscopy

In this thesis, the steady-state UV-Vis absorption spectra were acquired using a UV-2600 spectrophotometer manufactured by SHIMADZU. **Figure 2.3** illustrates a schematic representation of a UV-Vis absorption spectrophotometer. It employs two light sources: a tungsten lamp for visible wavelengths and a deuterium lamp for ultraviolet wavelengths. A mirror guides the light emitted from the lamp through a filter before it enters the monochromator. Within the monochromator, the beam of polychromatic light is dispersed into various monochromatic rays. These rays are split into two components: one directed towards the reference and the other transmitted through the sample. Both the transmitted light from the reference and the sample reach photodiode detectors. Subsequently, after several sequential data processing steps such as signal enhancement and analog-to-digital conversion (ADC), the final absorption spectra are recorded.

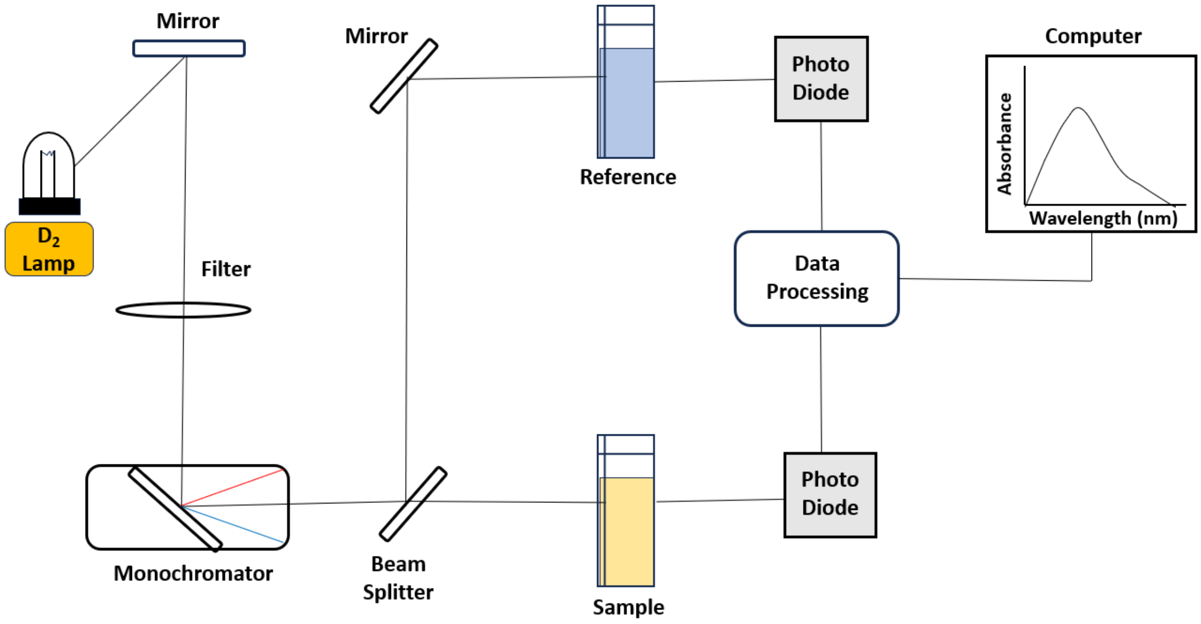

Figure 2.3. Schematic illustration of an UV-Vis absorption spectrophotometer.

UV-Vis absorption spectroscopy operates on the fundamental Beer-Lambert Law, which states that absorbance (A) correlates linearly with both the path length (l) and the concentration (c) of the sample, according to the equation $A = log\frac{I_0}{I} = \varepsilon cl$. Here, I_0 represents the intensity of the incident light, while I denotes the intensity of the transmitted light. The parameter ε, termed the molar extinction coefficient or molar absorptivity, is a constant of proportionality.

Throughout this thesis, absorption measurements were conducted with a fixed path length (l) of 1 cm and sample concentrations (c) not exceeding $10^{-5}\ M$.

2.3 Steady State Fluorescence Spectroscopy

The steady-state fluorescence emission measurements corroborated in the thesis were conducted using a fluorimeter (Fluorolog, Jobin-Yvon, Horiba). **Figure 2.4** provides a schematic overview of the fluorescence spectrophotometer setup. A continuous xenon (Xe) lamp serves as the excitation light source. The light emitted by the Xe lamp passes through an excitation monochromator, where it is split into monochromatic wavelengths and any undesired wavelengths (stray light) are blocked. The monochromator's motorized mechanism facilitates automatic selection and scanning of wavelengths. The monochromatic light of the desired wavelength is then used to excite the sample under examination. Subsequently, the emitted

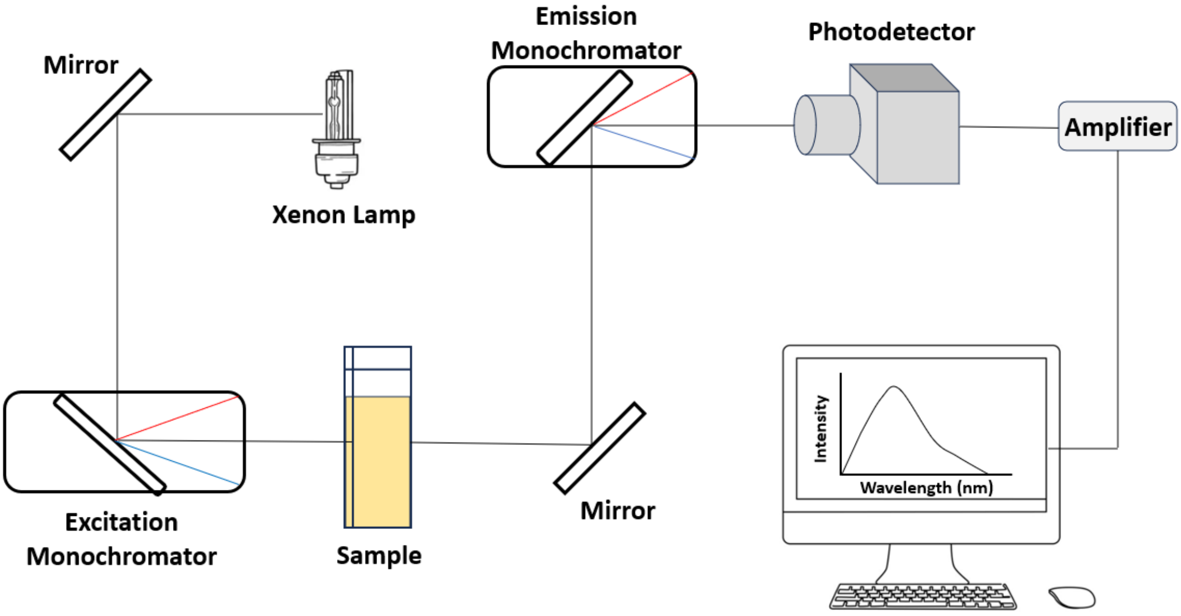

Figure 2.4. Schematic representation of fluorescence spectrophotometer set-up

fluorescence light travels to an emission monochromator positioned perpendicular to the path of the excitation light. The fluorescence emission is detected by a photomultiplier tube (PMT) and is projected onto a computer screen following amplification and appropriate electronic conversion.

2.4 Time Resolved Fluorescence Spectroscopy

The time-resolved fluorescence investigations detailed in the thesis primarily utilized the time-correlated single photon counting (TCSPC) technique[9,10]. For these studies, pulsed diode lasers operating at wavelengths of 409 nm and 375 nm were employed.

2.4.1 TCSPC Technique

The LifeSpec-ps instrument from Edinburgh Instruments, based in Livingston, U.K., was utilized for conducting time-correlated single photon counting (TCSPC) measurements. In these experiments, time-resolved fluorescence emission data were collected using the TCSPC setup operating in reverse mode.

Figure 2.5 presents a schematic depiction of a typical TCSPC setup in reverse mode. A pulsed diode laser serves as the excitation source, initiating the excitation of fluorophore molecules

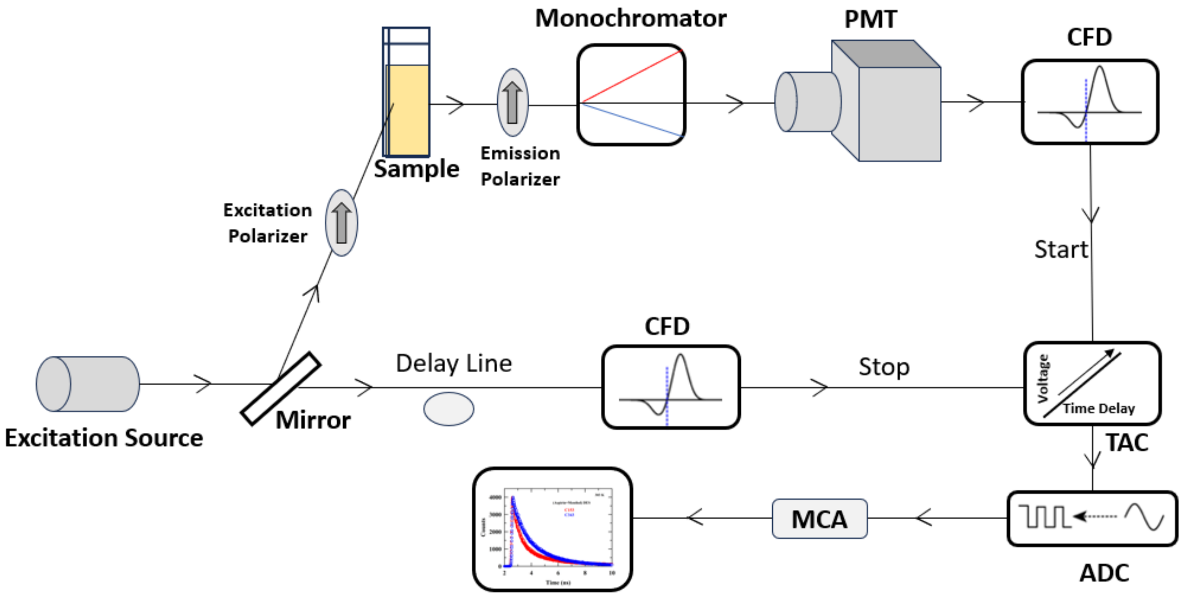

Figure 2.5 Schematic representation of a TCSPC set-up in reverse mode

within the sample contained in a quartz cuvette. Upon excitation, the first emitted photon triggers a signal, which is then routed through a constant fraction discriminator (CFD) to determine its arrival time. Subsequently, the signal proceeds to a time-to-amplitude converter (TAC), where a voltage ramp is initiated.

In the reverse mode of TCSPC, a simultaneous signal is generated when the second excitation pulse from the laser interacts with the sample. This signal also passes through the CFD and then to the TAC to terminate the voltage ramp. The output pulse from the TAC, proportional to the delay time (Δt) between the start and stop signals, undergoes analog-to-digital conversion (ADC) and is transmitted to a multichannel analyzer (MCA) for the computation of numerical values. Repeating this process multiple times generates a decay histogram comprising photon counts and time channels within the MCA.

2.4.2 Data Analysis

2.4.2.1 Solvation Dynamics

In solvation dynamics studies, we typically record 14-16 decay curves at equally spaced wavelengths across the steady-state emission spectrum of a fluorophore dissolved in the sample. This technique, also known as Stokes shift dynamics, allows for a comprehensive investigation into the process of solvation, which is the interaction between the solvent molecules and the excited state of the fluorophore. By examining how the fluorescence intensity changes over time and at different wavelengths, one can gain insights into the dynamics of the solvation process. In most of experiments performed in this thesis coumarin 153 (C153)[11–13] and coumarin 343 (C343)[14,15] has been employed as the local reporter. Note that in solvation dynamics measurements we have used 409 nm wavelength laser as an excitation light source with the full with at half maxima (FWHM) of the instrument response function to be ~90 ps. The distinctive feature of dynamic Stokes shift is the decay at the blue end and subsequent rise followed by decay at the red end wavelengths, relative to the peak of the steady-state emission spectrum. In TCSPC, the fluorescence decay $\left(N(t)\right)$ is the result of convolving the instrument response function (IRF) $\left(R(t)\right)$ with the sample's response $\left(I(t)\right)$. To extract $I(t)$ from the $N(t)$ and $R(t)$ data, an iterative reconvolution method employing nonlinear least square analysis was utilized. This involved fitting experimental $I(t)$ using a summation of multi-exponential functions: $I(t) = \sum_{i=1}^{N} \alpha_i \exp\left(-\frac{t}{\tau_i}\right)$, where α_i and τ_i represent the pre-exponential factors and characteristic lifetimes, respectively. Subsequently, time-resolved emission spectra (TRES) were reconstructed from the intensity decays collected for each system, following established protocols. The fluorescence decays obt[9,13,16]ained at various wavelengths (λ_j) were then fitted with multi-exponential functions,

$$I(\lambda_j t) = \sum_{i=1}^{N} \alpha_i(\lambda_j) \exp\left(-t/\tau_i(\lambda_j)\right), \tag{2.13}$$

where $\sum_i \alpha_i(\lambda_j) = 1$.

Following this, a new series of normalized intensity decays were generated to ensure that the time-integrated intensity at each wavelength matched the steady-state intensity at that wavelength, denoted as $F(\lambda_j)$. The normalization factor is

$$H(\lambda_j) = \frac{F(\lambda_j)}{\int_0^\infty I(\lambda_j, t)dt} = \frac{F(\lambda_j)}{\sum_i \alpha_i(\lambda_j)\tau_i(\lambda_j)} \tag{2.14}$$

This normalization factor, $H(\lambda_j)$, was then multiplied with $I(\lambda_j, t)$ to obtain the appropriate normalized function.

$$I'(\lambda_j, t) = H(\lambda_j)I(\lambda_j, t) = \alpha_i'(\lambda_j)exp(-t/\tau_i(\lambda_j)) \tag{2.15}$$

Here $\alpha_i'(\lambda_j) = H(\lambda_j)\alpha_i(\lambda_j)$. Utilizing the value of $I'(\lambda_j, t)$ TRES at any wavelength and any time can be calculated. To facilitate further analysis, the TRES were transformed into frequency representation, with appropriate intensity weighting by λ^2. Subsequently, each TRES was fitted with a log-normal shape function to establish a continuous spectrum representation. The peak frequencies derived from these fitted spectra were then employed to construct the solvation response function[13], $S(t)$.

$$S(t) = \frac{(\nu(t) - \nu(\infty))}{(\nu(0) - \nu(\infty))} \tag{2.16}$$

In this context, $\nu(0)$, $\nu(t)$ and $\nu(\infty)$ represent the frequency (typically the peak frequency) for the reconstructed time-resolved emission spectrum at $t = 0$ (immediately after excitation), at any given moment t, and at a sufficiently long time $t = \infty$ when the solvent has completely relaxed.

The solvation response function $S(t)$ is a normalized function that transitions from unity at $t = 0$ to zero at $t = \infty$ as the solvent environment relaxes in response to the immediate alteration in the charge distribution of the solute (fluorophore) due to photo-excitation. It's expected that $\nu(\infty)$ will match the steady-state emission peak frequency for a particular system. However, in some cases, the steady-state emission spectrum might exhibit a slight blue shift compared to the time-resolved emission spectrum at $t = \infty$, indicating that the excited fluorophore is surrounded by a solvent environment that hasn't completely relaxed. This discrepancy is attributed to steady-state emission from the excited solute within an incompletely relaxed solvent environment, causing the observed blue shift.

Subsequently, the average solvation time τ_s was determined by integrating the measured decay of $S(t)$ over time:

$$\langle\tau_s\rangle = \int_0^\infty dtS(t) = \int_0^\infty dt[\textstyle\sum_i \alpha_i \exp(-t/\tau)] = \sum_i \alpha_i \tau_i \tag{2.17}$$

where $\sum_i \alpha_i = 1$, and α_i and τ_i are the amplitude and time constants respectively, related with the i-th component of $S(t)$ decay.

2.4.2.2 Rotational Dynamics

The time-correlated single photon counting (TCSPC) technique is also employed to investigate the reorientational dynamics of fluorophores dissolved in a medium and to explore the time-dependent frictional profile of the medium[9,16,17]. The fundamental principle underlying reorientational dynamics measurements relies on selectively exciting fluorophores with absorption transition dipoles parallel to the electrical vector of polarized excitation light. The emission intensity decays collected through parallel ($I_{para}(t)$) and perpendicular ($I_{perp}(t)$) emission polarizations are contingent upon the reorientation of the excited fluorophore and evolve over time. As time progresses, the disparity between $I_{para}(t)$ and $I_{perp}(t)$ gradually diminishes. Leveraging this loss of anisotropy enables the extraction of information regarding reorientational dynamics, provided that the fluorophore's lifetime, dissolved within a given medium, is comparable to or greater than its reorientational time. Time dependent fluorescence anisotropy is defined as[9],

$$r(t) = \frac{I_{para}(t) - I_{perp}(t)}{I_{para}(t) + 2I_{perp}(t)} \tag{2.18}$$

The polarization characteristics of the optical setup significantly influence the measured anisotropy, necessitating a correction to mitigate errors stemming from instrumental polarization preferences. This correction factor, denoted as the geometric factor (G), represents the ratio between the transmission efficiency for vertically polarized light and that of horizontally polarized light, and is calculated as: $G = \frac{I_{para}(t)}{I_{perp}(t)}$. The geometric factor ($G$) is determined through the tail matching of vertically (parallel) and horizontally (perpendicular) polarized fluorescence emission intensity decays. Consequently, the corrected time-resolved fluorescence anisotropy, $r(t)$, is expressed as:

$$r(t) = \frac{I_{para}(t) - GI_{perp}(t)}{I_{para}(t) + 2GI_{perp}(t)} \tag{2.19}$$

The obtained $r(t)$ values were subsequently fitted using single and multi-exponential functions:

$$r(t) = r(0) \sum_i \alpha_i \exp(-t/\tau_i) \tag{2.20}$$

where r(0) represents the initial anisotropy. α_i and τ_i denote the amplitude and time constant of the i-th decay component, respectively. The summation is constrained by $\sum_i \alpha_i = 1$.

In this thesis, the initial anisotropy $r(0)$ was set to specific values: 0.376 for C153[17], 0.35 for C343[14], and 0.38 for trans-2-[4-(dimethylamino)styryl]-benzothiazole (trans-DMASBT)[18], while fitting $r(t)$. The average rotational correlation time (τ_{rot}) was subsequently estimated using the following formula:

$$\langle \tau_{rot} \rangle = \int_0^{\infty} dr[r(t)/r(0)] = \sum_i \alpha_i \tau_i \tag{2.21}$$

2.5 Ultrafast Streak Camera

In the context of a streak camera, "streak" refers to the display of the temporal evolution of a light pulse as a continuous line, or streak, on an oscilloscope or other display device. The streak camera is able to capture this temporal evolution by spreading out the light pulse in time using a deflection device (such as a sweep circuit) and then recording the resulting streak of light on a detector. This allows for time-resolved measurements of light emission, with high temporal and spectral resolution A schematic diagram is presented in **Figure 2.6** to illustrate the detection technique of time-resolved fluorescence decay using a streak camera.

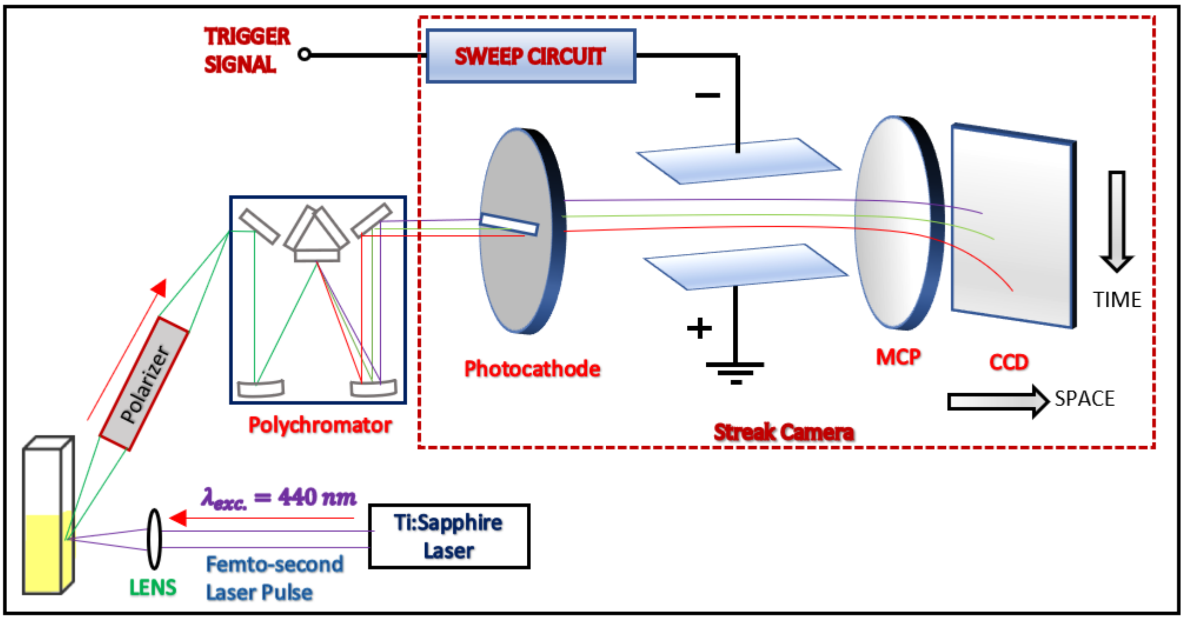

Figure 2.6. Schematic diagram of time resolved fluorescence experiment using streak camera

The excitation source is a femtosecond laser pulse with an excitation wavelength of 440nm. The resulting fluorescence is collected at a right angle with respect to the excitation, passed through a polarizer placed at the magic angle (54.70°) polarization, and directed towards a spectrograph or polychromator. The fluorescence light is then diffracted by a grating and directed towards the input slit of the streak camera, where it is selected and converted into a stream of electrons. The stream of electrons is then directed towards the streak tube. As the electrons pass through the streak tube, they are deflected by an electric field that varies over time, and this field is synchronized with the pulsed laser. The synchronization causes the electrons to be deflected in proportion to the time delay between different parts of the fluorescence pulse, thus generating a two-dimensional image on the screen of the streak camera.

References

1 C. J. F. Böttcher, O. C. van Belle, P. Bordewijk and A. Rip, *Theory of electric polarization, Volume 2*, Elsevier Scientific Publishing Company, Netherlands, 1996.

2 J. C. Maxwell, *A Treatise on Electricity and Magnetism*, Clarendon press, 1881.

3 P. J. W. Debye, *Polar Molecules*, Chemical Catalog Company, Incorporated, 1929.

4 K. S. Cole and R. H. Cole, *J. Chem. Phys.*, 1941, **9**, 341–351.

5 D. W. Davidson and R. H. Cole, *J. Chem. Phys.*, 1950, **18**, 1417–1417.

6 D. W. Davidson and R. H. Cole, *J. Chem. Phys.*, 1951, **19**, 1484–1490.

7 S. Havriliak and S. Negami, *Polymer*, 1967, **8**, 161–210.

8 Bevington, P. R. and D. K. Robinson, *Data reduction and error analysis for the physical sciences*, McGraw-Hill:, New York, 3rd Edition, 1969.

9 JR Lakowicz, *Principles of Fluorescence Spectroscopy*, Springer, New York, 3rd Edition, 2006.

10 D. V. O'Connor and D. Phillips, *Time Correlated Single Photon Counting*, Academic Press London, 1984.

11 B. Guchhait, H. Al Rasid Gazi, H. K. Kashyap and R. Biswas, *J. Phys. Chem. B.*, 2010, **114**, 5066–5081.

12 E. Tarif, J. Mondal and R. Biswas, *J. Phys. Chem. B.*, 2019, **123**, 9378–9387.

13 M. L. Horng, J. A. Gardecki, A. Papazyan and M. Maroncelli, *J. Phys. Chem.*, 1995, **99**, 17311–17337.

14 S. Koley, H. Kaur and S. Ghosh, *Phys. Chem. Chem. Phys.*, 2014, **16**, 22352–22363.

15 E. Tarif, J. Mondal and R. Biswas, *J. Mol. Liq.*, 2020, **303**, 112451.

16 D. J. S. Birch and R. E. Imhof, *Topics in Fluorescence Spectroscopy, Vol. 1: Techniques.*, Plenum Press, New York, 1991.

17 M. L. Horng, J. A. Gardecki and M. Maroncelli, *J. Phys. Chem. A.*, 1997, **101**, 1030–1047.

18 S. K. Saha, P. Purkayastha, A. B. Das and S. Dhara, *J. Photochem. Photobiol. A: Chem.*, 2008, **199**, 179–187.

Chapter 3

Temperature Dependent Dielectric Relaxation Measurements of (Acetamide + K/Na SCN) Deep Eutectic Solvents: Decoding the Impact of Cation Identity via Computer Simulations

3.1 Introduction

Deep depression of freezing points for solid multi-component mixtures are known to depend on the identity of the guest components.[1–8] The subsequent variation in the eutectic temperature deeply influences the dynamical response of deep eutectic solvents (DESs). Several relaxation measurements, previous[9–12] as well as more recent ones,[13–18] provided ample support to this view. Interestingly, controlled X-ray or neutron scattering measurements keeping the host unchanged have not been carried out yet to explore the guest identity dependence of the solution structure, although a few experimental and simulation studies made attempts to elucidate the local environments in several DESs.[19–21] Differential scanning calorimetric (DSC) measurements of several amide DESs, on the other hand, revealed a dependence of the glass transition temperature (T_g) on the identity of the solute guests, reflecting a possible impact on the cooperativity and fragility of those systems[22]. Computer simulation studies of a few ionic acetamide DESs predicted anion dependence of the waiting time distributions associated with angular jumps and jump angle distributions of the host acetamide molecules[23,24] Picosecond-resolved fluorescence measurements,[25–29] fluorescence correlation spectroscopic experiments,[29,30] ultrafast Kerr effect spectroscopic measurements,[13,31] and dielectric relaxation (DR) studies[17,32] revealed significant impact of guest identity on the inhomogeneous relaxation kinetics of the systems investigated. A computer simulation study has recently predicted, similar to anion dependence of acetamide angular moves, a cation identity dependence of the translational jump frequencies and lengthscales[33] of the host acetamide molecules in (acetamide + potassium/sodium thiocyanate) DESs.

The experimental and simulation results discussed above suggest that an external control may be exercised to easily regulate certain physicochemical properties of a given set of DESs and their overall inhomogeneous relaxation features; and this external control is a choice of minor components. The modification of the static dielectric constant (ε_s) of the host acetamide (ε_s ~64)[17] in a few ionic and non-ionic DESs observed in MHz-GHz DR experiments supports this view. More specifically, the DR measurements of (acetamide + LiBr/NO_3/ClO_4) DESs showed that among the three anions considered, Br^- induced the maximum reduction of medium ε_s. Similar guest-induced reduction of ε_s has also been found in earlier measurements with electrolyte solutions of small molecular solvents[34–39] and binary mixtures of solvents with differing polarities[40,41]. This is important because guest-controlled tuning of ε_s provides a handle to alter not only the solvating power of a given medium but also the static solvent effects[32] on chemical reactions occurring in it. Moreover, the medium dynamics undergoes modifications, both at the microscopic (via the inter-species specific interactions) and at the macroscopic (through the solution viscosity, η) lengthscales, opening avenues for affecting reactions via solvent dynamic effects.[42–44] This is indeed the scenario as previous time-resolved fluorescence measurements[25,26,45] revealed ion identity dependence of the heterogeneous relaxation dynamics and the extent of viscosity-decoupling of relaxation times. Interestingly, these findings serve as important inputs for liquid solvent engineering for designing solvent media for tailoring chemical reactions. A recent simulation study on DR of (acetamide + LiBr/NO_3/ClO_4) has already indicated that the anion-acetamide interactions partially damage the liquid amide hydrogen bond (H-bond) network and frustrate the orientational order, eventually leading to anion-dependent reduction of the ε_s.[46]

However, a similar experimental or simulation study exploring the cation identity and concentration dependence of the DR response of ionic DESs has not been carried out yet. Given the simulation predictions of cation identity dependence of acetamide jump characteristics in (acetamide + K/NaSCN) DESs, the cation identity and concentration dependences of reorientational relaxations and H-bond fluctuations, and their connections to the DR should be studied in detail. The importance of such a study stems not only from the basic science aspects that connect the cooperativity with the T_g and its implications on DR of these DESs, but also from the need to estimate the cross-term (dipole-ion) contributions to the frequency-dependent total DR spectra. This requires a thorough and systematic experimental and computational DR studies involving temperature and cation concentration dependencies where the measured DR could be understood in microscopic terms through the decompositions of the total DR spectra (simulated) into three individual contributions (dipole-dipole, dipole-ion, and ion-ion), and via the analyses of the single particle collective reorientational relaxations and the H-bond fluctuation dynamics. Such a study has been performed here with [acetamide+K/NaSCN] DES having general composition $0.25[f\mathrm{KSCN} + (1-f)\mathrm{NaSCN}] + 0.75\mathrm{CH_3CONH_2}$ (where 0.25 and 0.75 are the mole fraction of salts and acetamide, respectively) in the frequency window of $0.2 \leq \nu/GHz \leq 50$ and temperature range $303 \leq T/K \leq 343$. The impact of successive replacement of K^+ by Na^+ was monitored by changing f between 0 and 1.

3.2 Experimental Details

3.2.1 Sample Preparation

Acetamide (≥99%, Sigma-Aldrich, $T_m \approx$ 352-354 K), NaSCN (≥99%, Sigma-Aldrich, $T_m \approx$ 560 K) and KSCN ((≥99%, Sigma-Aldrich, $T_m \approx$ 446.3 K) were vacuum dried (~300 K) over night before use. Sample preparation and measurements were done in a tightly humidity controlled (humidity level ~ 35%) and temperature-controlled lab. A tight control over the humidity was particularly necessitated by the hygroscopic nature of all the DES components considered here. In each measurement ~10 g of sample was prepared by mixing required amount of acetamide, NaSCN/KSCN in the following ratio $0.25[f\mathrm{KSCN} + (1-f)\mathrm{NaSCN}] + 0.75\mathrm{CH_3CONH_2}$ in a ~15 ml screw capped vial. The sample vial was then heated to ~345 K in an oil bath under constant stirring ~600 rpm for 3 hours until it formed a transparent liquid. Then the melt was allowed to cool to room temperature (~303 K) gradually. A transparent liquid thus formed maintained its liquid phase during the measurements and even much after the required experiments. The detailed description of the sample preparation could be found elsewhere.[26]

In addition, the glass transition temperatures (T_gs) of these DESs were determined using a differential scanning calorimeter (DSC, TA Instrument Q2000). The DSC scans were conducted over a temperature range of 193 K to 373 K with a heating/cooling rate of 10 K/min.

3.2.2 DR Measurement Details

The frequency dependent complex dielectric function of a given material is commonly represented as follows [47,48]

$$\varepsilon^*(\omega) = \varepsilon'(\omega) - \left[i\varepsilon''(\omega) + \frac{ik}{\omega\epsilon_0}\right], \qquad (3.1)$$

where ϵ_0 denotes the free space permittivity and k denotes the static conductivity of the medium. Note here that angular (ω) and linear (ν) frequencies are connected via the following relation, $\omega = 2\pi\nu$.

$\varepsilon'(\omega)$ is the real part of the complex permittivity and represents a measure of polarisation in a material, while the imaginary part, $\varepsilon''(\omega)$, represents the dielectric loss in the medium. The zero-frequency permittivity, $\varepsilon^*(\omega \to 0)$, is known as the static dielectric constant of the medium, ε_s. Determination of ε_s is non-trivial for conducting systems because of the divergence of the term containing $\frac{1}{\omega}$ as $\omega \to 0$. The permittivity at infinite frequency, $\varepsilon_\infty = \varepsilon^*(\omega \to \infty)$ arises from the electronic part of the polarizability and the intermolecular vibration. However, ε_∞ in our measurements contains contributions from electronic polarization as well as molecular polarization at high frequency because of our limitations in the frequency window (up to 50 GHz). Consequently, ε_∞ from our measurements would be higher than expected value, $\varepsilon_\infty \approx n^2$, where n being the refractive index of the medium.[45] Dielectric relaxation measurements were done in reflection technique using a PNA-L Network Analyzer (N5235B) coupled with a probe kit (85070E) operating in the frequency range $(0.2 \leq \left(\frac{\omega}{2\pi}\right)/GHz \leq 50)$. [14,49,50]

The calibration was performed using air, shorting block and water as open, short and load, respectively. Approximately 10 mL of the thermally equilibrated sample was taken for DR measurements in each time. The temperature was maintained in the precession of ± 0.5 K in each experiment.

3.2.3 Data Analysis

The experimentally measured temperature dependent complex dielectric function $\varepsilon^*(\omega)$ were fitted by using a sum of Havriliak-Negami (HN) functions[47]

$$\varepsilon^*(\omega) = \varepsilon_\infty + \sum_{j=1}^{n} \frac{\Delta\varepsilon_j}{\left[1 + \left(i\omega\tau_j\right)^{1-\alpha_j}\right]^{\beta_j}} \qquad (3.2)$$

where $0 \leq \alpha < 1$ and $0 < \beta \leq 1$. $\Delta\varepsilon_j$ denotes the amplitudes of the dispersion of j-th relaxation with time τ_j. Note that $\alpha_j = 0$ and $\beta_j = 1$ represents the relaxation via Debye model, whereas $\alpha_j = 0$ with $\beta_j < 1$ describes the Cole-Davidson (CD), and $\alpha_j < 1$ $\beta_j = 1$ the Cole-

Cole processes. Simultaneous fitting of the real part $\varepsilon'(\omega)$ and the imaginary part $\varepsilon''(\omega)$ of the measured data provided the relaxation parameters. The acceptance of the subsequent parameters was dictated by a goodness-of-fit parameter (χ^2) obtained via analysing the error employing a nonlinear least-squares method. For conducting solutions, conductivity correction is necessary and the modified equation can be written as follows,

$$\varepsilon^*(\omega) = \varepsilon_\infty + \sum_{j=1}^{n} \frac{\Delta\varepsilon_j}{\left[1 + \left(i\omega\tau_j\right)^{1-\alpha_j}\right]^{\beta_j}} - \frac{ik}{\omega\epsilon_0} \tag{3.3}$$

The “goodness-of-fit” parameter (χ^2) is described as follows[51]

$$\chi^2 = \frac{1}{2m - l} \sum_{i=1}^{m} \left[\left(\frac{\delta\varepsilon_i'}{\sigma(\varepsilon_i')} \right)^2 + \left(\frac{\delta\varepsilon_i''}{\sigma(\varepsilon_i'')} \right)^2 \right], \tag{3.4}$$

where m denotes the number of data triples $(\omega, \varepsilon', \varepsilon'')$, l the number of adjustable parameters, and $\delta\varepsilon_i$ and $\sigma(\varepsilon_i)$ are the residuals and standard deviation of the individual data points, respectively.

More detains about the measurement procedure and analysis can be found in Chapter 2

3.3 Theory and Computational Details

3.3.1 Theory

The DESs studied here are ionic systems and therefore the experimentally measured frequency dependent dielectric function contains contributions from dipole-dipole, ion-ion and dipole-ion interactions. The total DR response in such systems is better expressed in terms of the generalized frequency dependent dielectric function defined as[46,52,53]

$$\Sigma(\omega) = \frac{1}{3\epsilon_0 V k_B T} \mathcal{L}\left[-\frac{d}{dt}\phi_{tot}(t)\right], \tag{3.5}$$

where ϵ_0 is the free space permittivity, and $\phi_{tot}(t) = \langle \boldsymbol{M}_{tot}(0) \cdot \boldsymbol{M}_{tot}(t) \rangle$. The time dependent collective total dipole moment, $\boldsymbol{M}_{tot}(t)$, is then approximated as a sum of two contributions, $\boldsymbol{M}_{tot}(t) = \boldsymbol{M}_D(t) + \boldsymbol{M}_J(t)$, where $\boldsymbol{M}_D$ and $\boldsymbol{M}_J$ denote respectively the rotational and the translational components. Consequently,

$$\langle \boldsymbol{M}_{tot}(0).\boldsymbol{M}_{tot}(t) \rangle = \phi_{DD}(t) + \phi_{JJ}(t) + \phi_{DJ}(t), \tag{3.6}$$

where $\phi_{DD}(t) = \langle \boldsymbol{M}_D(0).\boldsymbol{M}_D(t)\rangle$, $\phi_{JJ}(t) = \langle \boldsymbol{M}_J(0).\boldsymbol{M}_J(t)\rangle$ and $\phi_{DJ}(t) = \langle \boldsymbol{M}_D(0).\boldsymbol{M}_J(t)\rangle + \langle \boldsymbol{M}_J(0).\boldsymbol{M}_D(t)\rangle$.

Note here that $\phi_{DD}(t)$, $\phi_{JJ}(t)$ and $\phi_{DJ}(t)$ represent respectively the rotational, the translational and the ro-translational (cross) contributions arising from the dipole-dipole, ion-ion and dipole-ion interactions in these systems. Laplace-Fourier transform of these individual correlation functions then provides the self and cross interaction contributions:

(i) dipole-dipole (rotational) part, $\mathcal{L}\left[-\frac{d}{dt}\phi_{DD}(t)\right] = \langle \boldsymbol{M}_D^2\rangle + i\omega\mathcal{L}_{DD}(\omega)$, (3.7)

(ii) ion-ion (translational) part, $\mathcal{L}\left[-\frac{d}{dt}\phi_{JJ}(t)\right] = \frac{i}{\omega}\mathcal{L}_{JJ}(\omega)$, (3.8)

(iii) dipole-ion (ro-translational) part, $\mathcal{L}\left[-\frac{d}{dt}\phi_{DJ}(t)\right] = -2\mathcal{L}_{DJ}(\omega)$. (3.9)

Note here that[46,52,54] $\mathcal{L}_{DD}(\omega) = \mathcal{L}[\langle \boldsymbol{M}_D(0).\boldsymbol{M}_D(t)\rangle]$, $\mathcal{L}_{JJ}(\omega) = \mathcal{L}[\langle \boldsymbol{J}(0).\boldsymbol{J}(t)\rangle]$ and $\mathcal{L}_{DJ}(\omega) = \mathcal{L}[\langle \boldsymbol{M}_{\boldsymbol{D}}(0).\boldsymbol{J}(t)\rangle]$ where $\boldsymbol{J}(t) = \frac{d\boldsymbol{M}_J(t)}{dt}$.

In our subsequent calculations, we have removed the $1/\omega$ divergence in the DR response for ionic media by determining first the value of the zero-frequency contribution, $\mathcal{L}_{JJ}(\omega = 0)$ and then subtracting it from the frequency dependent translational component, $\mathcal{L}_{JJ}(\omega)$[46,52] This was done as follows: $\mathcal{L}_{JJ}(\omega) - \mathcal{L}_{JJ}(\omega = 0) = \int_0^\infty dt\, e^{i\omega t}\langle \boldsymbol{J}(0).\boldsymbol{J}(t)\rangle - \int_0^\infty dt\,\langle \boldsymbol{J}(0).\boldsymbol{J}(t)\rangle$.

The individual contributions to the total DR response can then be expressed as follows:

(i) rotational DR response, $\varepsilon_{DD}(\omega) = \frac{1}{3\epsilon_0 V k_B T}\left(\langle \boldsymbol{M}_D^2\rangle + i\omega\mathcal{L}_{DD}(\omega)\right)$, (3.10)

(ii) translational response, $\varepsilon_{JJ}^c(\omega) = \frac{1}{3\epsilon_0 V k_B T}\frac{i}{\omega}\left(\mathcal{L}_{JJ}(\omega) - \mathcal{L}_{JJ}(0)\right)$, (3.11)

(iii) ro-translational spectra, $\varepsilon_{DJ}(\omega) = \frac{1}{3\epsilon_0 V k_B T}\mathcal{L}_{DJ}(\omega)$. (3.12)

The generalized frequency dependent dielectric function, after the zero-frequency conductivity correction, can be rewritten as follows[52] $\Sigma_0(\omega) = \varepsilon_{DD}(\omega) + \varepsilon_{JJ}^c(\omega) - 2\varepsilon_{DJ}(\omega)$, with $\varepsilon_{JJ}^c(\omega)$ representing the zero-frequency conductivity corrected ion-ion term. We mention here that $\Sigma(\omega)$ and $\Sigma_0(\omega)$ do not include the infinite-frequency dielectric constant (ε_∞).[54] Therefore, the ε_∞ value needs to be added to $\Sigma_0(\omega)$ for calculations of the static dielectric constant, ε_s.[55]

$\varepsilon_S - 1 = \lim_{\omega\to 0}\Sigma_0(\omega)$, or, $\varepsilon_s = \lim_{\omega\to 0}\left(\varepsilon_{DD}(\omega) + \varepsilon_{JJ}^c(\omega) - 2\varepsilon_{DJ}(\omega)\right) + 1.$

Notice here that ε_∞ is approximated as unity ($\varepsilon_\infty = 1,\ \omega \to \infty$). The DESs simulated here have been assumed as non-polarizable systems.[56] Other details for the calculations of $\Sigma_0(\omega)$, and the microscopic expressions for $\boldsymbol{M}_D(t)$ and $\boldsymbol{M}_J(t)$ are provided elsewhere[46,52,54] and thus not repeated here.

The total dipole moment ($\boldsymbol{M_D}$) generated collectively by all the dipolar molecules in a given system (acetamide molecules in the present DESs) can be approximated[47] as a sum of the individual molecular dipole moments ($\boldsymbol{\mu_i}$), $\boldsymbol{M_D} = \sum_i \boldsymbol{\mu_i}$. The short range orientational dipolar correlations, defined by the Kirkwood g factor (G_k), can then be calculated from the time dependent fluctuations of $\boldsymbol{M_D}$ via the following relation,[57,58]

$$G_k = \frac{\langle|\boldsymbol{M_D}(t)|^2\rangle - \langle|\boldsymbol{M_D}(t)|\rangle^2}{\mathrm{N}\boldsymbol{\mu}^2}, \qquad (3.13)$$

were N denotes the number of dipolar molecules in that given system, and $\boldsymbol{\mu}$ the average molecular dipole moment, $\boldsymbol{\mu}=\mathrm{N}^{-1}\sum_i \boldsymbol{\mu_i}$. $G_k = 1$ suggests that the orientations of the molecular dipoles are completely random with no correlations among themselves,[59] whereas $G_k > 1$ indicates parallel dipolar arrangements. $G_k < 1$, on the other hand, suggests anti-parallel orientations. A comparison of the G_k values between these DESs and neat molten acetamide can, therefore, reflect on the cation identity dependence of the dipolar orientations because their (K^+ and Na^+) dissimilar charge/radius ratios can differently perturb the H-bond network structure of liquid acetamide. This, in turn, will help in accessing a molecular-level picture of the cation dependence of the measured ε_s for these DESs.

The structural hydrogen bond relaxation, influenced by both translational and orientational dynamics of the participant molecules, can be expressed as follows[60–62]

$$C_{HB}(t) = \frac{\langle h(0)h(t)\rangle}{\langle h\rangle} \qquad (3.14)$$

In Eq. 3.14, $h(t)$ denotes the presence or absence of hydrogen bonds between two molecular entities at time *t*. Specifically, if a particular hydrogen bond exists both at *t*=0 and at time *t*, $h(t)$ assumes a value of unity; that is, $h(t) = 1.$ otherwise, $h(t) = 0$. This expression allows to monitor evolution of interspecies H-bonds over a period time, allowing particle movements and exchange of partners. This is different from continuous H-bond relaxation[62,63] where persistence of H-bond between given pairs are followed and time correlation constructed in order to estimate the H-bond lifetime. The following criteria were used to define a H-bond in the present simulations: (i) the distance criteria, $r_{DA} \leq r_{DA}^{c}$ and (ii) $r_{HA} \leq r_{HA}^{c}$ and (ii) the angle criteria, $150° \leq \angle \mathrm{DHA} \leq 180°$, where D, H, A stands for donor, hydrogen and acceptor atoms. The cut-off distances (r^{c}) were determined from the first minima of the corresponding RDFs. In-house codes were used to calculate $C_{HB}(t)$.

3.3.2 Computational Details

Molecular dynamics simulations of $[0.75\ \mathrm{CH_3CONH_2} + 0.25\ \mathrm{K/NaSCN}\ ]$ DESs were carried out in the temperatures range $313 \leq T/K \leq 343$ with 1200 molecules in each case. The interaction in the system was modelled via the OPLS-UA (optimized potential for liquid simulations – united atom) force field:[64]

$$U(r) = \sum_{bonds} k_r\left(r - r_{eq}\right)^2 + \sum_{angles} k_\theta\left(\theta - \theta_{eq}\right)^2 + \sum_{torsions}\left[\frac{V_1}{2}(1 + cos\varphi) + \frac{V_2}{2}(1 - cos2\varphi) + \frac{V_3}{2}(1 + cos3\varphi) + \frac{V_4}{2}(1 - cos4\varphi)\right] + \sum_{i<j}^{atoms} 4\varepsilon_{ij}\left[\left(\frac{\sigma_{ij}}{R_{ij}}\right)^{12} - \left(\frac{\sigma_{ij}}{R_{ij}}\right)^{6}\right] + \sum_{i<j}^{atoms} \frac{q_i q_j}{4\pi\epsilon_0 R_{ij}}. \qquad (3.15)$$

In the above equation, the intermolecular bonded interaction is described by the harmonic potential with equilibrium bond distance r_{eq} and bond constant k_r , and the angle stretching with equilibrium bond angle θ_{eq} and angle constant k_θ. V_1, V_2, V_3 and V_4 represent the Fourier coefficients of tortional angle φ. The non-bonded interaction is described by the Lennard-Jones (LJ) potential and the Coulomb interactions where R_{ij} represents the intermolecular distance between the atoms i and j with partial charges q_i and q_j. σ and ε represent the van der Waals diameter and well-depth respectively. The cross LJ coefficients were obtained by applying the known geometric combination rules[65]: $\sigma_{ij} = \sqrt{\sigma_{ii}\sigma_{jj}}$ and $\varepsilon_{ij} = \sqrt{\varepsilon_{ii}\varepsilon_{jj}}$.

All simulations were performed in GROMACS-2018.3 MD package.[66] The force field parameters for acetamide and the ions ($\mathrm{Na^+}$, $\mathrm{K^+}$ and $\mathrm{SCN^-}$) were taken from the existing literature.[67–69]. The short-range van der Waals and the long-range electrostatic interactions were truncated at 1.2 nm. Particle Mesh Ewald (PME) was used to efficiently calculate the long-range electrostatic interaction with a Fourier grid spacing of 0.16 nm and a spline of order 4. Packmol[70] was used to build the initial configuration, and the equation of motion was integrated with the leapfrog algorithm.[71] Simulation was started in a comparatively large cubic box and periodic boundary condition maintained in all three directions. The initially generated configuration was energy-minimized through the steepest-descent algorithm implemented in the GROMACS package. After energy minimization, NVT equilibration of 5 ns were carried out at the desired temperature with the V-rescale[72] temperature coupling with time constant 0.5 ps. After that, the resulting system was taken through an NPT equilibration for 10 ns in that temperature employing the V-rescale thermostat[72] (coupling constant 0.5ns) and the Berendsen barostat[73] (time constant of 2 ps). Subsequently, a production run of 250 ns was carried out in the same condition with a step of 2 fs and the trajectory were saved in an interval of 200 fs. The convergence of the value of ε_s with time was monitored in order to check the goodness of the simulation. All analyses were performed using in-house code, GROMACS[66] and TRAVIS[74,75] software.

3.4 Results and Discussion

3.4.1 Experiments

3.4.1.1 Temperature Dependent DR Data: Effects of Successive Replacement of K^+ by Na^+

Figure 3.1 depicts K^+ concentration dependent $\varepsilon'(\omega)$ and $\varepsilon''(\omega)$ of the experimental DR spectra for the $0.25[f\mathrm{KSCN} + (1-f)\mathrm{NaSCN}] + 0.75\mathrm{CH_3CONH_2}$ DESs with f = 1, 0.8, 0.6, 0.4, 0.2 and 0, at five different temperatures in the range, T = 303 – 343 K. Multi-Debye (3 or 4 Debye) fit parameters to these experimental DR spectra along with the corresponding temperature dependent viscosities[76] (η) are summarized in **Tables 3.A.1 – 3.A.5** (Appendix 3.A). The fastest DR time constant in these multi-Debye fits was constrained to 5 ps uniformly across the cation concentrations and temperature because of the inaccessibility of frequency beyond 50 GHz to the present measurements.

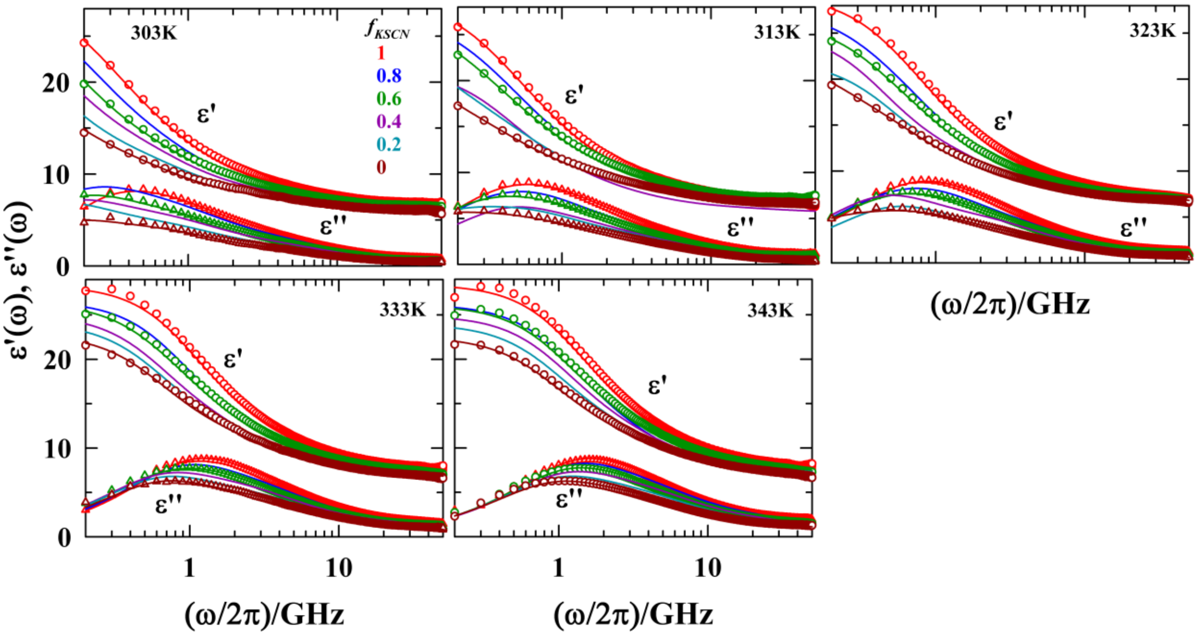

Figure 3.1. KSCN concentration dependent real ($\varepsilon'(\omega)$) and imaginary ($\varepsilon''(\omega)$) components of the experimental DR spectra of the DESs, $0.25[f\,\mathrm{KSCN} + (1-f)\,\mathrm{NaSCN}] + 0.75\mathrm{CH_3CONH_2}$ in the measurement frequency window, $0.2 \leq \left(\frac{\omega}{2\pi}\right)/GHz \leq 50$, at five different temperatures. Solid lines passing through the experimental data points are the multi-Debye fits (with fit parameters summarized in a Table 3.A.1 – 3.A.5). Representations are colour-coded.

Note in these tables that the DR of $\mathrm{Na^+}$-DES at 303 K contains a dominant nanosecond component (~50% with a time constant ~1.5 ns) which vanishes with the increase of either the solution temperature or $\mathrm{K^+}$ concentration. This highlights the role of solution viscosity in generating a nanosecond DR component in these ionic DESs. The experimental DR spectra also reflect that the non-Debye (or multi-step) relaxation is inherent to these ionic DESs, and the impact of $\mathrm{Na^+}$on ε_s of neat molten acetamide is more pronounced than that of $\mathrm{K^+}$. The last statement follows from the findings of the present measurements that have found $\varepsilon_s \sim 20-28$ (see **Table 3.A.1 – 3.A.5,** Appendix 3.A) for these ionic acetamide DESs, and data from previous experiments reporting ε_s ~64 for neat molten acetamide[17,46,77]. Also note in this figure that the low frequency DR dynamics becomes more accessible with the increase of solution temperature. This accessibility to low frequency DR dynamics is relatively more restricted for $\mathrm{Na^+}$- DES as this system is more viscous than $\mathrm{K^+}$- DES. High viscosity coupled with significant solution conductivity renders analysis of low frequency DR data of these ionic DESs somewhat tricky[17,34,78] and the estimated ε_s values may involve large inaccuracies. $\mathrm{K^+}$concentration dependent ε_s values, presented in **Figure 3.A.1** (Appendix 3.A) highlight this difficulty where the estimated ε_s values show a rather irregular temperature dependence. This makes a definitive discussion on the temperature dependence of ε_s at different *f* values (from *f* =0 to 1) somewhat tentative, although it is clear that the ε_s values spread out more with temperature as Na^+ successively replaces K^+ in these DESs. A connection between the K^+concentration dependent ε_s values and the average number of H-bonds per acetamide molecule in these systems will be explored later in this chapter when simulation results are presented.

Next, we show in **Figure 3.2**, the contributions of each of the relaxation steps of the multi-Debye fits to the measured frequency dependent DR spectra in K^+ and Na^+ DESs at two representative temperatures, *T* = 313 and 343 K.

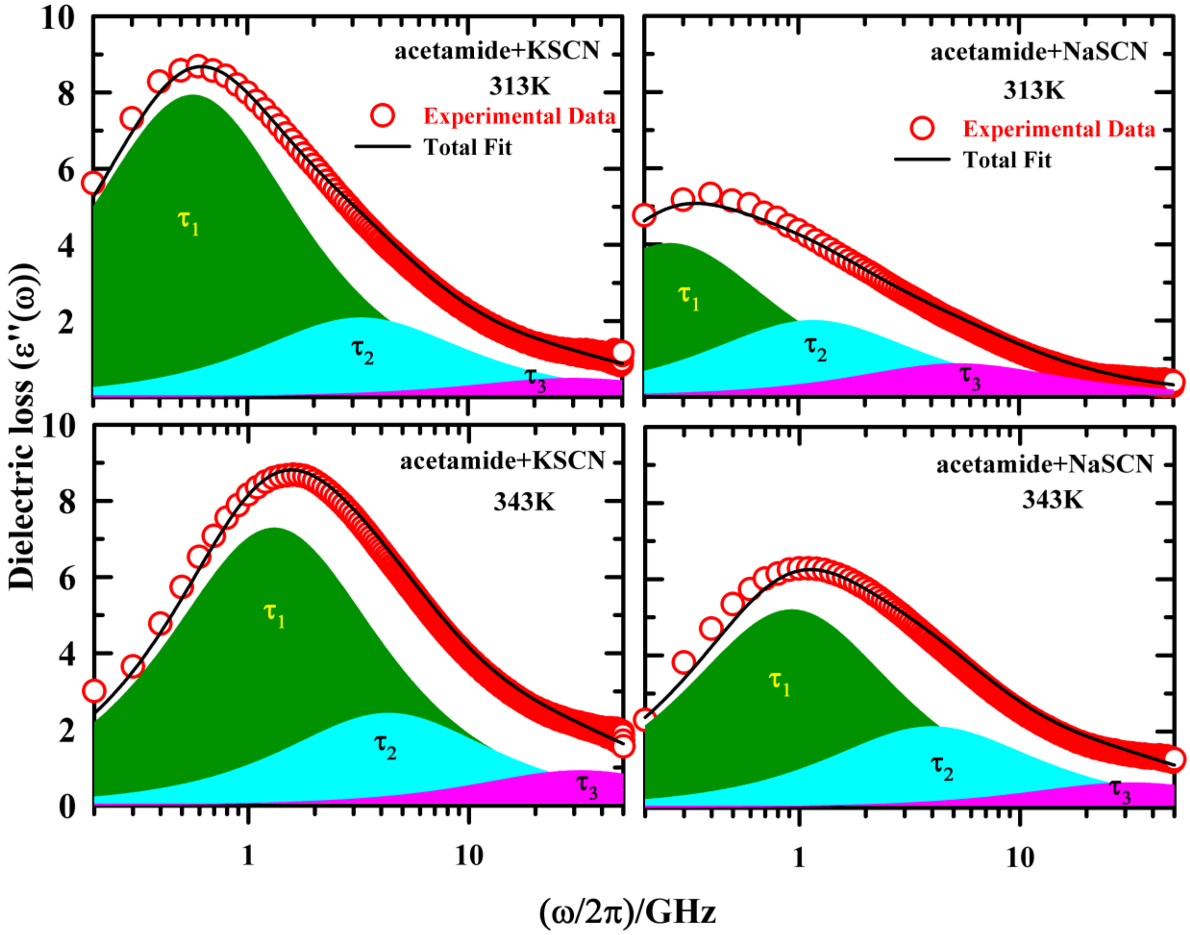

Figure 3.2. Deconvolution of the measured frequency dependent dielectric loss (ε'') spectra into their individual time component contributions for $0.25[f\mathrm{KSCN} + (1-f)\mathrm{NaSCN}] + 0.75\mathrm{CH_3CONH_2}$ DESs at f =1 (left panel) and 0 (right panel). Red circles represent the experimental data and the solid lines going through them denote the multi-Debye fits (summarized in the above tables). Different time component contributions are colour coded. Deconvolutions for two representative temperatures are shown.

Clearly, the slowest of the 3-step relaxations in both the K^+ and Na^+ DESs makes dominating contributions, while the fastest process contributes the least. Note that the contribution of the fastest process is although smaller but substantial in order to fully comprehend the DR spectra. This observation suggests that measurements extending to further higher frequencies (>50 GHz) are required for a more quantitative detection of the faster dipole moment fluctuation dynamics in these DESs. This is interesting considering the fact that ions present in such systems can considerably weaken the H-bond network among the acetamide molecules[46], reducing the high frequency contributions to the DR that are known to arise from the collective intermolecular vibrations and librations of associated liquids.[16,79–81] Simulations (presented later) show that this high frequency DR response in these ionic DESs originates from the ion-dipole cross correlation and ion current contributions.

Cole-Cole representations obtained from experimental DR spectra are shown in **Figure 3.A.2** (Appendix 3.A). Here, $\varepsilon''(\omega)$ is shown as a function of $\varepsilon'(\omega)$, depicting the impact of replacement of K^+ by Na^+ on the frequency dependent DR of (acetamide + K/NaSCN) DESs at four representative temperatures in the range, T = 313 – 343 K. For a dipolar system with single Debye relaxation time, a Cole-Cole plot ($\varepsilon''(\omega)$ vs $\varepsilon'(\omega)$) generates a semicircle ('Debye semicircle') with a radius,[47] $(\varepsilon_s - \varepsilon_\infty)/2$. For the Debye semicircles shown in this figure, $\varepsilon'(\omega)$ and $\varepsilon''(\omega)$ were calculated by using the experimental ε_s, ε_∞ and the average DR time ($\langle\tau_{DR}\rangle$) as follows:[47] $\varepsilon'(\omega) = \varepsilon_\infty + [\varepsilon_s - \varepsilon_\infty]/[1 + (\omega\langle\tau_{DR}\rangle)^2]$ and $\varepsilon''(\omega) = [\varepsilon_s - \varepsilon_\infty]\omega\langle\tau_{DR}\rangle/[1 + (\omega\langle\tau_{DR}\rangle)^2]$. A comparison between the experimental and the calculated Cole-Cole plots, also presented in **Figure 3.A.2** (Appendix 3.A) reflects that at each of the temperatures shown, experimental DR data for both the DESs deviate from the calculated Debye semicircles. This indicates the existence of inherent multi-Debye relaxation processes in these systems.

The Cole-Cole plot revels a distinct asymmetry for both the DESs. Following the established protocol[82] we then plotted (**Figure 3.A.3,** Appendix 3.A) the contributions of each relaxation steps (as a single Debye process) for the K^+ and Na^+ DESs at two representative temperatures, T = 313 and 343 K. **Figure 3.A.3** (Appendix 3.A) revels that components with longer time scales contribute more significantly while those with shorter time scales contribute to a lesser extent. This reflects a hierarchical pattern in their respective contributions.

The temperature dependence of the average DR rates in these media is explored next in **Figure 3.3**, where *inverse* of $\langle\tau_{DR}\rangle$ values obtained from multi-Debye fits to the measured DR spectra at different K^+ concentrations are shown as a function of *inverse* temperature (upper panel). Clearly, the average DR rates ($\langle\tau_{DR}\rangle^{-1}$) follow Arrhenius-type temperature dependence in the narrow temperature range considered (T = 303 - 343 K). Note in this figure that the slopes of these data (E_a^{DR}/R , E_a^{DR} being the activation energy and R the universal gas constant) remain nearly insensitive to K^+ concentration. This is presented in the lower panel where the estimated DR activation energies are shown as a function of K^+ concentration and compared with the corresponding viscosity activation energies (E_a^{η}) determined from the temperature dependent viscosity data available already in the literature[26,33,76] (see **Figure 3.A.4**, Appendix 3.A). This near independence of E_a^{DR} on K^+ concentration is interesting and originating from the increased viscosity decoupling of $\langle\tau_{DR}\rangle$ in Na^+ rich DESs. This is shown in the inset of the lower panel, while the fractional viscosity dependence of $\langle\tau_{DR}\rangle$ at different K^+ concentrations and the subsequent determination of the fraction power (p) are depicted in **Figure 3.A.5** (Appendix 3.A). The difference in viscosity decoupling of average relaxation times between Na^+- DES and K^+- DES found here was also detected earlier in time-resolved fluorescence measurements of solute solvation and rotation times[26] and in simulations of centre-of-mass diffusions and reorientational relaxations[33].

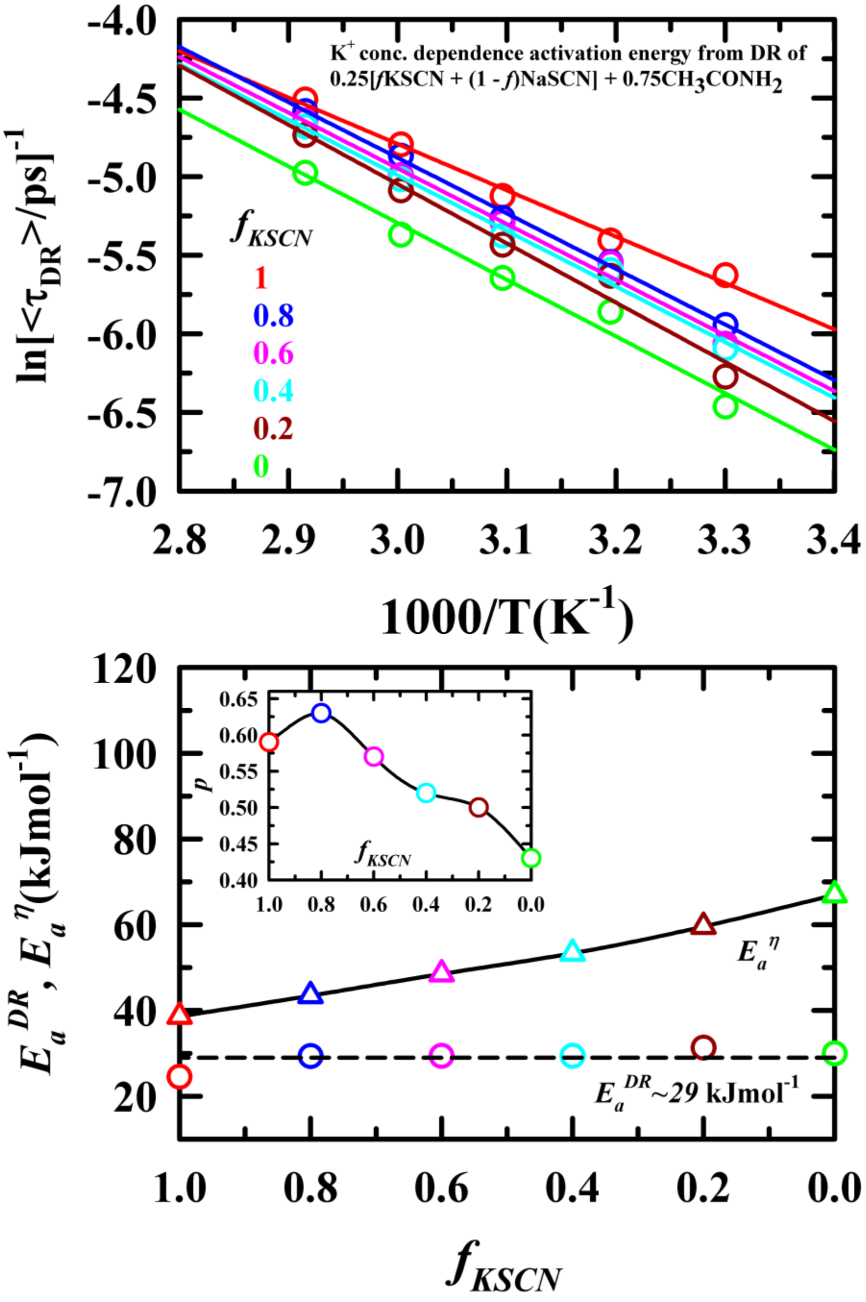

Figure 3.3. *Upper panel*: Arrhenius plot of $\ln\left(1/\langle\tau_{DR}\rangle\right)$ vs $1/T$ for $0.25[f\mathrm{KSCN}+(1-f)\mathrm{NaSCN}]+0.75\mathrm{CH_3CONH_2}$ DESs at six different f values (or $\mathrm{K^+/Na^+}$ concentrations). Solid lines represent linear fits through experimental data. *Lower panel*: Comparison of activation energies estimated from the temperature dependent average DR times and viscosities of these DESs. Note that gap between the activation energies is widening upon successive replacement $\mathrm{K^+}$ by $\mathrm{Na^+}$ in these media. *Inset* shows the cation ($\mathrm{K^+/Na^+}$) concentration dependence of the value of the decoupling parameter (p) obtained from the temperature dependent $\langle\tau_{DR}\rangle$ and η and subsequent fit to the following equation: $ln[\langle\tau_{DR}\rangle] = A + pln[\frac{\eta}{T}]$. The lines joining the activation energy data (lower panel) are guides to eyes. Representations are colour coded.

The above difference in viscosity decoupling therefore indicates dissimilar interactions of Na^+ and K^+ with the host acetamide molecules, affecting differently the H-bond network structure in these ionic acetamide DESs. The impact of successive replacement of K^+ by Na^+ on solution structure is further reflected in the K^+concentration dependent glass transition temperatures (T_g), shown in **Figure 3.4**, where representative DSC thermograms at two different K^+ concentrations (f = 1 and 0) are displayed in the inset.

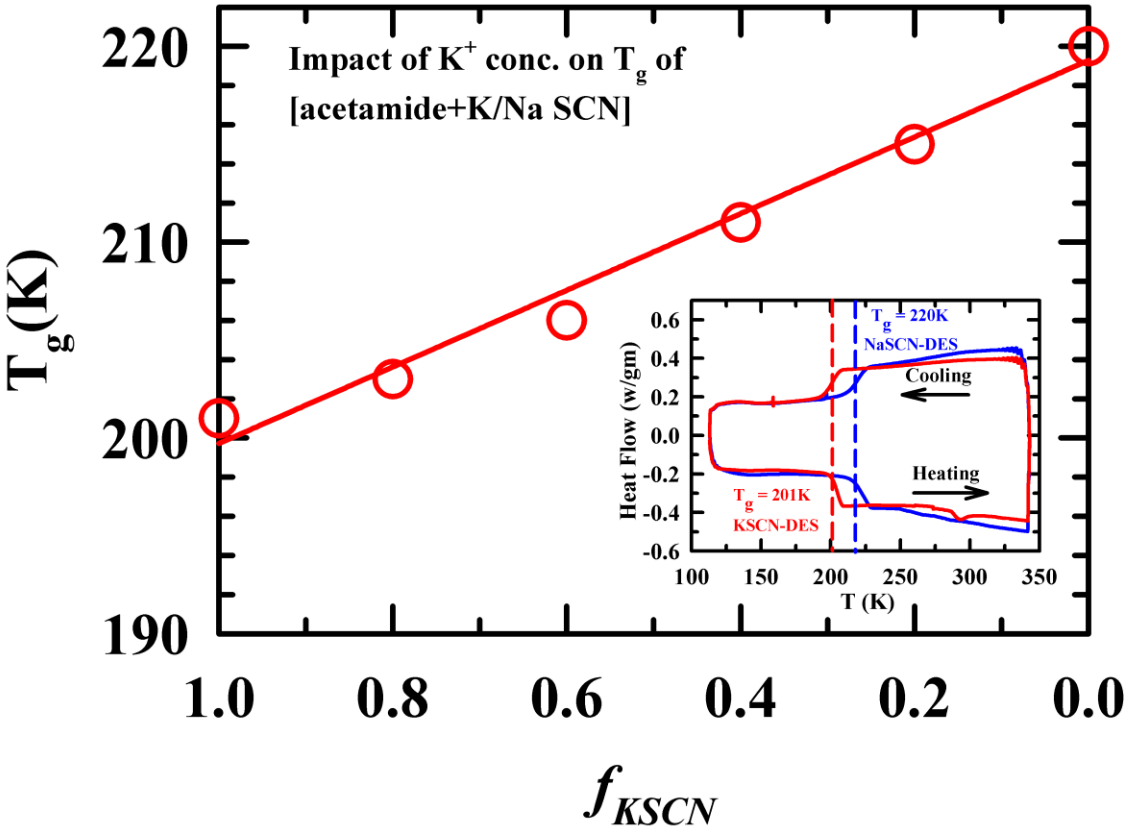

Figure 3.4. Cation (K^+/Na^+) concentration dependence of the measured glass transition temperature (T_g) in $0.25[f\mathrm{KSCN} + (1-f)\mathrm{NaSCN}] + 0.75\mathrm{CH_3CONH_2}$ DESs. The straight line going through the data points is a linear fit through the experimental data and indicates increase of T_g upon increasing Na^+ concentration. *Inset* shows representative differential scanning calorimetric (DSC) traces for DESs at f=1 and 0. T_gs are indicated by the vertical dashed lines. Representations are colour coded.

The DSC thermograms for each of the six different K^+ concentrations are provided separately in **Figure 3.A.6** (Appendix 3.A). Note that the value of T_g for Na^+-DES determined here is in good agreement with that reported (T_g = 221K) in earlier measurements.[22] Data in **Figure 3.4** clearly indicate that T_g increases with the increase of Na^+ concentration in DES, suggesting the system becoming more fragile[22,83–85] upon successive replacement of K^+ by Na^+. This increased fragility renders stronger dynamic cooperativity, enabling dipolar relaxation in Na^+-DES to exhibit relatively stronger viscosity decoupling than in K^+-DES. Subsequently, the glycerol-like fragility[86,87] of these ionic DESs limits the range of temperature for temperature dependent measurements.

3.4.2 Simulations

3.4.2.1 Comparison with Experiments: Qualitative Agreement

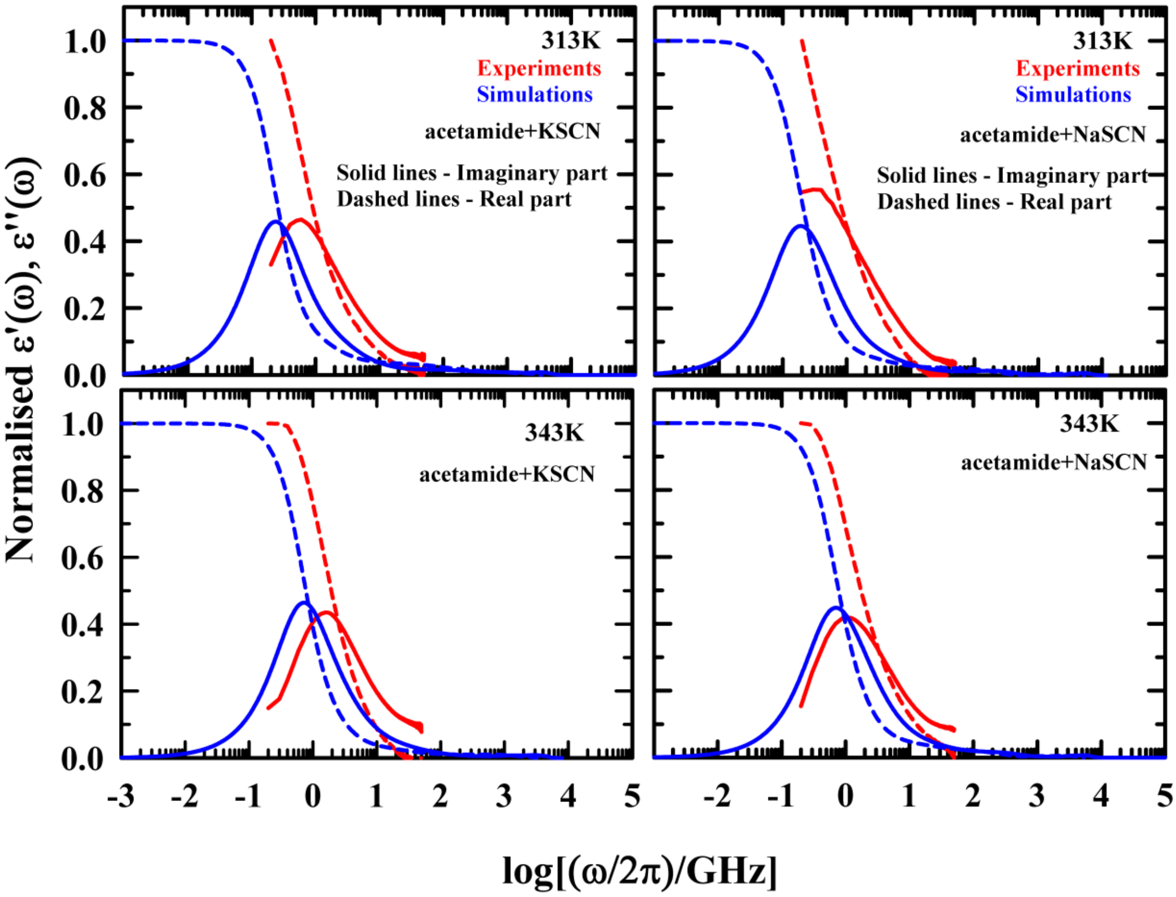

Figure 3.5. Comparison between the normalised experimental and simulated real and imaginary components of DR in $0.25[f\mathrm{KSCN} + (1-f)\mathrm{NaSCN}] + 0.75\mathrm{CH_3CONH_2}$ DESs at f = 1(*left panels*) and 0 (*right panels*). Results are shown for two representative temperatures, 313K (*upper panels*) and 343K (*lower panels*). Simulated and experimental spectra (both the real and imaginary components) are presented after appropriate normalizations as follows: $(\varepsilon'(\omega) - \varepsilon_\infty)/(\varepsilon_s - \varepsilon_\infty)$ and $\varepsilon''(\omega)/\,(\varepsilon_s - \varepsilon_\infty)$. Representations are color-coded.

A direct comparison between the simulated and experimental DR spectra in **Figure 3.5** demonstrates clearly the quantitative disagreement between them. The necessary DR parameters for generating the simulated $\varepsilon'(\omega)$ and $\varepsilon''(\omega)$ are summarized in **Table 3.A.6** (Appendix 3.A). The comparison is done here for DR at 313 K and 343 K, while the same for the other two temperatures (323 K and 333 K) are shown in **Figure 3.A.7** (Appendix 3.A). Note these parameters were obtained from the established protocol discussed in the theory section. The fit parameters summarized in **Table 3.A.6** (Appendix 3.A) suggest a significant slowing down of the DR upon replacement of K^+ by Na^+ in these DESs. Notice in these figures that the main relaxation peaks in the simulated imaginary components ($\varepsilon''(\omega)$) appear uniformly at lower frequencies than those in experiments. The corresponding simulated real components ($\varepsilon'(\omega)$) are also shifted to lower frequencies accordingly at these temperatures. This relatively slower DR in simulations is inherited from the model interaction potential[46,67,77] employed to represent acetamide in the present work and therefore highlights the insufficiency of the relevant force field parameters to reproduce the experimental DR. However, a simple frequency scaling, as shown in **Figure 3.A.8** (Appendix 3.A), brings the simulated and experimental spectra much closer. This suggests that the present simulations are able to capture the basic aspects of the DR in these complex ionic systems qualitatively correctly. This is important in generating a qualitative understanding of the impact of successive replacement of K^+ by Na^+ on DR of these systems.

Figure 3.A.9 (Appendix 3.A) presents simulated amplitude-normalized Cole-Cole plots for these DESs at two representative temperatures and compares with those from experiments. Notice that both the simulated and experimental curves show deviations from the predicted Cole-Cole single-Debye descriptions of DR in these systems. However, the comparison presented in **Figure 3.A.9** (Appendix 3.A) demonstrates that the deviations from the single-Debye Cole-Cole behaviour captured by the present simulations are much weaker than those exhibited by the corresponding experiments. This is interesting because simulations, as found in experiments, predicted multi-Debye relaxations in these ionic DESs. A closer inspection of the simulated data, on the other hand, reflects that the simulated relaxations are, on an average, are ~2-2.5 times slower than those in experiments. This difference might be the principal factor that did not allow the present simulations to reproduce the experimental deviations depicted in **Figure 3.A.9** (Appendix 3.A).

3.4.2.2 Spectral Decompositions: Contributions from Cross Correlations

While discussing the temperature dependent DR in **Figure 3.1**, we noticed that ε_s of neat molten acetamide was decreased more in the presence of Na^+ than K^+ in these ionic DESs. The possibility of a dynamical origin for this dielectric decrement was not mentioned there, although different abilities of these alkali metal cations in randomising molecular dipolar orientations via disruptions of acetamide H-bond network was suggested as a possible reason for such an impact.

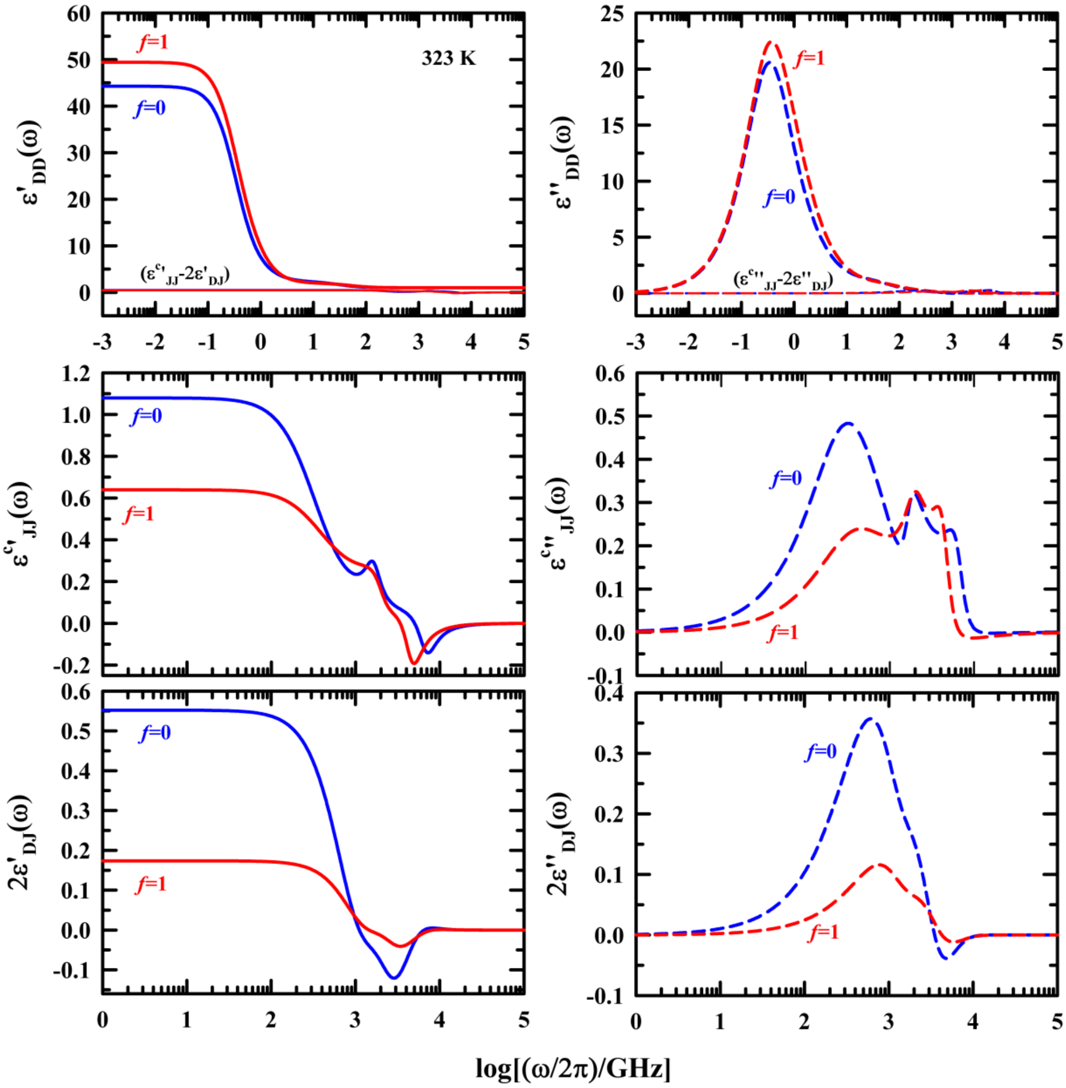

Figure 3.6. Decomposition of the total simulated DR spectra into rotational (dipole-dipole), translational (current-current) and ro-translational (dipole-current) contributions, $\Sigma_0(\omega) = \varepsilon_{DD}(\omega) + \varepsilon_{JJ}^c(\omega) - 2\varepsilon_{DJ}(\omega)$. Spectral decompositions are shown for the DESs $0.25[f\ \mathrm{KSCN} + (1-f)\ \mathrm{NaSCN}] + 0.75\mathrm{CH_3CONH_2}$ at 323 K for f = 1 and 0. Horizontal lines in the upper panels indicate the joint contributions of the term, $[\varepsilon_{JJ}^c(\omega) - 2\varepsilon_{DJ}(\omega)]$, reflecting a negligible contribution to the total spectra with respect to that by the dipole-dipole term.

Figure 3.6 investigates the dynamical origin for the observed dielectric decrement via decomposition of the total frequency dependent dielectric spectrum into three interaction contributions, $\Sigma_0(\omega)$ = $\varepsilon_{DD}(\omega)$ + $\varepsilon_{JJ}^{c}(\omega)$ - $2\varepsilon_{DJ}(\omega)$, and presents results for K^+ and Na^+ DESs (that is, f = 1 and 0, respectively) at a representative temperature, T = 323 K. The results for the system at f = 0.6 are provided in **Figure 3.A.10** (Appendix 3.A). The real and imaginary components of these interaction contributions, shown respectively in the left and right panels, clearly show that the dipole-dipole contribution (ε_{DD}) overwhelmingly dominates the low frequency wing ($\omega/2\pi \leq 1$ GHz) of the simulated $\Sigma_0(\omega)$, allowing the ion-dipole (cross term) and ion-ion contributions to become somewhat important at the higher frequencies with peaks in their imaginary components at ~1 THz. Even with such comparatively tiny contributions, both the real and imaginary components of $\varepsilon_{DJ}(\omega)$ and $\varepsilon_{JJ}^{c}(\omega)$ do show cation identity dependence but in the reverse order with respect to that found for the real and imaginary components of the dipole-dipole term, $\varepsilon_{DD}(\omega)$. The most important finding in this figure is, however, that a small positive contribution arises in the low frequency regime ($\omega/2\pi$ ~10 GHz) from the combined real components of the term, [$\varepsilon_{JJ}^{c}(\omega)$ - $2\varepsilon_{DJ}(\omega)$], and makes a small addition to the real component of the dipole-dipole contribution, $\varepsilon_{DD}(\omega)$. It is therefore abundantly clear that the ion-ion and the dipole-ion (cross) interaction contributions, both positive and small, do not reduce the zero frequency values of the dielectric constants of these ionic DESs. This suggests that dynamical contributions arising from these components do not contribute to the observed ion-induced decrement of ε_s in these ionic acetamide DESs with respect to that for neat molten acetamide. Qualitatively similar results were also found earlier when we analysed, through the spectral decompositions as performed here, the frequency dependent dielectric response of (acetamide + LiBr/NO_3/ClO_4) DESs.[46]

3.4.2.3 Correlation Between ε_s and H-bond Network: Impact of Cation identity

A correlation between the measured ε_s values and H-bond network was already suggested in the connection of **Figure 3.A.1** (Appendix 3.A) which showed decrease of ε_s both upon increasing the solution temperature and Na^+ concentration. We would first examine the temperature effects on average number of H-bonds per acetamide molecule, $\langle n_{HB} \rangle$, in K^+ and Na^+ DESs because intermolecular H-bond network is known to critically influence the local dipolar correlations in polar liquids. Following the calculation procedure available in the literature[23,88] (and briefly discussed in Theory Section III.A), the temperature dependent $\langle n_{HB} \rangle$ values were determined for DESs at f = 1 and 0. The results are presented in **Figure 3.7** which indicate that temperature reduces $\langle n_{HB} \rangle$ for both K^+ and Na^+ DESs, and $\langle n_{HB} \rangle$ in Na^+ DES is less than that in K^+ DES at all the temperatures considered.

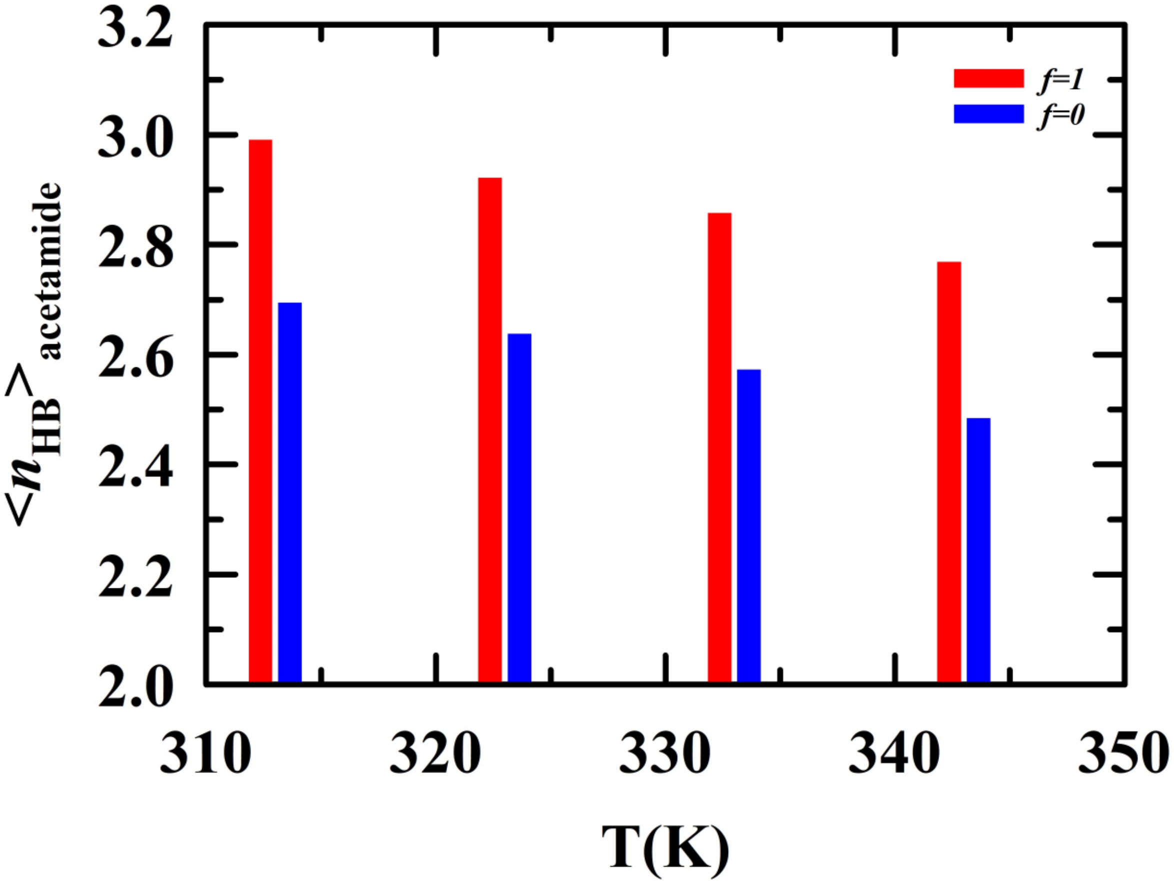

Figure 3.7. Temperature dependence of the average number of H-bonds per acetamide molecule, $\langle n_{HB} \rangle$, in the DESs, $0.25[f\,\mathrm{KSCN} + (1-f)\,\mathrm{NaSCN}] + 0.75\mathrm{CH_3CONH_2}$, for f = 1 and 0. Notice that $\langle n_{HB} \rangle$ is larger in K^+- DES than that in Na^+- DES, and $\langle n_{HB} \rangle$ for both the systems are gradually decreasing with temperature.

Subsequently, the Na^+ (or K^+) concentration dependence of $\langle n_{HB} \rangle$ at a representative temperature, T = 323 K, was determined and the correlation with the corresponding measured

ε_s values examined. The results are presented in **Figure 3.8** which shows that ε_s in these systems decreases rather sharply with the reduction in the average number of H-bonds per molecule. The data in this figure also reflect that H-bond network structure in these solutions becomes increasingly disrupted as K^+ is successively replaced by Na^+. This hints at a stronger interaction of acetamide with Na^+ than K^+ and this can be understood by the difference in their respective charge-by-radius (q/r) ratios.[89]

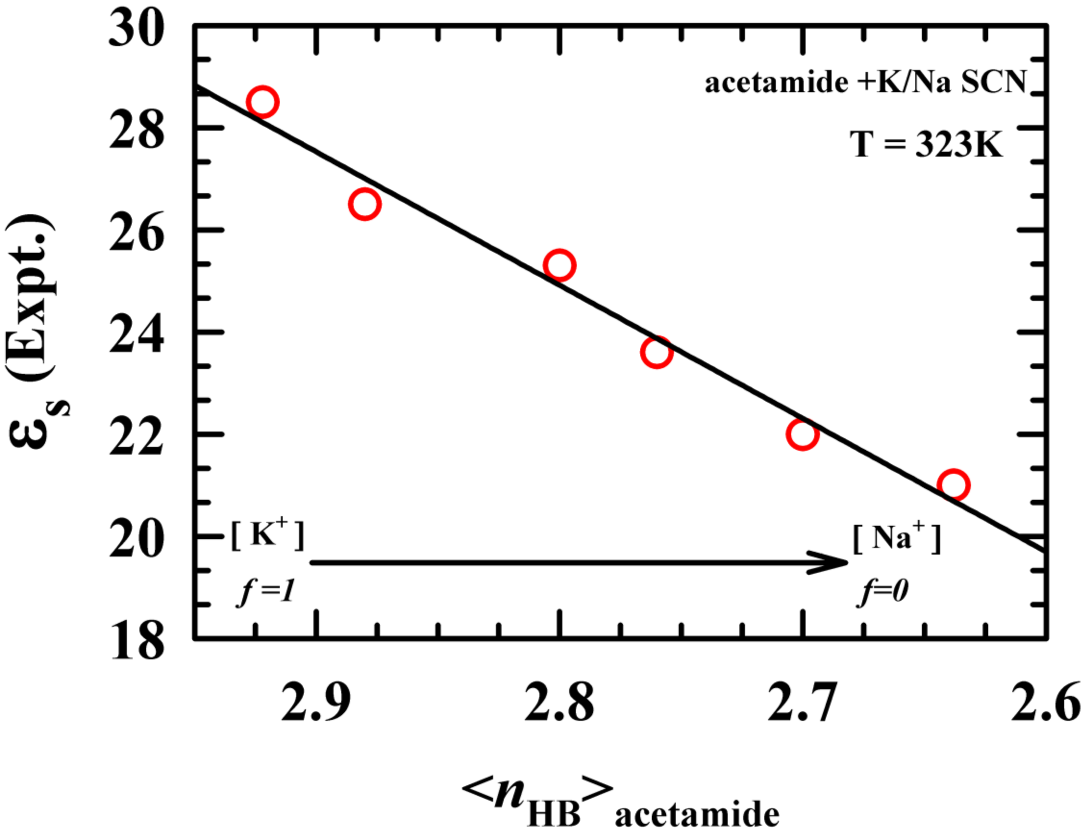

Figure 3.8. Dependence of the static dielectric constant (ε_s) on the average number of H-bonds per acetamide molecule, $\langle n_{HB} \rangle$. Note in this plot that the measured values of ε_s are shown as a function of $\langle n_{HB} \rangle$ in the DESs, $0.25[f\ \mathrm{KSCN} + (1-f)\ \mathrm{NaSCN}] + 0.75\mathrm{CH_3CONH_2}$ calculated for six different values of f at 323 K. Notice the decrease of $\langle n_{HB} \rangle$ with the decrease of f. The straight line going through the data represent a linear fit to the equation, $\varepsilon_s = m\langle n_{HB} \rangle + \mathrm{C}$, with $m = \frac{d\varepsilon_s}{d\langle n_{HB} \rangle} = 26.1$ and $\mathrm{C} = -48.1$.

3.4.2.4 Local Dipolar Orientational Correlations and ε_s: Dependence on Cation Identity

The strong correlation between ε_s and $\langle n_{HB} \rangle$ observed in **Figure 3.8** raises the following question: how does the ion-induced disruption of H-bond network reduce ε_s? Because ε_s is related to thermal equilibrium polarization fluctuations and thus a response function,[57,90] the cations, Na^+ and K^+, must be differently disturbing the local orientational dipolar correlations among the acetamide molecules. For a strongly dipolar liquid, one can approximate the original relation[57,91] as, $\varepsilon_s \sim 2\pi\beta\rho\mu^2 g_K$, where $\beta = (k_B T)^{-1}$and g_K is the Kirkwood g factor defining the short range orientational correlations. Subsequently, g_K was shown to be the asymptotic value of the r – dependent Kirkwood g factor defined as, $G_K(\boldsymbol{r}) = \langle \boldsymbol{\mu_1} \cdot \boldsymbol{M_D}(\boldsymbol{r}) \rangle / \mu^2$, with $\boldsymbol{\mu_1}$ as the reference dipole 1 at the centre of a sphere with radius r, and $\boldsymbol{M_D} = [\sum_i \boldsymbol{\mu_i}]_{\boldsymbol{r}}$, representing the sum total of dipoles in that sphere. $G_K(\boldsymbol{r}) \rightarrow g_K$ at $\boldsymbol{r} \geq \boldsymbol{r_K}$, $\boldsymbol{r_K}$, the Kirkwood correlation length, being typically of a few molecular diameter lengths beyond which the local dielectric constant assumes the value of macroscopic dielectric constant ε_s. The above relation for $G_K(\boldsymbol{r})$ provides an avenue to understand the impact of ions on short range dipolar correlations and thus on ε_s.

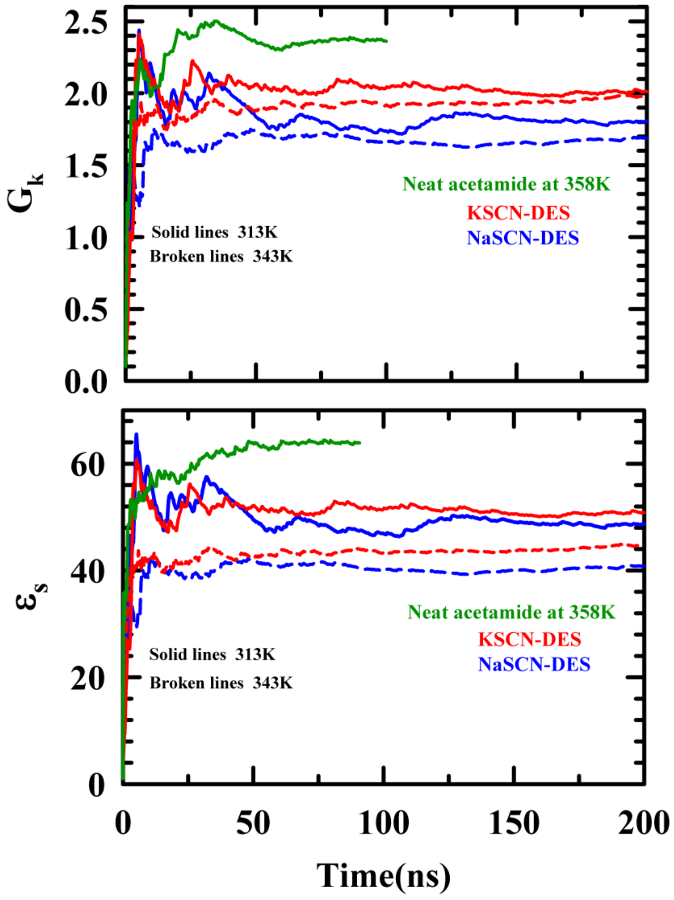

Figure 3.9. Time evolution of the Kirkwood g factor (G_k) (*upper panel*) and the static dielectric constant (ε_s) (*lower panel*) in simulations for the DESs, $0.25[f\ \mathrm{KSCN} + (1-f)\ \mathrm{NaSCN}] + 0.75\mathrm{CH_3CONH_2}$ at f = 1 and 0. The results are shown for two representative temperatures, 313K and 343K. Note the values of G_k and ε_s are larger at f = 1 than those at f = 0. In addition, both G_k and ε_s decrease with temperature. Representations are color-coded.

The time-dependent fluctuations of G_K, calculated from Eq. 3.13, for these two DESs at two representative temperatures (313 K and 343 K) are compared in the upper panel of **Figure 3.9**. The results for neat molten acetamide (358 K) are also shown in the same panel in order to facilitate the comparison of the effects on short range orientational correlations between Na^+ than K^+ . Notice that the fluctuations of G_K soften with time and progress toward convergence. The comparison of the G_K values between these DESs and molten acetamide clearly indicates that the short range orientational dipolar correlations are significantly reduced by the ions (over that in molten acetamide). Moreover, G_K values at longtime are smaller for Na^+ than K^+, confirming the partial randomization of the short range orientational correlations being more pronounced in the presence of Na^+ than that of K^+. A closer inspection also reveals that the rise of solution temperature reduces the orientational dipolar correlations, the disruptive impact being stronger for Na^+ than K^+. These results explain in microscopic terms the cation identity and temperature dependencies of the experimental ε_s presented already in **Figure 3.8**.

Because G_K is intimately connected to ε_s, we have also presented simulated ε_s for these two DESs in the lower panel of **Figure 3.9**. Notice here that ε_s presented in this figure were calculated from the variance of the total dipole moment,[58,77,92] $\varepsilon_s = 1 + \frac{\langle |\boldsymbol{M_D}(t)|^2\rangle - \langle |\boldsymbol{M_D}(t)|\rangle^2}{3\epsilon_0 V k_B T}$, and mirror the fluctuations shown by G_K in the upper panel. The temperature and cation dependencies also follow that of G_K, reflecting only the intimate relationship between ε_s and G_K discussed already. The later observation bolsters the explanations provided for the temperature and cation dependencies of the measured ε_s values in terms of reduced short range dipolar correlations and H-bond rupture by $\mathrm{Na}^+$and K^+. However, we would like to mention that the cation-induced reduction of ε_s predicted by these simulations is much weaker than observed in experiments. This may have originated from the insufficient description of the interactions between the ions and the acetamide molecules.

3.4.2.5 Origin of Multiple DR Timescales: Connections to Cation Dependent Reorientational Relaxations and Structural H-bond Fluctuations

We next explore the interconnection between the experimentally measured DR timescales, and those from simulated reorientational and structural H-bond relaxation dynamics. The relation that connects the molecular rotation times (τ_M) to the rank dependent (ℓ) average collective single particle reorientational correlation times ($\langle\tau_\ell\rangle$) is given by[14,93,94], $\tau_M = \frac{\ell(\ell+1)}{2}\langle\tau_\ell\rangle$. If random molecular rotations dominate the experimental DR times, then one may write, $\tau_M \approx \tau_{DR} = \langle\tau_{\ell=1}\rangle$, because DR measurements probe the first rank ($\ell = 1$) dipolar reorientations. We obtained the cation dependent $\langle\tau_{\ell=1}\rangle$ from the simulated rank dependent collective single particle reorientational correlation functions ($C_\ell(t)$), $\langle\tau_{\ell=1}\rangle = \int_0^\infty dt\ C_\ell(t)$. The reorientation dynamics of acetamide molecules was simulated via following the time dependent changes in orientation of a unit vector ($\mathbf{u}(t)$) connecting C(-CH_3) and N(-NH_2) atoms of a given CH_3CONH_2 molecule,[88,95] $C_\ell(t) = \langle P_\ell[\mathbf{u}(0)\cdot\mathbf{u}(t)]\rangle/\langle P_\ell[\mathbf{u}(0)\cdot\mathbf{u}(0)]\rangle$, with P_ℓ denoting the rank dependent Legendre polynomial.

The cation dependence of the simulated first rank $C_\ell(t)$ decays at two representative temperatures (313 K and 343 K) are shown in **Figure 3.10**, while the simulated temperature dependent decays are provided in **Figure 3.A.11** (Appendix 3.A).

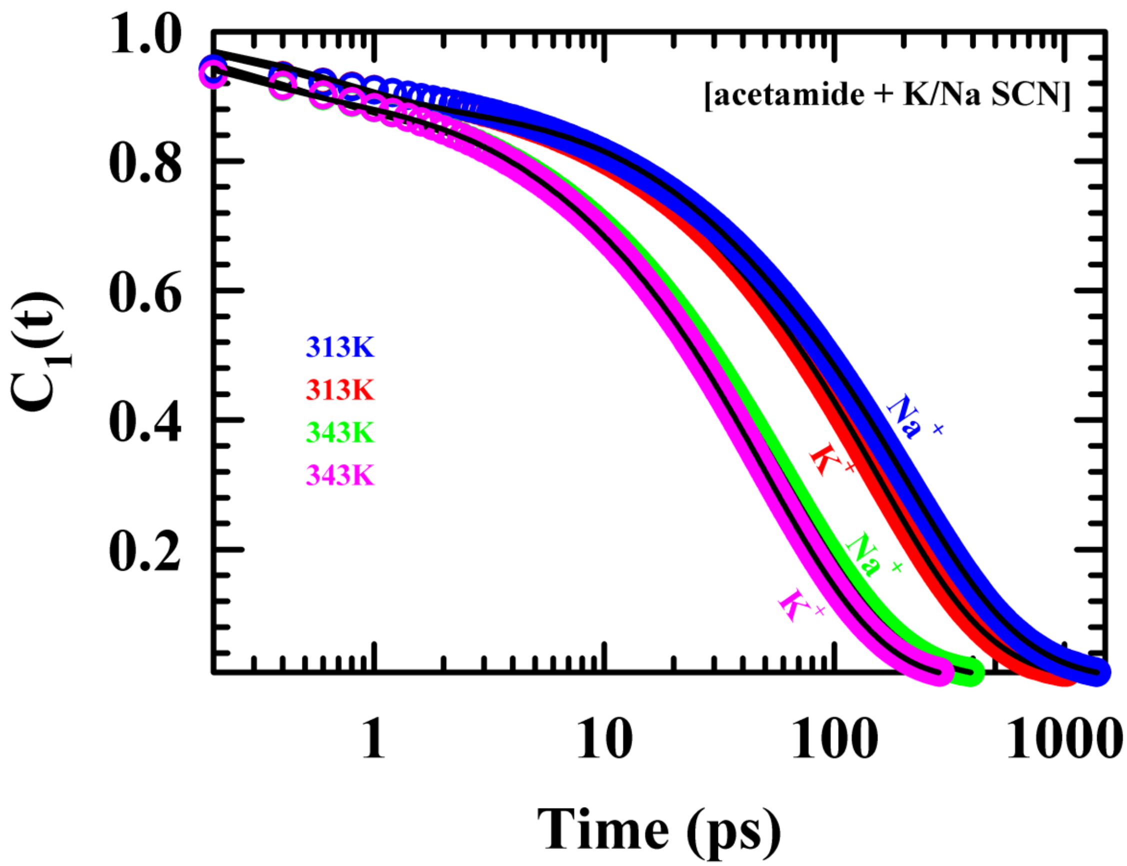

Figure 3.10. Simulated first rank reorientational correlation functions, $C_1(t)$, for the DESs, $0.25[f\ \mathrm{KSCN} + (1 - f)\ \mathrm{NaSCN}] + 0.75\mathrm{CH_3CONH_2}$ at f = 1 and 0, at two representative temperatures, 313K and 343K. Lines through the simulated data are multiexponential fits. Representations are color-coded.

Multi-exponential fit parameters required to describe these decays are summarized in **Table 3.A.7** (Appendix 3.A). Note the dependence of the $C_\ell(t)$ decays on both the cation identity and solution temperature. A comparison between the simulated reorientational relaxation time constants in **Table 3.A.7** (Appendix 3.A) and those from DR measurements summarized in **Tables 3.A.1 – 3.A.5** (Appendix 3.A) reveal that the slowest of the $C_\ell(t)$ decay time constants correlate well with those from DR measurements, although the corresponding amplitudes differ greatly. This makes $\langle\tau_{DR}\rangle \neq \langle\tau_{\ell=1}\rangle$ for these DESs. In addition, the simulated values for $\langle\tau_{\ell=1}\rangle$ at these temperatures indicate normal coupling with the simulated viscosities[33] in comparison to a significant decoupling observed between the measured average DR times, $\langle\tau_{DR}\rangle$, and the experimental viscosities. This difference in viscosity coupling (or decoupling) is arising probably from the insufficiency of the model force field parameters and was also observed earlier[32] for (acetamide+LiBr/NO_3/ClO_4) DESs. These observations notwithstanding, the comparison between the $C_{\ell}(t)$ decay times and experimental DR times clearly reflects that the latter derives contributions from the collective single particle reorientational relaxations.

The next aspect we examine is the interconnection between the cation dependent structural H-bond relaxation dynamics and DR dynamics in these DESs. Such a connection is expected as DR involves dipolar reorientations compelling the intermolecular H-bonds in associated liquids to undergo breaking and reformation. This was indeed noticed while exploring the origin of DR timescales in neat molten acetamide[16], and touched upon by other authors while explaining the composition dependence of experimental DR timescales in binary aqueous mixtures of 1,4-dioxane[96] and monohydroxy alcohols.[97] The structural H-bond correlation function, $C_{HB}(t)$, which allows H-bond breaking fleetingly and reformation at intermediate times and is different from the continuous H-bond correlation function, is given by,[60–63,98–100] $C_{HB}(t) = \langle h(0)h(t)\rangle/\langle h\rangle$, with $h(t')$ being unity if a pair of molecules remain H-bonded at time t' and zero otherwise. The average structural H-bond correlation time, $\langle \tau_{HB}^{C}\rangle$, is then obtained via time integration, $\langle \tau_{HB}^{C}\rangle = \int_0^{\infty} dt\ C_{HB}(t)$.

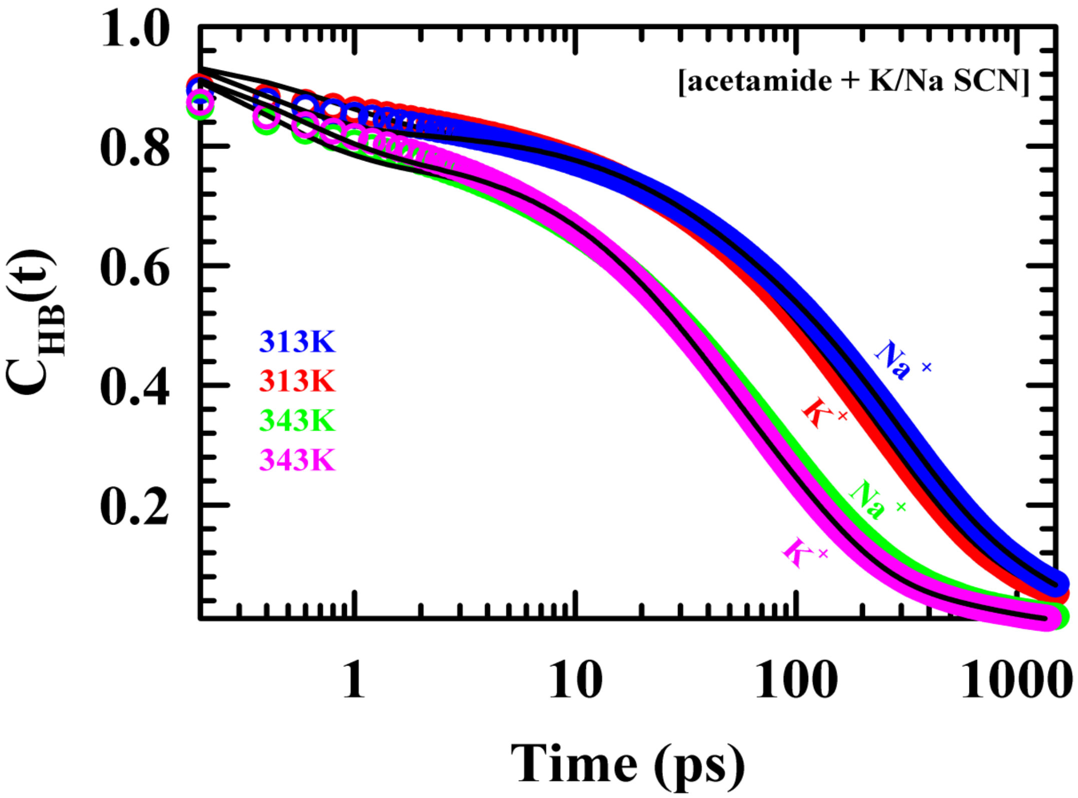

Figure 3.11. Simulated structural H-bond corelation function, $C_{HB}(t)$, for the DESs, $0.25[f\ \mathrm{KSCN} + (1-f)\ \mathrm{NaSCN}] + 0.75\mathrm{CH_3CONH_2}$ at f = 1 and 0, at two representative temperatures, 313K and 343K. Lines through the simulated data represent multiexponential fits. Representations are color-coded.

Figure 3.11 presents the cation dependent $C_{HB}\ (t)$ decays at two representative temperatures, 313 K and 343 K, while **Table 3.A.8** (Appendix 3.A) summarizes the multi-exponential fit parameters required to describe the simulated $C_{HB}\ (t)$ for these two systems at four different temperatures. Decays shown in this figure demonstrate the dependence on cation identity as $C_{HB}\ (t)$ is sensitive to medium viscosity through centre-of-mass diffusions of the participating molecules. This connection to translational displacements renders the slowest relaxation time constant (~15-20%) in the nanosecond regime which were absent in the simulated $C_{\ell}(t)$ decays. The second (with ~50% amplitude) and third (~15-20%) slower time constants of $C_{HB}\ (t)$ decays are in the same range as that were found in the present DR measurements. These factors combine to make $\langle\tau_{HB}^{C}\rangle$ values at these temperatures qualitatively similar to measured $\langle\tau_{DR}\rangle$ values. This is shown in **Table 3.1**, which immediately confirms the that DR in these systems not only derives contributions from the structural H-bond fluctuation dynamics and the collective single particle reorientational relaxations but recognizes the cation identity also. This cation identity dependence is further extended to the corresponding activation energies as well. This is shown in **Figure 3.A.12** (Appendix 3.A) where a comparison among activation energies reflects qualitatively similarity of cation dependence between experiments and simulations but with simulated activations energies somewhat higher than experiments in all the cases considered.

Table 3.1. Temperature dependent average times from experimental DR, first rank reorientational correlation functions and structural H-bond relaxation of DESs, $0.25[f\ \text{KSCN} + (1-f)\ \text{NaSCN}] + 0.75\text{CH}_3\text{CONH}_2$ for f = 1 and 0 at two representative temperatures.

Acetamide+KSCN				
T(K)	**313**	**323**	**333**	**343**
$\langle\boldsymbol{\tau_{DR}}\rangle$/(ps)	221	163	122	90
$\langle\boldsymbol{\tau_{\ell=1}}\rangle$/(ps)	145	94	65	47
$\langle\boldsymbol{\tau_{HB}^{c}}\rangle$/(ps)	340	208	151	107

Acetamide+NaSCN				
$\langle \tau_{DR} \rangle$/(ps)	387	283	215	126
$\langle \tau_{\ell=1} \rangle$/(ps)	197	125	85	57
$\langle \tau_{HB}^{c} \rangle$/(ps)	396	255	175	126

3.5 Concluding Remarks

In summary, a complete temperature and K^+ concentration dependent exepimental study of DR in the DESs, $0.25[f\,\mathrm{KSCN} + (1-f)\,\mathrm{NaSCN}] + 0.75\mathrm{CH_3CONH_2}$ at six different concentrations of KSCN was conducted to investigate the effects on dielectric behaviour of successive replacements of K^+ by Na^+(cation identity). The DR measurements were carried out in the frequency window, $0.2 \leq \nu/GHz \leq 50$, and the temperature range considered was, $303 \leq T/K \leq 343$. Experimental DRS revealed multi-Debye relaxations with the solution dynamics becoming increasingly slower as K^+ concentration was progressively replaced by Na^+. This successive decrease of K^+ concentration was also resulted decrease of the solution static dielectric constant (ε_s). Cole-Cole plots of the the experimental DR data showed a larger deviation from the single Debye behaviour for Na^+-DES than K^+-DES. Temperature dependent average DR times, $\langle \tau_{DR} \rangle$, exhibited a fractional viscosity dependence with DR in Na^+-DES being relatively more viscosity decoupled than in K^+-DES. DSC measurents supported this observation by indicating T_g being higher for Na^+-DES than that in K^+-DES.

Computer simulations of DR in the DESs, $0.25[f\,\mathrm{KSCN} + (1-f)\,\mathrm{NaSCN}] + 0.75\mathrm{CH_3CONH_2}$, at a few repersentative cation (K^+/Na^+) concentrations and temperatures were carried out in order to provide microscopic explanations for the above experimental observations. Simulated DR, although predicted polarization dynamics slower than those measured in experiments, reproduced multi-Debye relaxations qualitatively correctly. Simulated first rank collective single particle reorientational relaxations and structural H-bond fluctuation dynamics indicated that the measured DR timescales are intimately connected to dipolar reorientation dynamics and structural H-bond relaxations. The reduction in the static dielectric constant values in these DESs (over that of the neat molten acetamide) were found to be connected to the decrease of the average number of H-bonds per acetamide molecule and the consequent frustrations in the dipole orientations (quantified by the Kirkwood g factor).

Decompositions of the simulated frequency dependent total dielectric spectra into the dipole-dipole, ion-ion and dipole-ion interaction contributions indicated an overwhelming dominance of the dipolar term in the GHz regime, where the ion-ion and dipole-ion contribitions were nearly negligible. The latter two terms assumed some importance at the THz frequency range. This spectral decomposition therefore strongly suggested that the dielectric decrement observed in experiments originated mainly from the frustration of the dipolar orientation order caused by the ion-induced partial damage of the H-bond network structure of acetamide molecules. Further analyses suggested that the cation identity dependence of the dielectric properties arose from the differential abilities of these two alkali metal cations to frustrate the dipolar order via damaging the H-bond network. We would like to mention that our present simulations were carried out employing model potentials where polarizability was implicitly treated within the force field parameters. Considering that explicit treatment of polarization may affect transport quantities,[101,102] one may think of employing model potentials where polarizabilities are explicitly treated. However, use of such polarizable force fields may not critically change the final conclusion of the present work. This is because the dipole-dipole contribution ($\varepsilon_{DD}(\omega)$) overwhelmingly dominates the total frequency dependent dielectric response, whereas the contributions from the dipole-ion cross correlation ($\varepsilon_{DJ}(\omega)$) and the ion-ion correlation ($\varepsilon_{JJ}^{c}(\omega)$) are tiny and nearly insignificant. Considering a huge simulation cost associated with the use of polarizable force field and knowing that such an attempt would not produce any new and qualitatively different insight about the DR dynamics investigated here, we refrained from such an exercise.

Appendix 3.A

Table 3.A.1. Parameters obtained from simultaneous multi-Debye fits to the real (ε') and the imaginary (ε'') components of the measured frequency dependent DR spectra of $0.25[f\text{KSCN} + (1-f)\text{NaSCN}] + 0.75\text{CH}_3\text{CONH}_2$ DESs at 303 K. Measurements were done at different K^+ concentration by varying f . Note f = 1 denotes the complete absence of Na^+ and f = 0 the complete absence of K^+. Both 3-Debye and 4-Debye fit parameters are shown for DR in this DES at f = 0. Measured conductivities (k) and experimental viscosities (η, from literature) are also shown.

T = 303 K													
f	ε_s	$\Delta\varepsilon_1$	τ_1 (ps)	$\Delta\varepsilon_2$	τ_2 (ps)	$\Delta\varepsilon_3$	τ_3 (ps)	$\Delta\varepsilon_4$	τ_4 (ps)	ε_∞	$\langle\tau_{DR}\rangle$* (ps)	k (s/m)	$\eta(cp)$
1	26.7			15.7 (78%)	355	3.8 (19%)	49	0.6 (3%)	5	6.6	286	0.35	86.50
0.8	24.4			13.9 (78%)	385	3.6 (20%)	49	0.4 (2%)	5	6.5	309	0.28	120.6
0.6	21.8			11.9 (78%)	397	3.2 (21%)	47	0.2 (1%)	5	6.5	317	0.20	178.5
0.4	19.9			10.3 (76%)	381	3.0 (22%)	46	0.2 (2%)	5	6.3	301	0.18	276.10
0.2	17.4			8.4 (76%)	381	2.6 (23%)	44	0.1 (1%)	5	6.3	298	0.13	487.9
0	20	8.0 (58%)	1001	4.3 (31%)	200	1.6 (11%)	29			6.1	641	0.07	965.4
	21	7.2 (48%)	1521	5.6 (37%)	295	2 (13%)	40	0.2 (2%)	5	6	847	0.07	

$$*\langle\tau_{DR}\rangle = \frac{\sum_{i=1}^{n} a_i\tau_i}{\sum_{i=1}^{n} a_i}$$

Table 3.A.2. Parameters obtained from simultaneous multi-Debye fits to the real (ε') and the imaginary (ε'') components of the measured frequency dependent DR spectra of $0.25[f\text{KSCN} + (1-f)\text{NaSCN}] + 0.75\text{CH}_3\text{CONH}_2$ DESs at 313 K. Both 3-Debye and 4-Debye fit parameters are shown for DR in this DES at f = 0.

T = 313 K													
f	ε_s	$\Delta\varepsilon_1$	τ_1 (ps)	$\Delta\varepsilon_2$	τ_2 (ps)	$\Delta\varepsilon_3$	τ_3 (ps)	$\Delta\varepsilon_4$	τ_4 (ps)	ε_∞	$\langle\tau_{DR}\rangle$ (ps)	k (s/m)	$\eta(cP)$
1	27.4			15.9 (76%)	279	4.1 (20%)	47	1.0 (5%)	5	6.4	221	0.50	48.85
0.8	25.9			14.2 (75%)	324	4.0 (21%)	57	0.7 (4%)	5	7.0	256	0.39	63.83
0.6	24.6			13.1 (74%)	337	4.0 (23%)	53	0.6 (3%)	5	6.9	261	0.32	87.27
0.4	20.6			10.7 (71%)	356	3.6 (24)	60	0.7 (5%)	6	5.6	269	0.24	126.3
0.2	20.7			10.5 (72%)	367	3.3 (23%)	55	0.7 (5%)	5	6.2	279	0.20	204.3
0	16.7	7.4 (69%)	482			2.8 (26%)	77	0.6 (5%)	5	5.9	351	0.10	355.9
	20.2	8.2 (61%)	576	3.8 (28%)	122	1.4 (10%)	26	0.1 (1%)	5	6.7	387	0.13	

Table 3.A.3. Parameters obtained from simultaneous multi-Debye fits to the real (ε') and the imaginary (ε'') components of the measured frequency dependent DR spectra of $0.25[f\mathrm{KSCN} + (1-f)\mathrm{NaSCN}] + 0.75\mathrm{CH_3CONH_2}$ DESs at 323 K.

T = 323 K													
f	ε_s	$\Delta\varepsilon_1$	τ_1 (ps)	$\Delta\varepsilon_2$	τ_2 (ps)	$\Delta\varepsilon_3$	τ_3 (ps)	$\Delta\varepsilon_4$	τ_4 (ps)	ε_∞	$\langle\tau_{DR}\rangle$ (ps)	k (s/m)	$\eta(cp)$
1	28.4			15.8 (73%)	209	4.5 (21%)	45	1.3 (6%)	5	6.8	163	0.74	30.20
0.8	26.5			14.4 (73%)	250	4.4 (22%)	50	1.0 (5%)	5	6.7	193	0.55	37.43
0.6	25.3			13.5 (72%)	257	4.2 (23%)	48	0.9 (5%)	5	6.8	199	0.46	47.81
0.4	23.6			12.3 (71%)	286	4.1 (24%)	52	0.9 (5%)	5	6.3	216	0.36	65.10
0.2	22.0			11.0 (71%)	303	3.7 (24%)	50	0.6 (5%)	5	6.6	229	0.27	98.31
0	19.6			8.7 (69%)	383	3.6 (28%)	72	0.4 (3%)	5	6.9	283	0.17	155.7

Table 3.A.4. Parameters obtained from simultaneous multi-Debye fits to the real (ε') and the imaginary (ε'') components of the measured frequency dependent DR spectra of $0.25[f\mathrm{KSCN} + (1-f)\mathrm{NaSCN}] + 0.75\mathrm{CH_3CONH_2}$ DESs at 333 K.

T = 333 K													
f	ε_s	$\Delta\varepsilon_1$	τ_1 (ps)	$\Delta\varepsilon_2$	τ_2 (ps)	$\Delta\varepsilon_3$	τ_3 (ps)	$\Delta\varepsilon_4$	τ_4 (ps)	ε_∞	$\langle\tau_{DR}\rangle$ (ps)	k (s/m)	$\eta(cp)$
1	28.8			15.3 (71%)	158	4.9 (23%)	41	1.4 (6%)	5	7.2	122	1.05	20.48
0.8	26.5			13.9 (70%)	172	4.5 (23%)	44	1.6 (7%)	5	6.5	130	0.86	23.79
0.6	26			13.4 (70%)	190	4.5 (24%)	43	1.2 (6%)	5	6.9	144	0.70	29.02
0.4	24.2			12.1 (67%)	207	4.5 (25%)	47	1.4 (8%)	5	6.2	151	0.57	37.58
0.2	23.3			11.5 (69%)	218	4.1 (25%)	44	1.0 (6%)	5	6.7	162	0.45	52.56
0	21.2			9.2 (64%)	303	4.2 (29%)	67	0.9 (7%)	5	6.9	215	0.27	78.08

Table 3.A.5. Parameters obtained from simultaneous multi-Debye fits to the real (ε') and the imaginary (ε'') components of the measured frequency dependent DR spectra of $0.25[f\mathrm{KSCN} + (1 - f)\mathrm{NaSCN}] + 0.75\mathrm{CH_3CONH_2}$ DESs at 343 K.

T = 343 K													
f	ε_s	$\Delta\varepsilon_1$	τ_1 (ps)	$\Delta\varepsilon_2$	τ_2 (ps)	$\Delta\varepsilon_3$	τ_3 (ps)	$\Delta\varepsilon_4$	τ_4 (ps)	ε_∞	$\langle\tau_{DR}\rangle$ (ps)	k (s/m)	$\eta(cp)$
1	28.4			14.6 (69%)	118	4.8 (23%)	36	1.8 (8%)	5	7.2	90	1.43	14.35
0.8	26.2			13.9 (69%)	128	4.5 (23%)	35	1.7 (8%)	5	6.1	98	1.19	16.08
0.6	26			12.9 (68%)	136	4.6 (24%)	37	1.5 (8%)	5	7.0	102	1.05	18.81
0.4	24.7			12.1 (66%)	148	4.7 (26%)	37	1.4 (8%)	5	6.5	108	0.87	23.27
0.2	24.0			11.0 (65%)	159	4.7 (27%)	41	1.3 (8%)	5	6.9	114	0.73	30.80
0	22.5			10.3 (64%)	178	4.3 (27%)	42	1.4 (9%)	5	6.5	126	0.53	43.08

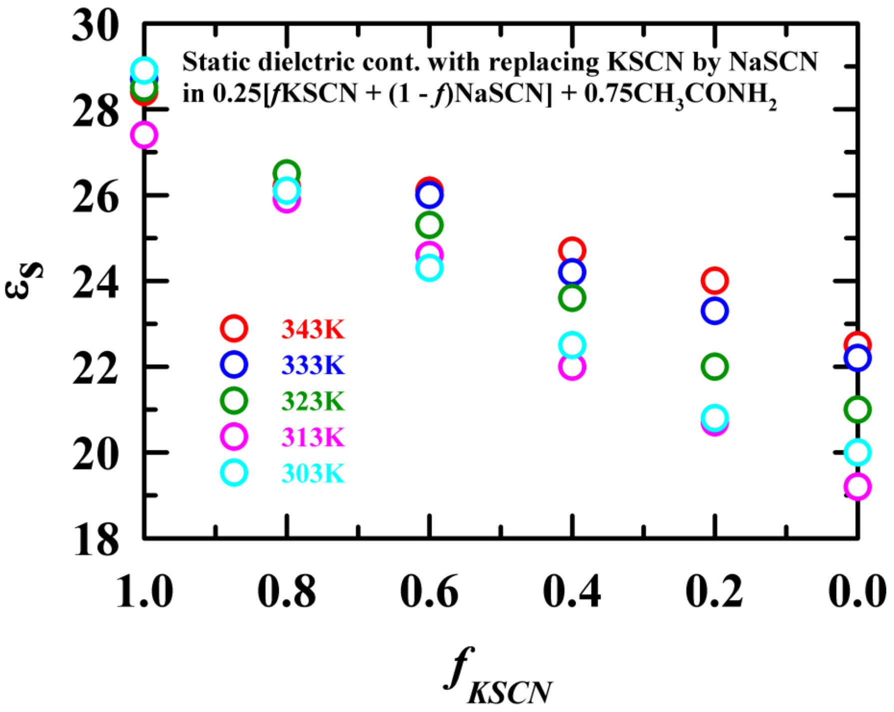

Figure 3.A.1. KSCN concentration dependent static dielectric constant (ε_s) of $0.25[f\mathrm{KSCN} + (1 - f)\mathrm{NaSCN}] + 0.75\mathrm{CH_3CONH_2}$ DESs at different temperatures. Representations are colour-coded. Note the decrease of ε_s with the decrease of $\mathrm{K^+}$ concentration in these media.

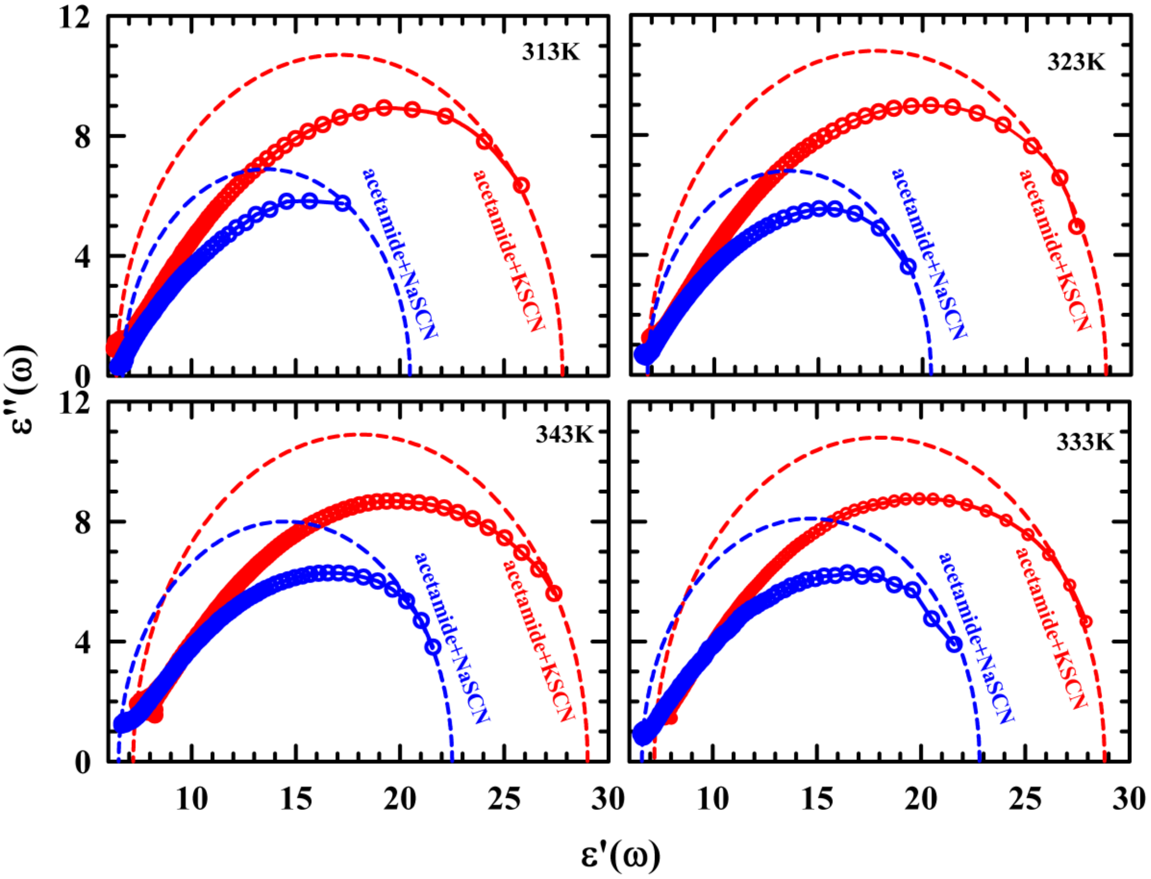

Figure 3.A.2. Cole-Cole plots comparing the experimental DR of $0.25[f\text{KSCN} + (1 - f)\text{NaSCN}] + 0.75\text{CH}_3\text{CONH}_2$ DESs at f = 1 and 0 for four different temperatures, along with their Debye semicircles in four different temperatures. Symbols with line represents the experimental data points. Dashed lines represent the Debye semicircles (formed via Cole-Cole plots) for hypothetical dipolar systems relaxing via a single Debye process with time constant equal to the measured average DR time, $\langle\tau_{DR}\rangle$, responsible for dispersion from the measured ε_s to the measured ε_∞. These Debye semicircles for hypothetical dipolar liquids were constructed by using the following relation: $\varepsilon'(\omega) = \varepsilon_\infty + \frac{\varepsilon_s - \varepsilon_\infty}{1+\omega^2(\langle\tau_{DR}\rangle)^2}$ and $\varepsilon''(\omega) = \frac{(\varepsilon_s - \varepsilon_\infty)\omega\langle\tau_{DR}\rangle}{1+\omega^2(\langle\tau_{DR}\rangle)^2}$. Representations are colour coded.

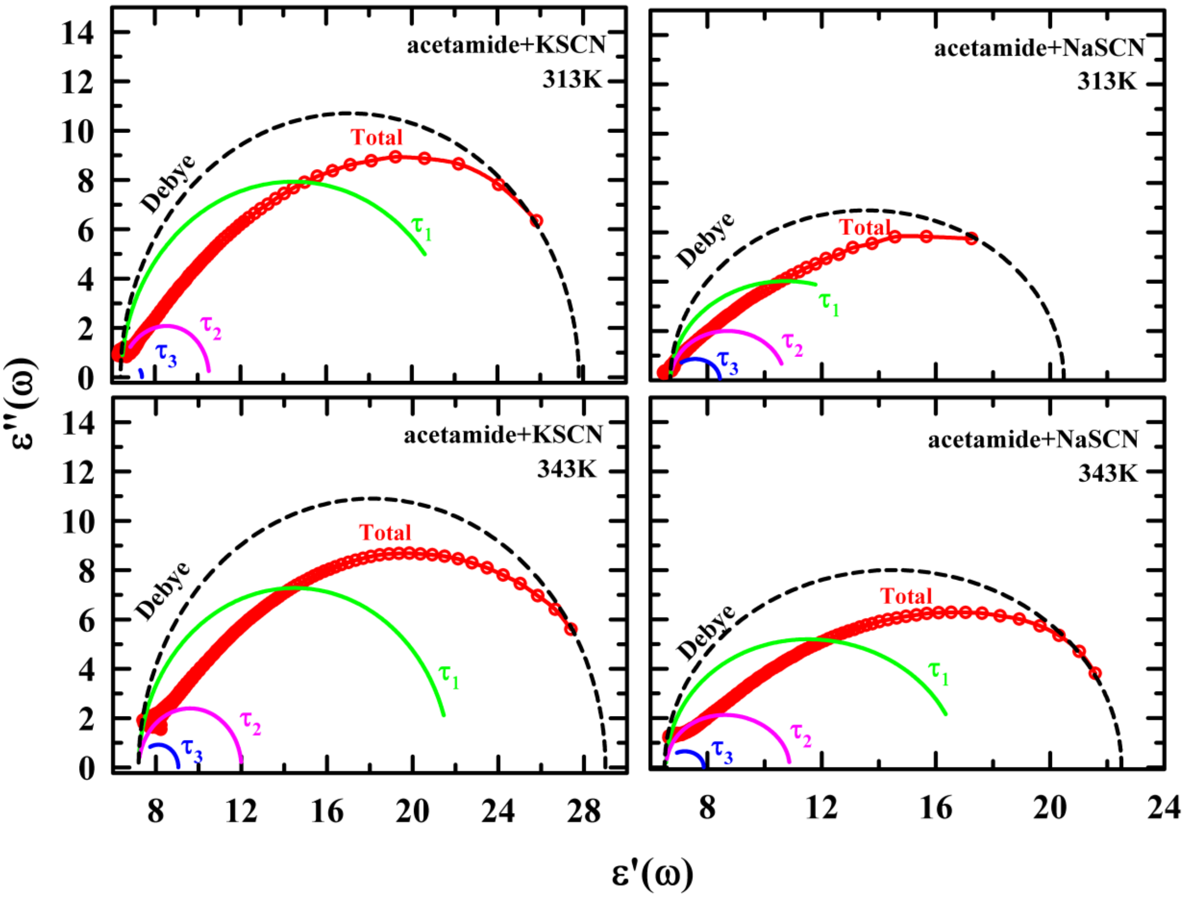

Figure 3.A.3. Deconvolution of the Cole-Cole spectra into the contributions from each time components detected in DR measurements of $0.25[f\mathrm{KSCN}+(1-f)\mathrm{NaSCN}]+0.75\mathrm{CH_3CONH_2}$ DESs at f = 1 (*left panels*) and 0 (*right panels*) at two representative temperatures. Multi-Debye fit parameters required to fit the experimental DR spectra are provided in Tables 3.A.1-3.A.5 (Appendix 3.A). Representations are color-coded.

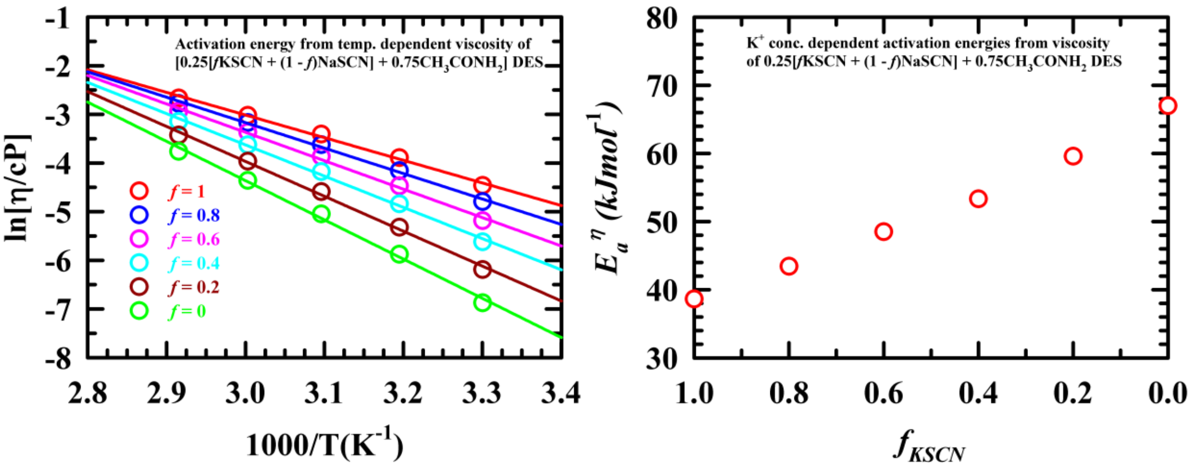

Figure 3.A.4. *Left panel*: Arrhenius plots for temperature dependent viscosity coefficients (η) for $0.25[f\ \mathrm{KSCN}\ +\ (1-f)\ \mathrm{NaSCN}]\ +\ 0.75\mathrm{CH_3CONH_2}$ DESs. Solid lines through the data sets represent the linear fits. *Right panel*: the corresponding K^+ concentration dependence of the activation energies, E_a^{η}. Representations are colour coded.

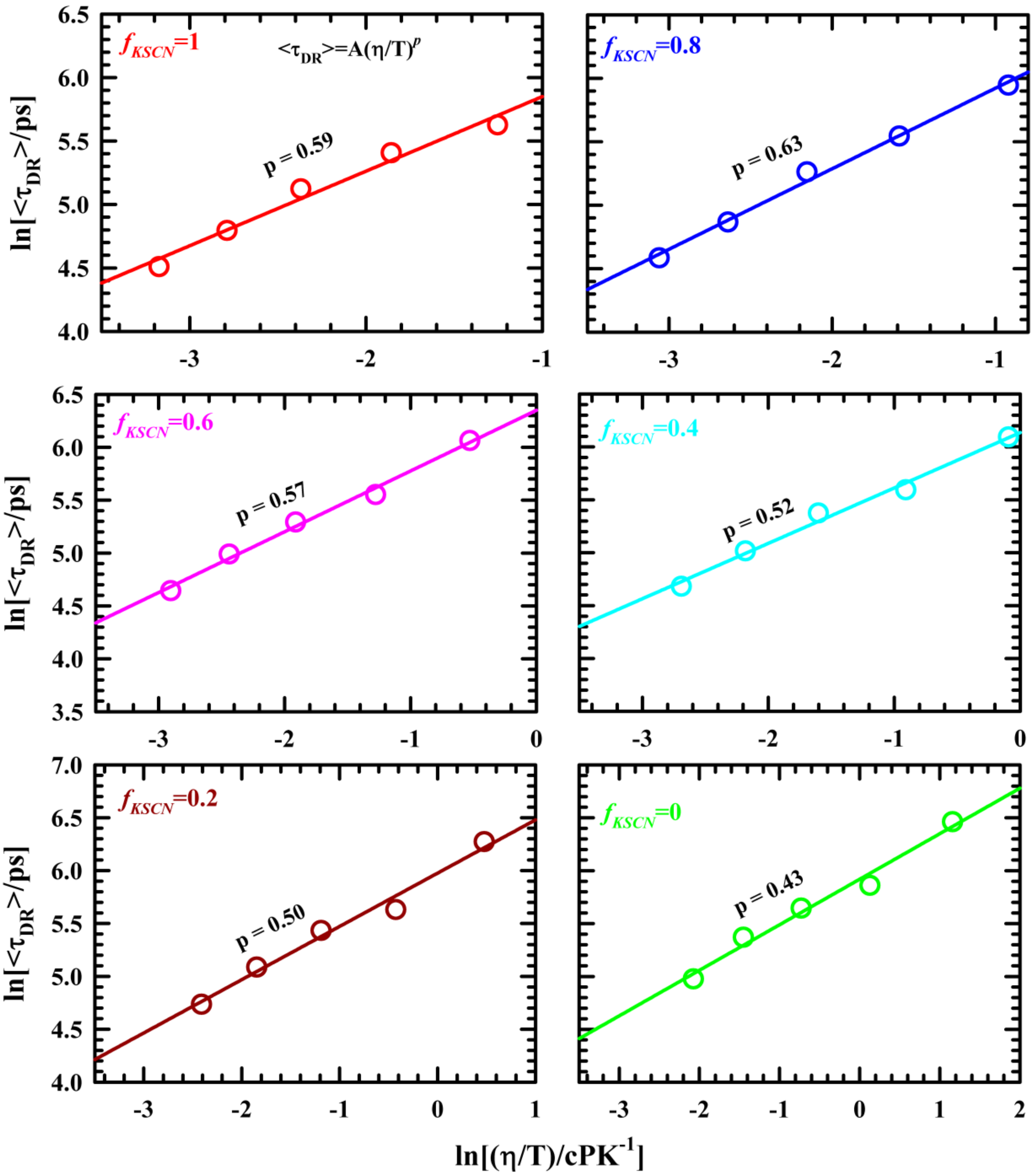

Figure 3.A.5. Viscosity coupling of the experimental average DR times for DESs, $0.25[f\ \mathrm{KSCN} + (1-f)\,\mathrm{NaSCN}] + 0.75\mathrm{CH_3CONH_2}$, at six different K^+ concentrations. Temperature dependent average DR times are plotted as a function of temperature reduced viscosity in a log-log plot. Lines through the experimental data represent linear fits to the following expression, $ln[<\tau_{DR}>] = A + pln[\frac{\eta}{T}]$, with p-values shown in the respective panels.

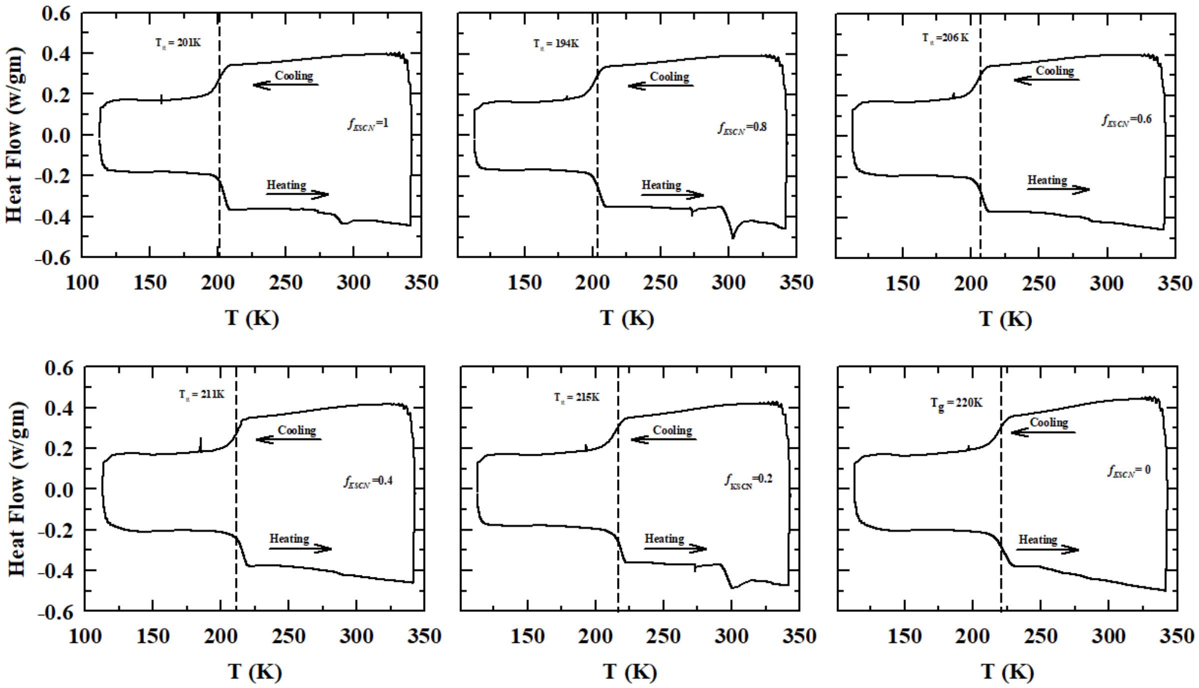

Figure 3.A.6. Differential scanning calorimetry (DSC) heating traces for $0.25[f\text{KSCN} + (1-f)\,\text{NaSCN}] + 0.75\text{CH}_3\text{CONH}_2$ DESs in six different K^+ concentrations. Glass transition temperatures (T_g) are determined from the two slopes of heating and cooling curves as indicated by the dashed lines. Notice that the successive replacement of K^+ by Na^+ leads to an elevation of the T_g.

Table 3.A.6. Temperature dependent parameters obtained from simultaneous fits of simulated real (ε') and imaginary (ε'') components of the simulated DR spectra of [acetamide+ K/Na SCN].

[acetamide+ KSCN]										
T(K)	ε_s	$\Delta\varepsilon_1$	τ_1 (ps)	$\Delta\varepsilon_2$	τ_2 (ps)	$\Delta\varepsilon_3$	τ_3 (ps)	$\Delta\varepsilon_4$	τ_4 (ps)	$\langle\tau\rangle$ (ps)
313	48.65	43.36 (91%)	681	2.86 (6%)	67	0.95 (2%)	1.8	0.48 (1%)	0.7	623
323	49.41	39.70 (82%)	456	6.78 (14%)	153	0.97 (2%)	3.2	0.97 (2%)	0.6	395
333	46.81	40.77 (89%)	305	3.21 (7%)	51	0.92 (2%)	2.1	0.92 (2%)	0.2	275
343	43.35	36.84 (87%)	208	3.39 (8%)	54	0.85 (2%)	5.1	1.27 (3%)	0.3	185
[acetamide+ NaSCN]										
T(K)	ε_s	$\Delta\varepsilon_1$	τ_1 (ps)	$\Delta\varepsilon_2$	τ_2 (ps)	$\Delta\varepsilon_3$	τ_3 (ps)	$\Delta\varepsilon_4$	τ_4 (ps)	$\langle\tau\rangle$ (ps)
313	47.29	34.25 (74%)	957	9.26 (20%)	378	1.39 (3%)	33	1.39 (3%)	1.2	784
323	44.28	39.82 (92%)	463	1.30 (3%)	82	1.30 (3%)	5	0.87 (2%)	0.2	429
333	44.14	32.79 (76%)	390	8.63 (20%)	119	0.86 (2%)	5	0.86 (2%)	0.2	320
343	42.08	32.04 (78%)	252	6.98 (17%)	86	0.82 (2%)	6	1.23 (3%)	0.4	212

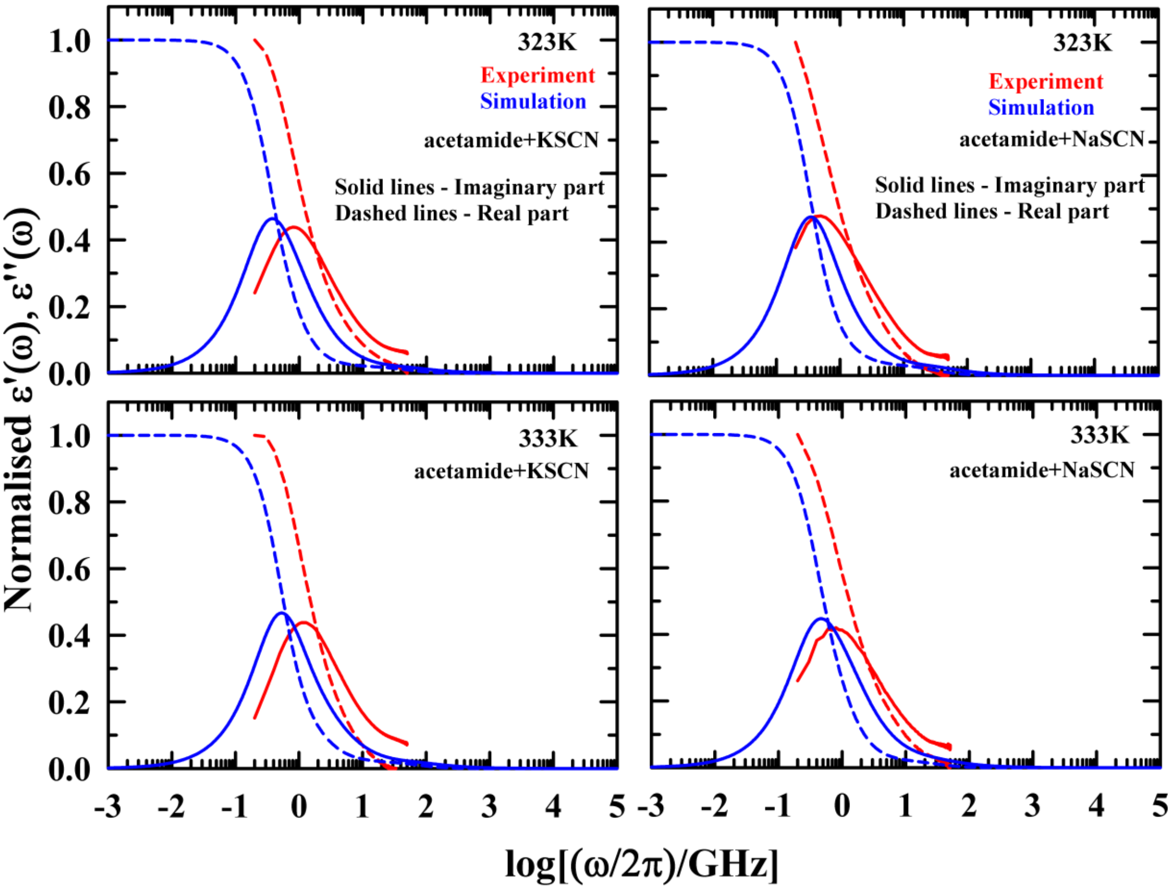

Figure 3.A.7. Comparison between the experimental and the simulated real and imaginary components of the DR spectra of $0.25[f\mathrm{KSCN} + (1 - f)\,\mathrm{NaSCN}] + 0.75\mathrm{CH_3CONH_2}$ DESs at f=1 (*left panels*) and f=0 (*right panels*) at two representative temperatures, 323K and 333K. Simulated and experimental spectra (both the real and imaginary components) are presented after carrying out appropriate normalization via the following relations: Real component → $(\varepsilon'(\omega) - \varepsilon_\infty)/(\varepsilon_s - \varepsilon_\infty)$, (broken lines); Imaginary component → $\varepsilon''(\omega)/\,(\varepsilon_s - \varepsilon_\infty)$, (solid lines). Representations are colour coded.

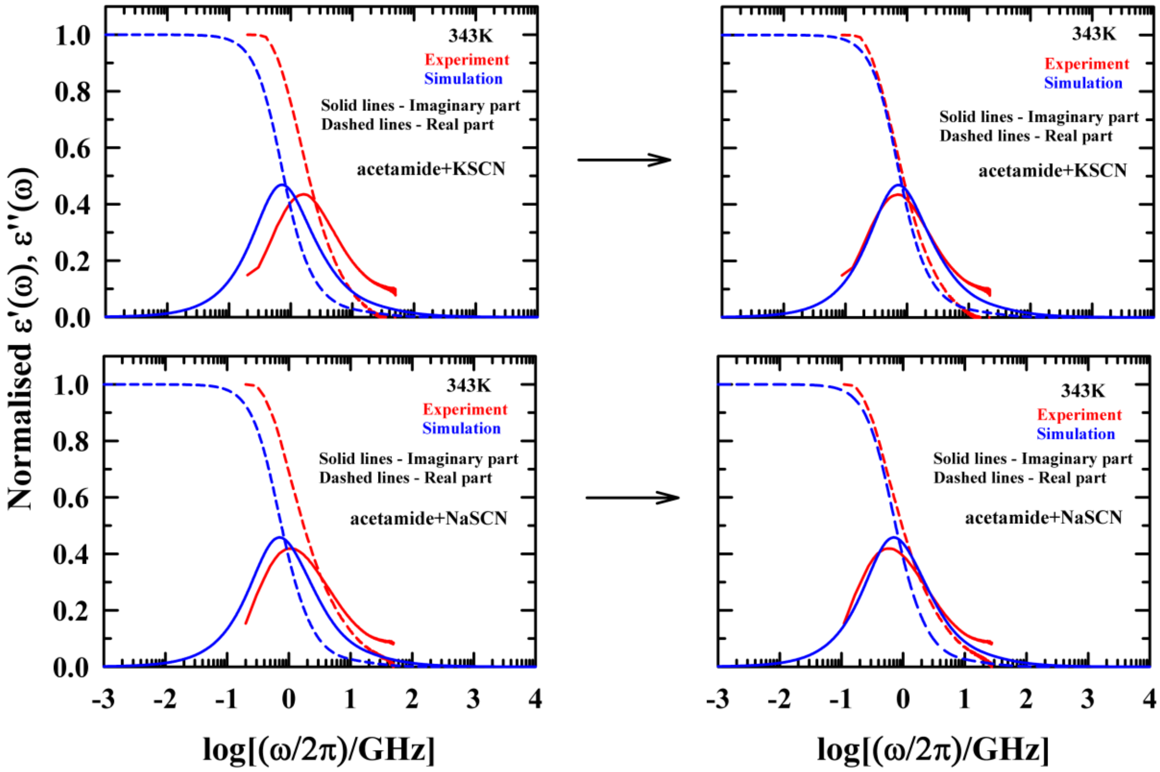

Figure 3.A.8. Representative figure showing that after translational shifts, the experimental real and imaginary components of the DR spectra of the DESs at f =1 (*upper panels*) and f=0 (*lower panels*) match well with the corresponding simulated spectra. The comparison is shown only for a representative temperature, T= 343K. The translational shifts employed were as follows: $\Delta\nu_{exp}^{New} = \Delta\nu_{exp}^{Old} * 0.55$ at f=0 and $\Delta\nu_{exp}^{New} = \Delta\nu_{exp}^{Old} * 0.43$ at f=1.

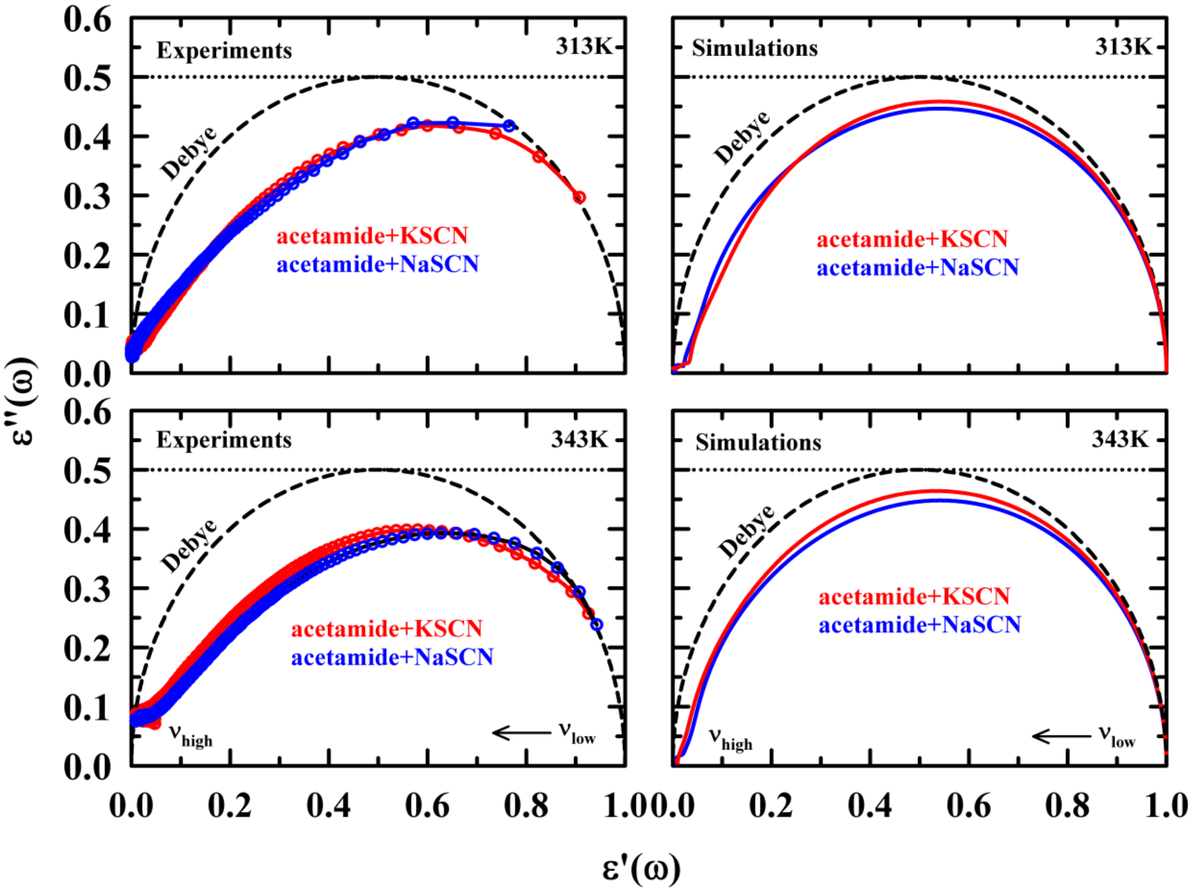

Figure 3.A.9. A comparison between experimental (*left* panels) and simulated (*right* panels) DR, via Cole-Cole description, for $0.25[f\text{KSCN} + (1 - f)\text{NaSCN}] + 0.75\text{CH}_3\text{CONH}_2$ DESs at f = 1 and 0. Results are shown for two representative temperatures, 313 K (*upper panels*) and 343 K (*lower panels*). Dashed black lines indicate the Debye semicircle for the respective systems. Simulated and experimental spectra (both the real and imaginary components) are presented after appropriate amplitude normalization as follows: $(\varepsilon'(\omega) - \varepsilon_\infty)/(\varepsilon_s - \varepsilon_\infty)$ and $\varepsilon''(\omega)/\,(\varepsilon_s - \varepsilon_\infty)$, respectively. All representations are color-coded.

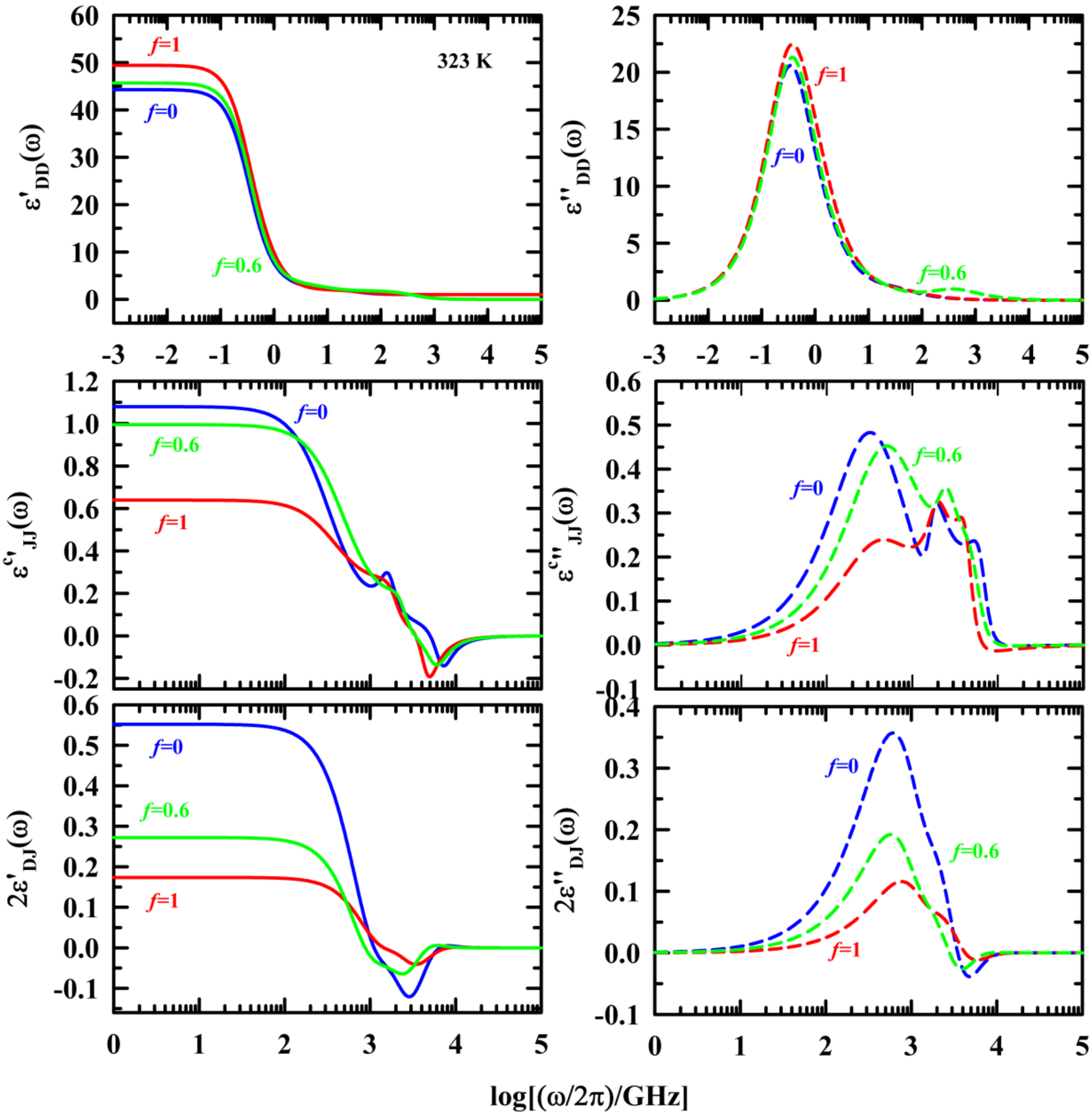

Figure 3.A.10. Decomposition of the total simulated DR spectra into dipole-dipole (*DD*), ion-ion (*JJ*)and dipole-ion (*DJ*) interaction contributions: $\Sigma_0(\omega) = \varepsilon_{DD}(\omega) + \varepsilon_{JJ}^{c}(\omega) - 2\varepsilon_{DJ}(\omega)$. $\varepsilon_{JJ}^{c}(\omega)$ is the ion-ion contribution after the zero-frequency conductivity correction. *Left panels* present the *real* components of the simulated rotational (dipole-dipole), translational (current-current) and ro-translational (dipole-ion) contributions to the total spectra ($\Sigma_0(\omega)$), while the *right panels* present the corresponding *imaginary* components. These simulated spectra are for $0.25[f\text{KSCN} + (1 - f)\text{NaSCN}] + 0.75\text{CH}_3\text{CONH}_2$ at *f*=0, 0.6 and 1. Calculations were done at one representative temperature, T = 323 K.

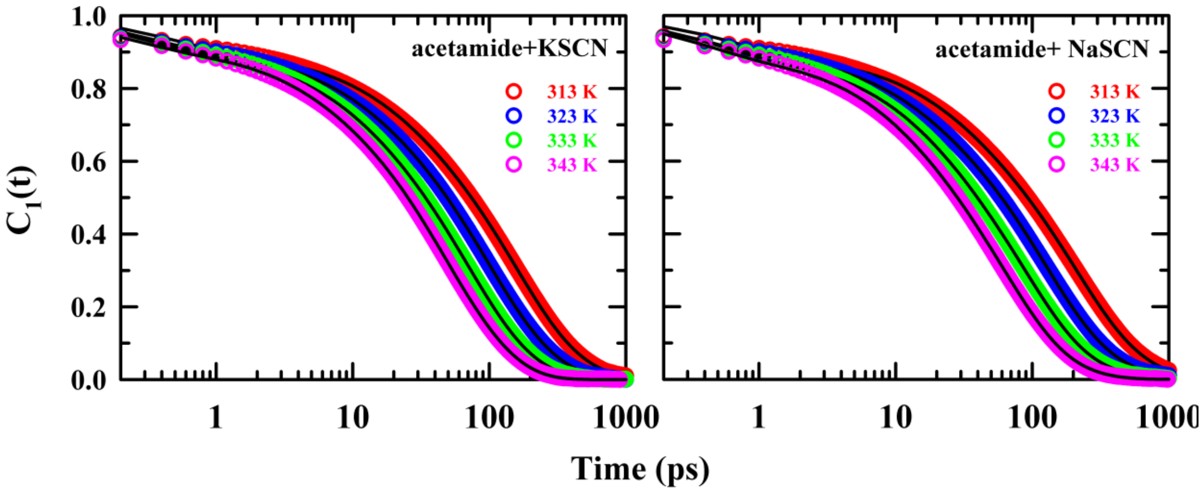

Figure 3.A.11. Simulated first rank ($\ell = 1$) collective single particle reorientational correlation functions, $C_1(t)$, for acetamide in $0.25[f\text{KSCN} + (1-f)\text{NaSCN}] + 0.75\text{CH}_3\text{CONH}_2$ at f=1 (*left panel*) and at f=0 (*right panel*) for four different temperatures. Lines through the simulated data represent the multi-exponential fits (fit parameters summarized below in **Table 3.A.7**). Representations are color-coded.

Table 3.A.7. Multi-exponential fit parameters required to describe the simulated first rank ($\ell = 1$) collective single particle reorientational correlation functions ($C_1(t)$) for acetamide in $0.25[f\text{KSCN} + (1-f)\text{NaSCN}] + 0.75\text{CH}_3\text{CONH}_2$ DESs at f=1 and 0. $\langle\tau_{\ell=1}\rangle$ denotes amplitude-weighted average reorientational correlation times.

[acetamide+ KSCN]									
T(K)	a_1	τ_1(ps)	a_2	τ_2(ps)	a_3	τ_3(ps)	a_4	τ_4(ps)	$\langle\tau_{\ell=1}\rangle(ps)$
313	0.20	314	0.57	140	0.13	21	0.10	0.5	145
323	0.36	168	0.43	75	0.11	12	0.10	0.4	94
333	0.31	119	0.48	57	0.11	9	0.10	0.3	65
343	0.54	71	0.28	29	0.09	5	0.09	0.2	47
[acetamide+ NaSCN]									
T(K)	a_1	τ_1(ps)	a_2	τ_2(ps)	a_3	τ_3(ps)	a_4	τ_4(ps)	$\langle\tau_{\ell=1}\rangle(ps)$
313	0.20	461	0.55	184	0.14	26	0.11	0.6	197
323	0.20	300	0.58	109	0.12	14	0.10	0.4	125
333	0.12	250	0.63	84	0.14	14	0.11	0.5	85
343	0.15	141	0.60	58	0.14	10	0.11	0.4	57

Table 3.A.8. Multi-exponential fit parameters required to describe the structural hydrogen bond autocorrelation function ($C_{HB}(t)$) for $0.25[f\mathrm{KSCN} + (1-f)\mathrm{NaSCN}] + 0.75\mathrm{CH_3CONH_2}$ DESs at f=1 and 0 for four different temperatures. $\langle \tau_{HB}^{c} \rangle$ denote amplitude-weighted average structural H-bond lifetimes.

[acetamide+ KSCN]									
T(K)	a_1	τ_1(ps)	a_2	τ_2(ps)	a_3	τ_3(ps)	a_4	τ_4(ps)	$\langle \tau_{HB}^{c} \rangle (ps)$
313	0.17	1240	0.52	237	0.15	39	0.17	0.40	340
323	0.16	792	0.52	148	0.14	27	0.19	0.40	208
333	0.10	791	0.50	132	0.21	29	0.20	0.40	151
343	0.09	614	0.48	96	0.23	23	0.21	0.40	107
[acetamide+ NaSCN]									
T(K)	a_1	τ_1(ps)	a_2	τ_2(ps)	a_3	τ_3(ps)	a_4	τ_4(ps)	$\langle \tau_{HB}^{c} \rangle (ps)$
313	0.23	1178	0.48	252	0.12	32	0.17	0.4	396
323	0.16	990	0.48	190	0.16	32	0.20	0.4	255
333	0.13	798	0.48	138	0.19	27	0.20	0.4	175
343	0.10	704	0.47	108	0.22	23	0.21	0.4	126

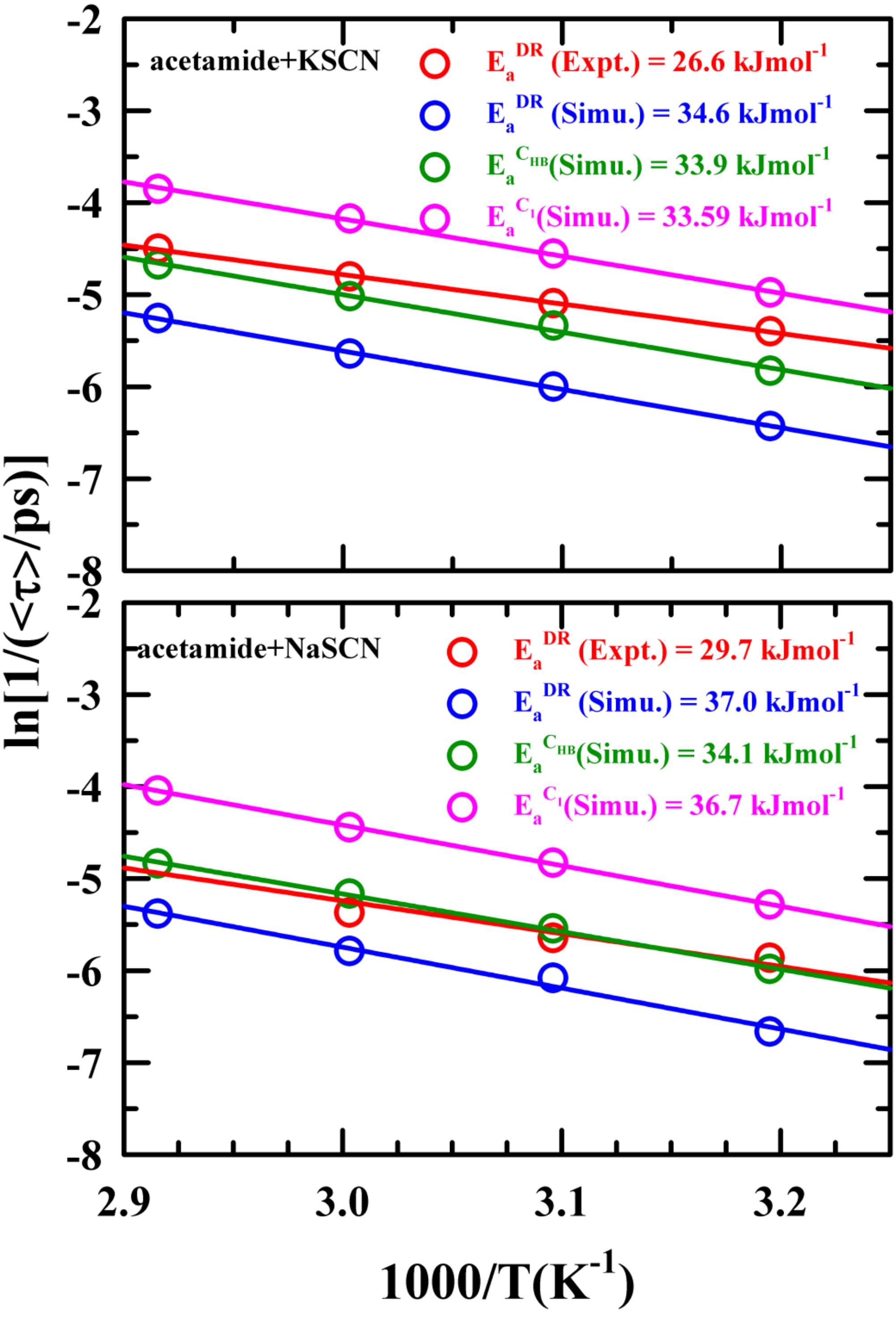

Figure 3.A.12. Activation energies estimated from the experimental and simulated average DR times, and the simulated average structural H-bond lifetimes and reorientational correlation times ($\langle\tau_{HB}^{c}\rangle$ and $\langle\tau_{\ell=1}\rangle$, respectively) for the DESs, $0.25[f\mathrm{KSCN} + (1-f)\mathrm{NaSCN}] + 0.75\mathrm{CH_3CONH_2}$ DESs at f=1 (*upper panel*) and 0 (*lower panel*). The activation energies are mentioned inside these panels. Representations are colour coded.

References

1 E. L. Smith, A. P. Abbott and K. S. Ryder, *Chem. Rev.*, 2014, **114**, 11060–11082.

2 B. B. Hansen, S. Spittle, B. Chen, D. Poe, Y. Zhang, J. M. Klein, A. Horton, L. Adhikari, T. Zelovich, B. W. Doherty, B. Gurkan, E. J. Maginn, A. Ragauskas, M. Dadmun, T. A. Zawodzinski, G. A. Baker, M. E. Tuckerman, R. F. Savinell and J. R. Sangoro, *Chem. Rev.*, 2021, **121**, 1232–1285.

3 G. Berchiesi, G. G. Lobbia, V. Bartocci and G. Vitali, *Thermochim. Acta*, 1983, **70**, 317–324.

4 G. Berchiesi, G. G. Lobbia, M. A. Berchiesi and G. Vitali, *J. Therm. Anal.*, 1984, **29**, 729–732.

5 G. G. Lobbia, G. Berchiesi and G. Poeti, *Thermochim. Acta*, 1984, **74**, 247–250.

6 G. Berchiesi, M. De Angelis, G. Rafaiani and G. Vitali, *J. Mol. Liq.*, 1992, **51**, 11–38.

7 A. Schulz, P. Lunkenheimer and A. Loidl, *J. Chem. Phys.*, 2021, **155**, 044503.

8 D. Reuter, P. Münzner, C. Gainaru, P. Lunkenheimer, A. Loidl and R. Böhmer, *J. Chem. Phys.*, 2021, **154**, 154501.

9 A. Amico, G. Berchiesi, C. Cametti and A. Di Biasio, *J. Chem. Soc., Faraday Trans. 2*, 1987, **83**, 619–626.

10 G. Berchiesi, G. Rafaiani, G. Vitali and F. Farhat, *J. Therm. Anal. Calorim.*, 2007, **44**, 1313–1319.

11 G. Berchiesi, G. Vitali, R. Płowiec and S. Barocci, *J. Chem. Soc., Faraday Trans. 2*, 1989, **85**, 635–641.

12 G. Berchiesi, *J. Mol. Liq.*, 1999, **83**, 271–282.

13 R. Biswas, A. Das and H. Shirota, *J. Chem. Phys.*, 2014, **141**, 134506.

14 J. Rajbangshi, K. Mukherjee and R. Biswas, *J. Phys. Chem. B.*, 2021, **125**, 5920–5936.

15 K. Mukherjee, E. Tarif, A. Barman and R. Biswas, *Fluid Phase Equilibr.*, 2017, **448**, 22–29.

16 K. Mukherjee, S. Das, E. Tarif, A. Barman and R. Biswas, *J. Chem. Phys.*, 2018, **149**, 124501.

17 K. Mukherjee, A. Das, S. Choudhury, A. Barman and R. Biswas, *J. Phys. Chem. B.*, 2015, **119**, 8063–8071.

18 K. Mukherjee, S. Das, E. Tarif, A. Barman and R. Biswas, *J. Chem. Phys.*, 2018, **149**, 124501.

19 H. Srinivasan, V. K. Sharma, R. Mukhopadhyay and S. Mitra, *J. Chem. Phys.*, 2020, **153**, 104505.

20 H. Srinivasan, V. K. Sharma, V. G. Sakai, J. P. Embs, R. Mukhopadhyay and S. Mitra, *J. Phys. Chem. B.*, 2020, **124**, 1509–1520.

21 H. Srinivasan, V. K. Sharma, S. Mitra, R. Biswas and R. Mukhopadhyay, *Phys. B: Condens. Matter*, 2019, **562**, 13–16.

22 S. N. Tripathy, Z. Wojnarowska, J. Knapik, H. Shirota, R. Biswas and M. Paluch, *J. Chem. Phys.*, 2015, **142**, 184504/1-10.

23 S. Das, R. Biswas and B. Mukherjee, *J. Phys. Chem. B.*, 2015, **119**, 11157–11168.

24 S. Das, R. Biswas and B. Mukherjee, *J. Chem. Phys.*, 2016, **145**, 84504.

25 B. Guchhait, S. Daschakraborty and R. Biswas, *J. Chem. Phys.*, 2012, **136**, 174503.

26 B. Guchhait, H. Al Rasid Gazi, H. K. Kashyap and R. Biswas, *J. Phys. Chem. B.*, 2010, **114**, 5066–5081.

27 H. A. R. Gazi, B. Guchhait, S. Daschakraborty and R. Biswas, *Chem. Phys. Lett.*, 2011, **501**, 358–363.

28 S. Dinda, A. Sil, A. Das, E. Tarif and R. Biswas, *J. Mol. Liq.*, 2022, **349**, 118126.

29 S. S. Hossain and A. Samanta, *J. Phys. Chem. B.*, 2017, **121**, 10556–10565.

30 N. Subba, E. Tarif, P. Sen and R. Biswas, *J. Phys. Chem. B.*, 2020, **124**, 1995–2005.

31 H. Shirota, J. Rajbangshi, M. Koyakkat, A. Baksi, M. Cao and R. Biswas, *J. Photochem. Photobiol. A: Chem.*, 2023, **437**, 114504.

32 K. Mukherjee, S. Das, J. Rajbangshi, E. Tarif, A. Barman and R. Biswas, *J. Phys. Chem. B.*, 2021, **125**, 12552–12567.

33 S. Banerjee, P. K. Ghorai, D. Maji and R. Biswas, *J. Phys. Chem. B*, 2022, **126**, 10146–10155.

34 R. Buchner, G. T. Hefter and P. M. May, *J. Phys. Chem. A.*, 1999, **103**, 8–9.

35 R. Buchner, G. T. Hefter and J. Barthel, *J. Chem. Soc., Faraday Trans.*, 1994, **90**, 2475–2479.

36 H. M. A. Rahman, G. Hefter and R. Buchner, *J. Phys. Chem. B*, 2012, **116**, 314–323.

37 J. Barthel, M. Kleebauer and R. Buchner, *J. Solution Chem.*, 1995, **24**, 1–17.

38 R. Buchner and G. Hefter, *J. Solution Chem.*, 2002, **31**, 521–535.

39 B. Gestblom and J. Sjöblom, *J. Solution Chem.*, 1986, **15**, 259–268.

40 P. Petong, R. Pottel and U. Kaatze, *J. Phys. Chem. A*, 1999, **103**, 6114–6121.

41 T. Sato and R. Buchner, *J. Phys. Chem. A*, 2004, **108**, 5007–5015.

42 T. Pradhan and R. Biswas, *J. Phys. Chem. A.*, 2007, **111**, 11524–11530.

43 J. T. Hynes, in *J. D. Simon (Ed.) Dodrecht: Kluwer*, Springer, Dordrecht, 1994, pp. 345–381.

44 G. van der Zwan and J. T. Hynes, *Chem. Phys.*, 1991, **152**, 169–183.

45 B. Guchhait, S. Das, S. Daschakraborty and R. Biswas, *J. Chem. Phys.,* 2014, **140**, 104514.

46 D. Maji and R. Biswas, *J. Chem. Phys.*, 2023, **158**, 174503.

47 C. J. F. Böttcher, O. C. van Belle, P. Bordewijk and A. Rip, *Theory of electric polarization, Volume 2*, Elsevier Scientific Publishing Company, Netherlands, 1996.

48 F. Kremer and A. Schönhals, in *Springer: Berlin, Germany*, eds. F. Kremer and A. Schönhals, Springer Berlin Heidelberg, Berlin, Heidelberg, 2003.

49 K. Mukherjee, A. Barman and R. Biswas, *J. Chem. Phys.*, 2019, **151**, 184901.

50 E. Tarif, K. Mukherjee, A. Barman and R. Biswas, *J. Chem. Sci.*, 2019, **131**, 1–12.

51 Bevington, P. R. and D. K. Robinson, *Data reduction and error analysis for the physical sciences*, McGraw-Hill:, New York, 3rd Edition, 1969.

52 C. Schröder and O. Steinhauser, *J. Chem. Phys.*, 2010, **132**, 244109.

53 M. Neumann and O. Steinhauser, *Chem. Phys. Lett.*, 1983, **102**, 508–513.

54 C. Schröder, J. Hunger, A. Stoppa, R. Buchner and O. Steinhauser, *J. Chem. Phys.*, 2008, **129**, 184501.

55 J. M. Caillol, D. Levesque and J. J. Weis, *J. Chem. Phys.*, 1986, **85**, 6645–6657.

56 M. Neumann and O. Steinhauser, *Chem. Phys. Lett.*, 1984, **106**, 563–569.

57 J. G. Kirkwood, *J. Chem. Phys.*, 1939, **7**, 911–919.

58 M. Neumann, *J. Chem. Phys.*, 1986, **85**, 1567–1580.

59 L. Saiz, E. Guàrdia, J.-À. Padró, J. Chem Phys, E. Guà rdia and ngel Padró, *J. Chem. Phys.*, 2000, **113**, 2814–2822.

60 A. Luzar and D. Chandler, *Nature*, 1996, **379**, 55–57.

61 D. C. Rapaport, *Mol. Phys.*, 1983, **50**, 1151–1162.

62 A. Chandra, *Phys. Rev. Lett.*, 2000, **85**, 768.

63 A. Luzar and D. Chandler, *Phys. Rev. Lett.*, 1996, **76**, 928.

64 W. L. Jorgensen, D. S. Maxwell and J. Tirado-Rives, *J. Am. Chem. Soc.*, 1996, **118**, 11225–11236.

65 M. P. Allen and D. J. Tildesley, *Computer Simulation of Liquids*, Oxford University Press, Oxford, 2nd Edition., 2017.

66 H. J. C. Berendsen, D. van der Spoel and R. van Drunen, *Comput. Phys. Commun.*, 1995, **91**, 43–56.

67 J. A. Aguilar-Pineda, G. A. Méndez-Maldonado, E. Núñez-Rojas and J. Alejandre, *Mol. Phys.*, 2015, **113**, 2716–2724.

68 B. Doherty, X. Zhong, S. Gathiaka, B. Li and O. Acevedo, *J. Chem. Theory Comput.*, 2017, **13**, 6131–6145.

69 K. P. Jensen and W. L. Jorgensen, *J. Chem. Theory Comput.*, 2006, **2**, 1499–1509.

70 L. Martinez, R. Andrade, E. G. Birgin and J. M. Martínez, *J. Comput. Chem.*, 2009, **30**, 2157–2164.

71 R. W. Hockney, S. P. Goel, J. W. Eastwood, R. W. Hockney, S. P. Goel and J. W. Eastwood, *J. Comput. Phys.*, 1974, **14**, 148–158.

72 G. Bussi, D. Donadio and M. Parrinello, *J. Chem. Phys.*, 2007, **126**, 9901.

73 H. J. C. Berendsen, J. P. M. Postma, W. F. Van Gunsteren, A. Dinola and J. R. Haak, *J. Chem. Phys.*, 1994, **81**, 3684.

74 M. Brehm, M. Thomas, S. Gehrke and B. Kirchner, *J. Chem. Phys.*, 2020, **152**, 164105.

75 M. Brehm and B. Kirchner, *J. Chem. Inf. Model.*, 2011, **51**, 2007–2023.

76 G. Kalita, N. Rohman and S. Mahiuddin, *J. Chem. Eng. Data.*, 1998, **43**, 148–151.

77 D. Maji, S. Indra and R. Biswas, *J. Chem. Sci.,* 2021, **133**, 104.

78 T. Chen, G. Hefter and R. Buchner, *J. Phys. Chem. A*, 2003, **107**, 5025–4031.

79 H. K. Kashyap, T. Pradhan and R. Biswas, *J. Chem. Phys.*, 2006, **125**, 9.

80 J. C. Yong and E. W. Castner, *J. Chem. Phys.*, 1993, **99**, 113–125.

81 B. Bagchi and R. Biswas, *Adv. Chem. Phys., Bd*, 1999, **109**, 207–433.

82 S. Mukherjee, S. Mondal, S. Acharya and B. Bagchi, *J. Phys. Chem. B*, 2018, **122**, 11743–11761.

83 M. Paluch, Z. Wojnarowska and S. Hensel-Bielowka, *Phys. Rev. Lett.*, 2013, **110**, 015702.

84 K. L. Ngai and M. Paluch, *J. Chem. Phys.*, 2004, **120**, 857–873.

85 Q. Qin and G. B. McKenna, *J. Non-Cryst. Solids*, 2006, **352**, 2977–2985.

86 B. Guchhait, S. Das, S. Daschakraborty and R. Biswas, *J. Chem. Phys.*, 2014, **140**, 104514.

87 M. D. Ediger, C. A. Angell and S. R. Nagel, *J. Phys. Chem.*, 1996, **100**, 13200–13212.

88 S. Das, R. Biswas and B. Mukherjee, *J. Phys. Chem. B.*, 2015, **119**, 274–283.

89 K. J. Atkins, P. W., de Paula J., Atkins' Physical Chemistry, *Oxford University Press, Oxford*, 2017.

90 H. Fröhlich, *Theory of dielectrics: dielectric constant and dielectric loss.*, Oxford, Clarendon Press, 1949.

91 C. Zhang, J. Hutter and M. Sprik, *J. Phys. Chem. Lett.*, 2016, **7**, 2696–2701.

92 M. Neumann, *Mol. Phys.*, 1983, **50**, 841–858.

93 Madden P and Kivelson D, *Adv. Chem. Phys.*, 1984, **56**, 467–566.

94 B. Bagchi, *Molecular Relaxation in Liquids.*, Oxford University Press, USA, New York, First Edition., 2012.

95 J. P. Hansen and I. R. McDonald, *Theory of Simple Liquids*, Academic Press, Third Edition., 2006.

96 S. Schrödle, G. Hefter and R. Buchner, *J. Phys. Chem. B.*, 2007, **111**, 5946–5955.

97 T. Sato and R. Buchner, *J. Mol. Liq.*, 2005, **117**, 23–31.

98 A. Luzar, *J. Chem. Phys.*, 2000, **113**, 10663–10675.

99 R. Kumar, J. R. Schmidt and J. L. Skinner, *J. Chem. Phys.*, 2007, **126**, 204107.

100 S. Indra and R. Biswas, *Mol. Simul.*, 2015, **41**, 471–482.

101 T. Ishida, *J. Non-Cryst. Solids*, 2011, **357**, 454–462.

102 T. Yan, C. J. Burnham, M. G. Del Pópolo and G. A. Voth, *J. Phys. Chem. B*, 2004, **108**, 11877–11881.

Chapter 4

Temperature Dependent Dielectric Relaxation Measurements of (Betaine+Urea+Water) Deep Eutectic Solvent in Hz-GHz Frequency Window: Microscopic Insights into Constituent Contributions and Relaxation Mechanisms

4.1 Introduction

Engineering of reaction media and solvents facilitating development of sustainable green technology is one of the focal points in recent research. The goal of green technology is to protect the environment from the harm caused by conventional organic solvents.[1–4] These common and conventional solvents are often detrimental to the local eco-system because they can enter into the food-chain in the long run and induce toxicity to human health. The environmentally benign group of solvents is an important cog in the wheel that drives the development of sustainable green technology by either reducing or completely avoiding the use of traditional organic solvents in industrial and technological sectors. Room temperature ionic liquids,[5,6] gas expanded liquids,[7,8] room temperature super critical fluids[9,10] and their aqueous mixtures, and deep eutectic solvents (DESs)[11–14] have been introduced in the past which were thought to be comparatively less toxic to the environment. Interestingly, DESs possess several advantages over ILs when one considers the ease of synthesis and transportation.[15] Moreover, DESs in some cases may offer far cheaper alternatives to ILs.

Recently, a new class of DESs called naturally abundant DESs (NADESs) have attracted attention because of their inherent greenness, superior non-toxicity, sustainability, and thin environmental footprints.[16–18] It is known that DESs, although prepared at higher temperatures through melting of multi-component mixtures, retain stable liquid phase at or around the room temperature through metastability caused by the combining effects of extensive inter-species interactions and gain in entropy. NADESs are also prepared through the same protocol. The components of NADESs are commonly chosen from plant primary metabolites, including carbohydrates, amino acids, organic acids, sugar alcohols, and urea.[19–21] These green solvents are now being increasingly used for various applications, including complex chemical species dissolution,[22] reaction media,[23] CO_2 and SO_2 absorption,[24,25] pharmaceutical solubilization,[26,27] agrochemical applications,[28] cosmetic preparations,[29] food flavouring[30] additives, Li-ion battery electrolytes,[31] biodiesel production,[32] extraction of bioactive substances,[33] and drug delivery.[34,35] Biological processes in organisms are often impeded by poor dissolution of metabolites by lipids and hindered transportation through cell membranes.[36,37] NADESs can overcome this difficulty by enhancing solubility in lipids and permeability through membranes, facilitating the functioning of living cell organisms.[38,39]

Despite the rising popularity of NADESs as potential substitutes for hazardous organic solvents in large-scale industrial applications, the interrelationship between structure and dynamics within these media has remained largely unexplored. In contrast, considerable research efforts have been directed towards conventional molecular solvents, with extensive investigations conducted using a variety of experimental techniques, such as, neutron diffraction,[40–42] pulsed field gradient NMR,[43,44] dielectric relaxation,[45–47] 2D-IR,[48,49] and time-resolved fluorescence.[50–56] Moreover, experimental studies were followed up by developing molecular theories [57–59] and performing computer simulations,[60,61] in order to provide microscopic understanding of solvent dynamics and their impact on chemical reactions[62–65] occurring in solution phase. Fortunately, several attempts have been made in recent years for gaining molecular-level understanding of ionic deep eutectic solvents, such as, (acetamide + electrolyte),[66–70] (choline chloride + urea),[71–74] and (choline chloride + glycerol).[75–77] However, there has been much less efforts toward exploring the interrelationship between structure and dynamics of NADESs.[78–81] Time resolved anisotropy and dynamic Stokes shift measurements of (glucose+urea+water)[82] and (betaine+urea+water)[83] NADESs revealed strong fractional viscosity dependence for solute rotation and solvation times. Subsequent computer simulations suggested dramatic distortion of orientational structure of water in (glucose+urea+water) NADESs and water clustering.[84] However, no study has been carried out so far to explore the inherent dynamics of this important system and then to correlate the measured and/or computed dynamics to the microscopic solution structure.

Here we report a combined experimental and computer simulation study of dielectric relaxation (DR) of another important NADES composed of betaine, urea and water in the weight ratio, Betaine:Urea:Water :: 11.7:12:1, and relate the measured DR response to the individual component contributions. **Scheme 4.1** presents the chemical structures of betaine and urea molecules. DR spectroscopy offers a measurement technique for monitoring the fluctuation dynamics of collective dipole moment of a given system and thus connects the structural fluctuations at the microscopic level to the measured polarization response.[46,85,86] Our DR measurements were performed employing a broad frequency window (20 Hz to 50 MHz) over a moderate temperature range, T = 303-343 K. A comparison between the simulated and experimental DR spectra highlighted a good agreement, allowing logical explanations of the measured temperature dependent relaxations in terms of microscopic dynamics revealed by simulations. The decomposition of the simulated DR spectra into the individual constituent and their cross-species interaction contributions suggested that relaxations involving betaine molecules dominated the experimental DR response of the system. Furthermore, our simulations presented here demonstrated the connections between the dielectric relaxation, and the structural hydrogen bond (H-bond) fluctuations and the collective single particle reorientational relaxations. A careful examination of the structural aspects of water molecules presents in this NADES suggested extensive damage to the tetrahedral H-bond network structure of bulk water, forcing the water molecules to behave as a weakly polar solvent with a value of the static dielectric constant as low as 2.

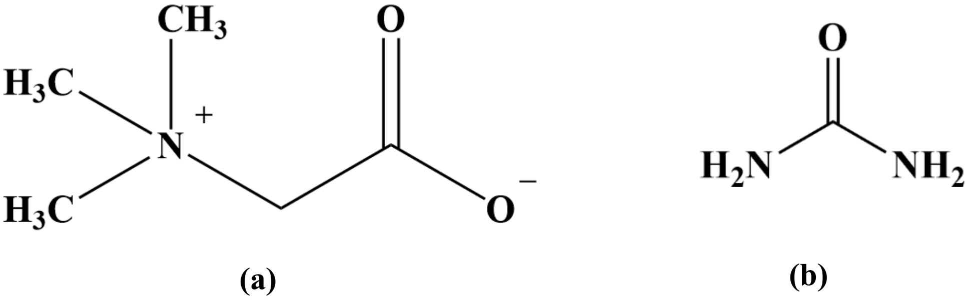

Scheme 4.1 Chemical structures of (a) betaine and (b) urea molecules.

4.2. Experimental Details

4.2.1 Sample Preparation

Betaine (≥99.0%, Sigma-Aldrich, melting point T_m~574 K) and urea (≥98%, Sigma-Aldrich, T_m~405-408 K) were purchased and subjected to overnight vacuum drying at room temperature (303 K) before use. Millipore water was utilized for sample preparation. In a screw-capped container, the required quantities of betaine, urea, and water were combined in the weight ratio of 11.7:12:1. Subsequently, this mixture was heated to a temperature of 343K, while maintaining constant stirring at 600 rpm, in an oil bath. A clear and transparent liquid was formed after ~2 hours. The molten mixture was then allowed to cool gradually to room temperature. A comprehensive description of the sample preparation procedure can be found elsewhere.[83] All experimental procedures were conducted in a tightly humidity-controlled laboratory environment with a humidity level maintained at ~35%.

4.2.2 DR Measurement Details

The frequency dependent complex dielectric function of a system is expressed as follows,[85,87]

$$\varepsilon^*(\omega) = \varepsilon'(\omega) - \left[i\varepsilon''(\omega) + \frac{ik}{\omega\epsilon_0}\right] \quad , \qquad (4.1)$$

where ϵ_0 denotes the free space permittivity and k denotes the conductivity of the medium. Note that the angular (ω) and the linear (ν) frequencies are connected through the well-known relation, $\omega = 2\pi\nu$. $\varepsilon'(\omega)$ and $\varepsilon''(\omega)$ are respectively the real and imaginary parts of the complex permittivity. The zero-frequency permittivity is known as the static dielectric constant (ε_s) of the medium. The permittivity at infinite frequency, $\varepsilon_\infty = \varepsilon(\omega \to \infty)$, arises from the electronic part of the polarizability and the intermolecular vibration

Our experimental approach employed three distinct setups to measure the dielectric response in the frequency window, 20 Hz - 50 GHz:

(i) A low frequency impedance analyzer (E4990A) equipped with liquid test fixture (16452A), covering a frequency range from 20 Hz to 10 MHz.[88]

(ii) A middle-frequency impedance analyzer (E4991B)[89] coupled with an open-ended coaxial line probe, featuring a dielectric probe kit (85070E), and a high-temperature coaxial cable with high temperature probe, encompassing a frequency range from 10 MHz to 500 MHz.

(iii) A PNA-L network analyzer (N5235B) complemented by an open-ended coaxial probe kit (N1501A), facilitating measurements across the frequency spectrum from 500MHz – 50GHz.[90]

Precise temperature control during the DR measurements was maintained through the usages of a magnetic stirrer cum hot plate for both high and middle frequency measurements. Temperature stability was assured by placing a thermometer at the same level as the probe end during each measurement. In case of low frequency (20Hz – 10MHz) measurements, the sample holder fixture was submersed in a water bath, kept on the magnetic stirrer-cum-hot plate. This arrangement maintained the desired temperature throughout experiment.

4.2.3 Data Analysis

The complex dielectric function $\varepsilon^*(\omega)$ obtained from experiment for the NADES in various temperature were fitted using Havriliak-Negami (HN) equation.[87]

$$\varepsilon^*(\omega) = \varepsilon_\infty + \sum_{j=1}^{n} \frac{\Delta\varepsilon_j}{\left[1 + \left(i\omega\tau_j\right)^{1-\alpha_j}\right]^{\beta_j}} \tag{4.2}$$

where $0 \le \alpha < 1$ and $0 < \beta \le 1$. $\Delta\varepsilon_j$ represents the amplitudes of the relaxation of the dispersion of j-th relaxation with relaxation time τ_j. Notably, when $\alpha_j = 0$ and $\beta_j = 1$, it signifies relaxation following the Debye model, while $\alpha_j = 0$ describes the Cole-Davidson (CD) model and $\beta_j = 1$ corresponds to Cole-Cole (CC) model. Data collected by the low frequency, middle frequency and high frequency set-ups were placed together and then simultaneously fitted with different combination of Debye, CC and CD models. Fitting quality was estimated by checking the "goodness-of-fit" parameter (χ^2). This is as follows,[91]

$$\chi^2 = \frac{1}{2m - l} \sum_{i=1}^{m} \left[\left(\frac{\delta\varepsilon_i'}{\sigma(\varepsilon_i')} \right)^2 + \left(\frac{\delta\varepsilon_i''}{\sigma(\varepsilon_i'')} \right)^2 \right] \tag{4.3}$$

Where m denotes the number of data triples $(\omega, \varepsilon', \varepsilon'')$, l is the number of adjustable parameters, and $\delta\varepsilon_i$ and $\sigma(\varepsilon_i)$ are the residuals and standard deviation of the individual data points, respectively.

More details about the DR measurement details and data analysis can be found in Chapter 2.

4.3 Theory and Computational Details

4.3.1. Theory

The simulated frequency-dependent dielectric function, $\varepsilon(\omega)$ can be obtained from the normalised total dipole moment autocorrelation function, $\phi(t)$, which is given by[87,92]

$$\phi(t) = \frac{\langle \boldsymbol{M}(0).\boldsymbol{M}(t) \rangle}{\langle |\boldsymbol{M}(0)|^2 \rangle} , \tag{4.4}$$

where $\boldsymbol{M} = \sum_i \boldsymbol{\mu}_i$, where μ_i is the dipole moment of the individual dipolar molecules.

Linear response theory approximates the inherent dynamics of a system by examining its response when subjected to a weak external electric field. The resulting frequency-dependent dielectric function is subsequently derived as follows,[93,94]

$$\frac{\varepsilon(\omega) - 1}{\varepsilon_s - 1} = \mathcal{L}_{i\omega}\left[-\frac{d\phi(t)}{dt}\right] \quad . \qquad (4.5)$$

Using $\varepsilon_s = 1 + \frac{\langle \boldsymbol{M}^2\rangle - \langle \boldsymbol{M}\rangle^2}{3\epsilon_0 V k_B T}$ and performing the Laplace–Fourier transform ($\mathcal{L}_{i\omega}$), we write,

$$\varepsilon(\omega) - 1 = \frac{4\pi}{3Vk_BT}\{\langle \boldsymbol{M}(0)^2\rangle + i\omega\mathcal{L}_{i\omega}[\langle \boldsymbol{M}(0).\boldsymbol{M}(t)\rangle]\} \ , \qquad (4.6)$$

where,

$$\mathcal{L}_{i\omega}[f(t)] = \int e^{i\omega t} f(t)dt \qquad (4.7)$$

The real and imaginary parts of the complex dielectric function can be given by,

$$\varepsilon(\omega) = \varepsilon'(\omega) - i\varepsilon''(\omega). \qquad (4.8)$$

We can analyse the frequency-dependent dielectric function contributions by assuming that the total collective dipole moment of the system, $\boldsymbol{M_T}(t)$, is a sum total of the individual collective moments:

$$\boldsymbol{M_T}(t) = \boldsymbol{M_B}(t) + \boldsymbol{M_U}(t) + \boldsymbol{M_W}(t) \ , \qquad (4.9)$$

where $\boldsymbol{M_B}(t)$ denotes the collective dipole moment arising from betaine molecules, $\boldsymbol{M_U}(t)$ from urea and $\boldsymbol{M_W}(t)$ from water molecules in this NADES.

Subsequently, the collective dipole moment autocorrelation function can be shown as a sum of several intra-species and inter-species contributions as follows:

$$\begin{aligned}\langle \boldsymbol{M_T}(0).\boldsymbol{M_T}(t)\rangle &= \langle[\boldsymbol{M_B}(0) + \boldsymbol{M_U}(0) + \boldsymbol{M_W}(0)].[\boldsymbol{M_B}(t) + \boldsymbol{M_U}(t) + \boldsymbol{M_W}(t)]\rangle \\ &= \langle \boldsymbol{M}_B(0).\boldsymbol{M}_B(t)\rangle + \langle \boldsymbol{M}_U(0).\boldsymbol{M}_U(t)\rangle + \langle \boldsymbol{M}_W(0).\boldsymbol{M}_W(t)\rangle \\ &+ \langle \boldsymbol{M}_B(0).\boldsymbol{M}_U(t)\rangle + \langle \boldsymbol{M}_B(t).\boldsymbol{M}_U(0)\rangle + \langle \boldsymbol{M}_B(0).\boldsymbol{M}_W(t)\rangle + \langle \boldsymbol{M}_B(t).\boldsymbol{M}_W(0)\rangle \\ &+ \langle \boldsymbol{M}_U(0).\boldsymbol{M}_W(t)\rangle + \langle \boldsymbol{M}_U(t).\boldsymbol{M}_W(0)\rangle \ . \qquad (4.10)\end{aligned}$$

From the consequence of microscopic reversibility[95]

$\langle \boldsymbol{M}_B(0).\boldsymbol{M}_U(t)\rangle$, $\langle \boldsymbol{M}_B(0).\boldsymbol{M}_W(t)\rangle$, and $\langle \boldsymbol{M}_U(0).\boldsymbol{M}_W(t)\rangle$ equals to $\langle \boldsymbol{M}_B(t).\boldsymbol{M}_U(0)\rangle$, $\langle \boldsymbol{M}_B(t).\boldsymbol{M}_W(0)\rangle$ and $\langle \boldsymbol{M}_U(t).\boldsymbol{M}_W(0)\rangle$, respectively. Therefore, Eq. (4.10) simplifies to [96–98]

$$\begin{aligned}\langle \boldsymbol{M}(0).\boldsymbol{M}(t)\rangle &= \langle \boldsymbol{M}_B(0).\boldsymbol{M}_B(t)\rangle + \langle \boldsymbol{M}_U(0).\boldsymbol{M}_U(t)\rangle + \langle \boldsymbol{M}_W(0).\boldsymbol{M}_W(t)\rangle \\ &\quad + 2\langle \boldsymbol{M}_B(0).\boldsymbol{M}_U(t)\rangle + 2\langle \boldsymbol{M}_B(0).\boldsymbol{M}_W(t)\rangle + 2\langle \boldsymbol{M}_U(0).\boldsymbol{M}_W(t)\rangle \qquad (4.11)\end{aligned}$$

Following Eq. 4.6, the total $\varepsilon(\omega)$ may be expressed as a sum of the individual component contributions.

$$\varepsilon(\omega) = 1 + \varepsilon_{BB}(\omega) + \varepsilon_{UU}(\omega) + \varepsilon_{WW}(\omega) + 2\varepsilon_{BU}(\omega) + 2\varepsilon_{BW}(\omega) + 2\varepsilon_{UW}(\omega), \qquad (4.12)$$

where $\varepsilon_{ij}(\omega) = \frac{1}{3\epsilon_0 V k_B T}\{\langle \boldsymbol{M}_i(0)\boldsymbol{M}_j(0)\rangle + i\omega\mathcal{L}[\langle \boldsymbol{M}_i(0).\boldsymbol{M}_j(t)\rangle]\}$.

Following Eq. 4.8, the complex dielectric function, $\varepsilon(\omega)$, can be written in terms of the real and the imaginary components as follows,

$$\varepsilon'(\omega) - i\varepsilon''(\omega) = [1 + \varepsilon'_{BB}(\omega) + \varepsilon'_{UU}(\omega) + \varepsilon'_{WW}(\omega) + 2\varepsilon'_{BU}(\omega) + 2\varepsilon'_{BW}(\omega) + 2\varepsilon'_{UW}] - i[\varepsilon''_{BB}(\omega) + \varepsilon''_{UU}(\omega) + \varepsilon''_{WW}(\omega) + 2\varepsilon''_{BU}(\omega) + 2\varepsilon''_{BW}(\omega) + 2\varepsilon''_{UW}]$$
(4.13)

where $\varepsilon'(\omega) = 1 + \varepsilon'_{BB}(\omega) + \varepsilon'_{UU}(\omega) + \varepsilon'_{WW}(\omega) + 2\varepsilon'_{BU}(\omega) + 2\varepsilon'_{BW}(\omega) + 2\varepsilon'_{UW}$

and $\varepsilon''(\omega) = \varepsilon''_{BB}(\omega) + \varepsilon''_{UU}(\omega) + \varepsilon''_{WW}(\omega) + 2\varepsilon''_{BU}(\omega) + 2\varepsilon''_{BW}(\omega) + 2\varepsilon''_{UW}$.

4.3.2 Computational Details

All atom molecular dynamics simulation was performed using the GROMACS-5.1.1 software package[99] at four different temperatures, 313 K, 323 K, 333 K and 343 K. The simulated systems accurately mirrored the experimental proportions, consisting of 180 betaine, 360 urea and 100 water molecules. OPLS (optimized potentials for liquid simulations) all-atom type model force field[100] was employed to model the bonded and non-bonded interactions of urea and betaine molecules. For water molecules, the SPC/E model[101] was considered. The forcefield parameters for urea and betaine molecules were generated using the LigParGen software.[102–104]

Initially, we conducted simulations for reproducing a few physical properties, such as, experimental density, viscosity, and dielectric constant. However, we noticed that the simulated density and viscosity deviated by more than 10%, and the dielectric relaxation exhibited a much slower relaxation compared to that measured in experiments. To address these discrepancies, one of the following two approaches might be considered: (i) implementing a polarizable force field,[105,106] which associates with a substantial computational cost, or (ii) adjusting the atomic charges of the system molecules to tackle the polarizability issue in an average yet ad *hoc* manner. We adopted the latter because this saved simulation cost and was also motivated by the fact that this was employed earlier in a few cases.[107–110] Subsequently, a notable adjustment was made to the atomic charges of betaine and urea, setting them to 0.9e. This refinement resulted in a closer match to experimental density, viscosity, and dielectric relaxation timescales. The atomic representations of betaine, urea and water are shown in **Figure 4.A.1** (Appendix 4.A). Furthermore, the force field parameters employed in this study are provided in **Table 4.A.1 - 4.A.3** (Appendix 4.A)**.** The functional form of the potential is as follows:[100]

$$U(r) = \sum_{bonds} k_r\left(r - r_{eq}\right)^2 + \sum_{angles} k_\theta\left(\theta - \theta_{eq}\right)^2 + \sum_{torsions}\left[\frac{V_1}{2}(1 + cos\varphi) + \frac{V_2}{2}(1 - cos2\varphi) + \frac{V_3}{2}(1 + cos3\varphi) + \frac{V_4}{2}(1 - cos4\varphi)\right] + \sum_{i<j}^{atoms} 4\varepsilon_{ij}\left[\left(\frac{\sigma_{ij}}{R_{ij}}\right)^{12} - \left(\frac{\sigma_{ij}}{R_{ij}}\right)^{6}\right] + \sum_{i<j}^{atoms} \frac{q_i q_j}{4\pi\varepsilon_0 R_{ij}} \qquad (4.14)$$

In the above equation, the intermolecular bonded interaction is described by a harmonic potential with equilibrium bond distance r_{eq} and bond constant k_r and the angle stretching with equilibrium bond angle θ_{eq} and angle constant k_θ. V_1, V_2, V_3 and V_4 represent the Fourier coefficients of tortional angle φ. The non-bonded interaction is defined by Lennard-Jones and coulombic interaction where R_{ij} represents the intermolecular distance between the atoms i and j with partial charges q_i and q_j. σ and ε represents the van der walls diameter and well-depth respectively. The geometric combination rules have been employed for the LJ coefficient as $\sigma_{ij} = \sqrt{\sigma_{ii}\sigma_{jj}}$ and $\varepsilon_{ij} = \sqrt{\varepsilon_{ii}\varepsilon_{jj}}$.

The initial configuration of the simulation box containing required numbers of urea, betaine, and water was constructed utilizing the PACKMOL software.[111] Within the simulation framework the short-range van der Waals interaction and electrostatic interaction were truncated at a distance of 1.2 nm, while the Particle Mesh Ewald (PME)[112] technique was used to efficiently calculate the long-range electrostatic interaction by using a Fourier grid spacing of 0.16 nm and a spline of order 4. The configuration, thus generated, was energy minimized through the steepest-descent algorithm implemented in the GROMACS package. Following energy minimization, two essential equilibration phases were conducted, first, NVT equilibration of 5 ns, during which the system's temperatures was controlled using the V-rescale temperature coupling with time constant 0.5 ps. After that, the resulting system was taken through an NPT equilibration for 10 ns in that temperature with the V-rescale thermostat[113] with coupling constant 0.5ns. The relevant pressure control was achieved using the Berendsen barostat[114] with time constant of 2 ps. For all NPT equilibrated systems at each of the temperatures considered, a production run of 300ns each was performed and trajectories saved for analysis.

The Green – Kubo relation,[115,116] denoted by Eq. (4.15), was utilized to determine the shear viscosity coefficient from equilibrium simulation trajectory.

$$\eta = \frac{V}{6k_BT}\int_0^\infty dt < P_{\alpha\beta}(0)P_{\alpha\beta}(t) > \qquad (4.15)$$

In this equation, η, V, k_B and T represents the shear viscosity coefficient, box volume, Boltzmann constant and temperature of the system respectively. $P_{\alpha\beta}$ denotes the cross-diagonal terms of the pressure tensor. To calculate η at each of the temperatures considered, we divided each 100 ns long trajectories into 20 equal segments of 5 ns. These segments were then treated as individual trajectories. Subsequently, Eq. 4.15 was applied to calculate η from each of the independent trajectories, and averaged to obtain an overall mean value.

The structural H-bond relaxation, influenced by both translational and orientational diffusions is quantified by using the following expression:[117–119]

$$C_{HB}(t) = \frac{\langle h(0)h(t)\rangle}{\langle h\rangle} \qquad (4.16)$$

In Eq. 4.16, the variable $h(t)$ denotes the presence or absence of H-bond between two molecular entities at time *t*. Specifically, if a particular H-bond exists both at $t = 0$ and at time t, $h(t) = 1$; otherwise, $h(t) = 0$. However, breaking of H-bond in the intermediate time is not considered here. The distance criteria employed: (i) $r_{DA} \leq r_{DA}^c$ and (ii) $r_{HA} \leq r_{HA}^c$, and the angle criteria used: $150° \leq \angle\mathrm{DHA} \leq 180°$, where D, H, and A stands respectively for donor, hydrogen and acceptor atoms. The cut-off distance (r^c) was derived from the first minima of the corresponding RDFs.

We studied the reorientational dynamics of molecules by monitoring the decay behaviour of the first rank collective single particle reorientational time correlation function,[120] $C_1(t)$:

$$C_1(t) = \frac{\langle P_1 | \boldsymbol{u}(0) \cdot \boldsymbol{u}(t) | \rangle}{\langle P_1 | \boldsymbol{u}(0) \cdot \boldsymbol{u}(0) | \rangle} , \qquad (4.17)$$

where P_1 and $\boldsymbol{u}$ denote respectively the first-order Legendre polynomial and the backbone vector of a molecule. Molecular representations presented in this chapter is generated from VMD[121] and all the analyses were conducted using in-house codes and TRAVIS.[122,123]

4.3.3 Validation of the Model Interaction Potential

Subsequently, we carried out a fidelity assessment on the force field parameters employed in our simulations. **Figure 4.1** presents a comparison between the simulated and experimental[83] viscosities and densities (insets), suggesting a good reproducibility of these measured quantities by the present simulations. Such a close agreement also provides us with the confidence that these model interaction potentials will be able to describe, at least qualitatively correctly, the salient features of the experimental DR. Note that the dependence of η on the upper limit of integration in Eq. 4.15 is presented in **Figure 4.A.2** (Appendix 4.A), which suggests that the relevant integrals converged within the simulation time. Our simulated η values are the converged values of each of these integrals (**Figure 4.A.2**).

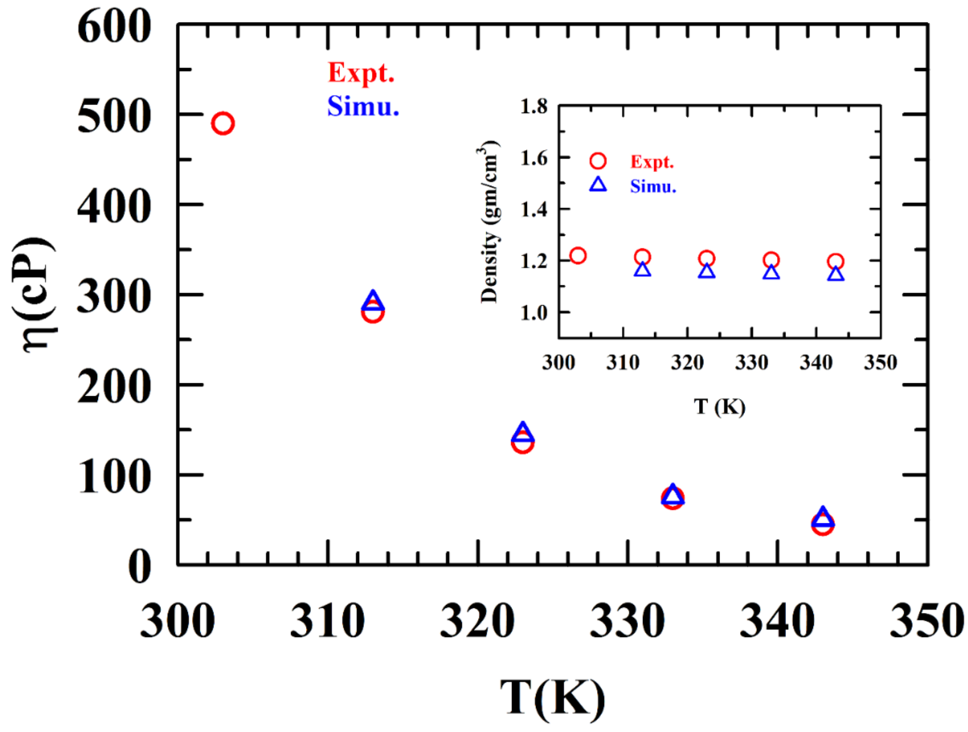

Figure 4.1. Comparison between the simulated and experimental viscosities (η) and densities of (betaine+urea+water) DES at different temperatures. Eq. 4.15 was used to calculate the η values. All representations are colour-coded.

4.4 Results and Discussions

4.4.1 Experiments

4.4.1.1 Temperature Dependent DR Data

Figure 4.2 (a) and (b) represent the temperature dependent real $\varepsilon'(\omega)$ and imaginary $\varepsilon''(\omega)$ parts of the measured dielectric relaxation (DR) spectra of (betaine+urea+water) DES in the frequency regime, $0.0001 \le \left(\frac{\omega}{2\pi}\right)/\text{GHz} \le 50$, along with 4-Debye fits. Fit parameters are summarized in **Table 4.1** where temperature dependent viscosities are also tabulated.

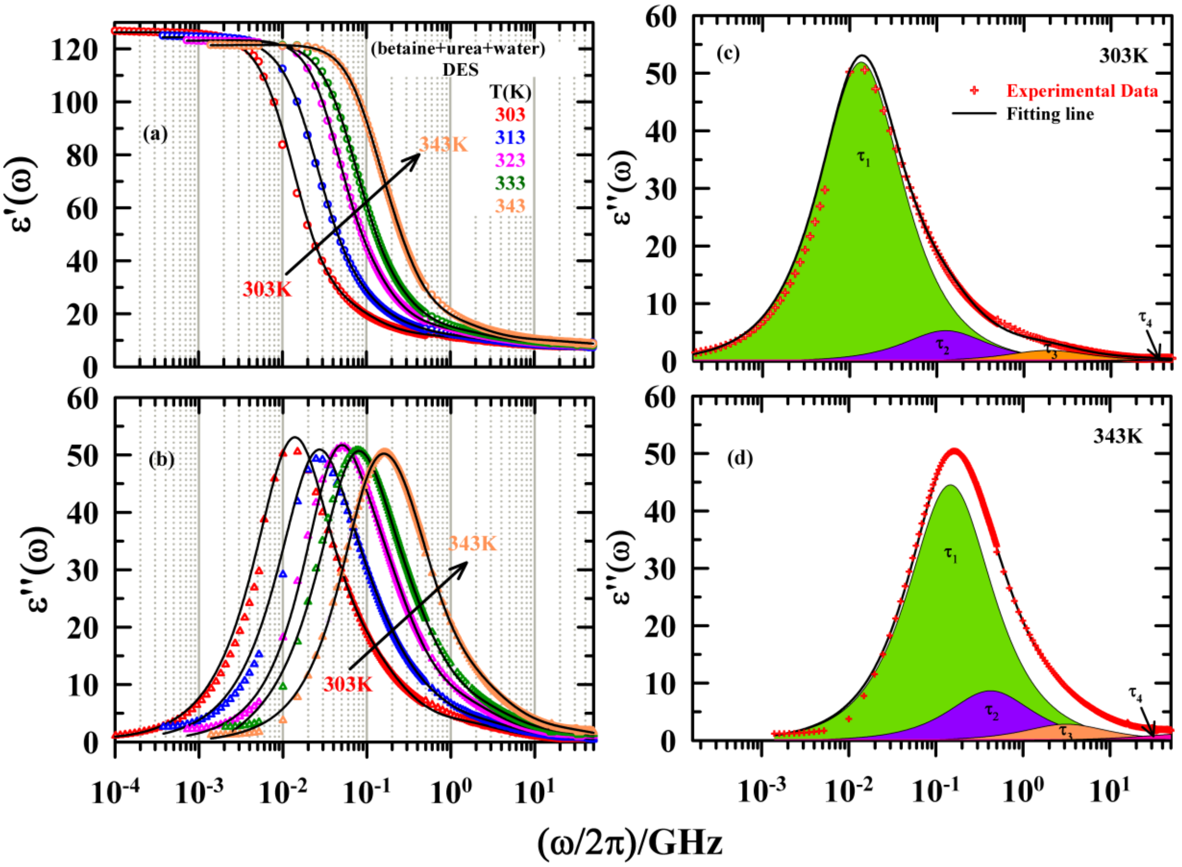

Figure 4.2. *Left panels*: (a) Real $\varepsilon'(\omega)$ and (b) imaginary parts $\varepsilon''(\omega)$ of the measured dielectric relaxation spectra of (betaine+urea+water) DES at five different temperatures. Experimental data are represented by symbols of different colours, whereas the solid lines going through them denote the 4-Debye fits. *Right panels*: (c) and (d) show the decomposition of the imaginary part ($\varepsilon''(\omega)$), into different relaxation components at two representative temperatures, 303K and 343K. Shaded area in panels (c) and (d) indicate the relative contributions of the different relaxation timescales to the total DR. Each representation is colour coded.

The experimental DR spectra were subjected to fits employing the Cole-Cole, Cole-Davidson, and multi-Debye models. Through a careful analysis of the residuals and χ^2 (the goodness-of-fit parameter) values associated with these fits, the 4-Debye model was found to provide the best description of the experimental data. **Figure 4.A.3** (Appendix 4.A) presents a visual comparison of residuals obtained from different fitting approaches.

Table 4.1. Parameters obtained from simultaneous 4-Debye fits to the real (ε') and the imaginary (ε'') components of the measured DR spectra for (betaine+urea+water) DES at six different temperatures.

T(K)	ε_s	$\Delta\varepsilon_1$	$\tau_1{}^b$ (ns)	$\Delta\varepsilon_2$	τ_2 (ns)	$\Delta\varepsilon_3$	τ_3 (ps)	$\Delta\varepsilon_4$	τ_4 (ps)	ε_∞	$n_D{}^c$	$\varepsilon_\infty - n_D^2$	$\langle\tau_{DR}^{Expt.}\rangle^d$ (ns)	η^e(cP)
303	126	103.8 (87%)[a]	11.7	10.6 (9%)	1.3	3.8 (3%)	84	0.5 (1%)	5	7.6	1.4966	5.3603	10.4	540
313	124.3	97.9 (84%)	6.1	13.4 (11%)	0.98	4.6 (4%)	75	0.6 (1%)	5	7.8	1.4969	5.5593	5.2	281
323	123.8	96.7 (83%)	3.1	13.7 (12%)	0.60	4.5 (4%)	59	1.1 (1%)	4	7.7	1.4970	5.4591	2.6	136
333	122.8	94.4 (82%)	2.1	13.9 (12%)	0.51	5.4 (5%)	56	1.5 (1%)	4	7.7	1.4972	5.4584	1.8	74
338	122.7	92.0 (81%)	1.4	15.4 (13%)	0.41	5.2 (5%)	46	1.5 (1%)	4	8.5	1.4975	6.2576	1.2	57
343	122.1	89.1 (78%)	1.1	17.3 (15%)	0.38	5.7 (5%)	51	1.8 (2%)	4	8.2	1.4976	5.9573	0.9	45

a) numbers in parentheses indicate dispersion amplitude percentage; b) τ_is are better than ±5% of the reported values; c) refractive index from an earlier study[83]; d) $\langle\tau_{DR}^{Expt.}\rangle = \frac{\sum_{i=1}^{n} a_i\tau_i}{\sum_{i=1}^{n} a_i}$; e) viscosity data from an earlier study[83].

Notice in **Figure 4.2** (a) that a plateau emerges at each temperature at lower frequency regime, suggesting that we have identified the static dielectric constant (ε_s) of the system in the measured frequency window. Notice here that the measured ε_s values are much higher than those of bulk water[124] and molten urea,[125] and even larger than that of room temperature liquid formamide.[126] Such a large value of ε_s is expected to make NADES a suitable solvent for hosting a variety of chemical reactions in solution phase.[127,128] The observed decrease in ε_s upon raising the solution temperature may be understood in terms of temperature-induced reduction in the mean-squared fluctuations of the system's collective dipole moment.[70,92,129] The peak of the imaginary part ($\varepsilon''(\omega)$), shown in **Figure 4.2 (b)**, shifts gradually towards higher frequency with an increase in temperature. This shift indicates faster relaxation at higher temperature because of a concomitant decrease in solution viscosity. The relative contributions of the multiple relaxation components, shown graphically in **Figure 4.2** (c) and (d) for two representative temperatures, suggest that the slowest component dominates the DR while the fastest component contributes the least (nearly invisible). We also notice that the increase of temperature from 313 K to 343 K induces a transfer of relaxation amplitude from the slowest to the next relatively faster component or components. This transfer occurs systematically throughout the temperature range considered as highlighted by the decompositions of $\varepsilon''(\omega)$ at other temperatures shown in **Figure 4.A.4** (Appendix 4.A).

Temperature dependent relaxation timescales and amplitudes summarized in **Table 4.1** suggests that four distinctly different relaxation timescales characterize the measured DR of this system. The detected different timescales are $\tau_1 \sim 11 - 1$ ns, $\tau_2 \sim 1.2 - 0.4$ ns, $\tau_3 \sim 80 - 50$ ps, and $\tau_4 \sim 5$ ps. The fastest relaxation component, although accounts for ~1-2% of the total relaxation, persists throughout the temperature range. Despite it being relatively tiny, its presence cannot be ignored as suggested by a comparison of the residuals shown in **Figure 4.A.5** (Appendix 4.A). In addition, previous DR measurements of molten urea[125] reported a small relaxation component (~6%) with a time constant of ~5 ps. DR measurements of aqueous solutions of xylitol,[130–132] and ionic acetamide deep eutectics[68,70] also found similar timescales. Considering that extensive interspecies H-bond interactions govern the liquid phase structure of the present NADES and the previously studied systems,[68,70,130–132] detection of a fast relaxation component with time constant of ~5 ps for this DES is probably expected. Detection of relaxation processes faster than this is severely limited by the frequency window of the present measurement set-up and this is reflected in the large undetected portion shown by $\varepsilon_\infty - n_D^2$ values in **Table 4.1**.

Next, we discuss about the possible origin of the sub-100 ps timescale (τ_3) which is contributing ~3-5% to the total relaxation measured in the temperature range considered. DR measurements of molten urea revealed DR time scales[125] of ~90 ps and ~30 ps with amplitudes ~11% and ~83%, respectively. These timescales may be a potential source to the sub-100 ps timescale detected here. Interestingly, DR measurements of aqueous solutions of glyceline and reline reported dynamical timescales in this regime.[133] Considering the complex interactions of water in those aqueous DES solutions,[133] the restricted reorientation dynamics of water molecules in the present system may also give rise to the sub-100 ps timescale detected here.

The nanosecond relaxation time constant (τ_2), constituting ~9-15% of the total dispersion, becomes gradually faster from ~1.3 ns at 303 K to ~ 0.4 ns at 343 K with an increase of the dispersion amplitude, from 10% to 15%. This timescale has been preceded by a dominating (~78-87%) slow component with a time constant (τ_1) of ~1-11 ns in this temperature range. Interestingly, these two slow components together account for ~93-96% of the total relaxation measured here. Next, we would like to ask whether the hydrodynamic molecular rotations could give rise to such a dominant nanosecond DR component. Subsequent calculations of molecular rotation times for water, urea and betaine, calculated from the Stokes-Einstein-Debye relation employing the stick boundary condition[134] and the molecular van der Waals volumes[135] (V), $\tau_r = 3\eta V/k_B T$, suggests that these temperature dependent hydrodynamic rotation times (see **Table 4.A.4**, Appendix 4.A) are either faster or slower than those detected in the present experiments. One also notices that the temperature-dependent average DR times ($\langle\tau_{DR}^{Expt.}\rangle$), summarized in **Table 4.1**, follows the trend of the temperature-dependent medium viscosity, although the viscosity impact is not in accordance with the hydrodynamic prediction for a spherical solute with the stick boundary condition. Inclusion of the molecular aspect ratios (shape factor) is likely to modify these hydrodynamic rotation times,[69,136] and may even produce a good corroboration between the predicted and the measured timescales. However, such an agreement would be simply fortuitous because extensive interspecies H-bonding governs the liquid structure of the present system. Therefore, consideration of molecular rotations alone to understand the measured DR data appears unphysical and highly speculative. For a thorough microscopic understanding, one should separate the component contributions that constitute the total DR spectra and examine the dynamic friction profiles by following the collective single particle reorientational relaxations and the H-bond fluctuation dynamics.[137]

4.4.2 Simulations

4.4.2.1 Simulated DR Spectra: Comparison Between Experiments and Simulations

The left panel of **Figure 4.3** presents the simulated normalised total dipole moment autocorrelation function, $\phi(t)$, for (betaine+urea+water) DES at different temperatures. These simulated $\phi(t)$ were subsequently fitted to multi-exponential functions of time and the resulting fit parameters are summarized in **Table 4.A.5** (Appendix 4.A). As mentioned earlier in the theory section, these simulated fit parameters were utilised to construct the simulated DR spectra by following the established protocol.[97,98] The right panel of **Figure 4.3** illustrates the simulated DR spectra at four different temperatures, reflecting the temperature effects on the real $(\varepsilon'(\omega))$ and the imaginary ($\varepsilon''(\omega)$) parts of the total simulated DR spectra.

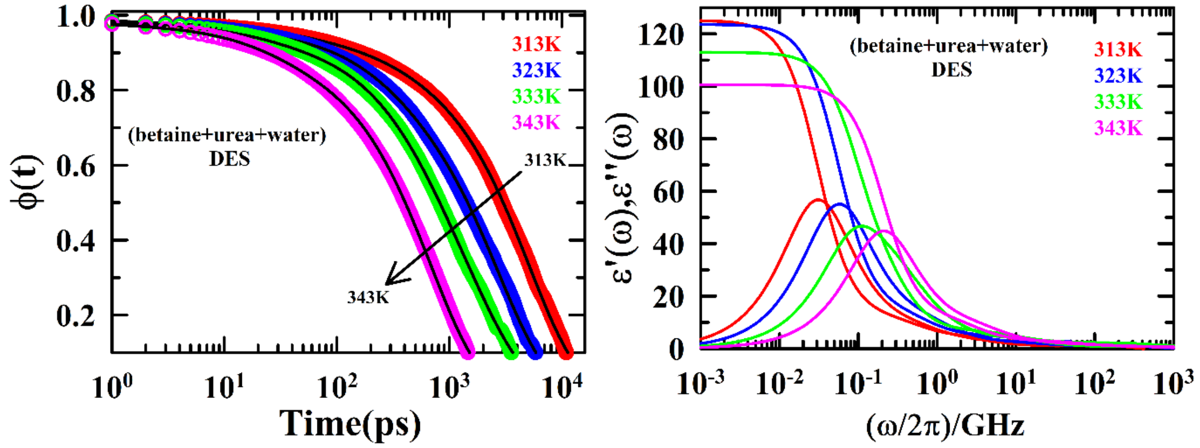

Figure 4.3. *Left panel*: Decays of the simulated total normalised dipole moment autocorrelation function, $\phi(t)$, for (betaine+urea+water) DES at four different temperatures. Open symbols denote the simulated data and solid lines represent multi-exponential fits through them. *Right panel:* Real and imaginary parts of the simulated DR spectra of the same DES at four different temperatures. All representations are colour coded.

Notice in the right panel that the values of the simulated static dielectric constant ($\varepsilon_S \equiv \varepsilon'(\omega \rightarrow 0)$ are in the range of what we found in experiments and decrease with the increase of the solution temperature. The decrease in ε_S may be attributed to the increased randomization of dipole correlations at higher temperatures because of a partial damage of the H-bond network of the solution structure.[70,129] This is shown in **Table 4.A.6** (Appendix 4.A), where the simulated average number of H-bonds per molecules decreases with increase of temperature. The imaginary part, $\varepsilon''(\omega)$, presented in the right panel of Figure **4.3,** shifts gradually toward higher frequency with the rise in temperature, indicating relaxation becoming faster at higher temperatures. This also correlates well with our experimental DR data. A direct comparison between our simulated and experimental DR spectra for four different temperatures are presented in **Figure 4.4**. Clearly, the agreement is quite good in general and relatively better in particular at the lower of the temperatures considered. Note, however, that such a close agreement may be serendipitous because the potentials employed in the simulations are non-polarizable and not specifically developed and parameterized for producing this DES.

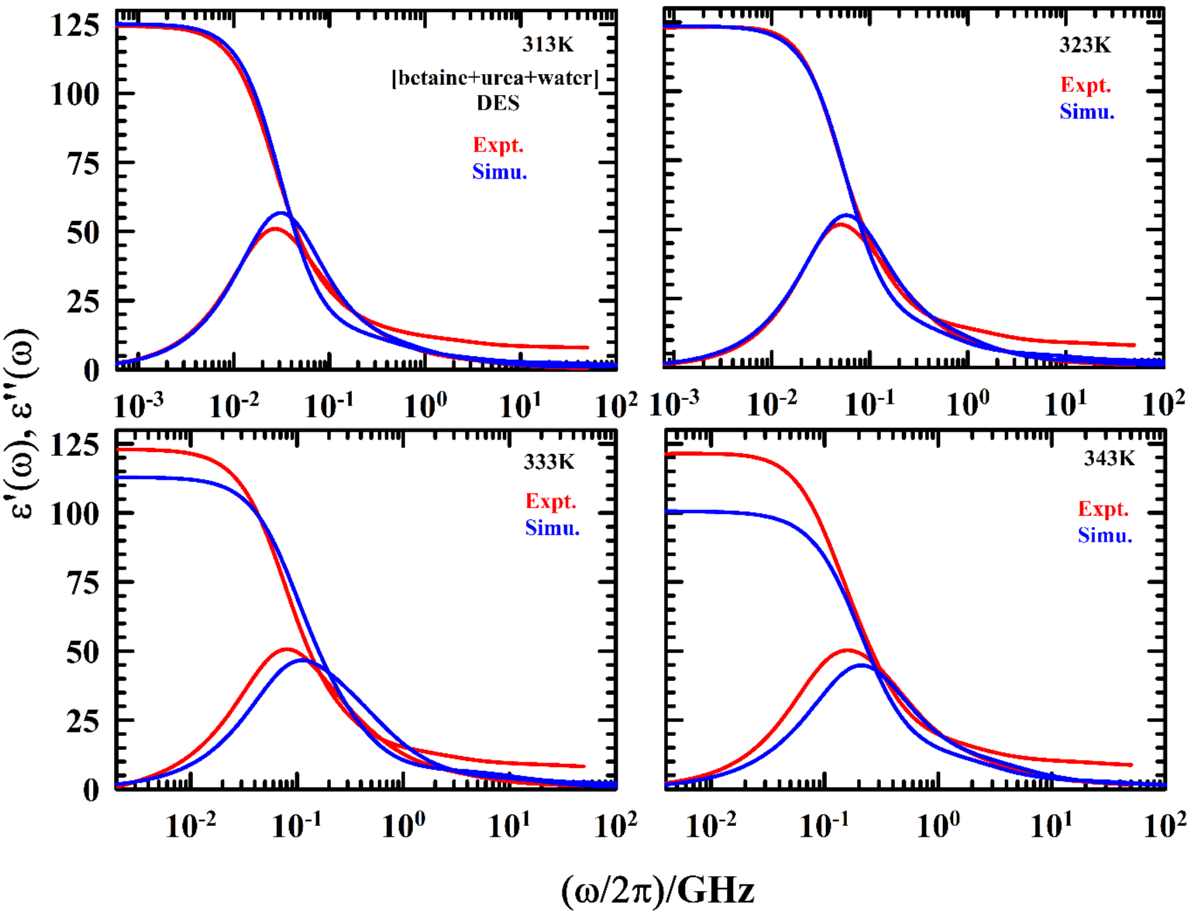

Figure 4.4. Comparison between experimental and simulated DR spectra (both real, $\varepsilon'(\omega)$, and imaginary, $\varepsilon''(\omega)$ parts) of (betaine+urea+water) DES at four different temperatures. All representations are colour coded.

Next, we compare in **Figure 4.5** the temperature dependent simulated average DR times at different temperatures with those from experiments (*upper panel*) and explore the viscosity coupling of the average DR times (*lower panel*). Clearly, the simulated average DR times agree well with those from experiments. The agreement is even better for the slowest DR time constant (*upper corner*), suggesting a small difference between the simulation and experiments in the amplitudes time constants that accompany the other relatively faster components of the full multi-Debye relaxation. A comparison of the amplitudes associated with the slowest relaxation component (*lower corner*) again highlights a close agreement between simulations and experiments. The viscosity coupling of the temperature dependent average DR times, explored in the lower panel by showing $\langle\tau_{DR}\rangle$ as a function of the temperature-reduced viscosity η/T, appears to suggest that both simulated and experimental relaxations were hydrodynamically controlled by the macroscopic solution viscosity. This is because the

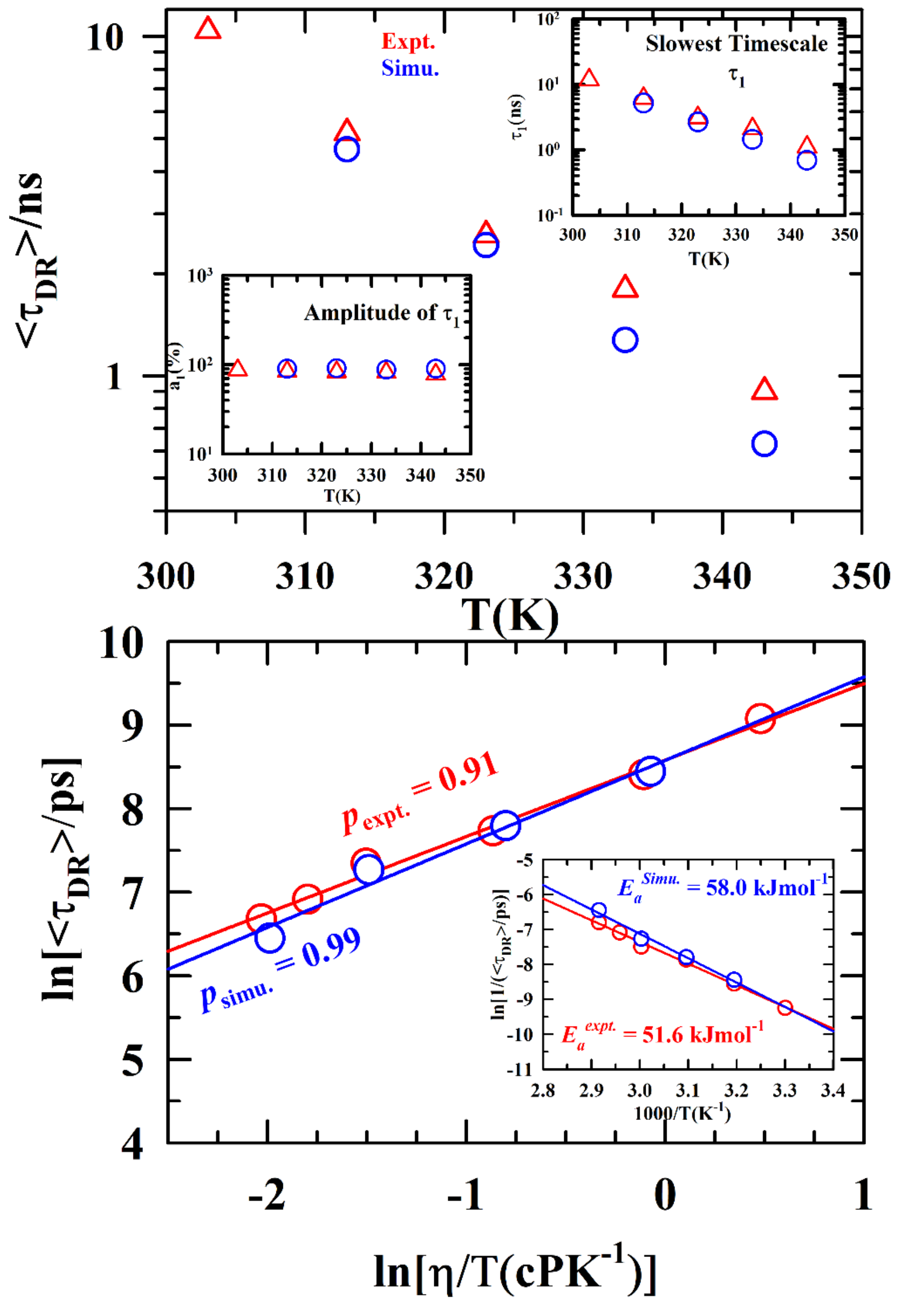

Figure 4.5. *Upper panel*: Comparison between the average DR times [$\langle\tau_{DR}\rangle$] from experiments and simulations for (betaine+urea+water) DES at four different temperatures. *Insets* represent a comparison of the slowest relaxation times, τ_1, and the associated amplitudes, a_1, between the experimental and the simulated DR. *Lower panel*: Temperature dependent average DR times from experiments and simulations are shown as a function of temperature-reduced viscosity in a log-log plot. Lines through the experimental data represent linear fits to the following expression, $ln[\langle\tau_{DR}\rangle] = A + pln[\frac{\eta}{T}]$, with p values shown in the respective plots. *Inset* represents activation energy obtained from Arrhenius plot of $\ln\left({}^{1}/_{\langle\tau_{DR}\rangle}\right)$ vs ${}^{1}/_{T}$ employing experimental and simulated data. Solid lines through the points represents the linear fits. All representations are colour coded.

exponent (p) of the relation, $\tau_{DR} \propto \left(\frac{\eta}{T}\right)^p$, assumes a value of near unity ($p \sim 1$). This is in sharp contrast with our earlier analysis that reflected a break-down of the SED relation while describing the experimental DR times in terms of the hydrodynamic molecular rotations. This apparent contradiction indicates that possibly the collective dynamics, *not* the individual molecular rotations, is involved in regulating the experimental DR where microscopic friction on a few or a set of collective dynamical variables controls the temporal profiles of the measured relaxations. The collective dynamics that relate to DR in this system of dipolar molecules with extensive intraspecies and interspecies H-bonding interactions is the collective single particle reorientational relaxations and the structural H-bond fluctuations. Interestingly, the simulated and experimental activations energies associated with the DR (*inset*, lower panel) compare well to that estimated earlier from the experimental temperature dependent viscosities (~56 kJmol^{-1}), [83] although the experimental activation energy (~51 kJmol^{-1}) is somewhat lower than the simulated value (~58 kJmol^{-1}). This is because of a relatively stronger viscosity decoupling of DR found in experiments (p = 0.91) than that predicted in simulations (p = 0.99).

4.4.2.2 Decomposition of Simulated DR Spectra: Origin of DR Timescales

This level of agreement encourages us to further decompose the simulated total DR spectra into the intra-species (self) and inter-species (cross) contributions. **Figure 4.6** shows the decomposition of the total DR spectra at two representative temperatures into the self (betaine-betaine, urea-urea and water-water) and cross (betaine-urea, betaine-water and urea-water) contributions, while the same at the other temperatures considered are presented in **Figure 4.A.6** (Appendix 4.A). The corresponding relaxation parameters of self and cross components are summarised in **Table 4.A.7 - 4.A.10** (Appendix 4.A).

It is evident from **Figure 4.6** and **Figure 4.A.6** (Appendix 4.A) that the self-interaction between the betaine molecules accounts for ~65% of the total DR dynamics, while the contributions from urea-urea and water-water are strikingly small (~7% and ~1%, respectively). It reflects a highly dipolar character of betaine, which maintains its zwitterionic form in solutions[138,139] with a positive charge on the amide nitrogen (N) atom and a negative charge on the carboxylic oxygen (O) atom. The interaction of betaine with urea, and water molecules accounts respectively for ~21% and ~5% of the total DR, highlighting the dominant role for betaine in the DR of this DES. From **Table 4.A.7 - 4.A.10** it is clear that the nanosecond DR time constant, although contributed by all the intra- and inter-species interactions, derives the largest amplitude (>65%) from the self-interaction of the betaine molecules. What surprises the most from this decomposition analysis is probably the finding of a nanosecond or near-nanosecond component arising from the self-interaction of water molecules at all these temperatures. The presence of such slow water molecules in a crowded environment like the present system suggests considerable interaction with other species, inducing a significant compromise of the water-water tetrahedral H-bond network structure of bulk water.[84,88] A huge reduction of the average number of water-water H-bonds per water molecule in this DES (~0.7) over that for bulk water (~3.7)[88] is evident in **Table 4.A.6** (Appendix 4.A). This damage of H-bond network is probably the reason for the predicted reduction of ε_S for water (from ~78[131,132] to ~2) and urea (from ~64[125] to ~10) in this DES shown in **Figure 4.A.7** (Appendix 4.A). Such a dramatic decrease of ε_S for water was reported earlier in both experimental[140] and simulation[141] studies of confined water, although the direct connection between the water-water H-bond network and $\varepsilon_S$was not explored in those previous studies.

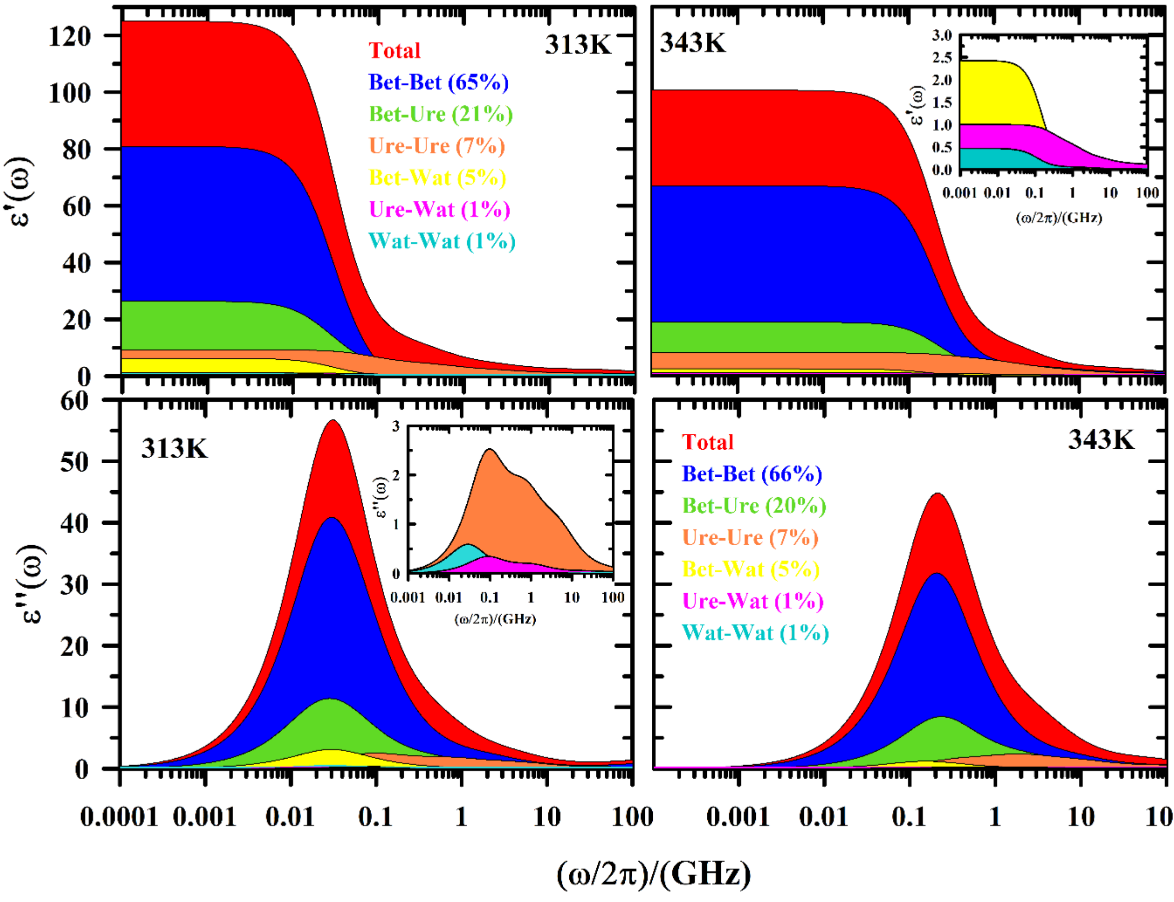

Figure 4.6. Spectral decomposition of real (ε') and imaginary (ε'') parts of the simulated DR spectra of (betaine+urea+water) DES at 313 and 343K. Contributions from self and cross

interactions to the total DR are represented employing colour-code along with percentage (%) amplitudes mentioned in the figure legends. *Insets* in the upper and lower panels of the figure show, employing expanded vertical scale, those contributions that are not visible in the main panels.

We are yet to connect the multiple timescales detected in our temperature dependent measurements to the individual component relaxations obtained after decomposition of the simulated total DR spectra. This is carried out now. A comparison of the experimental DR time constants summarized in **Table 4.1** with those from simulations provided in **Table 4.A.7 - 4.A.10** (Appendix 4.A) suggests the following: (i) the nanosecond timescale deriving contributions from all the self (intra-species) and cross (inter-species) interactions present in this DES, and (ii) the sub-nanosecond, the sub-100 ps and the sub-10 ps timescales originate from betaine-betaine, urea-urea, water-water, urea-water and betaine-urea interactions. Notice here that betaine-water interaction does not contribute to the sub-nanosecond and faster relaxations, suggesting that the interaction between them (water and betaine) is too strong to participate in the faster-than-nanosecond DR dynamics in this medium. It is therefore evident that each of the measured timescales cannot be assigned to a well-defined relaxation process within the system. Rather, they emerge from a superposition of a set relaxations resulting from inter- and intra-species interactions present in the system. Next, we explore the roles of reorientational relaxations of betaine, water and urea, and the structural H-bond fluctuations involving these species in generating the multiple DR timescales found in our experiments and simulations.

4.4.2.3 Understanding Multiple DR Timescales: Roles of Reorientational Relaxations and Structural H-bond Fluctuations

The collective dipole moment fluctuations that generate the frequency dependent dielectric response (and measured in experiments) and the rotational dynamics of a dipolar species is connected via a common thread, and that is, orientational fluctuations of the dipole vector.[137,142] This connection provides, within the continuum description of dipolar fluids, the following relation[137,143] between the average DR time ($\langle \tau_{DR} \rangle$) and the rank ($\ell$) dependent reorientational correlation time ($\langle \tau_{\ell=1} \rangle$), $\langle \tau_{DR} \rangle = \frac{\ell(\ell+1)}{2} \langle \tau_{\ell=1} \rangle$, ℓ being the rank of the Legendre polynomial denoted as P_ℓ. We have followed in our simulations the first rank (ℓ=1) reorientational correlation function defined as,[137,142] $C_1(t) = \langle P_1 |\boldsymbol{u}(0) \cdot \boldsymbol{u}(t)| \rangle / \langle P_1 |\boldsymbol{u}(0) \cdot \boldsymbol{u}(0)| \rangle$,where $\boldsymbol{u}$

denotes the backbone vector of the molecules considered (here betaine, urea and water). Note here that $C_\ell(t)$ describes the rank dependent reorientational relaxation for single dipoles in a potential energy surface constructed collectively by the neighbouring molecules. Consequently, $C_\ell(t)$ describes the rank dependent collective single particle reorientational dynamics and delineate the corresponding dynamic microscopic friction profile.

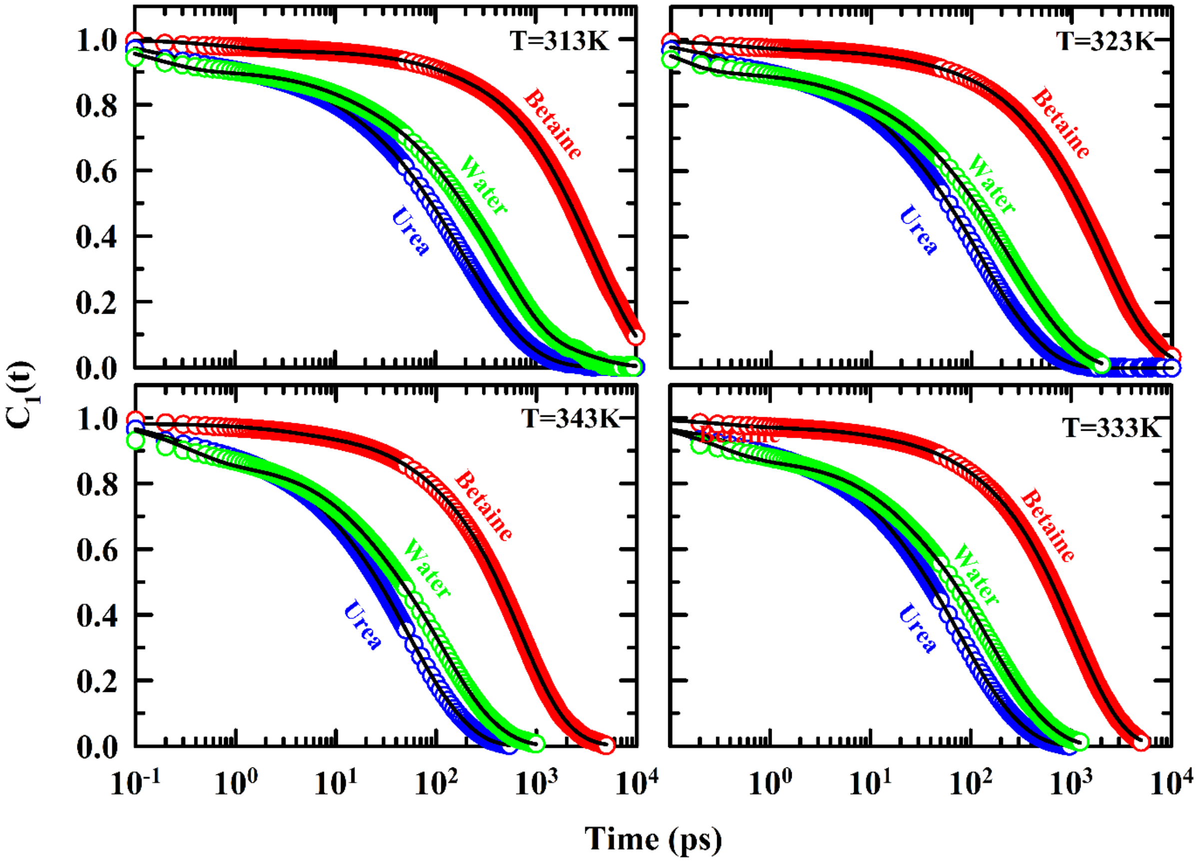

Figure 4.7. Temperature dependent first-rank collective single particle reorientational correlation functions, $C_1(t)$, for betaine, urea and water and their corresponding multi-exponential fits (lines). All representations are colour coded.

Figure 4.7 shows the simulated $C_1(t)$ decays for betaine, urea and water at four representative temperatures. Each of the molecules, H-bonded with others or free, contribute to these simulated ensemble-averaged $C_1(t)$ decays. Notice that these reorientational correlations, although becoming faster upon increasing the solution temperature, are spread over a large span of timescale, ranging from sub-picosecond to a few nanoseconds. It is quite interesting to note that the simulated reorientational correlations for both urea and water in this DES depict severely slowed down dynamics compared to those predicted for neat liquids[125,144] and aqueous binary mixtures.[145] Parameters obtained from fitting each of these decays to a sum of three exponential functions of time are summarized in **Table 4.A.11** (Appendix 4.A). A direct comparison between the simulated $C_1(t)$ decay time constants and the measured DR timescales (**Table 4.1**) suggests that the slowest DR timescale (τ_1) corroborate well with the slowest timescale of $C_1(t)$ decay of betaine molecules and may also contain contributions from water reorientation dynamics. The other three DR timescales (τ_2, τ_3 and τ_4), on the other hand, derive contributions from the reorientational relaxations of betaine, urea and water. Clearly, reorientation dynamics of any of these species could be assigned exclusively to account for any of the DR timescales measured in experiments.

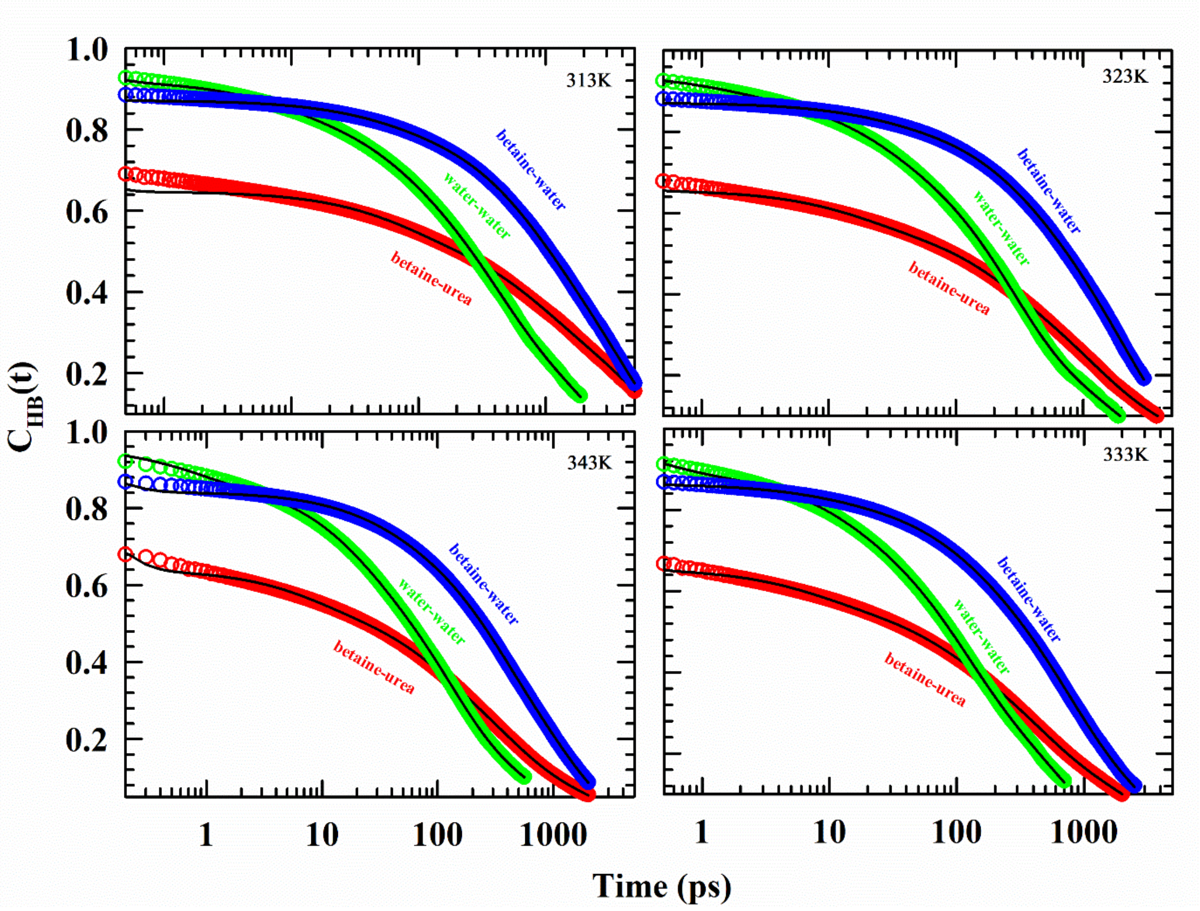

Figure 4.8. Structural H-bond relaxation of involving different donor-acceptor pairs in (betaine+urea+water) DES at four different temperatures. Lines through the data points represents multi-exponential fits. All representations are colour coded.

Figure 4.8 depicts the simulated structural H-bond fluctuation dynamics via the corresponding correlation function, $C_{HB}(t)$, at four different temperatures. Note here that we are showing $C_{HB}(t)$ decays for urea-betaine, water-betaine and water-water pairs, and not considering the possible urea-urea and urea-water pairs. This selection was based on the RDF peak intensities between the possible donor and acceptor atom pairs involved in the H-bonding. We considered those pairs only for which the RDF first peak intensities were greater than unity (**Figure 4.A.8**, Appendix 4.A). This does not, however, mean that pairs producing RDF peak intensities lower than unity are not involved in H-bonding. We simply consider a very low propensity of forming H-bonds for those pairs and exclude them from our subsequent analysis. Parameters obtained from fit of these simulated $C_{HB}(t)$ decays to multi-exponential functions of time are summarized in **Table 4.A.12** (Appendix 4.A). An inspection to the timescales provided in this table suggest that the slowest DR timescale derive contributions from the $C_{HB}(t)$ decays of betaine-urea and betaine-water pairs, whereas $C_{HB}(t)$ decays involving betaine-urea, betaine-water and water-water pairs contribute to the other faster DR timescales. It is therefore quite evident that the DR of this DES involves both collective single particle reorientation relaxation and the structural H-bond fluctuation dynamics, leaving out very limited scope for the hydrodynamic molecular rotations governed by the macroscopic solution viscosity.

4.5 Conclusion

We have performed a combined experimental and simulated DR study on a NADES composed of biodegradable components betaine, urea and water. Temperature dependent ($303 \leq T/K \leq 343$) DR measurements were performed employing three different set-ups to access a frequency coverage from 20Hz to 50 GHz. These measurements revealed existence of four distinct DR timescales, spreading from a few picoseconds to several nanoseconds. Interestingly, a one-to-one comparison between experimental and simulated DR spectra reveals a strikingly close agreement between the two. This resemblance further motivated us to decompose the simulated total DR spectra into the self and the cross-interaction contributions. The decomposition suggests that the betaine-betaine self-interaction contributes dominantly to the total DR with an amplitude of ~ 65%, whereas the self-interaction between urea and water molecules contributes the least. Among the cross-interactions, betaine-urea is the second dominant contributor to the total DR with an amplitude of ~20%, while the other two (betaine-water, urea-water) account for much less (~10%) of the total DR. The origins of the multiple DR timescales were further investigated via the temperature dependent simulations of the collective single particle reorientational dynamics ($C_1(t)$) and the structural H-bond relaxation ($C_{HB}(t)$). Analyses of the simulated $C_1(t)$ decays suggest that reorientational relaxations of betaine and water contribute to the slowest of the multiple DR timescales, while reorientations of urea, water and betaine contributes to the other relatively faster timescales. An inspection of the simulated $C_{HB}(t)$ decays reveal that the dominant nanosecond timescale is associated with the structural H-bond relaxation of betaine-urea and betaine-water pairs. The significant slow-down of water dynamics (~10 ps timescale in the neat water at 300 K to ~1 ns in this DES) has been linked to its extensive interaction with betaine and urea. This has also resulted a dramatic decrease of the average number of water-water H-bonds and reduction of the ε_s value.

Appendix 4.A

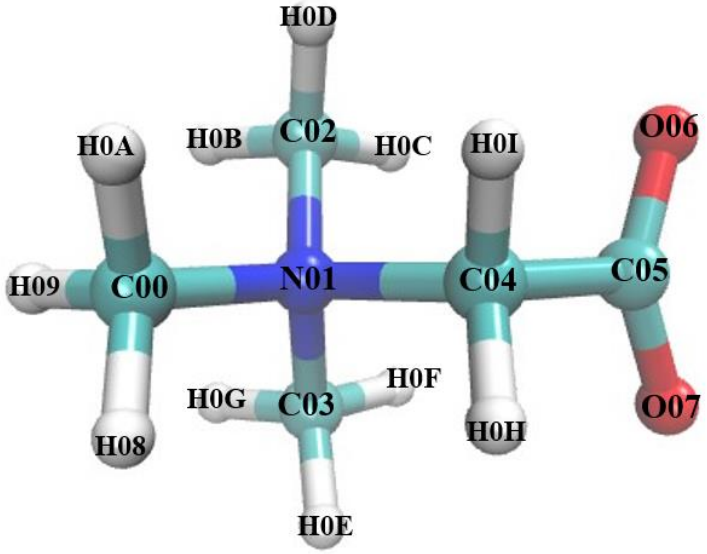

Betaine

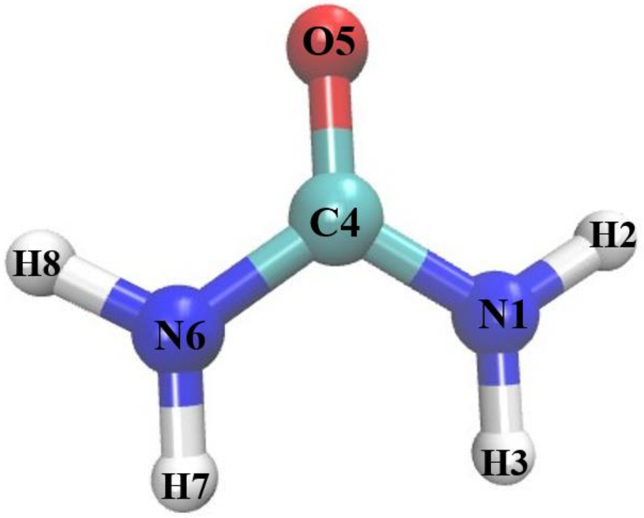

Water

Urea

Figure 4.A.1. Chemical structures of betaine, urea and water along with their atomic sites as used in our simulations.

Table 4.A.1. Partial charges and Lennard-Jones parameters for betaine molecule

Atom types	**Charge, e**	σ(Å)	$\varepsilon\ (kJmol^{-1})$
C00	-0.1614	3.50	0.27614
N01	-0.0223	3.25	0.71128
C02	-0.1436	3.50	0.27614
C03	-0.1428	3.50	0.27614
C04	-0.1865	3.50	0.27614
C05	0.4380	3.55	0.29288
O06	-0.5650	2.96	0.87864
O07	-0.5650	2.96	0.87864
H08	0.1202	2.50	0.12552
H09	0.1202	2.50	0.12552
H0A	0.1202	2.50	0.12552
H0B	0.1295	2.50	0.12552
H0C	0.1295	2.50	0.12552
H0D	0.1295	2.50	0.12552
H0E	0.1295	2.50	0.12552
H0F	0.1295	2.50	0.12552
H0G	0.1295	2.50	0.12552
H0H	0.1057	2.50	0.12552
H0I	0.1057	2.50	0.12552

Table 4.A.2. Partial charges and Lennard-Jones parameters for urea molecule

Atom types	**Charge, e**	σ(Å)	$\varepsilon\ (kJmol^{-1})$
N1	-0.4077	3.55	1.06692
H2	0.2484	0.00	0.00000
H3	0.2484	0.00	0.00000
C4	0.1116	3.75	0.65898
O5	-0.2898	2.96	1.31796
N6	-0.4077	3.55	1.06692
H7	0.2484	0.00	0.00000
H8	0.2484	0.00	0.00000

Table 4.A.3. Partial charges and Lennard-Jones parameters for SPC/E water molecule

Atom types	Charge, e	σ(Å)	$\varepsilon\ (kJmol^{-1})$
OW	-0.8476	3.16	0.65
HW	0.4238	0.00	0.00

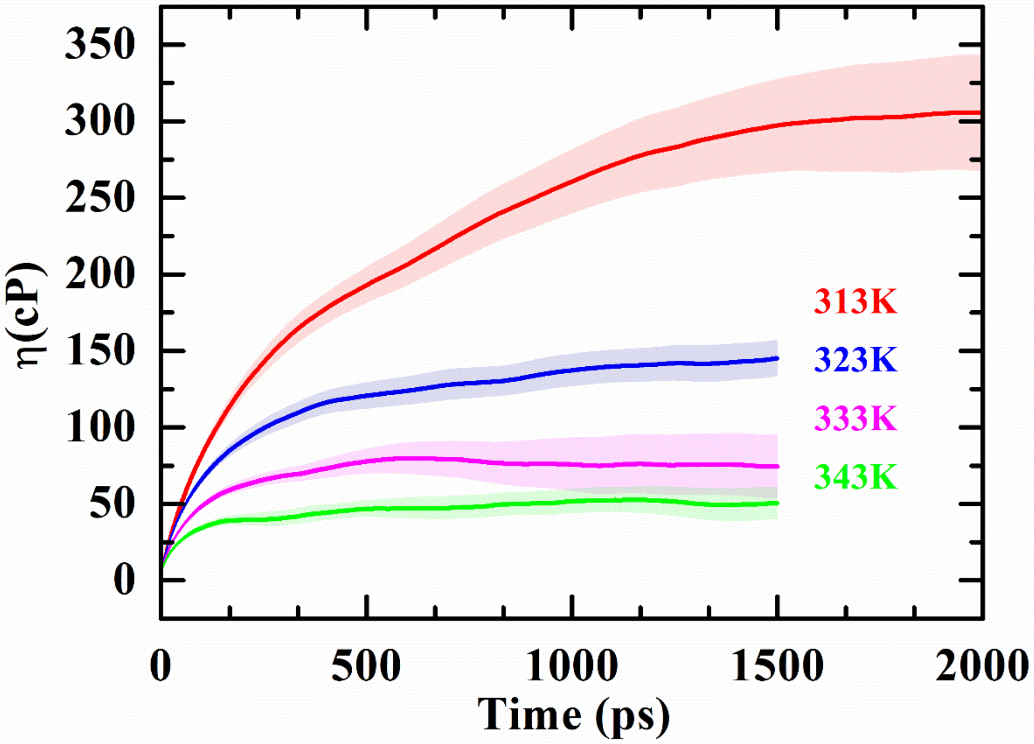

Figure 4.A.2. The dependence of η on the upper limit of integration in Green-Kubo integrals. The curves represent the averaged results derived from 15 – 20 individual trajectories. Shaded regions corresponding to each curve indicate the standard deviation error.

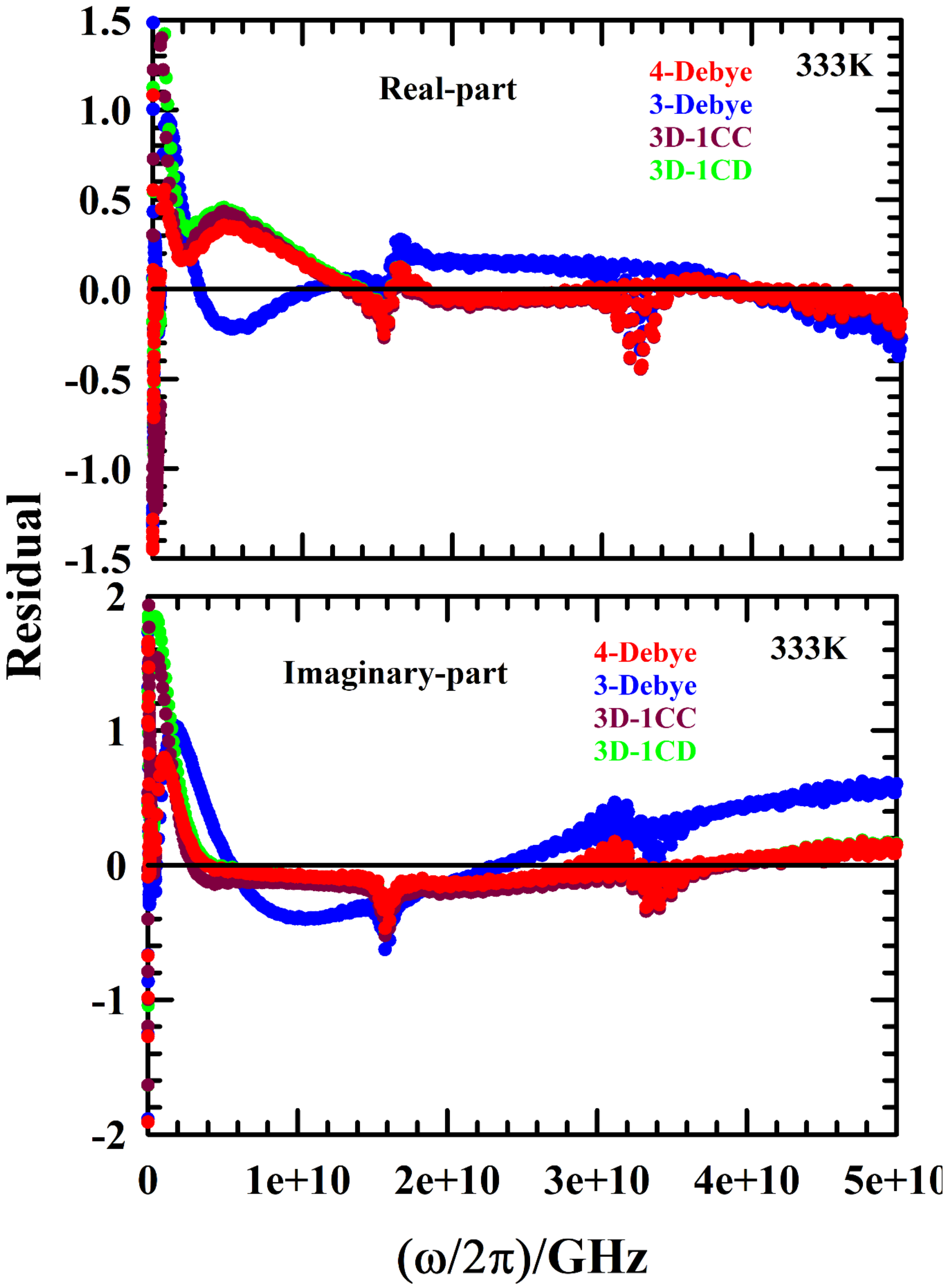

Figure 4.A.3. Comparison of the residuals (both real, ε', and imaginary part, ε'', components) among 3-Debye, 4-Debye, 3D-1CC, and 3D-1CD DR fits to DR spectra of (betaine+urea+water) DES at a representative temperature, 333 K. All representations are colour coded.

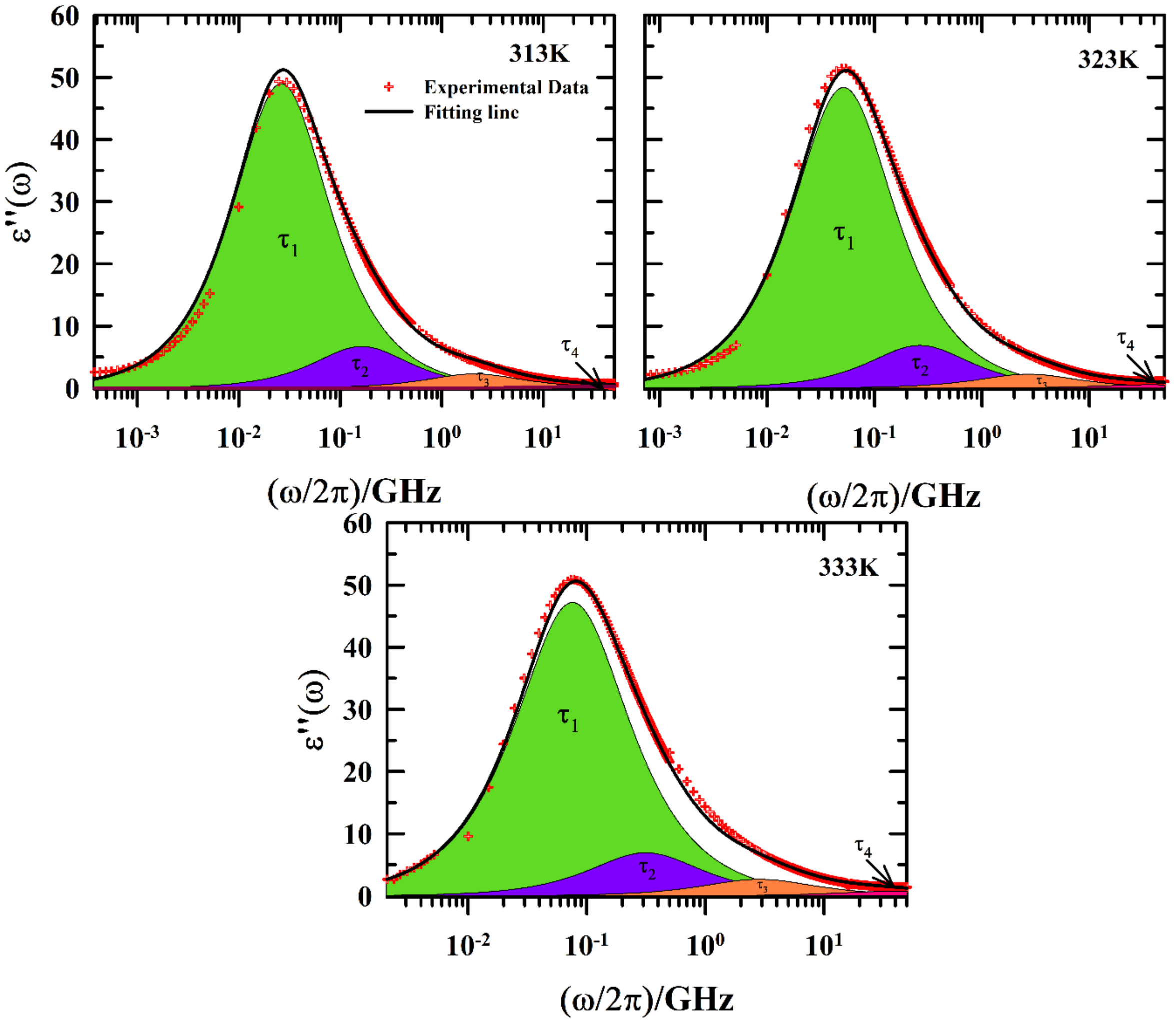

Figure 4.A.4. Decomposition of the measured frequency dependent dielectric loss (ε'') spectra into their individual time component contributions for (betaine+urea+water) DES at three different temperatures. Red pluses represent the experimental data and the solid lines going through them denote the multi-Debye fits. Different time scale contributions are colour coded.

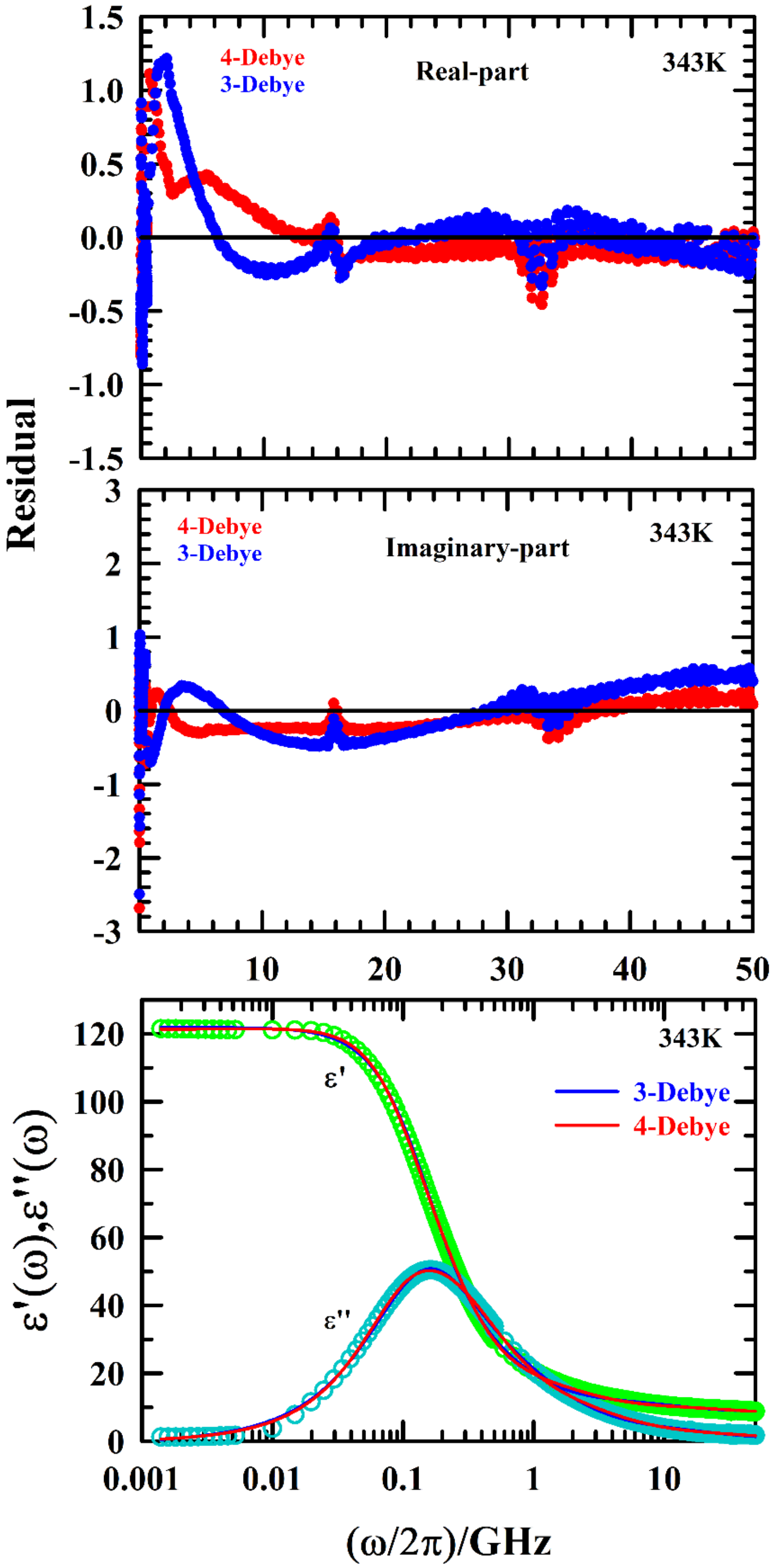

Figure 4.A.5. *Upper and middle panels:* Comparison of residuals (both real (ε') and imaginary (ε'') parts) between 3-Debye and 4-Debye fits at a representative temperature 343 K. *Lower panel*: 3-Debye and 4-Debye fits of the real and imaginary parts of the DR spectra at 343 K. All representations are colour coded.

Table 4.A.4. Hydrodynamic molecular rotation times for water, urea and betaine calculated by using the SED relation with stick boundary condition, $\tau = \frac{3\eta V}{k_B T}$. Note that the van der Waals volumes of water, urea and betaine used here were calculated from the reference.[135] The viscosity value at 303 K was obtained from the extrapolation of the high temperature data.

$T(K)$	η (cP)	Water ($V \approx 17 Å^3$) τ_r (ns)	Urea ($V \approx 54 Å^3$) τ_r (ns)	Betaine ($V \approx 121 Å^3$) τ_r (ns)
303	540	6.58	20.92	46.88
313	281	3.31	10.53	23.62
323	136	1.55	4.94	11.07
333	74	0.82	2.61	5.84

Table 4.A.5. Temperature dependent fit parameters for the simulated total dipole moment auto correlation functions for (betaine+urea+water) DES.

T/K	a_1	τ_1(ps)	a_2	τ_2(ps)	a_3	τ_3(ps)	a_4	τ_4(ps)	a_5	τ_5(ps)	ε_∞	$\langle \tau_{DR}^{simu.} \rangle$(ps)
313	0.90	5149	0.06	281	0.02	45	0.005	1.6	0.02	0.8	1	4652
323	0.81	2927	0.15	400	0.03	13	-	-	0.02	0.2	1	2431
333	0.70	1877	0.24	509	0.04	22	-	-	0.02	0.6	1	1436
343	0.88	715			0.08	43	0.02	2.6	0.01	0.4	1	632

Table 4.A.6. Average number of H-bonds per molecules from simulations

Temp	N(Ure)-O(Bet)		O(Water)- O1(Bet)		O(Water)- O(Water)
	Per urea	Per betaine	Per water	Per betaine	Per water
313K	1.79	3.58	1.57	0.87	0.71
323K	1.75	3.50	1.54	0.86	0.71
333K	1.71	3.42	1.53	0.85	0.68
343K	1.67	3.35	1.53	0.84	0.65

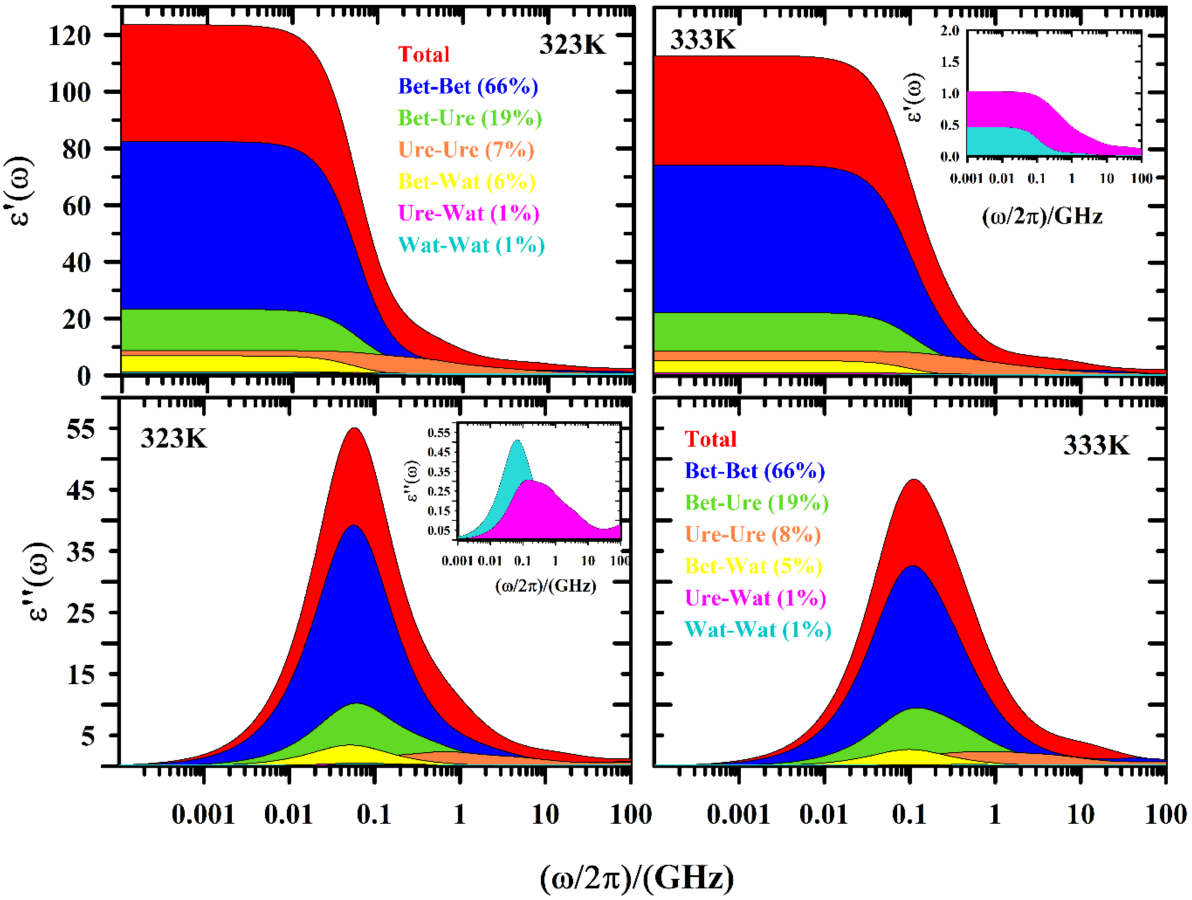

Figure 4.A.6. Spectral decomposition of real (ε') and imaginary (ε'') parts of the simulated DR spectra of (betaine+urea+water) DES at 323 and 333K. Contributions from the self and the cross interactions to the total DR are color-coded and the corresponding percentage (%) amplitudes mentioned in the figure legends. *Insets* of the figure panels show, in expanded vertical scales, the contributions that are not visible in the main panels.

Table 4.A.7. Dielectric relaxation parameters of the simulated total spectrum as well as individual spectra at 313 K

Component	ε_s	$\Delta\varepsilon_1$	τ_1 (ps)	$\Delta\varepsilon_2$	τ_2 (ps)	$\Delta\varepsilon_3$	τ_3 (ps)	$\Delta\varepsilon_4$	τ_4 (ps)	$\Delta\varepsilon_5$	τ_5 (ps)	$\Delta\varepsilon_6$	τ_6 (ps)
Total	125.1	112.6	5149	-	-	7.5	280	2.5	42	1.25	1.6	2.5	0.4
Bet-Bet	80.1	64.8	5757	12.1	2392	-	-	2.4	78	1.6	1	-	-
Ure-Ure	9.2	-	-	4.4	1900	2.4	214	1.4	33	0.9	1.2	-	-
Wat-Wat	1.1	-	-	0.6	1904	0.3	143	-	-	0.07	7.2	0.1	0.3
Bet-Ure	26.4	14.2	7366	9.8	3687	1.6	267			0.81	6	-	-
Bet-Wat	6.2	6.24	5314	-	-	-	-	-	-	-	-	-	-
Ure-Wat	1.2	1.18	5470	-	-	-	-	-	-	-	-	-	-

Table 4.A.8. Dielectric relaxation parameters of the simulated total spectrum as well as individual spectra at 323 K

Component	ε_s	$\Delta\varepsilon_1$	τ_1 (ps)	$\Delta\varepsilon_2$	τ_2 (ps)	$\Delta\varepsilon_3$	τ_3 (ps)	$\Delta\varepsilon_4$	τ_4 (ps)	$\Delta\varepsilon_5$	τ_5 (ps)	$\Delta\varepsilon_6$	τ_6 (ps)
Total	123.6	108.7	2927	-	-	9.9	400	-	-	2.5	13	2.5	0.2
Bet-Bet	82.4	78.3	2815	-	-	-	-	2.5	82	-	-	1.6	1.3
Ure-Ure	8.8	-	-	2.2	1898	3.7	233	1.9	33	-	-	1.1	1.2
Wat-Wat	1.1	-	-	0.47	1567	0.34	280	0.17	45	-	-	0.16	1
Bet-Ure	23.3	19.6	2704	-	-	3.5	350	-	-	0.23	9	-	-
Bet-Wat	6.9	6.88	3078	-	-	-	-	-	-	-	-	-	-
Ure-Wat	1.1	0.98	2480	0.05	873	-	-	-	-	0.04	7	-	-

Table 4.A.9. Dielectric relaxation parameters of the simulated total spectrum as well as individual spectra at 333 K

Component	ε_s	$\Delta\varepsilon_1$	τ_1 (ps)	$\Delta\varepsilon_2$	τ_2 (ps)	$\Delta\varepsilon_3$	τ_3 (ps)	$\Delta\varepsilon_4$	τ_4 (ps)	$\Delta\varepsilon_5$	τ_5 (ps)	$\Delta\varepsilon_6$	τ_6 (ps)
Total	112.9	79.0	1877	-	-	27.1	509	4.5	22	-	-	2.3	0.6
Bet-Bet	74.3	55.0	1729	-	-	17.1	534	-	-	2.2	3	-	-
Ure-Ure	8.8	-	-	2.6	685	2.7	160	1.3	32	-	-	1.1	1.4
Wat-Wat	1	-	-	0.28	837	0.38	234	0.19	33	-	-	0.15	0.9
Bet-Ure	22.4	15.9	1562	-	-	6.1	390			0.04	10	-	-
Bet-Wat	5.4	5.42	1614	-	-	-	-	-	-	-	-	-	-
Ure-Wat	0.9	0.84	1407	-	-	-	-	0.08	37	-	-	0.01	1.3

Table 4.A.10. Dielectric relaxation parameters of the simulated total spectrum as well as individual spectra at 343 K

Component	ε_s	$\Delta\varepsilon_1$	τ_1 (ps)	$\Delta\varepsilon_2$	τ_2 (ps)	$\Delta\varepsilon_3$	τ_3 (ps)	$\Delta\varepsilon_4$	τ_4 (ps)	$\Delta\varepsilon_5$	τ_5 (ps)	$\Delta\varepsilon_6$	τ_6 (ps)
Total	99.4	87.5	715	-	-	8.9	43	-	-	1.99	2.6	1.0	0.2
Bet-Bet	66.1	62.8	774	-	-	-	-	1.9	18	-	-	1.3	0.5
Ure-Ure	8.0	-	-	2.1	450	3.4	82	1.6	16	-	-	1.0	0.8
Wat-Wat	1	-	-	0.37	540	0.36	92	0.14	14	-	-	0.14	0.6
Bet-Ure	18.8	16.6	698	-	-	2.3	59	-	-	-	-	-	-
Bet-Wat	4.8	4.84	1042	-	-	-	-	-	-	-	-	-	-
Ure-Wat	0.9	0.56	1042	0.25	219	-	-	-	-	0.05	6	-	-

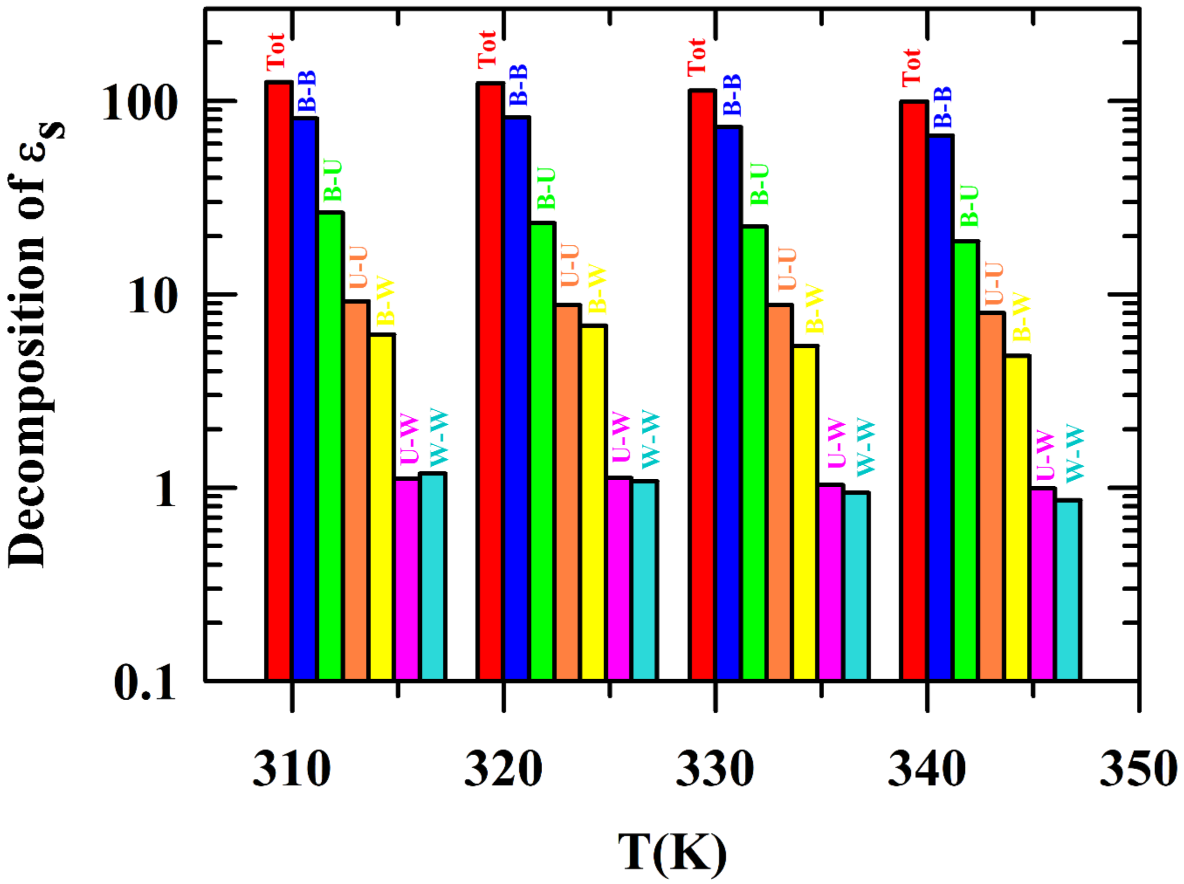

Figure 4.A.7. Contributions from the self and cross interactions to the total dielectric constant (ε_s) of the DES made of betaine, urea and water at four different temperatures. Notation used for representations are as follows: Total=Tot, Betaine=B, Urea=U and Water=W.

Table 4.A.11. Multi-exponential fit parameters for the simulated first-rank collective single particle reorientational correlation functions ($C_1(t)$) at four different temperatures for (betaine+urea+water) DES.

Betaine										
T/K	a_1	τ_1(ps)	a_2	τ_2(ps)	a_3	τ_3(ps)	a_4	τ_4(ps)	a_5	τ_5(ps)	$\langle\tau_{\ell=1}\rangle$ (ps)
313	0.71	4977	0.21	1372	0.04	101	-	-	0.04	0.9	3825
323	0.31	4300	0.55	1646	0.09	242	0.03	22	0.02	0.5	2261
333	0.71	1356	0.20	513	0.05	75	0.02	9	0.02	0.3	1069
343	0.23	1315	0.66	605	0.07	57	0.02	5	0.03	0.3	706
Urea											
T/K	a_1	τ_1(ps)	a_2	τ_2(ps)	a_3	τ_3(ps)	a_4	τ_4(ps)	a_5	τ_5(ps)	$\langle\tau_{\ell=1}\rangle$ (ps)
313	0.20	683	0.40	238	0.23	60	0.08	9	0.09	0.3	246
323	0.38	302	-	-	0.38	83	0.13	14	0.11	0.5	148
333	0.38	183	-	-	0.39	55	0.13	10	0.10	0.5	92
343	0.42	111	-	-	0.36	34	0.12	6	0.10	0.3	60
Water											
T/K	a_1	τ_1(ps)	a_2	τ_2(ps)	a_3	τ_3(ps)	a_4	τ_4(ps)	a_5	τ_5(ps)	$\langle\tau_{\ell=1}\rangle$ (ps)
313	0.11	3020	0.56	472	0.16	79	0.06	10	0.11	0.2	610
323	0.39	602	0.34	162	0.13	36	0.05	5	0.09	0.1	295
333	0.37	345	0.37	103	0.13	14	-	-	0.13	0.3	168
343	0.30	254	0.40	90	0.17	15	-	-	0.13	0.3	115

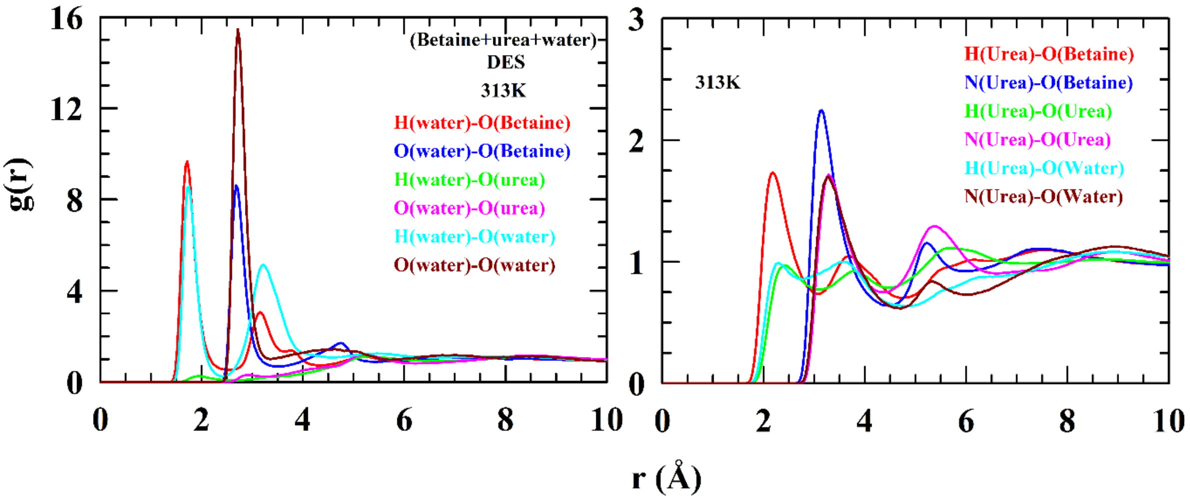

Figure A.A.8. Simulated radial distribution functions (RDFs) for different atom-sites of water with other components' atom site (left panel), and urea with others components' atom sites (right panel).

Table 4.A.12. Multiexponential fit parameters for the simulated structural H-bond relaxations $(C_{HB}(t))$ for urea-betaine, water-betaine and water-water pairs in (betaine+urea+water) DES at four different temperatures.

Betaine-Urea										
T(K)	a_1	τ_1(ps)	a_2	τ_2(ps)	a_3	τ_3(ps)	a_4	τ_4(ps)	a_5	τ_5(ps)	$\langle\tau_{HB}^{c}\rangle$
313	0.34	6361	0.17	984	0.09	213	0.07	23	0.33	0.1	2351
323	0.19	5589	0.27	942	0.12	167	0.07	16	0.34	0.1	1337
333	0.23	2358	0.26	343	0.09	61	0.07	7.1	0.33	0.1	638
343	0.17	1740	0.26	321	0.13	69	0.09	7.5	0.35	0.1	389
Betaine-Water											
313	0.59	4100	0.23	646	0.04	60	0.02	5.9	0.11	0.1	2750
323	0.51	2838	0.20	1034	0.12	252	0.03	22	0.12	0.1	1685
333	0.34	2276	0.40	560	0.10	93	0.03	8.4	0.13	0.1	1007
343	0.49	1160	0.29	237	0.06	31			0.15	0.1	639
Water-Water											
313	0.38	1892	0.39	312	0.10	52	0.06	7.3	0.07	0.2	1352
323	0.29	1805	0.49	241	0.11	21	0.04	1.6	0.06	0.1	644
333	0.41	600	0.39	90	0.09	11	-	-	0.08	0.4	282
343	0.25	597	0.46	109	0.16	17	-	-	0.09	0.7	202

References

1 M. Ikeda, *Toxicol Lett*, 1992, **64–65**, 191–201.

2 E. P. Cronkite, R. T. Drew, T. Inoue, Y. Hirabayashi and J. E. Bullis, *Environ Health Perspect*, 1989, **82**, 97–108.

3 D. Majumdar (neé Som), C. Dutta, A. K. Mukherjee and S. Sen, *Transp Res D Transp Environ*, 2008, **13**, 524–530.

4 M. B. Schenker and J. A. Jacobs, *Tubercle and Lung Disease*, 1996, **77**, 4–18.

5 M. Maroncelli, X. X. Zhang, M. Liang, D. Roy and N. P. Ernsting, *Faraday Discuss*, 2012, **154**, 409–424.

6 M. J. Earle and K. R. Seddon, *Pure Appl. Chem*, 2000, **72**, 1391–1398.

7 A. M. Scurto, K. Hutchenson and B. Subramaniam, *Gas-Expanded Liquids : Fundamentals and Applications*, 2009, 3–37.

8 J. P. Hallett, C. L. Kitchens, R. Hernandez, C. L. Liotta and C. A. Eckert, *Acc. Chem. Res.*, 2006, **39**, 531–538.

9 J. E. Lewis, R. Biswas, A. G. Robinson and M. Maroncelli, *J. Phys. Chem. B*, 2001, **105**, 3306–3318.

10 S. V Dzyuba and R. A. Bartsch, *Angew. Chem. Int. Ed.* **2003**, *42*, 148–150.

11 E. L. Smith, A. P. Abbott and K. S. Ryder, *Chem. Rev.*, 2014, **114**, 11060–11082.

12 B. B. Hansen, S. Spittle, B. Chen, D. Poe, Y. Zhang, J. M. Klein, A. Horton, L. Adhikari, T. Zelovich, B. W. Doherty, B. Gurkan, E. J. Maginn, A. Ragauskas, M. Dadmun, T. A. Zawodzinski, G. A. Baker, M. E. Tuckerman, R. F. Savinell and J. R. Sangoro, *Chem. Rev.*, 2021, **121**, 1232–1285.

13 T. El Achkar, H. Greige-Gerges and S. Fourmentin, *Environ Chem Lett*, 2021, **19**, 3397–3408.

14 Y. Liu, J. B. Friesen, J. B. McAlpine, D. C. Lankin, S. N. Chen and G. F. Pauli, *J. Nat. Prod.*, 2018, **81**, 679–690.

15 J. Płotka-Wasylka, M. de la Guardia, V. Andruch and M. Vilková, *Microchem. J.*, 2020, **159**, 105539.

16 Y. Dai, G. J. Witkamp, R. Verpoorte and Y. H. Choi, *Anal. Chem.*, 2013, **85**, 6272–6278.

17 M. Espino, M. de los Ángeles Fernández, F. J. V. Gomez and M. F. Silva, *TrAC - Trends in Analytical Chemistry*, 2016, **76**, 126–136.

18 W. C. Huang, D. Zhao, N. Guo, C. Xue and X. Mao, *J. Agric. Food Chem.*, 2018, **66**, 11897–11901.

19 S. Kaoui, B. Chebli, safa Zaidouni, K. Basaid and Y. Mir, *Sustain. Chem. Pharm.*, 2023, **31**, 100937.

20 H. Vanda, Y. Dai, E. G. Wilson, R. Verpoorte and Y. H. Choi, *Comptes Rendus Chimie*, 2018, **21**, 628–638.

21 Q. Q. Koh, Y. L. Kua, S. Gan, K. W. Tan, T. Z. E. Lee, W. K. Cheng and H. L. N. Lau, *Sustain. Chem. Pharm.*, 2023, **35**, 101218.

22 Y. L. Chen, X. Zhang, T. T. You and F. Xu, *Cellulose*, 2019, **26**, 205–213.

23 E. Durand, J. Lecomte, B. Baréa, G. Piombo, E. Dubreucq and P. Villeneuve, *Process Biochem.*, 2012, **47**, 2081–2089.

24 S. Sun, Y. Niu, Q. Xu, Z. Sun and X. Wei, *Ind. Eng. Chem. Res.*, 2015, **54**, 8019–8024.

25 M. B. Haider, D. Jha, B. Marriyappan Sivagnanam and R. Kumar, *J. Chem. Eng. Data*, 2018, **63**, 2671–2680.

26 E. Rozema, A. D. Van Dam, H. C. M. Sips, R. Verpoorte, O. C. Meijer, S. Kooijman and Y. H. Choi, *RSC Adv.*, 2015, **5**, 61398–61401.

27 C. Bakirtzi, K. Triantafyllidou and D. P. Makris, *J. Appl. Res. Med. Aromat. Plants*, 2016, **3**, 120–127.

28 I. Zahrina, M. Nasikin, E. Krisanti and K. Mulia, *Food Chem.*, 2018, **240**, 490–495.

29 K. M. Jeong, J. Ko, J. Zhao, Y. Jin, D. E. Yoo, S. Y. Han and J. Lee, *J. Clean Prod.*, 2017, **151**, 87–95.

30 C. G. González, N. R. Mustafa, E. G. Wilson, R. Verpoorte and Y. H. Choi, *Flavour Fragr. J.*, 2018, **33**, 91–96.

31 L. Millia, V. Dall'Asta, C. Ferrara, V. Berbenni, E. Quartarone, F. M. Perna, V. Capriati and P. Mustarelli, *Solid State Ion*, 2018, **323**, 44–48.

32 A. Hayyan, M. A. Hashim, M. Hayyan, F. S. Mjalli and I. M. Alnashef, *J. Clean Prod.*, 2014, **65**, 246–251.

33 M. H. Zainal-Abidin, M. Hayyan, A. Hayyan and N. S. Jayakumar, *Anal. Chim. Acta.*, 2017, **979**, 1–23.

34 I. M. Aroso, J. C. Silva, F. Mano, A. S. D. Ferreira, M. Dionísio, I. Sá-Nogueira, S. Barreiros, R. L. Reis, A. Paiva and A. R. C. Duarte, *Eur. J. Pharm. Biopharm.*, 2016, **98**, 57–66.

35 H. G. Morrison, C. C. Sun and S. Neervannan, *Int. J. Pharm.*, 2009, **378**, 136–139.

36 N. F. Hadley, *Prog. Lipid Res.*, 1989, **28**, 1–33.

37 M. J. Yang Nicole J. and Hinner, *Site-Specific Protein Labeling: Methods and Protocols*; Springer, New York 2015.

38 Y. H. Choi, J. van Spronsen, Y. Dai, M. Verberne, F. Hollmann, I. W. C. E. Arends, G.-J. Witkamp and R. Verpoorte, *Plant Physiol.*, 2011, **156**, 1701–1705.

39 Y. Dai, J. van Spronsen, G. J. Witkamp, R. Verpoorte and Y. H. Choi, *Anal. Chim. Acta.*, 2013, **766**, 61–68.

40 O. Yamamuro, T. Matsuo, H. Suga, W. I. F. David, R. M. Ibberson and A. J. Leadbetter, *Physica B Condens. Matter*, 1995, **213–214**, 405–407.

41 D. G. Montague, I. P. Gibson and J. C. Dore, *Mol. Phys.*, 1981, **44**, 1355–1367.

42 D. C. Steytler, J. C. Dore and D. C. Montague, *J. Non-Cryst. Solids.*, 1985, **74**, 303–312.

43 X. Gong, A. Bandis, A. Tao, G. Meresi, Y. Wang, P. T. Inglefield, A. A. Jones and W. Y. Wen, *Polymer,* 2001, **42**, 6485–6492.

44 R. Li, C. D'Agostino, J. McGregor, M. D. Mantle, J. A. Zeitler and L. F. Gladden, *J. Phys. Chem. B*, 2014, **118**, 10156–10166.

45 J. Barthel, M. Kleebauer and R. Buchner, *J. Solution Chem.*, 1995, **24**, 1–17.

46 R. Buchner and J. Barthel, *Annu. Rep. Prog. Chem., Sect. C: Phys. Chem.*, 2001, **97**, 349–382.

47 I. N. Daniels, Z. Wang and B. B. Laird, *J. Phys. Chem. C*, 2017, **121**, 1025–1031.

48 P. A. Cazade, H. Tran, T. Bereau, A. K. Das, F. Kläsi, P. Hamm and M. Meuwly, *J. Chem. Phys.* 2015, **142**, 212415.

49 S. Woutersen, Y. Mu, G. Stock and P. Hamm, *Chem. Phys.*, 2001, **266**, 137–147.

50 M. Sajadi, A. L. Dobryakov, E. Garbin, N. P. Ernsting and S. A. Kovalenko, *Chem. Phys. Lett.*, 2010, **489**, 44–47.

51 S. Arzhantsev, N. Ito, M. Heitz and M. Maroncelli, *Chem. Phys. Lett.*, 2003, **381**, 278–286.

52 M. L. Horng, J. A. Gardecki and M. Maroncelli, *J. Phys. Chem. A.*, 1997, **101**, 1030–1047.

53 M. L. Horng, J. A. Gardecki, A. Papazyan and M. Maroncelli, *J. Phys. Chem.*, 1995, **99**, 17311–17337.

54 E. W. Castner, M. Maroncelli and G. R. Fleming, *J. Chem. Phys.*, 1998, **86**, 1090.

55 R. Jimenez, G. R. Fleming, P. V. Kumar and M. Maroncelli, *Nature*, 1994, **369**, 471–473.

56 D. K. Sasmal, S. Ghosh, A. K. Das and K. Bhattacharyya, *Langmuir*, 2013, **29**, 2289–2298.

57 B. Bagchi and A. Chandra, *Adv. Chem. Phys.* 1991, **80**, 1–126.

58 B. Bagchi, *Annu. Rev. Phys. Chem.*, 1989, **40**, 115–141.

59 B. Bagchi and R. Biswas, *Adv. Chem. Phys., Bd*, 1999, **109**, 207–433.

60 S. Pothoczki, L. Pusztai and I. Bakó, *J. Phys. Chem. B.*, 2019, **123**, 7599–7610.

61 A. V. Gubskaya and P. G. Kusalik, *J. Phys. Chem. A.*, 2004, **108**, 7151–7164.

62 Hynes, J. T. *Charge Transfer Reactions and Solvation Dynamics*; Springer, Dordrecht, 1994; 345–381.

63 G. Van Der Zwan and J. T. Hynes, *J. Chem. Phys.*, 1998, **78**, 4174.

64 J. T. Hynes, H. J. Kim, J. R. Mathis and J. J. i Timoneda, *J. Mol. Liq.*, 1993, **57**, 53–73.

65 G. van der Zwan and J. T. Hynes, *Chem. Phys.*, 1991, **152**, 169–183.

66 R. Biswas, A. Das and H. Shirota, *J. Chem. Phys.*, 2014, **141**, 134506.

67 N. Subba, E. Tarif, P. Sen and R. Biswas, *J. Phys. Chem. B.*, 2020, **124**, 1995–2005.

68 K. Mukherjee, S. Das, J. Rajbangshi, E. Tarif, A. Barman and R. Biswas, *J. Phys. Chem. B.*, 2021, **125**, 12552–12567.

69 S. Das, R. Biswas and B. Mukherjee, *J. Chem. Phys.*, 2016, **145**, 84504.

70 J. Mondal, D. Maji and R. Biswas, *J Chem Phys* 2024, **160**, 084506.

71 S. S. Hossain and A. Samanta, *J. Phys. Chem. B.*, 2017, **121**, 10556–10565.

72 M. Santra, D. Kunzru and D. Rabari, *Comput. Theor. Chem.*, 2022, **1217**, 113921.

73 A. Yadav and S. Pandey, *J. Chem. Eng. Data.*, 2014, **59**, 2221–2229.

74 G. Shen and B. Andrioletti, *Molecules* 2022, **27**, 4131.

75 R. B. Leron, D. S. H. Wong and M. H. Li, *Fluid Phase Equilib.*, 2012, **335**, 32–38.

76 D. Yang, M. Hou, H. Ning, J. Zhang, J. Ma, G. Yang and B. Han, *Green Chemistry*, 2013, **15**, 2261–2265.

77 K. Zagajski Kučan and M. Rogošić, *J. Chem. Technol. Biot.*, 2019, **94**, 1282–1293.

78 Y. Dai, J. van Spronsen, G. J. Witkamp, R. Verpoorte and Y. H. Choi, *Anal. Chim. Acta*, 2013, **766**, 61–68.

79 Y. Dai and K. H. Row, *Molecules*, 2019, **24**, 2300.

80 I. Zahrina, M. Nasikin, E. Krisanti and K. Mulia, *Food Chem.*, 2018, **240**, 490–495.

81 Y. H. Choi, J. van Spronsen, Y. Dai, M. Verberne, F. Hollmann, I. W. C. E. Arends, G.-J. Witkamp and R. Verpoorte, *Plant Physiol.*, 2011, **156**, 1701–1705.

82 E. Tarif, J. Mondal and R. Biswas, *J. Phys. Chem. B.*, 2019, **123**, 9378–9387.

83 E. Tarif, J. Mondal and R. Biswas, *J. Mol. Liq.*, 2020, **303**, 112451.

84 A. Baksi, J. Rajbangshi and R. Biswas, *Phys. Chem. Chem. Phys.*, 2021, **23**, 12191–12203.

85 Kremer, F.; Schönhals, A. *Broadband Dielectric Spectroscopy*; Springer: Berlin, 2003.

86 J. G. Kirkwood, *J. Chem. Phys.*, 1939, **7**, 911–919.

87 C Böttcher, C. J. F.; Belle, O. C. van; Bordewijk, P.; Rip, A. *Theory of Electric Polarization,* Elsevier: Netherlands, 1996, vol 2.

88 N. C. Maity, A. Baksi, K. Kumbhakar and R. Biswas, *J Photochem. Photobiol. A Chem*, 2023, **439**, 114600.

89 E. Thoms, P. Sippel, D. Reuter, M. Weiß, A. Loidl and S. Krohns, *Scientific Reports*, 2017, **7**, 1–9.

90 K. Mukherjee, A. Das, S. Choudhury, A. Barman and R. Biswas, *J. Phys. Chem. B.*, 2015, **119**, 8063–8071.

91 Bevington; R., P.; Robinson, D. K. *Data Reduction and Error Analysis for the Physical Sciences*, McGraw-Hill: New York, 1969.

92 D. Maji, S. Indra and R. Biswas, *J. Chem. Sci.* 2021, **133**, 104.

93 M. Neumann, *Mol. Phys.*, 1983, **50**, 841–858.

94 C. Schröder and O. Steinhauser, *J. Chem. Phys.* 2010, **132**, 244109

95 F. Reif, *Fundamentals of statistical and thermal physics*, Waveland Press, 2009.

96 R. K. Murarka and T. Head-Gordon, *J. Phys. Chem. B.*, 2008, **112**, 179–186.

97 S. Boresch, P. Höchtl and O. Steinhauser, *J. Phys. Chem. B.*, 2000, **104**, 8743–8752.

98 S. Boresch, M. Willensdorfer and O. Steinhauser, *J Chem Phys*, 2004, **120**, 3333–3347.

99 H. J. C. Berendsen, D. van der Spoel and R. van Drunen, *Comput. Phys. Commun.*, 1995, **91**, 43–56.

100 W. L. Jorgensen, D. S. Maxwell and J. Tirado-Rives, *J. Am. Chem. Soc.*, 1996, **118**, 11225–11236.

101 P. Mark and L. Nilsson, *J. Phys. Chem. A.*, 2001, **105**, 9954–9960.

102 W. L. Jorgensen and J. Tirado-Rives, *Proc. Natl. Acad. Sci.*, 2005, **102**, 6665–6670.

103 L. S. Dodda, J. Z. Vilseck, J. Tirado-Rives and W. L. Jorgensen, *J. Phys. Chem. B.*, 2017, **121**, 3864–3870.

104 L. S. Dodda, I. Cabeza de Vaca, J. Tirado-Rives and W. L. Jorgensen, *Nucleic Acids Res.*, 2017, **45**, W331–W336.

105 J. A. Lemkul, J. Huang, B. Roux and A. D. Mackerell, *Chem. Rev.*, 2016, **116**, 4983–5013.

106 X. He, B. Walker, V. H. Man, P. Ren and J. Wang, *Curr. Opin. Struct. Biol.*, 2022, **72**, 187–193.

107 B. Doherty and O. Acevedo, *J. Phys. Chem. B.*, 2018, **122**, 9982–9993.

108 S. V. Sambasivarao and O. Acevedo, *J. Chem. Theory Comput.*, 2009, **5**, 1038–1050.

109 C. E. Fang, Y. C. Tsai, C. Scheurer and C. C. Chiu, *Polymers*, 2021, **13**, 1131.

110 K. Cui, A. Yethiraj and J. R. Schmidt, *J. Phys. Chem. B.*, 2019, **123**, 9222–9229.

111 L. Martinez, R. Andrade, E. G. Birgin and J. M. Martínez, *J. Comput. Chem.*, 2009, **30**, 2157–2164.

112 U. Essmann, L. Perera, M. L. Berkowitz, T. Darden, H. Lee and L. G. Pedersen, *J. Chem. Phys.*, 1998, **103**, 8577.

113 G. Bussi, D. Donadio and M. Parrinello, *J. Chem. Phys.*, 2007, **126**, 9901.

114 H. J. C. Berendsen, J. P. M. Postma, W. F. Van Gunsteren, A. Dinola and J. R. Haak, *J. Chem. Phys.*, 1994, **81**, 3684.

115 R. Kubo, The Fluctuation-Dissipation Theorem*, Rep. Prog. Phys.*, 1966, **29**, 255.

116 J. P. Hansen and I. R. McDonald, *Theory of Simple Liquids*, Academic Press, Third Edition., 2006.

117 A. Luzar and D. Chandler, *Nature*, 1996, **379**, 55–57.

118 D. C. Rapaport, *Mol. Phys.*, 1983, **50**, 1151–1162.

119 A. Chandra, *Phys. Rev. Lett.*, 2000, **85**, 768.

120 M. P. Allen and D. J. Tildesley, *Computer Simulation of Liquids*, Oxford University Press, 2nd Edition., 2017.

121 W. Humphrey, A. Dalke and K. Schulten, *J. Mol. Graph*, 1996, **14**, 33–38.

122 M. Brehm and B. Kirchner, *J. Chem. Inf. Model.*, 2011, **51**, 2007–2023.

123 M. Brehm, M. Thomas, S. Gehrke and B. Kirchner, *J. Chem. Phys.*, 2020, **152**, 164105.

124 B. B. Owen, R. C. Miller, C. E. Milner and H. L. Cogan, *J. Phys. Chem.*, 1961, **65**, 2065–2070.

125 K. Mukherjee, S. Das, E. Tarif, A. Barman and R. Biswas, *J. Chem. Phys.*, 2018, **149**, 124501.

126 B. P. Jordan, R. J. Sheppard and S. Szwarnowski, *J. Phys. D Appl. Phys.*, 1978, **11**, 695.

127 O. F. Stafford, *J. Am. Chem. Soc.*, 1933, **55**, 3987–3988.

128 R. A. Wallace, *Inorg Chem*, 1972, **11**, 414–415.

129 D. Maji and R. Biswas, *J. Chem. Phys.*, 2023, **158**, 174503.

130 I. Płowaś-Korus and R. Buchner, *J. Mol. Liq.*, 2021, **340**, 116838.

131 I. Płowaś-Korus and R. Buchner, *Phys. Chem. Chem. Phys.*, 2019, **21**, 24061–24069.

132 E. Tarif, K. Mukherjee, A. Barman and R. Biswas, *J. Chem. Sci.*, 2019, **131**, 1–12.

133 V. Agieienko and R. Buchner, *Phys. Chem. Chem. Phys.*, 2020, **22**, 20466–20476.

134 H. Jin, G. A. Baker, S. Arzhantsev, J. Dong and M. Maroncelli, *J. Phys. Chem. B.*, 2007, **111**, 7291–7302.

135 Y. H. Zhao, M. H. Abraham and A. M. Zissimos, *J. Org. Chem.*, 2003, **68**, 7368–7373.

136 C. M. Hu and R. Zwanzig, *J. Chem. Phys.*, 1974, **60**, 4354–4357.

137 B. Bagchi, *Molecular Relaxation in Liquids.*, Oxford University Press, USA, New York, First Edition., 2012.

138 J. Yang, N. Cai, H. Zhai, J. Zhang, Y. Zhu and L. Zhang, *Scientific Reports*, 2016, **6**, 1–9.

139 S. Ohsawa, T. Tokushima and K. Okada, *J. Phys. Chem. B*, 2021, **125**, 1881–1887.

140 R. Biswas, N. Rohman, T. Pradhan and R. Buchner, *J. Phys. Chem. B.*, 2008, **112**, 9379–9388.

141 S. Mondal and B. Bagchi, *J. Chem. Phys.* 2021, **154**, 044501.

142 B. Bagchi, *Nonequilibrium Statistical Mechanics: An Introduction with Applications*, CRC Press, New York, 1st Edition., 2023.

143 P. Madden and D. Kivelson, *Adv. Chem. Phys.*, 1984, **56**, 467–566.

144 B. Guchhait, R. Biswas and P. K. Ghorai, *J. Phys. Chem. B.*, 2013, **117**, 3345–3361.

145 A. Baksi and R. Biswas, *ACS Omega*, 2022, **7**, 10970–10984.

Chapter 5

Interaction and Dynamics in an Aspirin-Based Therapeutic Deep Eutectic Solvent: Temperature-Dependent Time Resolved Fluorescence Measurements and Computer Simulations

5.1 Introduction

Deep eutectic solvents[1–5] (DESs) represent a breakthrough in solvent engineering, offering a wide-spectrum choices for a variety of applications, ranging from suitable reaction media required in targeted large scale synthesis to designing appropriate drug delivery systems in biomedicine.[6–8] DESs are unique blends of two or more compounds that, when combined at specific mole ratios, provide a stable liquid phase through a remarkable depression of freezing points of the mixture components. The formation of liquid phase is supported by the extensive interspecies H-bonds between the constituents and the entropic gain for being in liquid state. One of the key advantages of DESs lies in their minimum ecological footprint. Unlike traditional organic solvents, DESs offer environmentally friendly alternatives, aligning with sustainability goals. This aspect is particularly significant considering the growing emphasis on reducing the impact of chemical processes on environment. DESs have been utilized across multiple domains that include applications as (i) suitable media for complex chemical species dissolution[9] and targeted reaction facilitators,[10] (ii) environment-cleaner through CO_2 and SO_2 absorption,[11,12] (iii) liquid phase host for pharmaceuticals[13,14] and career in agrochemical fields,[15] (iv) appropriate media for preparations of cosmetics[16] and food flavouring,[17] (v) liquid support for developing energy materials[18] and biodiesel production,[19] and (vi) extraction media for bioactive substances[20].

Moreover, several DESs have qualified as vehicles for controlled drug release, referred to as therapeutic deep eutectic solvents (THEDES).[21–30] Their unique solvent properties make them excellent candidates for dissolving active pharmaceutical ingredients (APIs). Several physicochemical properties of THEDES allow significant adjustments in the solubility, permeation, and absorption of APIs, often several times greater than those achievable with water alone.[31] APIs can be integrated either as part of the eutectic mixture or dissolved within a pre-existing eutectic mixture, providing flexibility in formulation and delivery strategies for enhanced therapeutic efficacy.[32]

THEDES comprises a diverse array of APIs including lidocaine, arginine, ibuprofen, benzoic acid, capric acid, phenylacetic acid, with thymol, menthol, choline chloride, and lauric acid employed as excipients. Researchers have explored THEDES for its potential in pharmaceutical activities, facilitating drug delivery[21,29,33,34] and solubility.[35–37] Researchers have also explored antiseptic and antibacterial properties of a few THEDES.[38,39] In some cases THEDES have shown promise in treating tuberculosis and cancer.[34,40,41]

Here we report preparation of a THEDES composed of aspirin and menthol at a molar ratio of 1:4. Aspirin is a widely used nonsteroidal anti-inflammatory drug[42,43] and known for its pain-relieving, anti-inflammatory, and fever-reducing properties. However, its limited solubility in water reduces its bioavailability and therapeutic efficacy. Menthol, a natural cyclic monoterpene alcohol,[44] is used as another component for its cooling and analgesic properties, and its ability to increase the solubility of aspirin. A previous study[24] reported enhancement of dissolution of aspirin with different molar ratios of menthol. The study revealed that the formation of (Aspirin+Menthol) THEDES occurs at a molar ratio of 1:3, at 313 K which is different from our findings. In fact, at 1:3 molar ratio and T=313 K, we ended up with a mixture of solid aspirin and liquid menthol at room temperature.

We would like to mention here that the interaction and dynamics of this THEDES and other similar systems have not been investigated yet, although several applications have taken place. We have performed here such a study with the present system by carrying out temperature dependent steady state and time resolved fluorescence measurements and computer simulations of the solution H-bond structure. Excitation wavelength dependent fluorescence emission measurements employing hydrophobic and hydrophilic probes (C153 and C343 respectively) revealed presence of substantial spatial heterogeneity in the medium. Temperature dependent dynamic fluorescence anisotropy measurements reflected a significant decoupling between medium viscosity and rotational dynamics by exhibiting fractional viscosity dependence of the solute rotation times. This decoupling was subsequently interpreted as a signature of temporal (dynamic) heterogeneity of the medium.

5.2 Experimental Details

5.2.1. Sample Preparation

DL-Menthol (purity ≥99%, obtained from Sigma-Aldrich, with a melting point of 307-309 K), laser-grade coumarin 153 (C153) (Sigma-Aldrich), and coumarin 343 (C343) (Sigma-Aldrich) were used without further purification. Acetylsalicylic acid/aspirin (purity ≥99%, obtained from Sigma-Aldrich, with a melting point of 407-409 K) was vacuum-dried overnight at approximately 300 K before utilization. The required amounts of aspirin and menthol in a 1:4 molar ratio was taken in a screw capped glass container. They were gently heated to around 343 K with continuous stirring at approximately 500 rpm in a hot oil bath for about 4 hours. Once a colourless transparent liquid was obtained, the temperature was lowered to 303 K, and the obtained liquid was allowed to cool gradually to room temperature (around 303 K). The resulting DES remained in a liquid state until 288 K, as observed in the DSC thermogram. Notably, this temperature (288 K) is much lower than the individual melting points of the constituents. The concentration of the external probes (C153 or C343) in the DES was maintained at $\leq 10^{-5}$ M for all optical measurements. Chemical structures of C153, C343 and the chemicals are depicted in **Scheme 5.1**. Sample preparation and measurements were conducted in a tightly humidity-controlled environment maintaining a humidity level of ~35%. For optical measurements, the DES was transferred to a preheated quartz cuvette with a path length of 1 cm and inserted into a preheated sample chamber for thermal equilibration. Sufficient time was allowed before measurements were taken at each desired temperature, with an uncertainty of ±1 K.

5.2.2 Density and Viscosity Measurements

Temperature dependent densities and viscosity coefficients of this DES were measured using a temperature controlled automated density-cum-sound analyser (Anton Paar, DSA5000) and micro viscometer (LOVIS 2000 M/ME, Anton Paar), respectively.[45,46] These data are summarized in **Table 5.A.1** (Appendix 5.A).

5.2.3 Differential Scanning Calorimetric (DSC) Measurements

The glass transition temperature (T_g) of the prepared DES was determined using a differential scanning calorimeter (DSC, TA Instrument Q2000).[47] The calorimetric trace is shown in **Figure 5.A.1** (Appendix 5.A), and it is worth noting that all measurements were conducted well above the T_g of this particular (Aspirin+Menthol) DES. The T_g for this system was found to be ~223 K.

5.2.4 Steady State Measurements

Steady-state absorption and fluorescence emission data were collected using a UV–Visible spectrophotometer (UV-2600, Shimadzu) and a fluorimeter (Fluorolog, Jobin-Yvon, Horiba) connected with a Peltier-temperature controller. Before analysis, solvent blanks were subtracted from the probe spectra. The spectra were then appropriately transformed to the frequency domain for further analysis and frequency determination.[48,49]

5.2.5 Time-Resolved Fluorescent Measurements

Time-resolved fluorescence measurements were conducted using the time-correlated single photon counting technique utilizing LifeSpec-ps instrument from Edinburgh Instruments, U.K. The details for this instrument can be found elsewhere.[50,51] Excitation wavelength was 409 nm LED source. The instrument response function (IRF) of the source had a full width at half-maximum (FWHM) of approximately 85 ps. The dynamic fluorescence anisotropy, $r(t)$, was obtained from the collected intensity decays as follows:

$$r(t) = \frac{I_{\mathrm{para}}(t) - \mathrm{GI}_{\mathrm{perp}}(t)}{I_{\mathrm{para}}(t) + 2\mathrm{GI}_{\mathrm{perp}}(t)}. \qquad (5.1)$$

The details about the measurement techniques and the analysis protocol can be found the previous literatures.[47,52]

For the dynamic Stokes shift measurements, 14-16 intensity decays (magic angle) were collected at equally spaced wavelengths across the steady state emission spectrum of either C343 or C153 dissolved in (Aspirin+Menthol) DES. Subsequently, time-resolved emission spectra (TRES) were reconstructed following an established protocol.[53–55] The time dependent progress of solvation of the excited dipolar solute was then monitored via the normalized solvation response function,[56]

$$S(t) = \frac{\nu(0) - \nu(\infty)}{\nu(x) - \nu(\infty)} \qquad (5.2)$$

where $\nu(x)$ representing the fluorescence frequency at time 0, t and ∞, respectively.

The details about the time-resolved measurements have been described in Chapter 2

5.3 Force field and Computational Details

Gromacs 5.1.1 simulation package[57] was used to perform the molecular dynamics simulations. Chemical structures of aspirin and menthol is provided **Figure 5.A.2** (Appendix 5.A) along with the atomic levels used in the simulations. The simulation was conducted at 323 K. CGenFF software[58,59] was used to generate CHARMM36 force field parameters[60,61] for aspirin and menthol molecules used in this simulation. The form of the potential energy function used in CHARMM36 is as follows: [62]

$$V(r) = \sum_{bonds} K_b (b - b_0)^2 + \sum_{angles} K_\theta (\theta - \theta_0)^2 + \sum_{dihedrals} K_\chi (1 + \cos{(n\chi - \delta)}) + \sum_{Urey-Bradley} k_{UB} (S - S_0)^2 + \sum_{impropers} K_\phi (\phi - \phi_0)^2 + \sum_{nonbonded\ atom\ paris} \left(\varepsilon_{ij} \left[\left(\frac{R_{min,ij}}{r_{ij}} \right)^{12} - \left(\frac{R_{min,ij}}{r_{ij}} \right)^{6} \right] + \frac{q_i q_j}{\varepsilon_D r_{ij}} \right) \qquad (5.3)$$

To achieve the experimental DES with a 1:4 molar ratio of aspirin and menthol, 240 aspirin molecules were mixed with 960 menthol molecules. We employed PACKMOL[63] to construct the initial configuration, and the simulation was initiated within a relatively large cubic box with periodic boundary conditions maintained in all three dimensions. Following this setup, we employed the leapfrog algorithm[64] to integrate the equations of motion. The initially generated configuration underwent energy minimization using the steepest-descent algorithm implemented in the GROMACS package. After energy minimization, we conducted a 10 ns NVT equilibration at the desired temperature (323K), utilizing the V-rescale[65] temperature coupling with a time constant of 0.5 ps. Subsequently, the resulting system underwent NPT equilibration for 10 ns at the same temperature, employing the V-rescale thermostat[65] with a coupling constant of 0.5 ns and the Berendsen barostat[66] with a time constant of 2 ps. Following equilibration, a production run of 100 ns was carried out under the same conditions, with a time step of 2 fs, and trajectory data were saved at intervals of 200 fs. All analyses were conducted using in-house code, GROMACS[57] and TRAVIS[67,68] software. The atomic charges and Lennard-Jones parameters utilized in this simulation are tabulated in **Table 5.A.2** and **Table 5.A.3** (Appendix 5.A), respectively. The validation of the force field was performed by comparing the experimental and simulated densities, as shown in **Figure 5.A.3** (Appendix 5.A). The densities exhibited close agreement, staying within a 5% margin of each other.

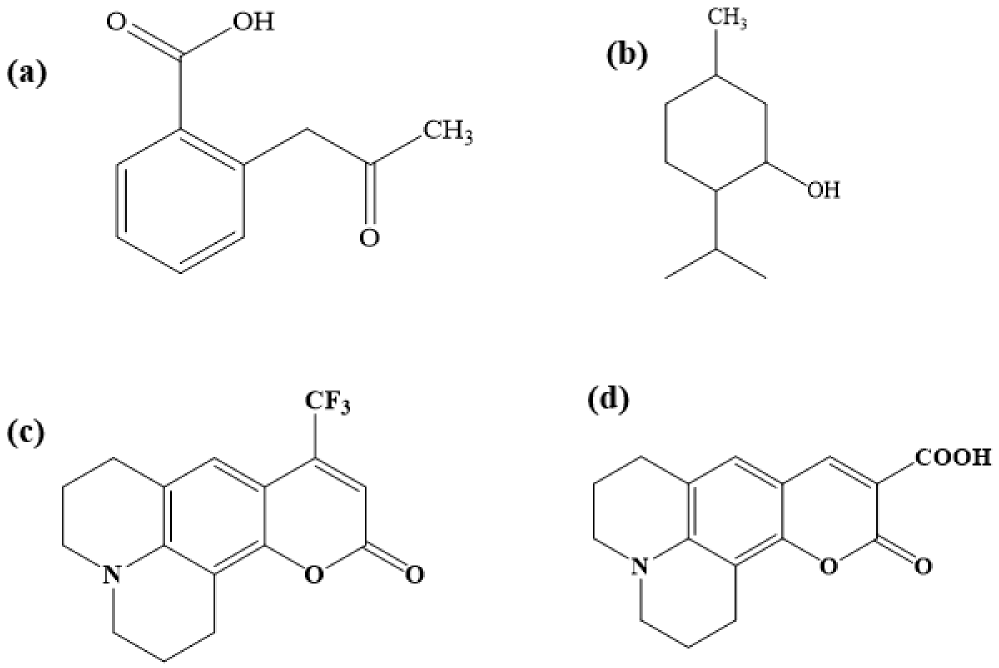

Scheme 5.1. Chemical structures of (a) aspirin, (b) menthol (c) coumarin 153 and (d) coumarin 343

5.4 Results and Discussion

5.4.1 Experiments

5.4.1.1 Steady State Absorption and Emission Spectra

The temperature-dependent steady-state absorption and emission spectra of C153 and C343 in (Aspirin+Menthol) DES are illustrated in **Figure 5.1**. Despite their different chemical nature, the spectral features of C153 and C343 show minimal sensitivity to temperature changes within the range considered (303 - 343K).[45,69]

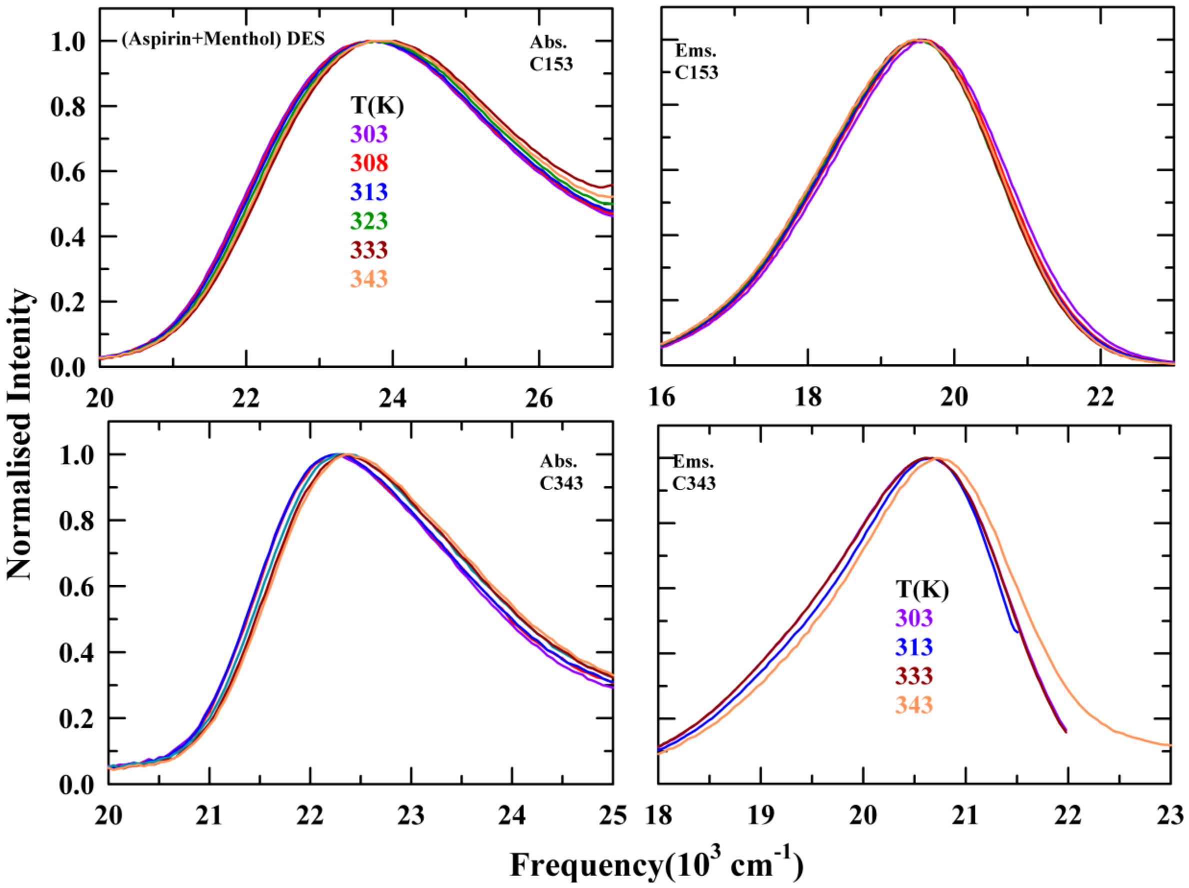

Figure 5.1. Temperature-dependent absorption (left) and emission (right) spectra of C153 and C343 in (Aspirin+Menthol) DES. Representations are colour defined.

It can be seen from the absorption spectra (*left panel*) that the absorption peak maximum of C153 ($\nu_{abs}^{C153} \sim 23808\ cm^{-1}$) is blue shifted compared to C343 ($\nu_{abs}^{C343} \sim 22300\ cm^{-1}$) while from the emission spectra (*right panel*) it is observed that the emission peak maximum of C153 ($\nu_{ems}^{C153} \sim 19549\ cm^{-1}$) is significantly red shifted compared to C343 ($\nu_{ems}^{C343} \sim 20630\ cm^{-1}$). This observation suggests that the two probes with different chemical nature reside probably in different micro-domains.

We compared the absorption and emission spectra of C153 in this medium with those of C153 in molecular solvents from available literature data[56] and we found that the spectral nature of C153 in chloroform closely resembles that observed in the present study. It is worth noting that the static dielectric constant (ε_s) of chloroform[56] is ~4.8 at 298 K, while aspirin and menthol possess ε_s values of approximately 6.83[70] at 274 K (solid) and 3.9[71] at 323 K (liquid), respectively. The close similarity in ε_s, which is a measure of system polarity, suggests that the solvent environment of the THEDES is similar to that of chloroform. Additionally, the relative Stokes shift of C153 (~700 cm^{-1}) in chloroform and the THEDES medium resides in a similar regime, supporting the above observation. Studies involving PFG NMR,[72] SAXS,[73] ultrafast fluorescence,[74] and molecular dynamics simulations[75] conducted on these DESs have indicated the existence of mesoscopic structures, revealing microscopic heterogeneity within the system.

The possible formation of micro-domains and hence the presence of spatial heterogeneity is investigated next by examining the excitation wavelength ($\lambda_{exc.}$) dependence of fluorescence emission of C153 and C343. The values of the $\lambda_{exc.}$ were chosen across the respective absorption spectra of the probes. The results from these measurements are provided in **Figure 5.2**. **Figure 5.2** (a) and (b) for these solute probes, where $\lambda_{exc.}$dependent emission peak frequencies, ν_{em}, spectral widths (full-width-at-half-maxima, Γ_{em}) and the total shift of the emission frequency, $\Delta\nu_{em}$, at different temperatures are shown. C153 in this DES exhibits a significant spectral shift (red shift ~ 800 cm^{-1}) at 303K, which decreases with temperature and becomes the lowest (~ 400 cm^{-1}) at 343K). This is a signature of spatial heterogeneity which softens upon increasing the solution temperature. Similar observation was made earlier[76] for trehalose based cryoprotectant systems. These emission energy shifts are accompanied by band narrowing (**Figure 5.2** (c)), with the extent of narrowing being smaller at higher temperature.

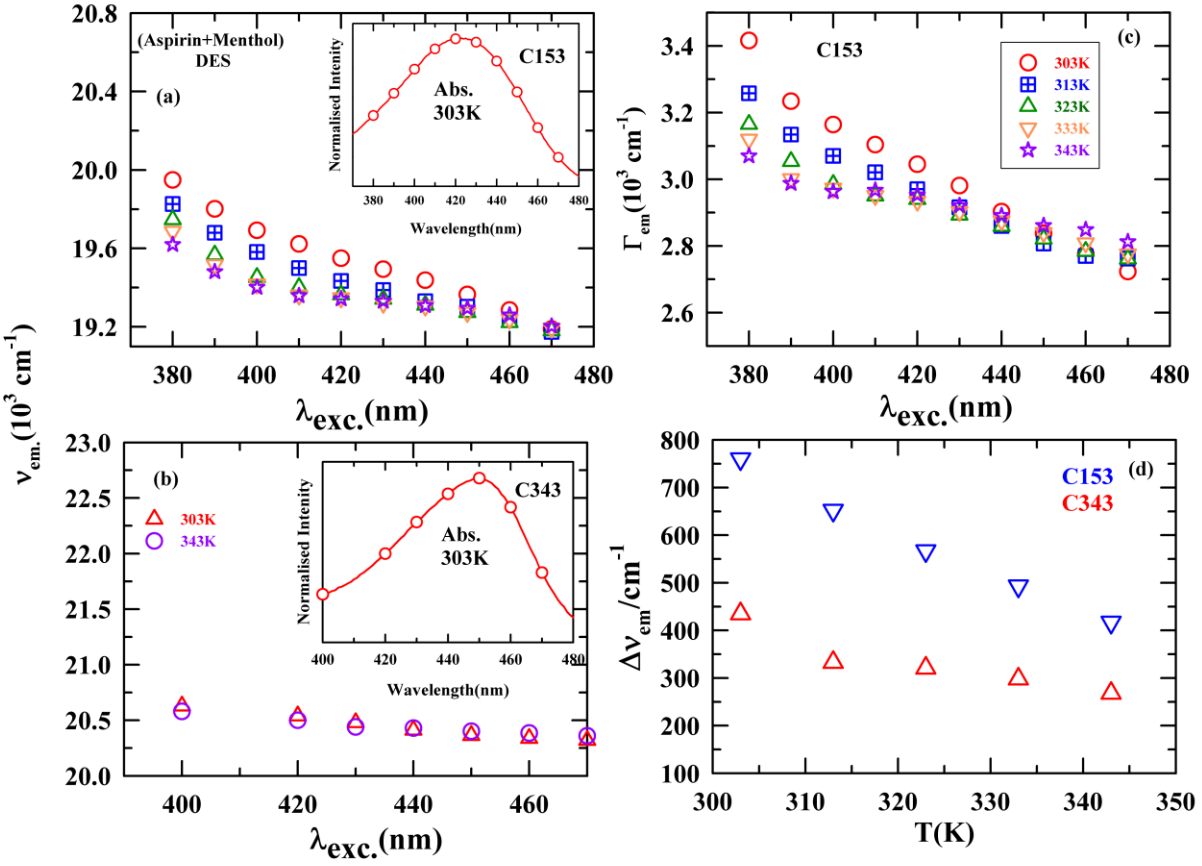

Figure 5.2. (a) & (b) Excitation wavelength ($\lambda_{exc.}$) dependence of fluorescence emission frequency ν_{em}, of C153 and C343 in (Aspirin+Menthol) DES at different temperatures. Inset shows the normalised absorptions with the photo excitation wavelengths indicated with circles in the spectra. (c) $\lambda_{exc.}$ of emission spectral width (Γ_{em}) of C153 at various temperatures. (d) Temperature dependent total spectral shift ($\Delta\nu_{em}$) in ν_{em} for (Aspirin+Menthol) DES. Note $\Delta\nu_{em}(T) = \nu_{em}(T, \lambda_{exc.,b}) - \nu_{em}(T, \lambda_{exc.,r})$, where $\lambda_{exc.,b/r}$ are the shortest (bluest) and longest (most red) wavelengths used for solute excitation.

is consistent with the general observation of polarity-induced red shift in emission peak frequency with concomitant spectral narrowing observed in common small molecular solvents.[56] In contrast to what was found for C153, C343 exhibits much weaker spectral shift with $\lambda_{exc.}$ and temperature dependence.

The above contrasting behaviour of spectral properties of C153 and C343 may be attributed to the preferential locations of these solutes owing to their different chemical natures. Specifically, C153 is hydrophobic, while C343 is hydrophilic. In our system containing aspirin and menthol, both of which have substantial hydrophobic core regions, C153 tends to interact with these hydrophobic segments and prefers residing in such environments. Detection of heterogeneity in a system critically depends on the interconversion rate among different solvation domains and the average lifetime of the dissolved probe.[77,78] Consequently, rapid fluctuation among the solvation domains could not be probed with a longer lifetime probe molecule. Under such a condition the system may appear as homogeneous. The extent of emission shift, $\Delta\nu_{em}$, of C153 in (Aspirin+Menthol) DES, (**Figure 5.2 (d)**), decreases gradually with temperature which can be attributed to temperature induced faster inter-conversions among different solvent domains/configurations around the solute molecules.[76,79] The micro domains surrounding C343 molecules, on the other hand, were probably much faster fluctuations and hence registering weaker inhomogeneity.

5.4.1.2 Fluorescence Lifetime Measurements

The fluorescence emission intensity decays (magic angle) of C153 and C343 in this DES were measured at different temperatures. Representative emission decays for both solutes are shown in **Figure 5.A.4** (Appendix 5.A). For both the solutes, the decays were best described by a sum of three exponential functions of time. Required fit parameters are provided in **Table 5.A.4** (Appendix 5.A). The average lifetime, $\langle\tau_{fl}\rangle$ was determined by using the relation, $\langle\tau_{fl}\rangle = \frac{\sum_i a_i\tau_i}{\sum_i a_i}$, where a_i and τ_i are the amplitude and time constant of the i-th decay, respectively. Data in **Table 5.A.4** indicate that the three decay components are characterized by well-separated time constants, the fastest being in 100–300 ps range and the slowest in 3–5 ns range. The other time constant covers 1–1.5 ns range. Interestingly, while the amplitude associated with τ_1 increases and that of τ_2 decreases with temperature for C153, the amplitudes remain unaffected by temperature variations for C343. Despite the intrinsic lifetimes of C153[56] and C343[45] in common solvents being ~5 ns, our measurements in this system reveal $\langle\tau_{fl}\rangle$ ~1 for the both solutes. This observation strongly suggests a notable contribution from non-radiative pathways to the overall emission decay. This can be explained by the following equation[80] ($\langle\tau_{fl}\rangle = 1/(K_r + K_{nr})$. Notably, a recent study[81] employing C153 in a (thymol+menthol) DES reported a similar value of $\langle\tau_{fl}\rangle$.

5.4.1.3 Solute Rotation: Decoupling from Medium Friction

The rotational dynamics of C153 and C343 within the (Aspirin+Menthol) DES were investigated in the temperature range 303K - 343K. **Figure 5.3** presents representative rotational anisotropy decays, $r(t)$, for C153 (upper panel) and C343 (lower panel) in this DES. **Figure 5.A.5** (Appendix 5.A) shows representative parallel and perpendicular fluorescence intensity decays for these solutes.

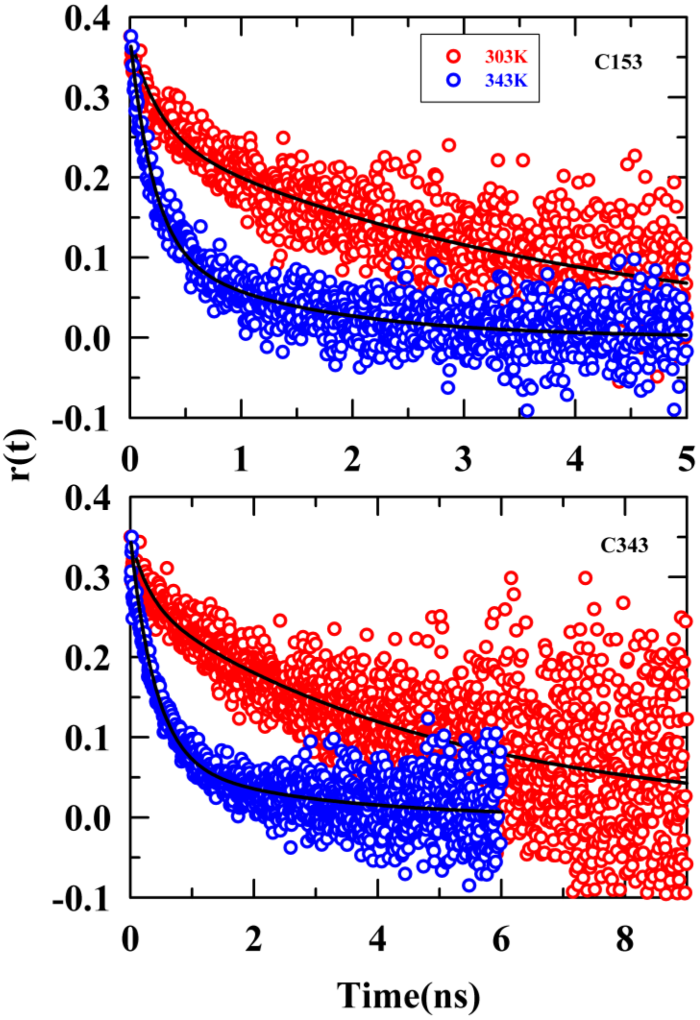

Figure 5.3. Time-resolved fluorescence anisotropy decays of C153 (upper panel) and C343 (lower panel) in (Aspirin+Menthol) DES at two representative temperatures 303 and 343K. Lines fitted to the data points represent bi-exponential fits. Representations are colour-coded.

The rotational anisotropy decays, $r(t)$, were fitted with bi-exponential fit functions, with the resulting parameters summarized in **Table 5.1**. For C153, the decay exhibits a bimodal pattern with a faster time constant of approximately 200 ps and another slower time constant decreasing from 4 ns to 1 ns within the temperature range of 303K to 343K. The amplitude associated with the faster component increases with temperature, while the amplitude linked to the longer time constant gradually decreases. Conversely, for C343, the faster sub-nanosecond time constant (~1ns – 0.4 ns) decreases with temperature, yet its associated amplitude gradually increases. Simultaneously, the slower time constant decreases from ~6 ns to 2.5 ns with temperature, accompanied by a decrement in its amplitude. Notice that the average rotation time, $\langle\tau_r\rangle$, of C153 in this DES is ~1.7 times faster than $\langle\tau_r\rangle$ of C343 throughout the experimental temperature range. This observation again confirms the preferential locations of these two solutes within the DES, thereby experiencing the local friction differently.

Table 5.1. The bi-exponential fit parameters for the temperature-dependent $(r(t))$ of C153 and C343 in the (Aspirin+Menthol) DES.

C153 in (Aspirin+Menthol) DES					
T (K)	a_1 (%)	τ_1 (ps)	a_2 (%)	τ_2 (ps)	$\langle\tau_r\rangle$ (ps)
303	32	256	68	3757	2653
313	37	128	63	2751	1793
323	46	256	54	1956	1171
333	57	237	43	1582	818
343	70	211	30	1396	568
C343 in (Aspirin+Menthol) DES					
303	29	1073	71	5869	4460
313	33	748	67	4112	3002
323	53	827	47	3243	1969
333	63	439	37	2964	1364
343	79	399	21	2533	853

To investigate the coupling between solute rotation and solvent viscosity, we plotted $\langle\tau_r\rangle$ as a function of temperature-reduced viscosity, η/T, in a log-log fashion in **Figure 5.4**, with data for C153 displayed in the upper panel and for C343 in the lower panel. The observed fractional viscosity dependence of the solute rotation times, represented by $\langle\tau_r\rangle \propto \left(\frac{\eta}{T}\right)^p$ with $p \approx 0.5$ for both C153 and C343, indicates significant temporal heterogeneity in the rotational relaxation rates within this therapeutic deep eutectic solvent. Such a strong fractional viscosity dependence has already been observed for solute rotation in ionic acetamide DESs,[51,52] and other DESs.[45,69] Notice that some recent studies of hydrophobic DESs composed of (menthol+lauric acid)[82] and (menthol+thymol)[81] reported mild temporal heterogeneity ($p \approx 0.8$) using C153 as fluorescent probe. Interestingly, despite their distinct chemical properties and different preferential locations in this DES (indicated by excitation wavelength dependence study), both C153 and C343 exhibit a similar decoupling from medium viscosity during rotational diffusion within this DES. Note that while C343 demonstrates weak spatial inhomogeneity within the medium, it displays a much stronger temporal heterogeneity. This observation of weak spatial inhomogeneity accompanied by relatively stronger temporal heterogeneity has previously been observed in naturally abundant deep eutectic solvents.[45]

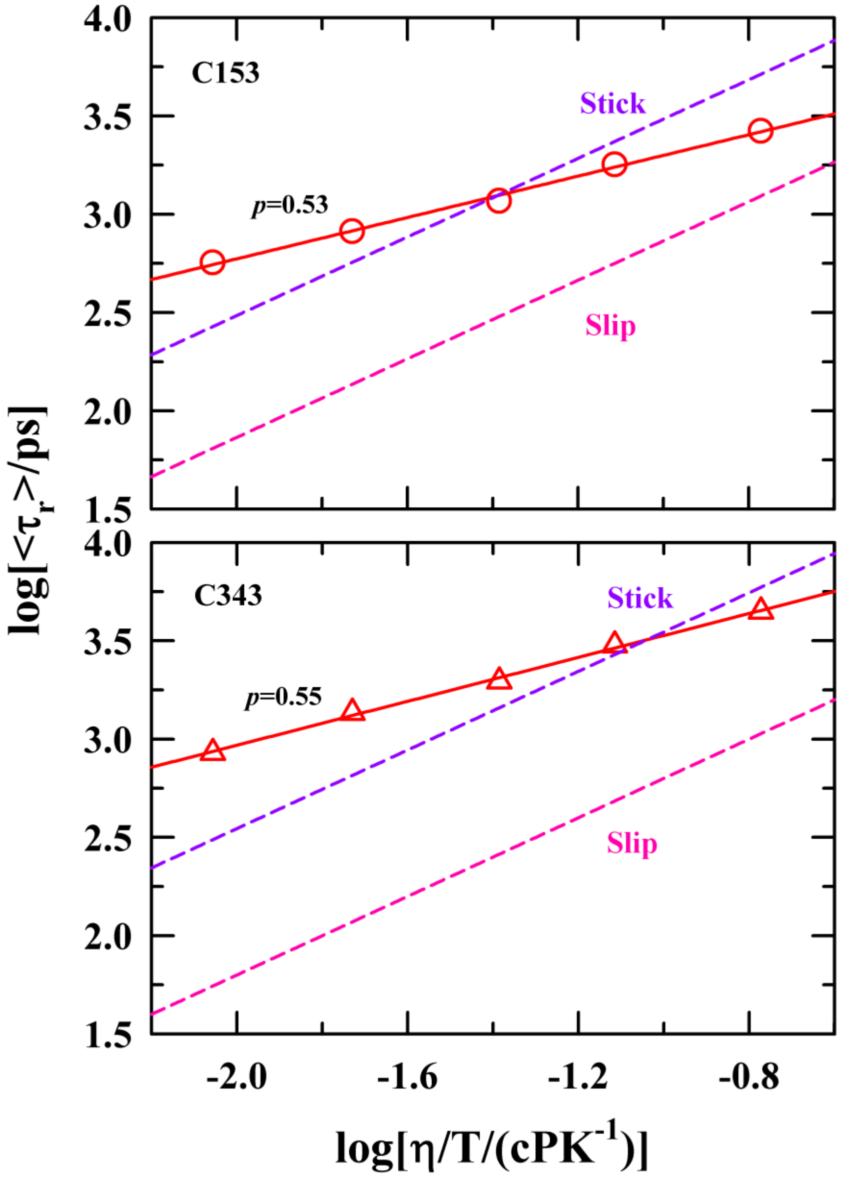

Figure 5.4. The viscosity coupling of average rotation times ($\langle\tau_r\rangle$) for molecules C153 and C343 within the (Aspirin+Menthol) DES system. The temperature-dependent average rotational times are depicted as a function of temperature-reduced viscosity $\left({}^{\eta}/_{T}\right)$ in a log-log format. The lines fitted to the data correspond to the expression: $log\langle\tau_r\rangle = A + plog\left({}^{\eta}/_{T}\right)$. Dashed lines denote the hydrodynamic (Stokes-Einstein-Debye) predictions.

In addition, **Figure 5.4** includes the hydrodynamic prediction for these two solutes (dashed lines), C153 and C343, calculated by using both the stick and the slip boundary conditions in the Stokes-Einstein-Debye (SED) formula,[83,84] $\tau_r = \frac{V\eta fC}{k_BT}$, where k_BT is the Boltzmann constant times temperature. The parameters utilized to calculate the slip rotation times are volumes $V^{C153} = 246$ Å^3 and $V^{C343} = 243$ Å^3, shape factors $f^{C153} = 1.71$ and $f^{C343} = 1.99$, $C_{slip}^{C153} = 0.24$[53] and $C_{slip}^{C343} = 0.18$.[85] For the stick boundary condition, $C_{stick} = 1$. From **Figure 5.4** it is clear that at lower temperatures the measured $\langle\tau_r\rangle$ falls between the slip and stick boundary predictions, and with increasing temperature it moves to super stick region.

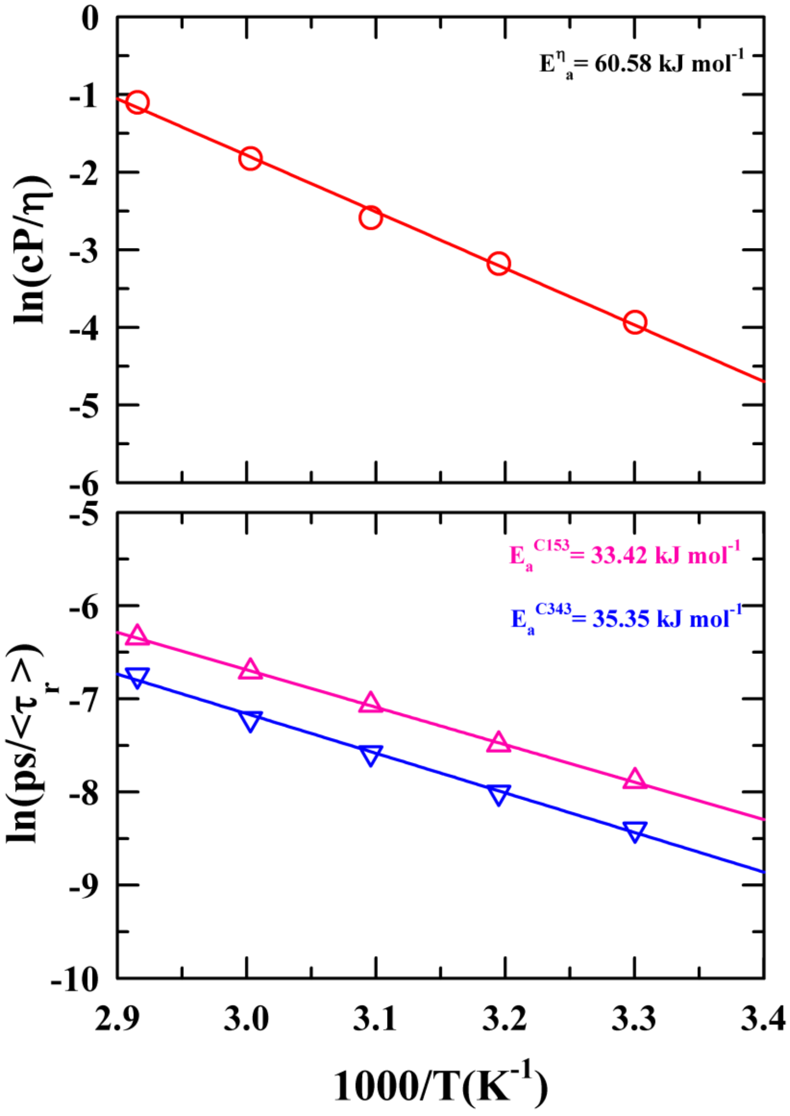

Figure 5.5. Arrhenius plot illustrating the temperature dependence of viscosity coefficients (η) for the (Aspirin+Menthol) DES, alongside the average rotation times ($\langle\tau_r\rangle$) of two different solutes, C153 and C343 dissolved within it. Solid lines depict fitted curves for each dataset, showcasing the different activation energies observed for η and ($\langle\tau_r\rangle$). Each representation is color-coded for clarity.

Further exploration into the relationship between medium friction and rotational dynamics is conducted by comparing the activation energy (E_a) associated with solute (C153/C343) rotation and the viscosity of the medium, as depicted in **Figure 5.5**. The upper panel of Figure 5 displays the activation energy associated with viscosity (E_a^{η}), which is approximately 60 kJmol^{-1}. In contrast, the activation energy estimated from solute (C153/C343) rotation (shown in the lower panel of **Figure 5.5**) is ~33-35 kJmol^{-1}, a value nearly half of the viscosity activation energy, E_a^{η}. This significant difference in estimated activation energies indicates that solute rotation is not entirely governed by the macroscopic medium viscosity, leading to a substantial degree of viscosity decoupling within this heterogeneous medium. Similar instances of viscosity decoupling could be found in ionic DES[47,69] and ionic liquid[86] media.

5.4.1.4 Solvation Dynamics

The characteristic pattern observed in fluorescence transients, involving decays only at shorter wavelengths (blue), and rise and decay at longer wavelengths (red), indicate presence of dynamic Stokes shift in this system. **Figure 5.A.6** (Appendix 5.A) presented the fluorescence transients of C153 in (Aspirin+Menthol) DES, collected at both blue and red emission wavelengths (480 nm and 620 nm, respectively), highlights this aspect. It is worth noting that similar measurements employing C343 did not reveal any Stokes shift dynamics. This, however, does not mean that excited C343 does not undergo the time-dependent solvation process in this medium. It does undergo but the solvation process is too fast to be detected by the temporal resolution (~85 ps) employed in the current measurements. This is because C343, due to its hydrophilic nature, prefers to reside in a micro-region created by the aspirin -OH, -COOH and menthol -OH groups and as a result, the solvation process of excited C343 is mostly carried out by the sub-picosecond collective H-bond excitations (solvent intermolecular vibrations and H-bond librations).[87,88] Following an established protocol, we constructed the time-resolved emission shift (TRES) of C153 in this DES at four different temperatures from 303 to 343 K. A representative TRES at 343 K has been displayed in the upper panel of **Figure 5.6**, along with the steady-state emission spectrum. The figure shows a shift of emission spectra towards lower energy with time indicating the presence of dynamic stokes shift in the medium. The blue shift observed in the steady-state spectrum compared to the TRES at $t = \infty$, here 5ns, suggests an incomplete equilibration of solvent environments surrounding the excited C153 in (Aspirin+Menthol) DES during steady-state fluorescence emission. This observation is also supported by the presence of substantial amount of $\lambda_{exc.}$ induced emission shift already shown in **Figure 5.2**.

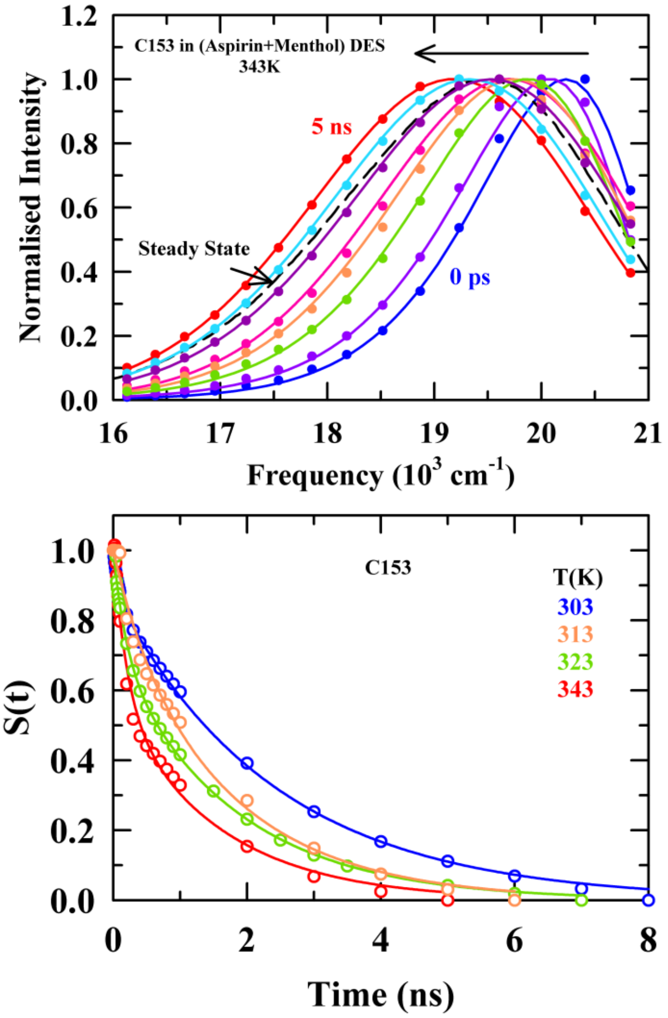

Figure 5.6. *Upper panel:* TRES at various time intervals is assembled from the intensity decays observed for C153 dissolved in the (Aspirin+Menthol) DES, along with the associated steady-state emission spectrum. The lower panel displays the solvation response function, S(t), of C153 in the (Aspirin+Menthol) DES at four different temperatures. Solid lines are bi-exponential fits through the data points.

The lower panel of **Figure 5.6** illustrates the temperature dependent decay of the measured solvation response function, $S(t)$, in presence of C153. At all the temperatures, $S(t)$ was fitted with bi-exponential functions and the corresponding fit parameters are tabulated in **Table 5.2**. The fit parameters in **Table 5.2** reveals that the measured solvation response predominantly consists of a faster sub-nanosecond component (around 100-400 ps), followed by a slower long-term decay occurring over nanosecond timescales (approximately 1-2 ns). The average solvation time, $\langle\tau_s\rangle$, decreases with increasing temperature of the medium is the reflection of viscosity effect. **Table 5.2** also presents the measured temperature dependent dynamic Stokes shift ($\Delta\nu^{obs.}$ ~1350 – 1050 cm^{-1}) for C153 in this system.

Table 5.2. Bi-exponential fit parameters of temperature-dependent solvation response functions, S(t), obtained for C153 in (Aspirin+Menthol) DES.

T/K	α_1	τ_1 (ps)	α_2	τ_2 (ps)	$\langle\tau_s\rangle$ (ps)	$\Delta\nu^{obs.}(cm^{-1})$
303	0.12	80	0.88	2407	2128	1354
313	0.17	481	0.83	1724	1350	1240
323	0.29	191	0.71	1776	1316	1199
343	0.42	206	0.58	1542	981	1049

We used Fee-Maroncelli[89] method to estimate the dynamic Stokes shift for C153 in this media ($\Delta\nu^{est.}(cm^{-1}) = 1182$) utilizing hexane as a non-polar solvent at 343K. We found that the estimated shift similar to observed dynamic Stokes shift of the medium with missing negligibly (~10%) of the estimated Stokes shift. Note that, the estimation of missing percentage may have inaccuracy which comes from the estimation dynamic stokes shift where non-polar reference (hexane) has a density of ~0.7 g/cc much lower than the current THEDES (~1.1 g/cc).

In **Figure 5.A.7** (Appendix 5.A), the temporal changes in FWHM are depicted across four distinct temperatures. The phenomenon of an initial rise in $\Gamma(t)$, and then levelling off with time to a stable plateau have been witnessed earlier for a variety of complex systems, ranging from neat solvents to ionic liquids and DESs[76,79]. Note also that $\Gamma(t)$ at $\tau = \infty$ is similar to Γ_{em} obtained from steady state measurements.

Now we shall talk about the possible origin of the solvation timescales observed for C153 in this DES. The slower nanosecond timescale (τ_1) bears the maximum amplitude (~70-80%) throughout the temperature range. This long time constant may involve the molecular diffusion and diffusion coupled molecular rotation in the system. The molecular rotation of aspirin and menthol molecules in this DES may provide this long timescale, although intermolecular and interspecies H-bonding may not allow free whole-body rotations. To examine the role of molecular rotation in solvation dynamics, we calculated the single molecular rotation time using the Stokes Einstein Debye (SED) relation with stick boundary condition, $\tau_r = \frac{3V\eta}{k_b T}$. and the values are tabulated in **Table 5.A.5** (Appendix 5.A). The calculated single molecular rotational timescales are comparable to the longer timescale observed in experiment and thus may contribute to the longer nanosecond timescale found in solvation dynamics. The faster sub nanosecond timescale (τ_2) may be originated from the structural H-bond relaxation formed between menthol -OH with aspirin -OH, -COOH sites. For a more quantitative understanding of the above solvation timescales, one should carry out simulations of the collective single particle reorientational relaxations and structural H-bond fluctuation dynamics.[90,91]

5.4.2 Simulations

5.4.2.1 Real-space Correlation and Atom-specific Interactions

We analyzed the real-space correlation between the centers of mass of aspirin and menthol molecules using radial distribution functions (RDF), $g(r)$, as shown in **Figure 5.7(a)**. The point at which the correlation begins to build varies with the size of the interacting molecules, suggesting that

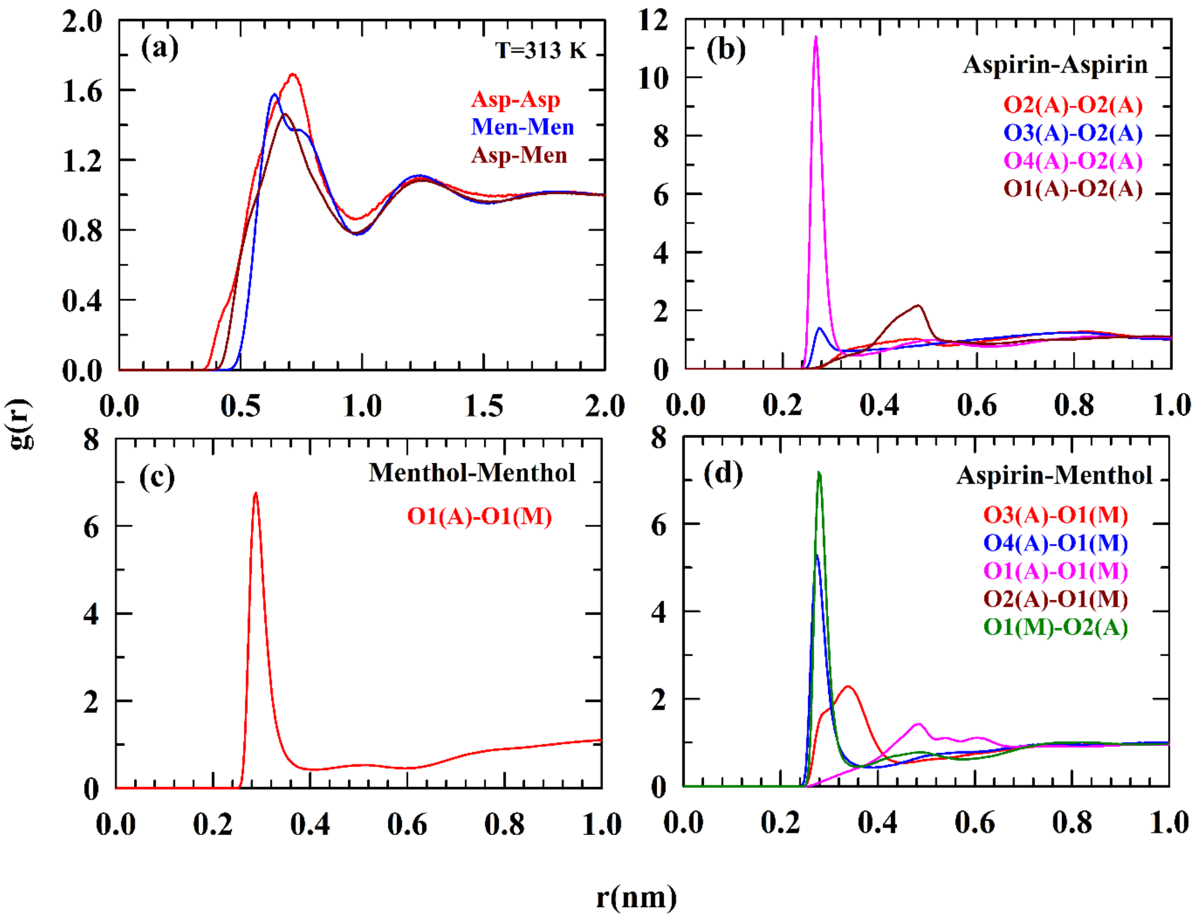

Figure 5.7. (a) COM-COM (COM*: centre of mass*) RDFs for Aspirin-Aspirin, Menthol-Menthol and Aspirin-Menthol. (b) & (c) Intraspecies intermolecular RDFs between different atoms of aspirin and menthol. (d) Interspecies intermolecular RDFs of aspirin and menthol atoms. Different atom pairs are colour coded in the respective plots.

menthol is slightly larger than aspirin. Similar peak heights and positions for both intra- and inter-species interactions indicate that these interactions occur at comparable extents and length scales. While these RDFs give an idea about the overall arrangement of molecules around each other, atom-specific RDFs can explore deeper. As H-bonds are a governing factor regarding the stability of deep eutectic solvents, we choose to analyze the interactions that might lead to the formation of H-bonds. **Figure 5.7(d)** represents interspecies RDFs between different oxygen atoms of aspirin and menthol. We have found that out of four pairs only O1(men)-O2(asp) and O1(men)-O4(asp) interactions are sharp and appear at a shorter distance, depicting the possibility of formation of H-bonds between them. As shown in **Figure 5.7(c)**, the O4(asp)-O2(asp) RDFs stand out significantly compared to others reflecting the propensity of forming

H-bonds. **Figure 5.7(b)** indicates menthol molecules can form H-bonds between themselves via O1 atoms.

5.4.2.2 H-bond Network

In the previous section, we have thoroghly discussed about the probability of formation of both intra- and inter-species H-bonds. Based upon geometric condition the formation of H-bond is dictated by both distance and anguar conditions.[92–94] Therefore, we have calculated radial angular distribution functions (RADFs) to explore the impact of both distance and angle. **Figure 5.8** shows RADFs for acceptor-donor-hydrogen atom triplets for various inter- and intra-species interactions. From this figure it is evident that there are four atom triplets which can satisfy the condition for forming H-bonds: (i) O1(men)---O1(men)—H20(men), (ii) O3(asp)---O2(asp)—H4(asp), (iii) O1(men)---O2(asp)—H4(asp) and (iv) O4(asp)---O1(men)—H20(men).

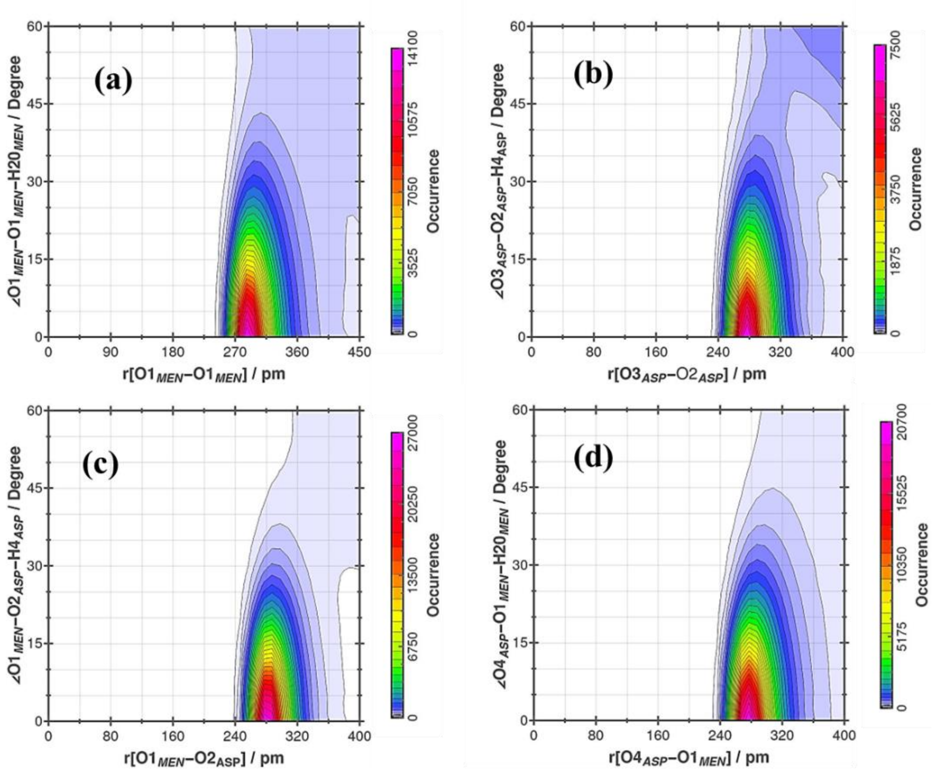

Figure 5.8. Radial angular distribution functions (RADFs) related to H-bonding interactions in (Aspirin+Menthol) DES. The plots refers to the following H-bond pairs(i) O1(men)---O1(men)—H20(men), (ii) O3(asp)---O2(asp)—H4(asp), (iii) O1(men)---O2(asp)—H4(asp) and (iv) O4(asp)---O1(men)—H20(men).

After identifying the H-bond pairs, we will now examine the degree to which these inter- and intra-species H-bonds form, impacting the stability of deep eutectic solvents (DESs). Average number of H-bonds per molecules in this DES has been shown in **Figure 5.9**. The number of different type of H-bonds are enumerated in **Table 5.A.5** (Appendix 5.A) to fully realise the ability of the participating molecules as donor as well as acceptor. From the following table it is clear that one aspirin molecule form H-bonds via two acceptor (O3 and O4) and one donor (O2) sites.

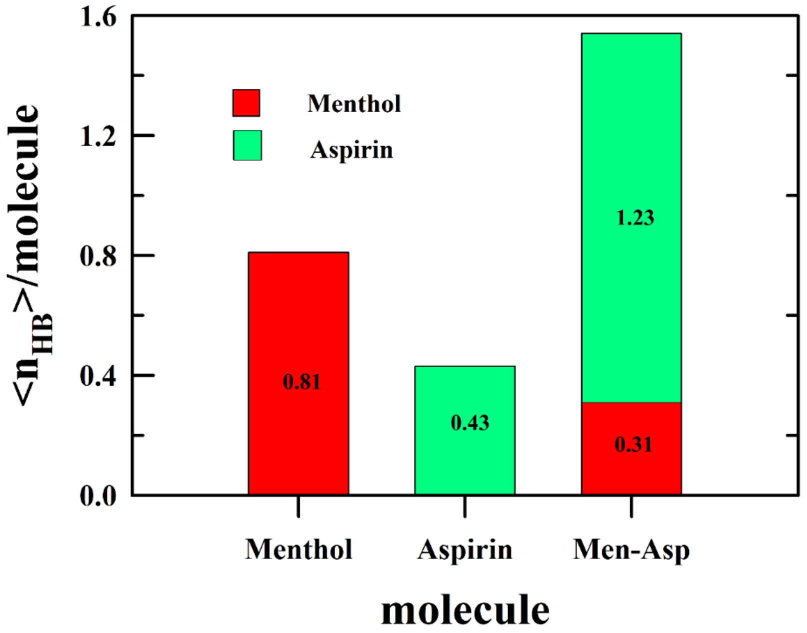

Figure 5.9. Average number of H-bonds per molecules in (Aspirin+Menthol) DES. The representations are colour coded.

Interestingly, aspirin forms only 0.43 H-bonds with itself while showing greater affinity towards menthol. Aspirin forms 0.67 and 0.56 number of H-bonds with menthol as donor and acceptor, respectively. This higher propensity of H-bond formation with menthol can be explained in terms of abundance of menthol molecules in the system. There are four menthol molecules present in the system for one aspirin. Hence, aspirin molecules find menthol molecules around to readily form H-bonds. Menthol molecules, on the other hand, form H-bonds intermolecularly with themselves to much greater extent compared to aspirin. On an average, an aspirin molecule forms 1.66 H-bonds, whereas a menthol molecule forms 1.12.

Therefore, it can be inferred that aspirin molecules are forming ~75% H-bonds with menthol and thus may stabilize the deep eutectic solvent.

5.5 Conclusion

In conclusion, we have carried out a combined experimental and simulation study to investigate the interaction and dynamics of an active pharmaceutical ingredient, aspirin containing DES. The structure aspect has been understood by calculating the atom-atom RDFs and RADFs between the aspirin and menthol molecules. The calculation of H-bonds per molecule indicates that aspirin forms fewer H-bonds with itself and demonstrates a stronger attraction towards menthol for H-bonding. Consequently, the extensive formation of intermolecular H-bonds may contribute for stabilizing the THEDES. Steady state fluorescence measurements with C153 detects strong spatial heterogeneity of the medium while C343 does not. Dynamic fluorescence anisotropy measurements, employing C153 and C343 exhibited bi-exponential dynamics of the solute rotation and demonstrated Arrhenius-type temperature dependence for average solute rotation times ($(\langle\tau_r\rangle)$). The activation energies for $\langle\tau_r\rangle$ were found to half ($\sim 33\ kJ\ mol^{-1}$) of those estimated from temperature-dependent viscosity measurements ($\sim 60\ kJ\ mol^{-1}$). Further decoupling from hydrodynamics is evidenced by the notable fractional viscosity dependence of $\langle\tau_r\rangle$, with p values nearly 0.5. This indicates significant temporal heterogeneity in the relaxation dynamics. Dynamic fluorescence Stokes shift measurements, with a temporal resolution of approximately ~85 ps, revealed dynamic shifts of around 1200 cm^{-1}. The solvation correlation function exhibited bi-exponential behaviour, with time constants ~0.2 ns and ~2 ns.

Appendix 5.A

Table 5.A.1. Temperature dependent density and viscosity of (Aspirin+Menthol) DES

T(K)	Density (g/cm^3)	Viscosity (cP)
303	1.01241	51.15
313	1.00532	24.05
323	0.99451	13.30
333	0.98615	6.21
343	0.97753	3.01

Uncertainty in density measurements: ±5%; and uncertainty in viscosity measurements: ±10%

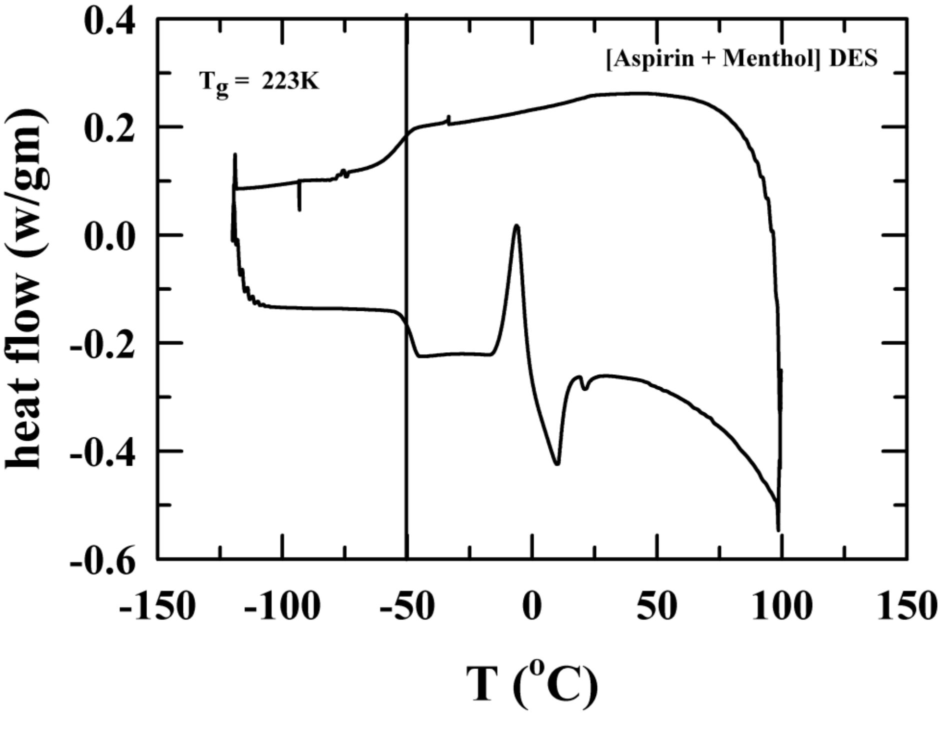

Figure 5.A.1. Differential scanning calorimetric (DSC) trace for (Aspirin+Menthol) DES. The glass transition temperature (T_g) is indicated.

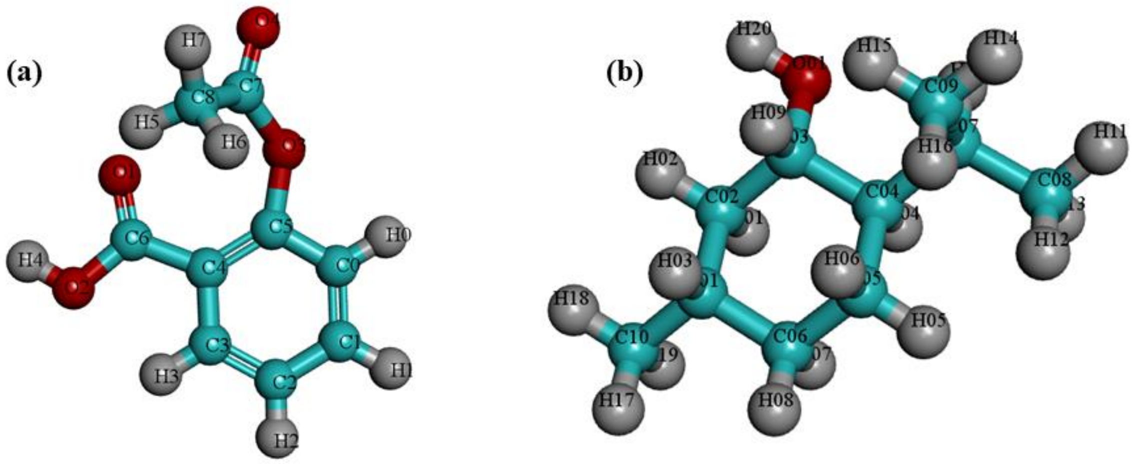

Figure 5.A.2. Chemical structures of (a) Aspirin, and (b) Menthol with atom levelling used in the simulation.

Table 5.A.2. Partial charges and Lennard-Jones (LJ) parameter for aspirin molecule

Atom types	Charge, e	$\sigma(nm)$	$\varepsilon\ (kJmol^{-1})$
C0	-0.1160	0.3550	0.2929
C1	-0.1150	0.3550	0.2929
C2	-0.1160	0.3550	0.2929
C3	-0.1200	0.3550	0.2929
C4	0.0770	0.3550	0.2929
C5	0.2100	0.3550	0.2929
H0	0.1150	0.2420	0.1255
H1	0.1150	0.2420	0.1255
H2	0.1150	0.2420	0.1255
H3	0.1150	0.2420	0.1255
C6	0.4500	0.3029	0.4100
O1	-0.4280	0.3029	0.5021
O2	-0.5160	0.3145	0.8037
H4	0.4300	0.0400	0.1925
O3	-0.4410	0.2940	0.4184
C7	0.8970	0.3029	0.4100
O4	-0.6310	0.3029	0.5021

C8	-0.3110	0.3653	0.3264
H5	0.0900	0.2388	0.1004
H6	0.0900	0.2388	0.1004
H7	0.0900	0.2388	0.1004

Table 5.A.3. Partial charges and Lennard-Jones (LJ) parameter for menthol molecule

Atom types	**Charge, e**	$\boldsymbol{\sigma(nm)}$	$\boldsymbol{\varepsilon\ (kJmol^{-1})}$
C01	-0.1810	0.3581	0.2343
C02	-0.0990	0.3564	0.1339
C03	0.1430	0.3564	0.1339
C04	-0.1780	0.3581	0.2343
C05	-0.0830	0.3564	0.1339
C06	-0.1830	0.3581	0.2343
H01	0.0900	0.2388	0.1464
H02	0.0900	0.2388	0.1883
H03	0.0900	0.2388	0.1464
H04	0.0900	0.2388	0.1464
H05	0.0900	0.2388	0.1883
H06	0.0900	0.2388	0.1464
H07	0.0900	0.2388	0.1883
H08	0.0900	0.2388	0.1464
H09	0.0900	0.2388	0.1464
C07	-0.0860	0.3564	0.1339
H10	0.0900	0.2388	0.1883
C08	-0.2700	0.3653	0.3264
H11	0.0900	0.2388	0.1004
H12	0.0900	0.2388	0.1004
H13	0.0900	0.2388	0.1004
C09	-0.2700	0.3653	0.3264
H14	0.0900	0.2388	0.1004
H15	0.0900	0.2388	0.1004
H16	0.0900	0.2388	0.1004

C10	-0.2710	0.3653	0.3264
H17	0.0900	0.2388	0.1004
H18	0.0900	0.2388	0.1004
H19	0.0900	0.2388	0.1004
O01	-0.6510	0.3145	0.8037
H20	0.4190	0.0400	0.1925

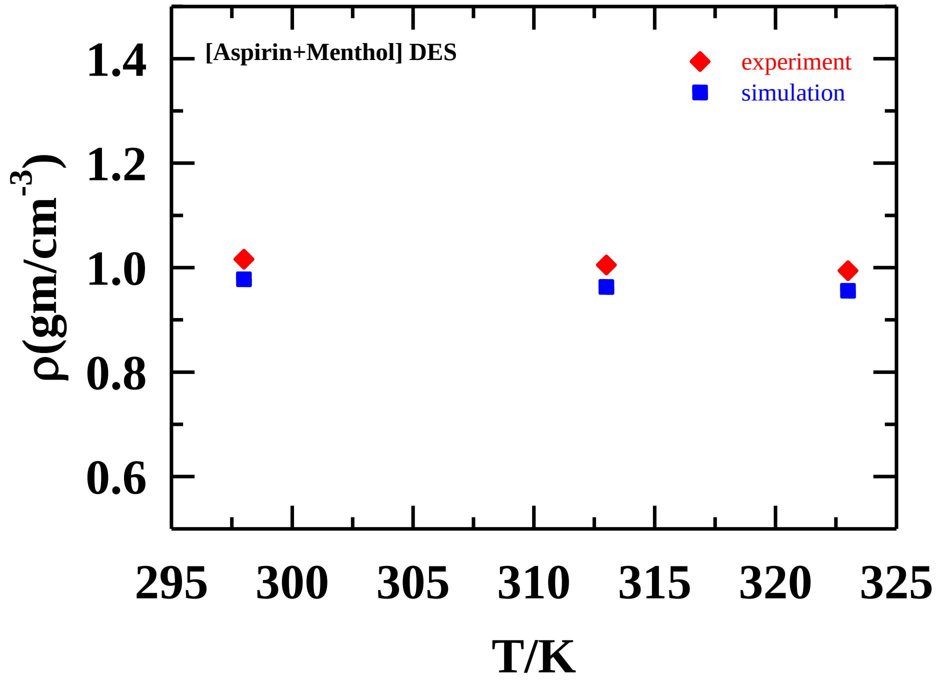

Figure 5.A.3. Comparison between experimental and simulated densities of (Aspirin+Menthol) DES at different temperatures.

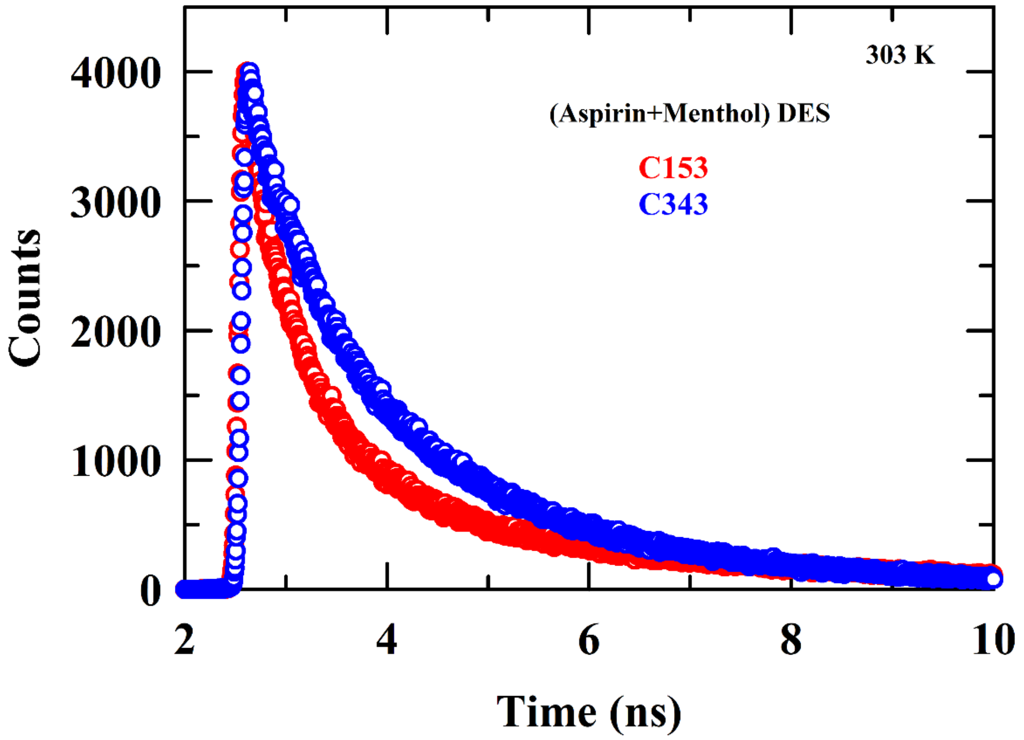

Figure 5.A.4. Representative emission decays of C153 and C343 in (Aspirin+Menthol) DES at a representative temperature 303K.

Table 5.A.4. Temperature dependent fluorescence decay parameters for C153 and C343 in (Aspirin+Menthol) DES.

C153 in (Aspirin+Menthol) DES							
T/K	α_1	τ_1/ps	α_2	τ_2/ps	α_3	τ_3/ps	$\langle\tau_{fl}\rangle/ps$
293	0.47	334	0.40	1303	0.14	4123	1240
303	0.60	267	0.31	1080	0.10	4352	911
313	0.68	210	0.23	0949	0.09	4475	774
323	0.71	190	0.18	0965	0.12	4552	840
333	0.73	151	0.14	0947	0.13	4567	822
343	0.74	129	0.14	1011	0.12	4730	807
C343 in (Aspirin+Menthol) DES							
293	0.35	362	0.51	1463	0.14	3146	1313
303	0.36	311	0.50	1379	0.14	3084	1227
313	0.37	261	0.47	1276	0.15	2887	1143
323	0.37	244	0.49	1210	0.14	2846	1072
333	0.36	201	0.51	1098	0.13	2790	996
343	0.36	210	0.52	1024	0.11	2753	929

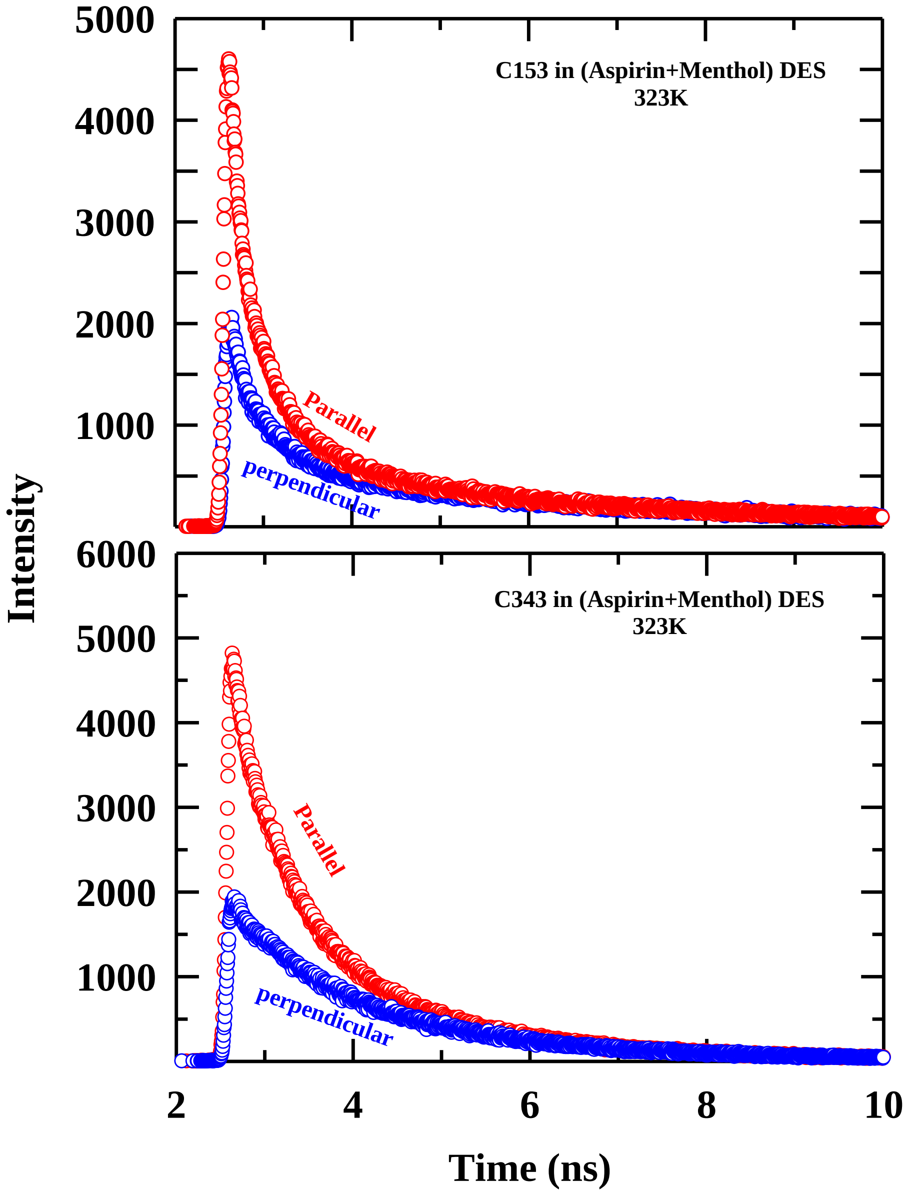

Figure 5.A.5. Representative fluorescence intensity decays of C153 (upper panel) and C343 (lower panel) in (Aspirin+Menthol) DES at 323 K, collected with different emission polarizations. Red circles denote intensity decays with parallel polarization, the blue ones with perpendicular polarization.

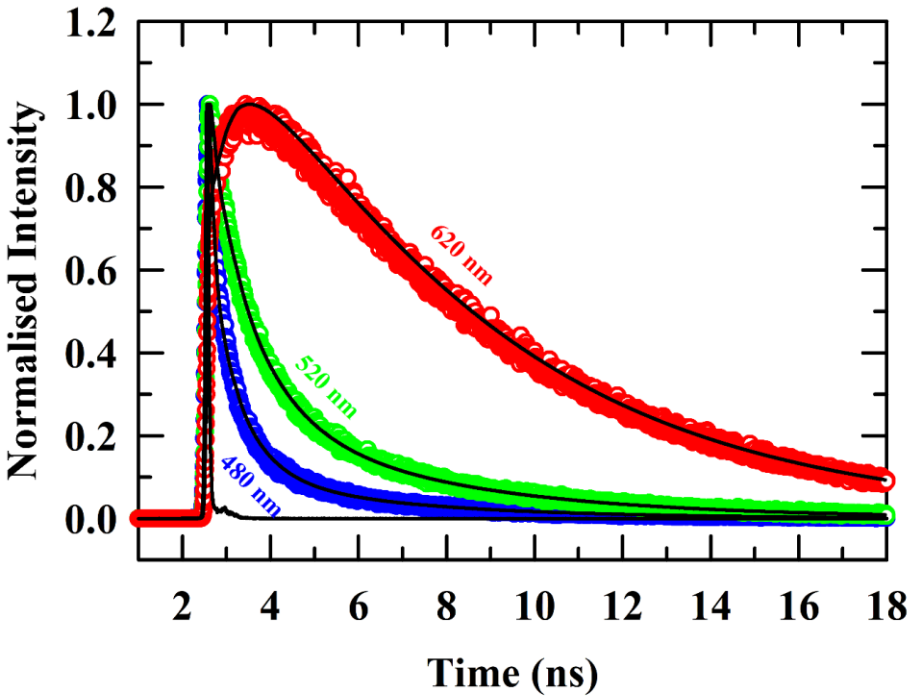

Figure 5.A.6. Representative intensity decay profiles of C153 dissolved in (Aspirin+Menthol) DES collected at the red and the blue end (wavelength) at 303 K. Circle symbols indicates the data points while lines through the data points represents exponential fits. IRF of the measurement set-up is also shown. All representations are colour coded.

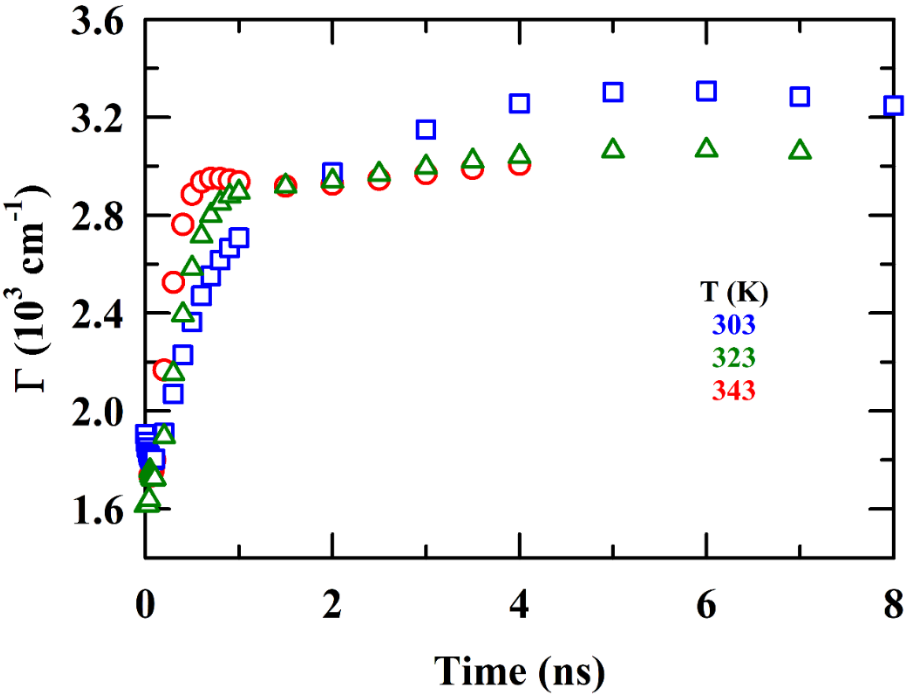

Figure 5.A.7. The time evolution of the full width at half maxima (FWHM) or widths $\Gamma(t)$ at three different temperatures.

Table 5.A.5. Hydrodynamic molecular rotation times for aspirin and menthol was calculated using the SED relation with stick boundary condition, $\tau_r = \frac{3V\eta}{k_b T}$. van der Waals volume of aspirin and menthol used here were calculated from the Ref. 1 indicated below.

T(K)	η (cP)	Aspirin ($V = 163$ Å^3) τ_r(ns)	Menthol ($V = 178$ Å^3) τ_r(ns)
303	51.15	5.98	6.53
313	24.05	2.72	2.97
323	13.30	1.46	1.59
333	6.21	0.67	0.72
343	3.01	0.31	0.34

Table 5.A.6. Number of H-bonds per molecules for different D-A-H triplets has been depicted.

Atom triplets	**Number of H-bonds per molcule**	
	Aspirin	Menthol
O3(asp)---O2(asp)—H4(asp)	0.43	-
O1(men)---O2(asp)—H4(asp)	0.67	0.17
O4(asp)---O1(men)—H20(men)	0.56	0.14
O1(men)---O1(men)—H20(men)	-	0.81
Total	1.66	1.12

References

1 T. El Achkar, H. Greige-Gerges and S. Fourmentin, *Environ. Chem. Lett.*, 2021, **19**, 3397–3408.

2 M. H. Zainal-Abidin, M. Hayyan, A. Hayyan and N. S. Jayakumar, *Anal. Chim. Acta*, 2017, **979**, 1–23.

3 B. B. Hansen, S. Spittle, B. Chen, D. Poe, Y. Zhang, J. M. Klein, A. Horton, L. Adhikari, T. Zelovich, B. W. Doherty, B. Gurkan, E. J. Maginn, A. Ragauskas, M. Dadmun, T. A. Zawodzinski, G. A. Baker, M. E. Tuckerman, R. F. Savinell and J. R. Sangoro, *Chem. Rev.*, 2021, **121**, 1232–1285.

4 Y. Liu, J. B. Friesen, J. B. McAlpine, D. C. Lankin, S. N. Chen and G. F. Pauli, *J. Nat. Prod.*, 2018, **81**, 679–690.

5 E. L. Smith, A. P. Abbott and K. S. Ryder, *Chem. Rev.*, 2014, **114**, 11060–11082.

6 M. M. Abdelquader, S. Li, G. P. Andrews and D. S. Jones, *Eur. J. Pharm. Biopharm.*, 2023, **186**, 85–104.

7 I. B. Qader and K. Prasad, *Pharm. Res.*, 2022, **39**, 2367–2377.

8 S. Emami and A. Shayanfar, *Pharm. Dev. Technol.*, 2020, **25**, 779–796.

9 Y. L. Chen, X. Zhang, T. T. You and F. Xu, *Cellulose*, 2019, **26**, 205–213.

10 E. Durand, J. Lecomte, B. Baréa, G. Piombo, E. Dubreucq and P. Villeneuve, *Process Biochem.*, 2012, **47**, 2081–2089.

11 S. Sun, Y. Niu, Q. Xu, Z. Sun and X. Wei, *Ind. Eng. Chem. Res.*, 2015, **54**, 8019–8024.

12 M. B. Haider, D. Jha, B. Marriyappan Sivagnanam and R. Kumar, *J. Chem. Eng. Data*, 2018, **63**, 2671–2680.

13 E. Rozema, A. D. Van Dam, H. C. M. Sips, R. Verpoorte, O. C. Meijer, S. Kooijman and Y. H. Choi, *RSC Adv.*, 2015, **5**, 61398–61401.

14 C. Bakirtzi, K. Triantafyllidou and D. P. Makris, *J. Appl. Res. Med. Aromat. Plants*, 2016, **3**, 120–127.

15 I. Zahrina, M. Nasikin, E. Krisanti and K. Mulia, *Food Chem.*, 2018, **240**, 490–495.

16 K. M. Jeong, J. Ko, J. Zhao, Y. Jin, D. E. Yoo, S. Y. Han and J. Lee, *J. Clean Prod.*, 2017, **151**, 87–95.

17 C. G. González, N. R. Mustafa, E. G. Wilson, R. Verpoorte and Y. H. Choi, *Flavour Fragr. J.*, 2018, **33**, 91–96.

18 L. Millia, V. Dall'Asta, C. Ferrara, V. Berbenni, E. Quartarone, F. M. Perna, V. Capriati and P. Mustarelli, *Solid State Ion*, 2018, **323**, 44–48.

19 A. Hayyan, M. A. Hashim, M. Hayyan, F. S. Mjalli and I. M. Alnashef, *J. Clean Prod.*, 2014, **65**, 246–251.

20 M. H. Zainal-Abidin, M. Hayyan, A. Hayyan and N. S. Jayakumar, *Anal. Chim. Acta*, 2017, **979**, 1–23.

21 I. M. Aroso, R. Craveiro, Â. Rocha, M. Dionísio, S. Barreiros, R. L. Reis, A. Paiva and A. R. C. Duarte, *Int. J. Pharm.*, 2015, **492**, 73–79.

22 J. M. Silva, R. L. Reis, A. Paiva and A. R. C. Duarte, *ACS Sustain. Chem. Eng.*, 2018, **6**, 10355–10363.

23 F. Mano, M. Martins, I. Sá-Nogueira, S. Barreiros, J. P. Borges, R. L. Reis, A. R. C. Duarte and A. Paiva, *AAPS Pharm Sci Tech*, 2017, **18**, 2579–2585.

24 I. M. Aroso, J. C. Silva, F. Mano, A. S. D. Ferreira, M. Dionísio, I. Sá-Nogueira, S. Barreiros, R. L. Reis, A. Paiva and A. R. C. Duarte, *Eur. J. Pharm. Biopharm.*, 2016, **98**, 57–66.

25 M. Mokhtarpour, H. Shekaari and A. Shayanfar, *J. Drug Deliv. Sci. Technol.*, 2020, **56**, 101512.

26 M. Saha, M. Saha, M. S. Rahman, M. N. Hossain, D. E. Raynie and M. A. Halim, *J. Phys. Chem. A*, 2020, **124**, 4690–4699.

27 M. S. Rahman, R. Roy, B. Jadhav, M. N. Hossain, M. A. Halim and D. E. Raynie, *J. Mol. Liq.*, 2021, **321**, 114745.

28 F. Al-Akayleh, H. H. Mohammed Ali, M. M. Ghareeb and M. Al-Remawi, *J. Drug Deliv. Sci. Technol.*, 2019, **53**, 101159.

29 M. H. Zainal-Abidin, M. Hayyan, G. C. Ngoh, W. F. Wong and C. Y. Looi, *J. Control. Release*, 2019, **316**, 168–195.

30 H. G. Morrison, C. C. Sun and S. Neervannan, *Int. J. Pharm.*, 2009, **378**, 136–139.

31 K. Florey, *Analytical Profiles of Drug Substances*, Academic Press, 1979, vol. 8, pp. 1–46.

32 S. Javed, B. Mangla, M. H. Sultan, Y. Almoshari, D. Sivadasan, S. S. Alqahtani, O. A. Madkhali and W. Ahsan, *Heliyon*, 2024, **10**, e29783.

33 S. N. Pedro, M. G. Freire, C. S. R. Freire and A. J. D. Silvestre, *Expert Opin. Drug Deliv.*, 2019, **16**, 497–506.

34 A. Roda, F. Santos, A. A. Matias, A. Paiva and A. R. C. Duarte, *J Supercrit. Fluids*, 2020, **161**, 104826.

35 A. Gutiérrez, S. Aparicio and M. Atilhan, *Phys. Chem. Chem. Phys.*, 2019, **21**, 10621–10634.

36 C. Lu, J. Cao, N. Wang and E. Su, *Med. Chem. Comm.*, 2016, **7**, 955–959.

37 A. R. C. Duarte, A. S. D. Ferreira, S. Barreiros, E. Cabrita, R. L. Reis and A. Paiva, *Eur. J. Pharm. Biopharm.*, 2017, **114**, 296–304.

38 M. Zakrewsky, A. Banerjee, S. Apte, T. L. Kern, M. R. Jones, R. E. D. Sesto, A. T. Koppisch, D. T. Fox and S. Mitragotri, *Adv. Healthc. Mater*, 2016, **5**, 1282–1289.

39 J. M. Silva, E. Silva, R. L. Reis and A. R. C. Duarte, *Sustain. Chem. Pharm.*, 2019, **14**, 100192.

40 F. Santos, M. I. P. S. Leitão and A. R. C. Duarte, *Molecules*, 2018, **24**, 55.

41 C. V Pereira, J. M. Silva, L. Rodrigues, R. L. Reis, A. Paiva, A. R. C. Duarte and A. Matias, *Sci. Rep.*, 2019, **9**, 14926.

42 D. J. Bjorkman, *Am. J. Med.*, 1998, **105**, 8S-12S.

43 D. D. Stevenson, *J. Allergy. Clin. Immunol.*, 1984, **74**, 617–622.

44 G. P. P. Kamatou, I. Vermaak, A. M. Viljoen and B. M. Lawrence, *Phytochemistry*, 2013, **96**, 15–25.

45 E. Tarif, J. Mondal and R. Biswas, *J. Phys. Chem. B.*, 2019, **123**, 9378–9387.

46 H. Shekaari, M. T. Zafarani-Moattar and S. N. Mirheydari, *J. Solution Chem.*, 2016, **45**, 624–663.

47 B. Guchhait, S. Daschakraborty and R. Biswas, *J. Chem. Phys.*, 2012, **136**, 174503.

48 R. Biswas, J. E. Lewis and M. Maroncelli, *Chem. Phys. Lett.*, 1999, **310**, 485–494.

49 T. Pradhan and R. Biswas, *J. Phys. Chem. A.*, 2007, **111**, 11524–11530.

50 T. Pradhan, H. A. R. Gazi and R. Biswas, *J. Chem. Phys.*, 2009, **131**, 54507.

51 H. A. R. Gazi, B. Guchhait, S. Daschakraborty and R. Biswas, *Chem. Phys. Lett.*, 2011, **501**, 358–363.

52 B. Guchhait, S. Das, S. Daschakraborty and R. Biswas, *J. Chem. Phys.*, 2014, **140**, 104514.

53 M. L. Horng, J. A. Gardecki and M. Maroncelli, *J. Phys. Chem. A.*, 1997, **101**, 1030–1047.

54 R. Biswas, A. R. Das, T. Pradhan, D. Touraud, W. Kunz and S. Mahiuddin, *J. Phys. Chem. B*, 2005, 109.

55 T. Pradhan, P. Ghoshal and R. Biswas, *J. Phys. Chem. A.*, 2008, **112**, 915–924.

56 M. L. Horng, J. A. Gardecki, A. Papazyan and M. Maroncelli, *J. Phys. Chem.*, 1995, **99**, 17311–17337.

57 H. J. C. Berendsen, D. van der Spoel and R. van Drunen, *Comput. Phys. Commun.*, 1995, **91**, 43–56.

58 K. Vanommeslaeghe, E. Hatcher, C. Acharya, S. Kundu, S. Zhong, J. Shim, E. Darian, O. Guvench, P. Lopes, I. Vorobyov and A. D. Mackerell, *J. Comput. Chem.*, 2010, **31**, 671.

59 W. Yu, X. He, K. Vanommeslaeghe and A. D. MacKerell, *J. Comput. Chem.*, 2012, **33**, 2451–2468.

60 K. Vanommeslaeghe and A. D. MacKerell, *J. Chem. Inf. Model.*, 2012, **52**, 3144–3154.

61 K. Vanommeslaeghe, E. P. Raman and A. D. MacKerell, *J. Chem. Inf. Model.*, 2012, **52**, 3155–3168.

62 A. D. MacKerell, J. Nilesh Banavali and N. Foloppe, *Biopolymers*, 2001, **56**, 257–265.

63 L. Martinez, R. Andrade, E. G. Birgin and J. M. Martínez, *J. Comput. Chem.*, 2009, **30**, 2157–2164.

64 R. W. Hockney, S. P. Goel, J. W. Eastwood, R. W. Hockney, S. P. Goel and J. W. Eastwood, *J. Comput. Phys.*, 1974, **14**, 148–158.

65 G. Bussi, D. Donadio and M. Parrinello, *J. Chem. Phys.*, 2007, **126**, 9901.

66 H. J. C. Berendsen, J. P. M. Postma, W. F. Van Gunsteren, A. Dinola and J. R. Haak, *J. Chem. Phys.*, 1994, **81**, 3684.

67 M. Brehm, M. Thomas, S. Gehrke and B. Kirchner, *J. Chem. Phys.*, 2020, **152**, 164105.

68 M. Brehm and B. Kirchner, *J. Chem. Inf. Model.*, 2011, **51**, 2007–2023.

69 E. Tarif, J. Mondal and R. Biswas, *J. Mol. Liq.*, 2020, **303**, 112451.

70 G. P. Johari, S. Kim and R. M. Shanker, *J. Pharm. Sci.*, 2007, **96**, 1159–1175.

71 C. D'Hondt and D. Morineau, *J. Mol. Liq.*, 2022, **365**, 120145.

72 S. Spittle, D. Poe, B. Doherty, C. Kolodziej, L. Heroux, M. A. Haque, H. Squire, T. Cosby, Y. Zhang, C. Fraenza, S. Bhattacharyya, M. Tyagi, J. Peng, R. A. Elgammal, T. Zawodzinski, M. Tuckerman, S. Greenbaum, B. Gurkan, M. Dadmun, E. J. Maginn and J. Sangoro, *Nat. Commun.*, 2022, **13**, 1–14.

73 A. Malik and H. K. Kashyap, *Phys. Chem. Chem. Phys.*, 2021, **23**, 3915–3924.

74 M. Tiecco, I. Di Guida, P. L. Gentili, R. Germani, C. Bonaccorso and A. Cesaretti, *J Mol Liq*, 2021, **331**, 115718.

75 A. Malik and H. K. Kashyap, *J. Chem. Phys* 2021*,* **155**, 044502.

76 S. Indra and R. Biswas, *J Phys Chem B*, 2016, **120**, 11214–11228.

77 Z. Hu and C. J. Margulis, *Proc. Natl. Acad. Sci.*, 2006, **103**, 831–836.

78 A. Samanta, *J. Phys. Chem. B.*, 2006, **110**, 13704–13716.

79 A. Das and R. Biswas, *J. Phys. Chem. B.*, 2015, **119**, 10102–10113.

80 JR Lakowicz, *Principles of Fluorescence Spectroscopy*, Springer, New York, 3rd Edition, 2006.

81 S. Srivastava, S. Sinha, S. Bhattacharjee and D. Seth, *Phys. Chem. Chem. Phys.,* 2024, **26**, 12638-12651.

82 N. Subba, N. Das and P. Sen, *J. Phys. Chem. B.*, 2020, **124**, 6875–6884.

83 F Perrin, *J. Phys. Radium*, 1934, **5**, 497–511.

84 H. Jin, G. A. Baker, S. Arzhantsev, J. Dong and M. Maroncelli, *J. Phys. Chem. B.*, 2007, **111**, 7291–7302.

85 G. B. Dutt and T. K. Ghanty, *J. Phys. Chem. B.*, 2003, **107**, 3257–3264.

86 P. K. Mandal, M. Sarkar and A. Samanta, *J. Phys. Chem. A.*, 2004, **108**, 9048–9053.

87 B. Bagchi and R. Biswas, *Adv. Chem. Phys., Bd*, 1999, **109**, 207–433.

88 B. Bagchi and R. Biswas, *Acc. Chem. Res.*, 1998, **31**, 181–187.

89 R. S. Fee and M. Maroncelli, *Chem. Phys.*, 1994, **183**, 235–247.

90 S. Das, R. Biswas and B. Mukherjee, *J. Chem. Phys.*, 2016, **145**, 84504.

91 J. Mondal, D. Maji and R. Biswas, *J Chem Phys* 2024, **160**, 084506.

92 A. Luzar and D. Chandler, *Phys. Rev. Lett.*, 1996, **76**, 928.

93 A. Luzar and D. Chandler, *Nature*, 1996, **379**, 55–57.

94 A. Chandra, *Phys. Rev. Lett.*, 2000, **85**, 768.

Chapter 6

Interaction and Dynamics of a Newly Prepared Multi-Component Molten Mixture: A Combined Dielectric Relaxation and Time-resolved Fluorescence Study

6.1 Introduction

It is impossible to ignore the increasing demand for solvents from mass production processes in the industry to the small-scale chemical reactions in the laboratory. Solvents are also used in our daily work for cooking and car-to-floor cleaning. A significant portion of the solvents used in industries or laboratories belongs to the category of traditional molecular organic solvents, which often are associated with serious environmental and health concerns.[1–4] The pursuit of environment-friendly and less harmful solvents has given rise to innovative alternatives with potentially milder ecological impacts. These include room-temperature supercritical fluids,[5–7] gas-expanded liquids,[8–10] room-temperature ionic liquids, [11–14] molten salt,[15] multi-component molten mixtures[16] and deep eutectic solvents (DESs).[17–22] Among these, DESs and/or molten mixtures offer an eco-friendly class of reaction media with tuneable solvent properties. These properties might be engineered to suit the need through appropriate selection of components. However, due to the transformation of the solid components to the liquid solvent, DESs and molten mixtures usually show high viscosity. This high viscosity at around room temperature restricts these solvent's application in many cases.[23] The introduction of water, as an extra component, in a molten mixture may sometime help reduce the viscosity of the medium and converts to a more suitable medium for application. Low-viscous molten mixtures are therefore naturally promising media for large scale industrial applications through appropriate replacements of conventional organic solvents.

A neat molten medium, for example, liquid acetamide at ~353 K (viscosity, $\eta \sim 2.2$ cP, boiling point ~495 K), is long known for its versatile solvent properties.[24,25] Molten urea is used as a solvating agent and reaction medium.[26,27] There exist several molten mixtures that were used in the past as electrolyte materials and reaction media.[28] DESs are also special molten mixtures in the sense that they maintain liquid phase at or around room temperature. One of the most important disadvantages of DESs are their high viscosity, which sometimes prohibits their widespread applications. [29–31]Recently, different co-solvents such as water, cyclohexane etc. have been mixed with the molten mixtures or DESs for tuning the medium viscosity and other physicochemical properties to the desired range and utilized as reaction media and other purposes. [18,32,33]

The selection of an appropriate solvent/reaction medium for a particular chemical reaction is predominantly guided by the knowledge of several physico-chemical properties (polarity, viscosity, etc.), solvent reorganization timescale and the timescale of a planned reaction. The timescale of solvent reorganization can be affected by the molecular interactions, and thus connected to the microscopic heterogeneity of the medium. The polarity of the medium, on the other hand contributes to the static control of the reaction kinetics via modifying the reaction barrier. The interrelationship between solvent effects and reaction kinetics then creates the necessary symbiosis between theory and experiments and provides a critical handle for the optimization of a reaction.[34–36]

Furthermore, diffusion is the primary mode of transportation within living cells and biological systems.[37,38] The intricate structure of the cell, including molecular crowding and cytoskeletal networks, gives rise to various unusual heterogeneous environments, non-linear changes in displacement over time, and subtle deviations from ergodic behaviour. Several models are used to understand the impact of heterogeneity in diffusion mechanics, including micelles, porous material, etc. [39–41] Interestingly, spatial and dynamical heterogeneity assumes greater importance for biological systems because chemical reactions occur inside living cells in complex environments at mild thermodynamic conditions following catalytic pathways. Therefore, understanding the heterogeneity of a reaction medium may help to understand the in-vitro biomolecular reactions, at least to some extent.[42]

In this study, we prepared a multicomponent molten mixture and examined several physical properties, such as, polarity, viscosity, and refractive index of this medium. Moreover, we measured the dynamics of this system by using dielectric relaxation (DR) spectroscopy[36,43–46] in the frequency range[47] $(0.2 \leq \nu/GHz \leq 50)$, and steady-state and time-resolved fluorescence spectroscopy techniques. DR spectroscopy is a versatile tool for exploring the inherent interaction and reorientational dynamics of a system containing dipolar molecules via tracking the system's dipole moment fluctuations. Fluorescence spectroscopy[48,49] is a popular tool which can track the spatial and temporal heterogeneity aspects of a multicomponent molten mixture indirectly using external fluorescence dyes. We initially formulated a low-viscosity molten blend using biocompatible components including sorbitol, urea, and water. The initial characterization involved measuring key parameters, such as, density, viscosity, and refractive index. Subsequently, we performed temperature-dependent $(303\,K \leq T \leq 343\,K)$ DR measurements in the frequency window $0.2 \leq \nu/GHz \leq 50$, which was characterized by multi-Debye relaxation dynamics with the average relaxation time spanning from ~400 ps to 100 ps. The measured static dielectric constant $(\varepsilon_s{\sim}80)$ of the system resembles that of water, suggesting a high dissolution power and lowering of reaction barrier[50–52] but the high viscosity might be a hindrance to the progress of diffusion-controlled chemical reactions. Steady-state emission employing two fluorescent dyes C153 and C343 reveals the medium is spatially homogeneous though the signature of moderate dynamic heterogeneity is observed from the fractional viscosity dependency of the rotational dynamics of the fluorescent solutes employed (C153 and C343). The viscosity coupling of average DR times also indicates presence of mild temporal heterogeneity, although a stricter comparison may highlight a relatively stronger decoupling for the average solute rotation times. This difference may arise from the preferential location of the solute probes.

6.2 Experimental Details

6.2.1 Sample Preparation

Sorbitol (≥98 %, Sigma-Aldrich, melting point T_m~371-373 K) and Urea (≥98%, Sigma-Aldrich, T_m~405-408 K) were vacuum-dried (~300 K) overnight before use. Millipore water was used for sample preparation. Laser grade coumarin 153 (C153) and coumarin 343 (C343) were used as received from Sigma-Aldrich. Sorbitol, urea and water [Sorbitol:Urea:Water:: 2:2:1; weight ratio] were taken in a glass vial and heated at ~348 K with constant stirring at ~400 rpm for ~1.5 h. A colourless transparent liquid (that is, molten mixture) was formed and cooled gradually to room temperature (~298 K) (see **Figure 6.A.1**, Appendix 6.A). We used nitrogen gas flow in the sample container to avoid any kind of oxidation at high temperatures. Chemical structures of C153, C343, sorbitol and urea are shown in **Scheme 6.1**.

For temperature-dependent DR measurements, 10 ml from the stock (molten mixture) was taken as a sample in a screw-capped vial and the target temperature for measurements was maintained by a magnetic stirrer cum hot plate.[53] Experiments were done in a humidity-controlled laboratory with humidity level maintained at ~35%.

For the optical measurements, the molten mixture was transferred to a quartz cuvette (path length 1 cm), which was already loaded (at one time) with a few grains of one of the fluorescent solutes considered (C153 or C343). Sufficient time was allowed for a proper dissolution of the solute probe in the sample before any measurements. Special care was taken to the temperature equilibration of the molten mixture while carrying out temperature-dependent measurements.

(A)

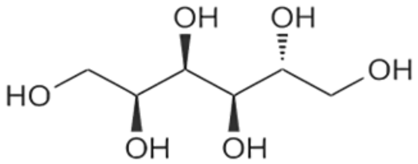

Sorbitol

(B)

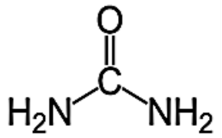

Urea

(C)

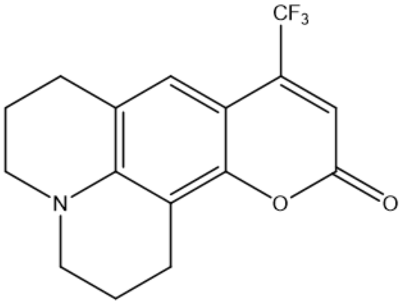

Coumarin 153

(D)

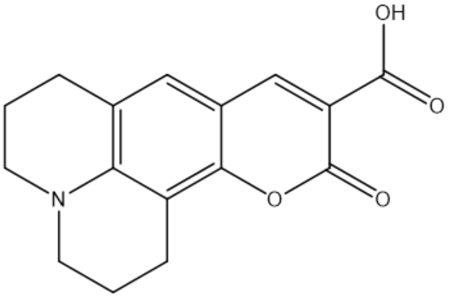

Coumarin 343

(E)

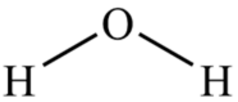

Water

Scheme 6.1. Chemical structures of (A) sorbitol (B) urea (C) coumarin 153 and (D) coumarin 343 (E) Water.

6.2.2 Refractive Index, Density and Viscosity Coefficient Measurements

Temperature-dependent refractive index (n_D), density (ρ) and viscosity coefficient (η) were measured using a refractometer (RUDOLPH, J357), an automated density-cum-sound analyser (Anton Paar, DSA5000) and a micro viscometer (AMVn, Anton Paar), respectively.[54,55] Temperature-dependent n_D, ρ and η are summarized in **Table 6.A.1** (Appendix 6.A).

6.2.3 Glass Transition Temperature Measurements

Differential scanning calorimetric experiments *were* performed (DSC Q2000 instrument) to estimate the glass transition temperature (T_g). The relevant DSC scan is shown in **Figure 6.A.2** (Appendix 6.A), which indicated[54,56] T_g ~200 K.

6.2.4 DR Measurement Details

The complex dielectric function of a given material can be represented by the following expression[44,57]

$$\varepsilon^*(\nu) = \varepsilon'(\nu) - \left[i\varepsilon''(\nu) + \frac{ik}{2\pi\varepsilon_0\nu}\right], \tag{6.1}$$

where ε_0 denotes the free space permittivity and k denotes the conductivity of the medium, $\varepsilon'(\nu)$ the frequency (ν) dependent real part of the complex dielectric function, $\varepsilon^*(\nu)$, and $\varepsilon''(\nu)$ the corresponding imaginary part. Notice that $\varepsilon'(\nu \to 0)$ is known as the static dielectric constant (ε_s) of the medium.

The required measurements were carried out utilizing a PNA-L network analyzer (N5235B) complemented by an open-ended coaxial probe kit (N1501A), facilitating measurements in the frequency window, 200 MHz - 50 GHz.[47,53] Data were collected by using the reflection mode and the required calibration was performed by measuring air, shorting block and water as open, short and load respectively.

6.2.5 DR Data Analysis

The measured complex dielectric function $\varepsilon^*(\nu)$ at each of the temperatures considered was fitted using the following equation.[57]

$$\varepsilon^*(\nu) = \varepsilon_\infty + \sum_{j=1}^{n} \frac{\Delta\varepsilon_j}{\left[1+\left(i2\pi\nu\tau_j\right)^{1-\alpha_j}\right]^{\beta_j}} \tag{6.2}$$

where $0 \leq \alpha < 1$ and $0 < \beta \leq 1$. $\Delta\varepsilon_j$ denotes the amplitudes of the dispersion of j$^{\text{th}}$ relaxation step with a relaxation time constant τ_j. Note that $\alpha_j = 0$ and $\beta_j = 1$ represents relaxation that follows the Debye model. $\alpha_j = 0$ describes the Cole-Devidson[58] (CD) relaxation, whereas $\beta_j = 1$ the Cole-Cole[59] (CC) relaxation. We first collected data from Impedance Analyzer in the relatively low-frequency range. Then We collected data from a Network Analyzer in the high-frequency range. Data collected by using the two instruments, the impedance analyzer and the network analyzer were combined together and subjected to simultaneously fits. Fitting quality was estimated by monitoring the "goodness-of-fit" parameter (χ^2),[60]

$$\chi^2 = \frac{1}{2m-l}\sum_{i=1}^{m}\left[\left(\frac{\delta\varepsilon_i'}{\sigma(\varepsilon_i')}\right)^2 + \left(\frac{\delta\varepsilon_i''}{\sigma(\varepsilon_i'')}\right)^2\right] \quad (6.3)$$

where denotes the number of data triples $(\nu, \varepsilon', \varepsilon'')$, l is the number of adjustable parameters, and $\delta\varepsilon_i$ and $\sigma(\varepsilon_i)$ are the residuals and standard deviation of the individual data points, respectively.

6.2.6 Steady-State and Fluorescence Measurements

Absorption and emission spectra of C153 and C343 dissolved in (sorbitol+urea+water) molten mixture were recorded by using a UV–VIS absorption spectrophotometer (UV-2600, Shimadzu) and a fluorimeter (Fluorolog, Jobin-Yvon, Horiba), respectively. A Peltier-temperature controller was used for the temperature dependent for absorption and steady-state fluorescence emission measurements. [61,62]

6.2.7 Time-Resolved Fluorescence Measurements

TCSPC (Time-correlated single photon counting, LifeSpec-ps, Edinburgh Instruments, U. K.) measurements employing a 409 nm excitation laser were carried out for pico-second resolved fluorescence data. The details of the instruments can be found elsewhere.[62,63] The full width at half-maximum (FWHM) of the instrument response function was ~90 ps using a scattering sample. Subsequently, fluorescence emission decays were collected in two different polarizations, parallel ($I_{para}(t)$), and perpendicular ($I_{perp}(t)$) with respect to the polarization of the exciting light.[61,64] The dynamic fluorescence anisotropy, $r(t)$, was obtained from the collected intensity decays as follows,

$$r(t) = \frac{I_{\text{para}}(t) - \text{GI}_{\text{perp}}(t)}{I_{\text{para}}(t) + 2\text{GI}_{\text{perp}}(t)} \quad (6.4)$$

The average rotational times, $\langle\tau_r\rangle$, of the solute probe in the molten mixture was calculated from the bi-exponential fits to the $r(t)$ decays as $\langle\tau_r\rangle = \int_0^\infty dt\ [r(t)/r_0]$=$\int_0^\infty dt \sum_{i=1}^{2} a_i$ exp(-t/τ_i)=$a_1\tau_1 + a_2\tau_2$with $a_1 + a_2 = 1$. The initial anisotropy (r_0) values for C153 and C343 were taken respectively as 0.376 [64] and 0.35[65]. The geometric factor, G, was determined by tail-matching the intensity decays, $I_{para}(t)$ and $I_{perp}(t)$, and found to be 1.8 ± 0.3 for C343 and 1.7±0.2 for C153.

More details about the experimental procedures and analysis are given in Chapter 2.

6.3 Results and Discussion

6.3.1 Dielectric Relaxation Measurements: Temperature Dependence

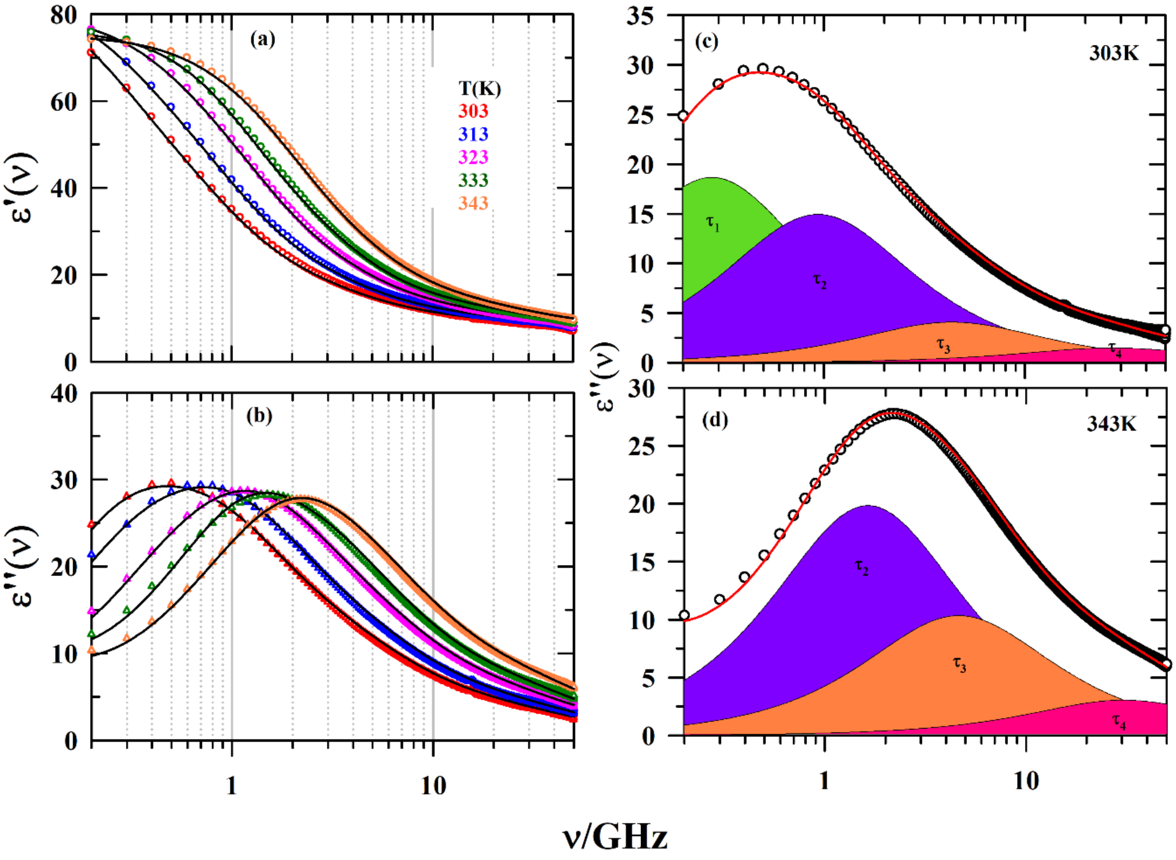

Figure 6.1. *Left panel*: (a) Real part $\varepsilon'(\nu)$ and (b) imaginary part $\varepsilon''(\nu)$ of experimental DR spectra of (sorbitol+urea+water) molten mixture in the frequency regime, $0.2 \le \nu/GHz \le 50$ at five distinct temperatures. Solid lines passing through the experimental data points represent the multi-Debye fits. *Right panel*: (c) & (d) represent the decomposition of imaginary part $\varepsilon''(\nu)$, in two representative temperatures, 303K and 343K. symbols show experimental data points, while lines through the data points represent fitting lines with the multi-Debye model.

The shaded area in (c) and (d) represents the contribution from various timescales to the total DR. Each representation is colour-coded.

Figure 6.1 (a) and (b) present the real $\varepsilon'(\nu)$ and imaginary $\varepsilon''(\nu)$ parts of the temperature-dependent DR spectra of (sorbitol+urea+water) molten mixture in the frequency regime $0.2 \leq \nu/GHz \leq 50$ along with the multi-Debye fits. Fit parameters are summarized in **Table 6.1**. The experimental DR spectra were also fit to Cole-Cole and Cole-Davidson descriptions but the 4-Debye fits provided the best description (guided by values of χ^2) of the data at lower temperatures (303K to 328K), while the 3-Debye fit functions adequately represented the data at higher temperatures (333K to 343K). A comparison of the residuals at the lowest and the highest in the temperature range considered (303K and 343K), illustrated in **Figure 6.A.3** (Appendix 6.A), shows the appropriateness of the chosen fit function. Notice that at higher temperatures, two slower timescales combine to form a single slower time constant, modifying the requirement from 4-Debye to 3-Debye fit functions.

Table 6.1. Parameters obtained from simultaneous multi-Debye fits to real (ε') and imaginary (ε'') components of the measured DR spectra for (sorbitol+urea+water) molten mixture in the temperature regime $303 \leq T/K \leq 343$.

T(K)	ε_s	$\Delta\varepsilon_1$	$\tau_1{}^b$ (ps)	$\Delta\varepsilon_2$	τ_2 (ps)	$\Delta\varepsilon_3$	τ_3 (ps)	$\Delta\varepsilon_4$	τ_4 (ps)	ε_∞	$n_D{}^c$	$\varepsilon_\infty - n_D^2$	$\langle\tau_{DR}\rangle^d$ (ps)	η^e(cP)
303	85.6	37.3 (48%)[a]	574	29.9 (38%)	170	8.2 (10%)	37	2.9 (4%)	6	7.3	-	-	343	33
308	84.8	32.3 (42%)	510	33.2 (43%)	157	8.7 (11%)	35	3.2 (4%)	6	7.5	1.4736	5.33	284	24
313	84.1	29.2 (38%)	470	35.1 (46%)	147	8.8 (12%)	34	3.4 (4%)	6	7.6	-	-	251	21
318	82.4	27.5 (37%)	369	34.5 (47%)	128	9.0 (12%)	31	3.6 (5%)	5	7.8	1.4740	5.63	199	16
323	79.9	20.7 (29%)	303	37.1 (51%)	115	10.2 (14%)	32	4.2 (6%)	5	7.8	-	-	151	14
328	79.3	19.5 (27%)	278	37.3 (52%)	108	10.3 (14%)	31	4.3 (6%)	5	7.8	1.4744	5.63	137	11
333	78.5	-	-	38.1 (54%)	164	26.5 (38%)	50	5.8 (8%)	6	8.1	-	-	108	9
338	78.1	-	-	30.0 (43%)	158	33.2 (47%)	50	6.5 (10%)	6	8.2	1.4765	5.92	93	8
343	77.6	-	-	24.3 (35%)	157	37.8 (55%)	49	7.1 (10%)	6	8.3	-	-	83	6

a: number in parentheses indicates dispersion step amplitude in percentage. *b*: uncertainty in measured τ_i is limited within ±5% of the reported values *c*: refractive index. *d*: $\langle\tau_{DR}\rangle = \frac{\sum_{i=1}^{n} a_i\tau_i}{\sum_{i=1}^{n} a_i}$. *e*: Viscosity values are better than ±5% of the reported values.

Fit parameters summarised in **Table 6.1** reveal a gradual decrease of ε_s value upon increasing the solution temperature. The peak in the imaginary component, $\varepsilon''(\omega)$, (**Figure 6.1(b)**) shifts to higher frequency with temperature. This indicates faster relaxation at higher temperatures because of the consequent decrease in the medium viscosity. Note the DR time constants are spread from sub-nanosecond to a few picoseconds (~0.6 ns - 5 ps) and the fastest of them (τ_4) persists throughout the temperature range considered. The amplitude associated with this component increases with temperature from 4% to 10%, suggesting the faster relaxations gaining weight upon raising the solution temperature. It is noteworthy that previous DR measurements on molten urea[66] on molten urea and water-xylitol mixture[67] reported a similar timescale. We would like to mention here that the fastest time DR time constant (~5 ps) is constrained in the present measurements by the highest frequency accessed (50 GHz). Therefore, any relaxation faster than this timescale has remained undetected. Calculated values of $\varepsilon_\infty - n_D^2$ at different temperatures shown in **Table 6.1** clearly indicate that a considerable part at the high frequency end has remained undetected. This means that the fit parameters summarized in **Table 6.1** will differ somewhat from those made available from full detection of the entire DR.

Next, we comment on the sub-50 picosecond (τ_3) timescale whose amplitude increases slowly but steadily with temperature till 328 K and then increases quite substantially on further increase of temperature. This happens because the slowest sub-nanosecond component disappears once the solution temperature increases beyond 328 K and consequently the 4-step relaxation process reduces to 3-step process. Previous measurements on molten urea[66] reported 2-Debye relaxation process with DR time constants of ~87 ps and ~29 ps, the latter with dominant amplitudes. Temperature dependent DR measurements of xylitol+water mixtures[67,68] also reported sub-50 ps timescale at a few compositions. Considering that sorbitol and xylitol are both polyols and can undergo similar H-bonding interactions with water molecules, sub-50 ps relaxation timescale can also derive contributions from sorbitol-water interactions.

We have already noticed that the multi-Debye fits to the measured DR spectra revealed two comparatively slower components with timescales, $\tau_1 \sim 0.3 - 0.6$ ns and $\tau_2 \sim 100 - 170$ ps at lower temperatures, which, upon further rise in temperature, merge to a single component with a relaxation time constant of ~160 ps. These components, depending on measurement temperature, account for dominant to substantial part of the detected DR and suggest participation of both dipolar reorientation dynamics and structural H-bond fluctuations.[53,66] We would first examine whether the hydrodynamic molecular rotations of urea, sorbitol and water in this medium could contribute to this relaxation component. The calculated molecular rotation times by using the formula, $\tau_r = \frac{3V\eta}{k_B T}$, provided in **Table 6.A.2** (Appendix 6.A) indicates that molecular rotations of urea and sorbitol are either much slower or faster than the measured timescales. Interestingly, the molecular rotation of water in this system closely resembles the experimental DR times. It doesn't, however, mean that the molecular rotation of water dominantly contributes to the measured DR dynamics. This is because the number of such free water molecules will be very small for two reasons: (i) the amount of water is little compared to other molecules in the system and (ii) due to formation of extensive interspecies hydrogen bonds with sorbitol and urea. A similar observation was found previously[47] where the molecular rotation of acetamide molecules closely resembled the measured DR times. Later, it was found that the structural hydrogen bond relaxation timescales and collective single-particle reorientational relaxation times explained the origin of those timescales. Therefore, the hydrodynamic molecular rotations of the component species are not responsible for this slowly relaxing component. Simulation studies of collective single-particle reorientational relaxation and structural H-bond fluctuations, as were done for other H-bonded systems,[53,66,69] should be carried out in order to identify the correct origin of this component.

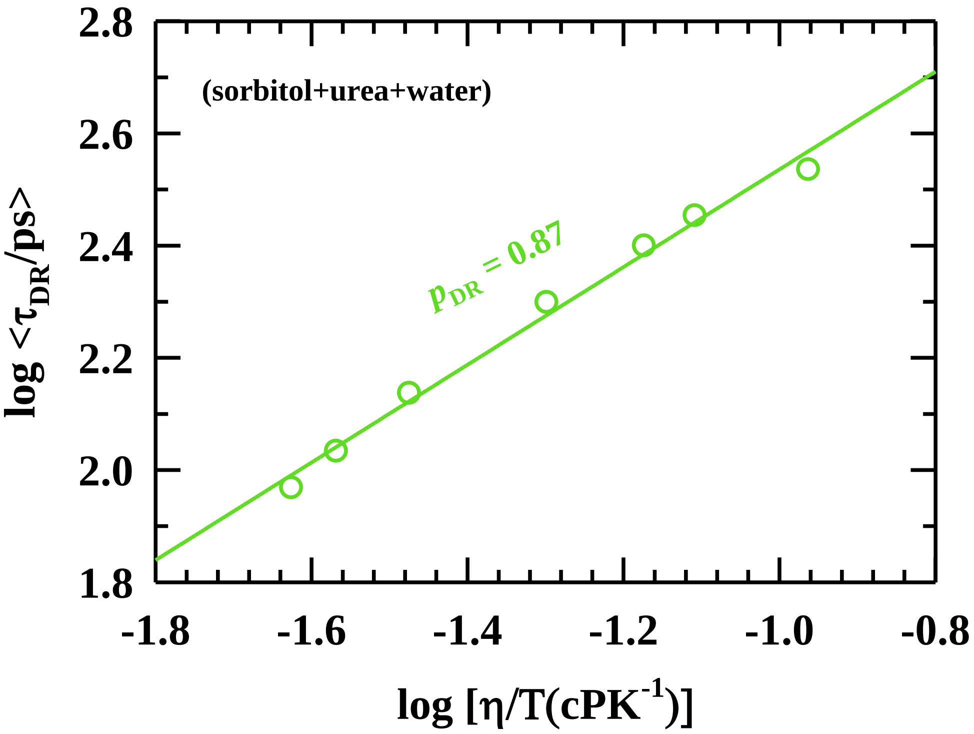

Figure 6.2. Coupling between medium viscosity and average DR time, $\langle\tau_{DR}\rangle$ are shown as a function of temperature-scaled viscosity (η/T) in a log-log fashion. Lines through the data represent fits to the following expression: $log\ \langle\tau_{DR}\rangle = A + p\ log\ [^{\eta}/_{T}]$.

The relationship between the temperature-dependent average DR times and viscosity, was explored in **Figure 6.2** by plotting $\langle\tau_{DR}\rangle$ against the temperature-reduced viscosity η/T, indicates that the DR dynamics are controlled by the macroscopic solution viscosity following hydrodynamic. This is evident from the exponent (p) in the relation, $\tau_{DR} \propto \left(\frac{\eta}{T}\right)^{p}$, which approaches unity (p ~ 0.87). Such a value suggests a dynamically homogeneous system. This finding contrasts with earlier observations where the breakdown of SED in predicting DR dynamics via single-particle rotation was noted. This apparent contradiction suggests that collective motion, rather than single molecular rotation, contributes to the DR dynamics.

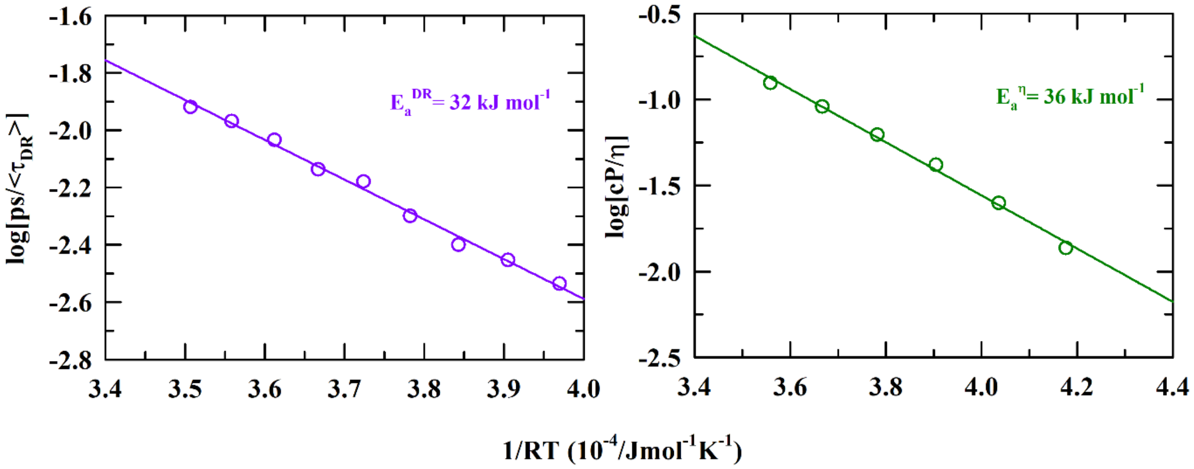

Figure 6.3. Arrhenius plot for temperature-dependent average DR times ($\langle\tau_{DR}\rangle$) for (sorbitol+urea+water) molten mixture (*left panel*) and temperature-dependent viscosity coefficient (η) (*right panel*). Solid lines represent linear fits through the respective data sets. Activation energies estimated are mentioned in the respective plots.

To further investigate the temperature dependence and dynamic heterogeneity of the system, we compared the activation energy associated with DR measurements to that of viscosity. **Figure 6.3** illustrates the Arrhenius-type temperature dependence of $\langle\tau_{DR}\rangle$ and the viscosity coefficient, η, with corresponding activation energies indicated in the respective plots. This comparison reveals that the activation energies from both measurements are in close proximity ($E_a^{\langle\tau_{DR}\rangle}$~32 kJ mol^{-1}, E_a^{η}~36 kJmol^{-1}), suggesting that the medium dynamics follow viscosity trends and thus are hydrodynamically controlled.

Note that the detection of dynamical heterogeneity in DR measurements involved the temperature-dependent average DR times, which essentially represent the collective dynamic response of the system. Thus, to explore heterogeneity in local environments, we need to probe different regions within the system. This underscores the importance of fluorescence spectroscopy, which can target specific regions of interest by selecting the appropriate probe molecules. Following this, we conducted steady-state and time-resolved fluorescence spectroscopic measurements to explore the system more closely.

6.3.2 Absorption and Steady-state Fluorescence Emission Measurements: Temperature Dependence and Medium Heterogeneity Signatures

Temperature-dependent absorption and emission spectra of C153 and C343 in (sorbitol+urea+water) molten mixture are shown in **Figure 6.4.** Spectra presented in this figure clearly indicates that the effects of solution temperature on the solute-medium interaction is very weak for both C153 and C343 in this molten mixture.

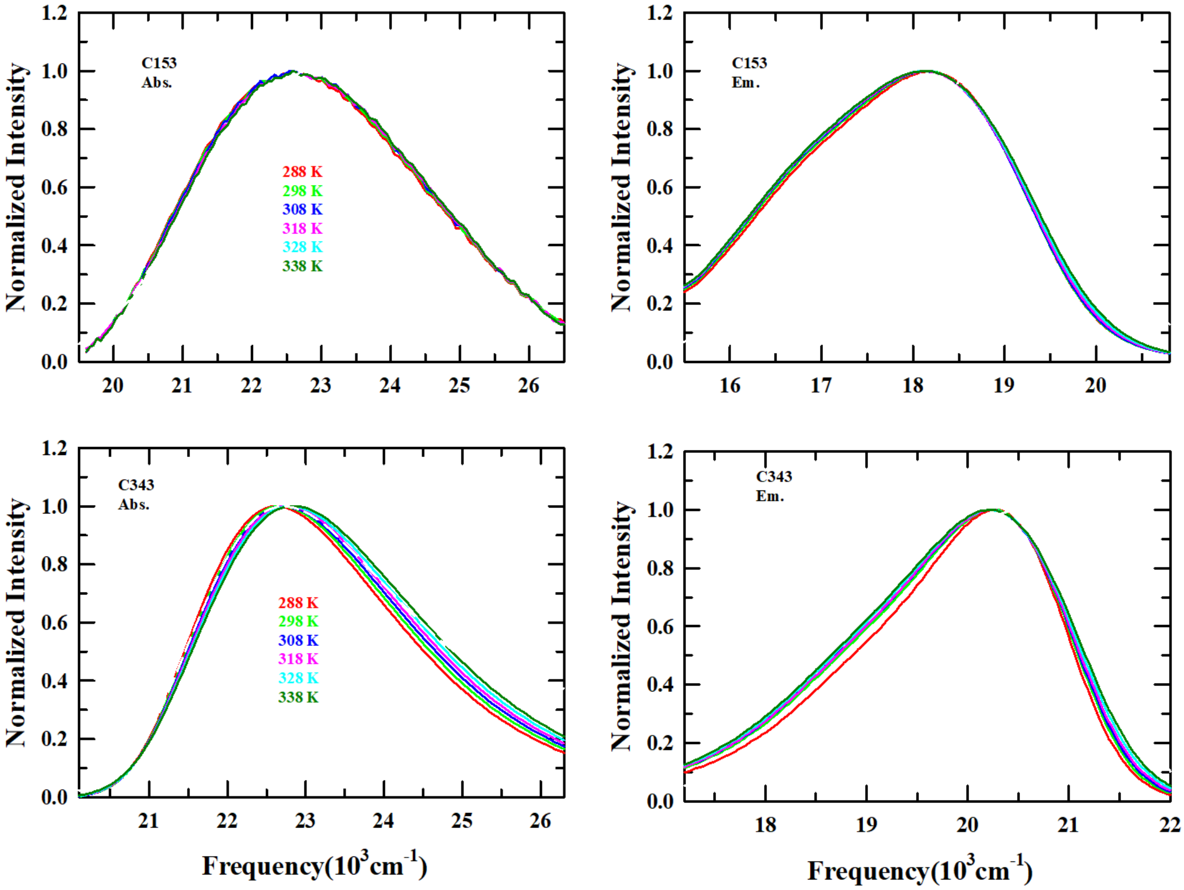

Figure 6.4. Temperature-dependent absorption and emission spectra of *C*153 (up panel) and *C*343 (lower) in (sorbitol+urea+water) molten mixture.

Next, we explore the spatial heterogeneity signatures via monitoring the excitation wavelength (λ_{exc}) dependence of the emission peak frequencies (ν_{em}) of C153 or C343 dissolved in this molten mixture. The results are shown in **Figure 6.5** where λ_{exc} dependent fluorescence emission spectral peak frequencies ($\nu_{em.}$) of both these solutes are shown along with the corresponding absorption spectra. The chosen λ_{exc} values are indicated by bullets on the respective absorption spectra. The λ_{exc} dependent total dispersions of the emission peak frequencies, $\Delta\nu_{em} = \nu_{em}\ (\lambda_{exc}^{blue}) - \nu_{em}\ (\lambda_{exc}^{red})$, are merely ~200 cm^{-1} for C153 and C343. This result suggests that these solute probes, characterized by average excited state fluorescence lifetimes of ~3 - 5 ns,[56,70,71] find this molten mixture as a nearly homogeneous solvent medium.

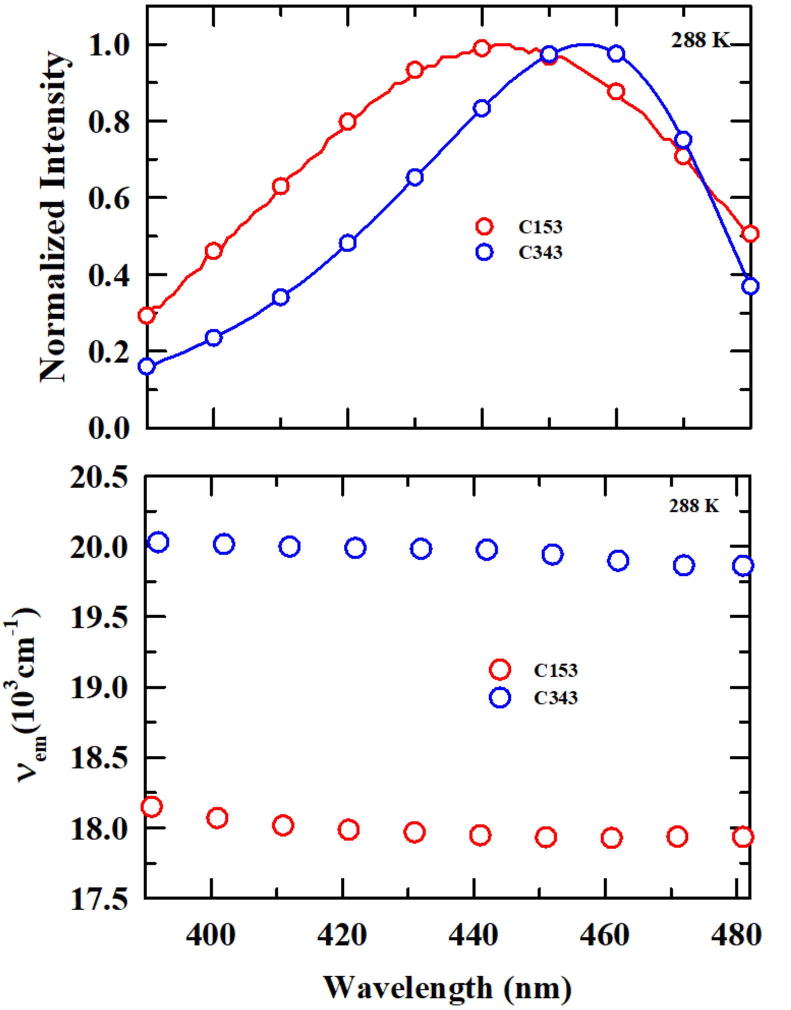

Figure 6.5. Representative absorption of C153 and C343 in (sorbitol+urea+water) molten mixture (*upper panel*). The circles on the absorption spectra indicate the wavelengths selected for excitation wavelength dependence studies. Excitation wavelength (λ_{exc}) dependence of the emission peak frequencies (ν_{em}) for C153 or C343 dissolved in (sorbitol+urea+water) molten mixture at 288 K (*lower panel*). Different data are colour-coded.

6.3.3 Rotational Dynamics of C153 and C343: Search for Dynamic Heterogeneity

The dynamic heterogeneity signatures are often searched via monitoring the coupling between the average relaxation time of a rate process in a given medium and the viscosity of that medium. For this, one requires temperature dependent measurements of both the relaxation timescales and the medium viscosity and then analysing the coupling of the average timescales to the medium viscosity through the lens of the celebrated Stokes-Einstein (SE) and/or Stokes-Einstein-Debye (SED) relation [67,72,73]: $\langle\tau_{expt}\rangle \propto \left(\frac{\eta}{T}\right)^p$, where p =1. Subsequently, any deviation from of p being unity is termed as a presence of dynamic heterogeneity in a given system. The dynamic heterogeneity connects to the spatial heterogeneity when one defines the dynamic heterogeneity as spatially varying relaxation rates.[74] In the present work, we have performed temperature dependent dynamic fluorescence anisotropy measurement[75] employing both C153 and C343 and then explored the viscosity coupling via examining the validity of the hydrodynamic predictions of the viscosity dependence of the measured average rotation times, $\langle\tau_r\rangle \propto \left(\frac{\eta}{T}\right)^p$. The measured fluorescence anisotropy decays are presented below and discussed.

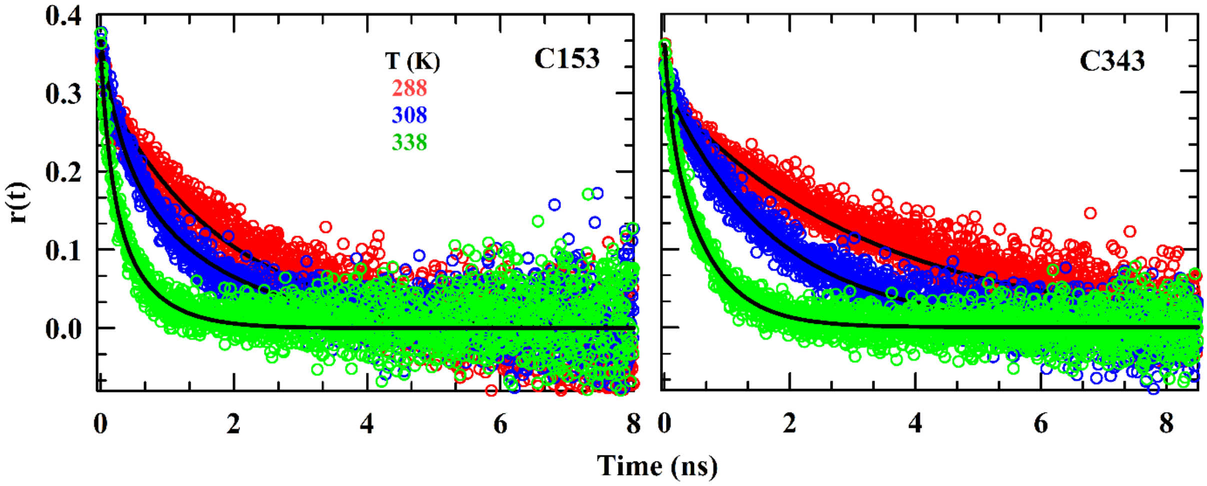

Figure 6.6. Rotational anisotropy decays of C153 (*left panel*) and C343 (*right panel*) in (sorbitol+urea+water) molten mixture at three different temperatures. Representations are colour-coded.

Fluorescence anisotropy decays, $r(t)$, constructed from the measured parallel ($I_{para}(t)$) and perpendicular ($I_{perp}(t)$) emission intensity decays for C153 and C343 in (sorbitol+urea+water) molten mixture are presented in **Figure 6.6**. The results are shown for a few temperatures. Representative decays of the parallel ($I_{para}(t)$) and the perpendicular ($I_{perp}(t)$) emission intensities for C153 and C343 provided in **Figure 6.A.4** (Appendix 6.A), suggest that rotational relaxations of these solutes in this media are complete within a few nanoseconds. Subsequently, the constructed $r(t)$ decays were found to fit bi-exponential functions of time, and the fit parameters are summarized in **Table 6.2**. These fit parameters indicate that the bimodal anisotropy decays contain faster and slower components with well-separated relaxation timescales. Notice that the average rotational times ($\langle\tau_r\rangle$) of C343 are ~30-50% longer than that measured for C153 in the temperature range studied, although their sizes do not differ much. However, the presence of $-\mathrm{CF_3}$ group in C153 and $-\mathrm{COOH}$ in C343 probably drives them to locate in microscopic regions of differing polarities in this molten mixture. As a result, the solute-solvent interactions differ for these solutes and this is reflected by their significantly different average rotation times.

Table 6.2. Bi-exponential fit parameters of temperature-dependent rotational anisotropy decays $(r(t))$ of C153 and C343 in (sorbitol+urea+water) molten mixture.

C153					
T(K)	a_1 (%)	τ_1 (ps)	a_2 (%)	τ_2 (ps)	$\langle\tau_r\rangle$ (ps)
288	11	125	89	2270	2034
298	12	81	88	1790	1559
308	34	300	66	1545	1120
318	48	350	52	1012	694
328	30	130	70	600	458
338	25	75	75	450	354
C343					
T(K)	a_1 (%)	τ_1 (ps)	a_2 (%)	τ_2 (ps)	$\langle\tau_r\rangle$ (ps)
288	24	57	76	3622	2766
298	12	29	88	2274	2004
308	7	49	93	1750	1642
318	17	192	83	1368	1172
328	19	166	81	957	806
338	27	127	73	671	526

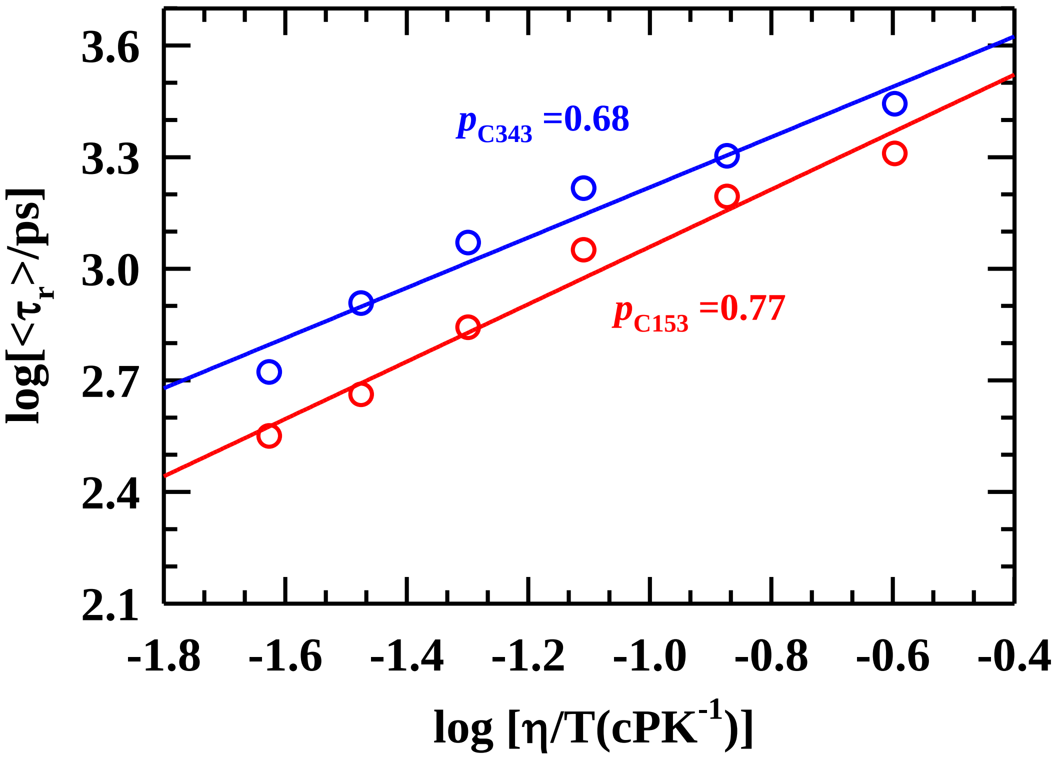

Figure 6.7. Copling of medium viscosity (η) with average rotational time ($\langle\tau_r\rangle$) for C153 and C343 in (sorbitol+urea+water) molten mixture, are shown as a function of temperature-scaled viscosity (η/T) against average rotational time, $\langle\tau_r\rangle$ in a log-log fashion. Lines through the data represent fits to the following expression: $log\ \langle\tau_r\rangle = A + p\ log\ [{}^{\eta}/_{T}]$.

The dynamic heterogeneity aspect of the medium was subsequently investigated by showing $\langle\tau_r\rangle$ in **Figure 6.7** as a function of temperature-reduced viscosity, $\left(\frac{\eta}{T}\right)$, in a log-log fashion for both the solutes C153 and C343. These average rotation times highlights a fractional viscosity dependence $p = 0.77$ and $p = 0.68$ for C153 (hydrophobic probe) and C343 (hydrophilic probe), respectively. These results indicate that both the solute reflect mild dynamic heterogeneity despite their different chemical nature (hydrophobic versus hydrophilic).

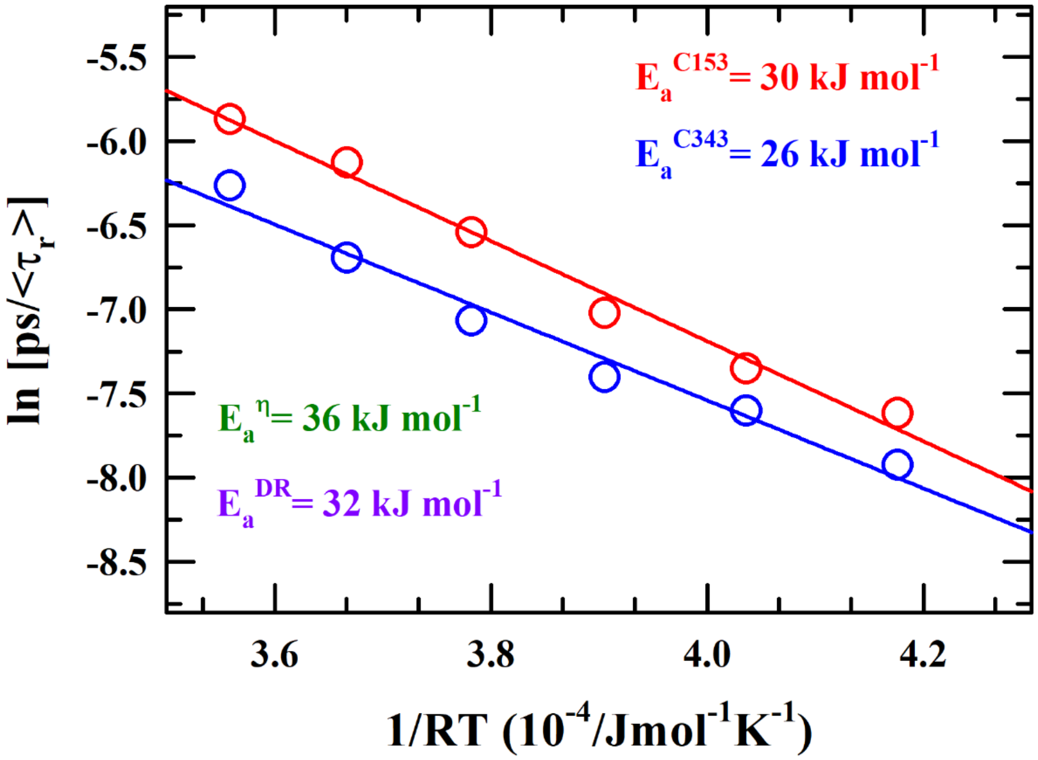

Figure 6.8. Arrhenius plot for temperature-dependent average rotation times ($\langle\tau_r\rangle$) of two different solutes, C153 and C343, dissolved in the molten mixture are shown here. Solid lines represent the linear fits through the respective data sets. Activation energies estimated are mentioned in the respective plots.

The dynamic heterogeneity aspect was further explored via comparing the activation energies related to solute rotation times, $\langle\tau_r\rangle$ for C153 and C343, $\langle\tau_{DR}\rangle$ and viscosity coefficient, η. In **Figure 6.8**, we present the Arrhenius-type temperature dependence of $\langle\tau_r\rangle$ for the two solutes. The corresponding activation energies are indicated in the respective plots alongside the activation energies obtained previously from $\langle\tau_{DR}\rangle$ and η are also shown. A comparison among these suggests activation energy exerted by medium viscosity is greater than the rotation of both the solutes indicating that the solute rotation is not fully governed by the medium viscosity. Rather, moderate viscosity decoupling between the two processes is observed. In contrast, the close resemblance between the viscosity activation energy and that of average DR times activation energy ($E_a^{\langle\tau_{DR}\rangle}$~32 kJ mol^{-1}) suggests that the medium dynamics follow the viscosity trends and thus follow the hydrodynamics. Two different observations of dynamic heterogeneity may come from differences between the two measurement techniques. DR measurements directly probe the medium dynamics by tracking the dipole moment fluctuation of the system and collective dynamic response of the medium is accessed to calculate such heterogeneity. On the other hand, the preferential position of the dye molecules in the medium and their length scale and time scales in fluorescence measurements dictate medium heterogeneity which is more local.

6.4 Conclusion

In summary, the present work demonstrates the preparation of a low viscous transparent multi-component molten mixture from biocompatible sorbitol, urea and water. The viscosity coefficient (η) of the molten mixture is comparably low and it has advantages over DES. A combined DR and fluorescence spectroscopic measurements were carried out to unveil the interaction, dynamics and heterogeneity aspect of the prepared molten mixture. DR spectroscopic measurements revealed the presence of 3/4-Debye relaxation dynamics of the system. The measured $\varepsilon_S{\sim}80$, of the system, resembles water making it a strong solvent with high solving power but dynamics are much slower than water. The absorption and emission results indicate that the interaction of the medium with hydrophobic C153 is more prominent than the hydrophilic C343. We found that the medium is spatially homogeneous within the lifetime of C153 and C343 though the signature of a mild dynamic heterogeneity is observed from the temperature-dependent fractional viscosity dependency of the rotational dynamic of used dye molecules (C153 and C343). This is in contrast to the DR spectroscopic findings where DR measurements found the system is dynamically homogeneous and it follows the viscosity trend of the system. Activation energy estimated from different measurement techniques supports the previous observation. This molten mixture can be utilised as a solvent media for reaction and also can be used for biomolecule stabilisation and activity improvement, as in Ace/Ure/Sor DESs.[76]

Appendix 6.A

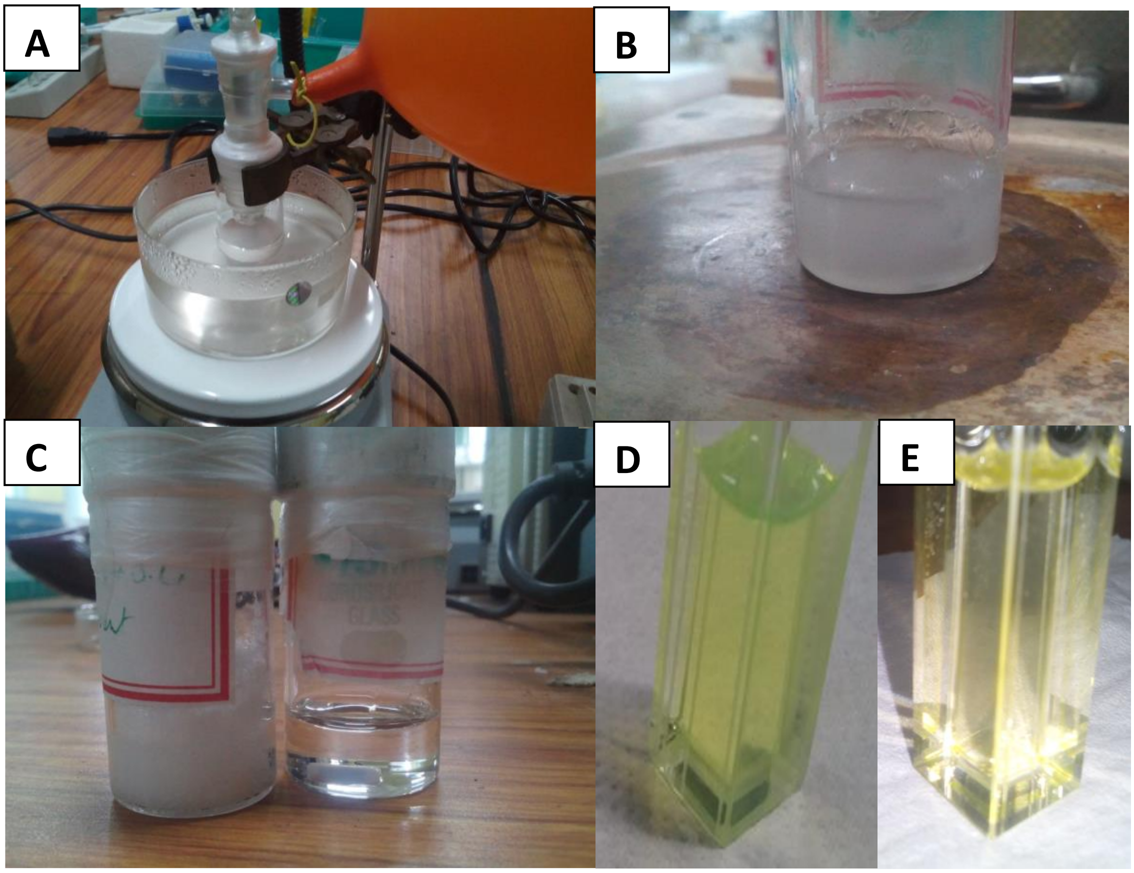

Figure 6.A.1. The molten mixture preparation setup is shown in '**A**'. 'B' represents a mixture at room temperature with a similar composition as (sorbitol+urea+water) molten mixture. '**C**' represents a solid mixture and a transparent molten mixture. 'D' and 'E' represent C343 and C153 solution in (sorbitol+urea+water) molten mixture.

Table 6.A.1. Temperature dependence of viscosity, density and refractive indices of (sorbitol+urea+water) molten mixture.

T (K)	Refractive Index	Density (g/cm^3)	Viscosity (cP)
288	1.4702	1.2953	73
298	1.4716	1.2888	40
308	1.4736	1.2823	24
318	1.4740	1.2756	16
328	1.4744	1.2688	11
338	1.4765	1.2619	8

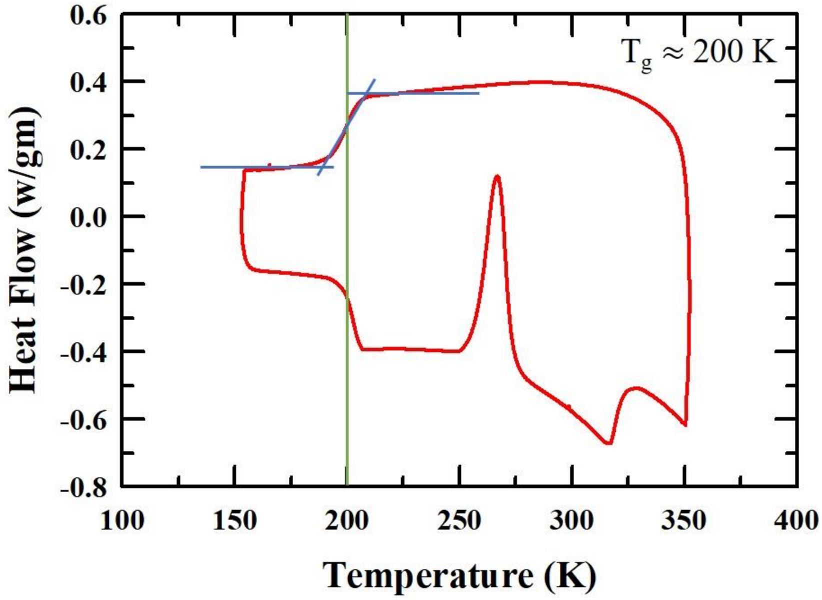

Figure 6.A.2. Differential scanning calorimetric (DSC) trace for (sorbitol+urea+water) molten mixture. The glass transition temperature (T_g) is indicated

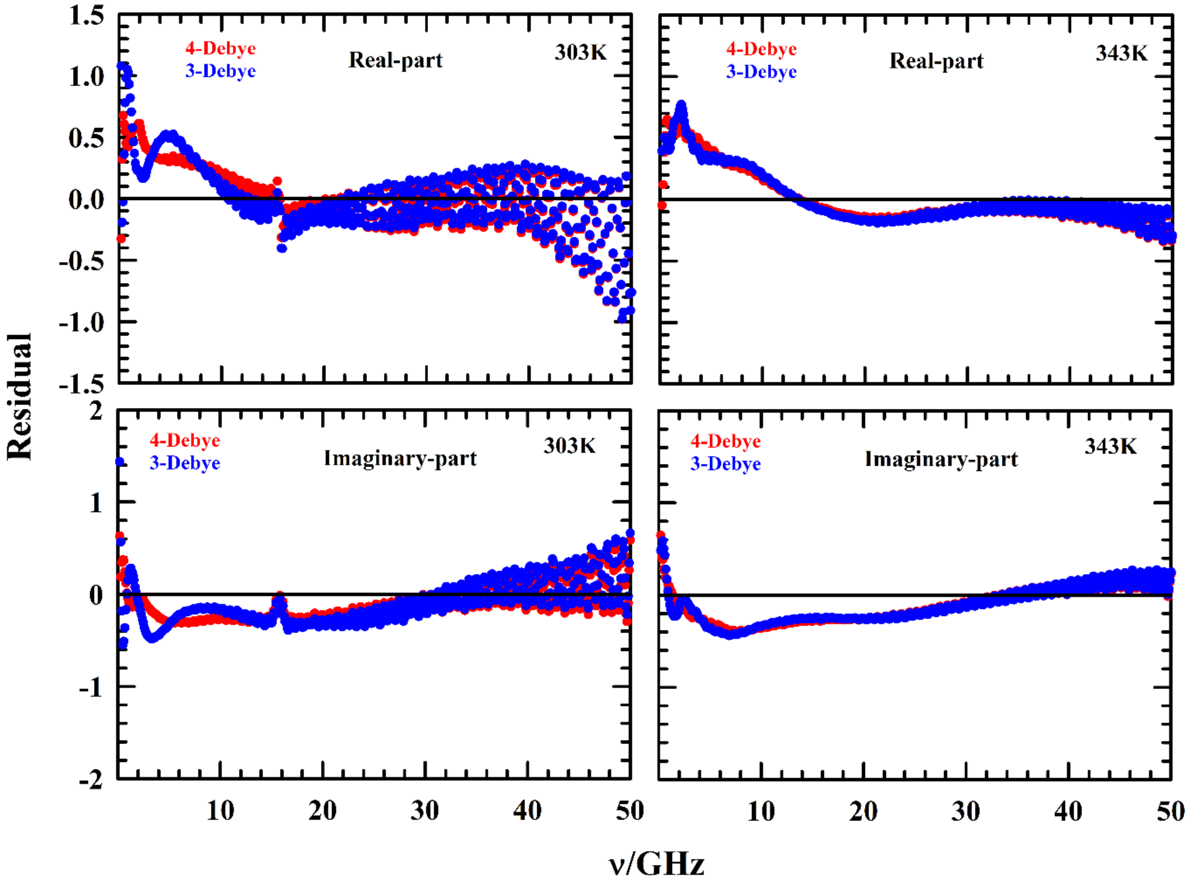

Figure 6.A.3. Residual comparison (both real (ε') and imaginary part (ε'')) between 3-Debye and 4-Debye DR fitting of (sorbitol+urea+water) molten mixture at two different temperatures, 303K (*left panel*) and 343K (*right panel*). All representations are colour-coded.

Table 6.A.2. Hydrodynamic molecular rotation times for sorbitol, urea and water were calculated using the SED relation with stick boundary condition, $\tau_r = \frac{3V\eta}{k_b T}$. van der Waals volume of sorbitol and urea used here were calculated using the reference.[1]

T(K)	η (cP)	Sorbitol ($V = 165$ Å^3) τ_r(ns)	Urea ($V = 54$ Å^3) τ_r(ns)	Water ($V = 17$ Å^3) τ_r(ns)
303	33	3.9	1.3	0.40
308	24	2.8	0.91	0.29
313	21	2.4	0.79	0.25
318	16	1.8	0.59	0.19
323	14	1.6	0.51	0.16
328	11	1.2	0.39	0.12
333	9	0.97	0.32	0.10
338	8	0.85	0.28	0.09
343	6	0.63	0.21	0.06

Reference:

1. Y. H. Zhao, M. H. Abraham, A. M. Zissimos, *J. Org. Chem.*, 2003, **68**, 7368.

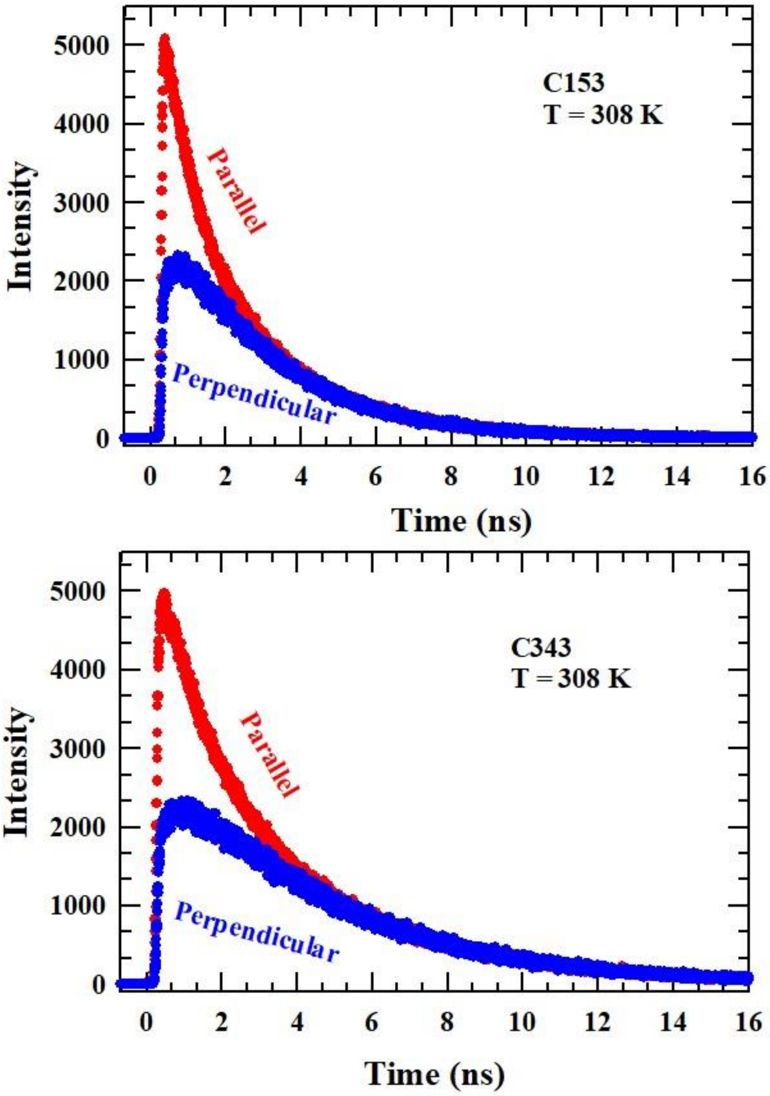

Figure 6.A.4. Representative fluorescence intensity decays of C153 (upper panel) and C343 (lower panel) in (sorbitol+urea+water) molten mixture DES at 308 K, collected with different emission polarizations.

References:

1 M. Ikeda, *Toxicol. Lett.*, 1992, **64–65**, 191–201.

2 M. Aksoy, *Environ Health Perspect.*, 1989, **82**, 193–197.

3 A. Çakmak, A. Ekici, M. Ekici, M. Arslan, A. Iteginli, E. Kurtipek and T. Kara, *Respir. Med.*, 2004, **98**, 52–56.

4 D. Majumdar (neé Som), C. Dutta, A. K. Mukherjee and S. Sen, *Transp. Res D Transp. Environ.*, 2008, **13**, 524–530.

5 R. Noyori, *Chem. Rev.*, 1999, **99**, 353–354.

6 A. Das, R. Biswas and J. Chakrabarti, *J. Phys. Chem. A.*, 2011, **115**, 973–978.

7 S. V Dzyuba and R. A. Bartsch, *Angew. Chem. Int. Ed.*, 2003, **42**, 148–150.

8 P. G. Jessop and B. Subramaniam, *Chem. Rev.*, 2007, **107**, 2666–2694.

9 J. P. Hallett, C. L. Kitchens, R. Hernandez, C. L. Liotta and C. A. Eckert, *Acc. Chem. Res.*, 2006, **39**, 531–538.

10 A. M. Scurto, K. Hutchenson and B. Subramaniam, *ACS Symposium Series*, 2009, **1006**, 3–37.

11 Z. Lei, B. Chen, Y.-M. Koo and D. R. MacFarlane, *Chem. Rev.*, 2017, **117**, 6633–6635.

12 T. Welton, *Chem. Rev.*, 1999, **99**, 2071–2083.

13 M. J. Earle and K. R. Seddon, *Pure Appl. Chem*, 2000, **72**, 1391–1398.

14 J. Płotka-Wasylka, M. de la Guardia, V. Andruch and M. Vilková, *Microchem. J.*, 2020, **159**, 105539.

15 S. V. Volkov, *Chem. Soc. Rev.*, 1990, **19**, 21.

16 Q. Sun, S. Zhu, Z. Shen, Y. Liu, C. Wu, L. Kang and Y. Yang, *Mater. Today Chem.*, 2023, **29**, 101419.

17 B. B. Hansen, S. Spittle, B. Chen, D. Poe, Y. Zhang, J. M. Klein, A. Horton, L. Adhikari, T. Zelovich, B. W. Doherty, B. Gurkan, E. J. Maginn, A. Ragauskas, M. Dadmun, T. A. Zawodzinski, G. A. Baker, M. E. Tuckerman, R. F. Savinell and J. R. Sangoro, *Chem. Rev.*, 2021, **121**, 1232–1285.

18 E. L. Smith, A. P. Abbott and K. S. Ryder, *Chem. Rev.*, 2014, **114**, 11060–11082.

19 T. El Achkar, H. Greige-Gerges and S. Fourmentin, *Environ. Chem. Lett.*, 2021, **19**, 3397–3408.

20 B. B. Hansen, S. Spittle, B. Chen, D. Poe, Y. Zhang, J. M. Klein, A. Horton, L. Adhikari, T. Zelovich, B. W. Doherty, B. Gurkan, E. J. Maginn, A. Ragauskas, M.

Dadmun, T. A. Zawodzinski, G. A. Baker, M. E. Tuckerman, R. F. Savinell and J. R. Sangoro, *Chem. Rev.*, 2021, **121**, 1232–1285.

21 Y. L. Chen, X. Zhang, T. T. You and F. Xu, *Cellulose*, 2019, **26**, 205–213.

22 S. Kaoui, B. Chebli, safa Zaidouni, K. Basaid and Y. Mir, *Sustain. Chem. Pharm.*, 2023, **31**, 100937.

23 G. Gygli, X. Xu and J. Pleiss, *Sci. Rep.*, 2020, **10**, 21395.

24 O. F. Stafford, *J. Am. Chem. Soc.*, 1933, **55**, 3987–3988.

25 D. H. Kerridge, *Chem. Soc. Rev.*, 1988, **17**, 181–227.

26 D. S. Baranov, S. F. Vasilevsky, B. Gold and I. V. Alabugin, *RSC Adv.*, 2011, **1**, 1745.

27 R. E. D. Clark, *Nature*, 1951, **168**, 876–876.

28 T. Voisin, A. Erriguible and C. Aymonier, *Sci. Adv.* 2020, **6**, 7770.

29 S. Gao, W. Tang, M. Zhao, S. Qie, W. Pang and L. Tian, *Asia-Pac. J. Chem. Eng.*, 2021, **16**, e2609

30 Y. Dai, G.-J. Witkamp, R. Verpoorte and Y. H. Choi, *Food Chem.*, 2015, **187**, 14–19.

31 Y. Huang, F. Feng, J. Jiang, Y. Qiao, T. Wu, J. Voglmeir and Z.-G. Chen, *Food Chem.*, 2017, **221**, 1400–1405.

32 Y. Dai, G.-J. Witkamp, R. Verpoorte and Y. H. Choi, *Anal. Chem.*, 2013, **85**, 6272–6278.

33 M. Vilková, J. Płotka-Wasylka and V. Andruch, *J. Mol. Liq.*, 2020, **304**, 112747.

34 J. Peon, D. Polshakov and B. Kohler, *J. Am. Chem. Soc.*, 2002, **124**, 6428–6438.

35 J. Najbar, R. C. Dorfman and M. D. Fayer, *J Chem Phys*, 1991, **94**, 1081–1092.

36 R. Buchner and J. Barthel, *Annu. Rep. Prog. Chem., Sect. C: Phys. Chem.*, 2001, **97**, 349–382.

37 P. C. Bressloff and J. M. Newby, *Rev. Mod. Phys.*, 2013, **85**, 135–196.

38 S. S Mogre, A. I. Brown and E. F. Koslover, *Phys. Biol.*, 2020, **17**, 061003.

39 A. M. Bosch and S. Assenza, *Pharmaceutics*, 2023, **15**, 573.

40 J. R. Darvin and M. A. Berg, *J. Phys. Chem. Lett.*, 2019, **10**, 6885–6891.

41 D. Bedrov, G. Smith and J. F. Douglas, *Polymer*, 2004, **45**, 3961–3966.

42 R. B. Jordan, *Reaction Mechanisms of Inorganic and Organometallic Systems*, Oxford University Press, 2007.

43 H. Fröhlich, *Theory of dielectrics; dielectric constant and dielectric loss.*, Oxford, Clarendon Press, 1949.

44 F. Kremer and A. Schönhals, *Broadband Dielectric Spectroscopy*, Springer Berlin, 2003.

45 T. Sato and R. Buchner, *J. Phys. Chem. A*, 2004, **108**, 5007–5015.

46 J. G. Kirkwood, *J. Chem. Phys.*, 1939, **7**, 911–919.

47 K. Mukherjee, A. Das, S. Choudhury, A. Barman and R. Biswas, *J. Phys. Chem. B.*, 2015, **119**, 8063–8071.

48 D. J. S. Birch and R. E. Imhof, *Topics in Fluorescence Spectroscopy, Vol. 1: Techniques.*, Plenum Press, New York, 1991.

49 B. Guchhait, H. Al Rasid Gazi, H. K. Kashyap and R. Biswas, *J. Phys. Chem. B.*, 2010, **114**, 5066–5081.

50 T. Pradhan and R. Biswas, *J. Phys. Chem. A.*, 2007, **111**, 11524–11530.

51 T. Pradhan, H. A. R. Gazi and R. Biswas, *J. Chem. Phys.*, 2009, **131**, 54507.

52 R. F. Grote, G. der Zwan and J. T. Hynes, *J Phys Chem*, 1984, **88**, 4676–4684.

53 J. Mondal, D. Maji and R. Biswas, *J Chem Phys* 2024, **160**, 084506.

54 A. Das and R. Biswas, *J Phys Chem B*, 2015, **119**, 10102–10113.

55 H. A. R. Gazi, H. K. Kashyap and R. Biswas, *J. Chem. Sci.*, 2015, **127**, 61–70.

56 E. Tarif, J. Mondal and R. Biswas, *J. Phys. Chem. B.*, 2019, **123**, 9378–9387.

57 C. J. F. Böttcher, O. C. van Belle, P. Bordewijk and A. Rip, *Theory of electric polarization, Volume 2*, Elsevier Scientific Publishing Company, Netherlands, 1996.

58 D. W. Davidson and R. H. Cole, *J. Chem. Phys.*, 1951, **19**, 1484–1490.

59 K. S. Cole and R. H. Cole, *J. Chem. Phys.*, 1941, **9**, 341–351.

60 Bevington, P. R. and D. K. Robinson, *Data reduction and error analysis for the physical sciences*, McGraw-Hill:, New York, Third Edition, 1969.

61 T. Pradhan and R. Biswas, *J. Phys. Chem. A*, 2007, **111**, 11514–11523.

62 H. A. R. Gazi, B. Guchhait, S. Daschakraborty and R. Biswas, *Chem. Phys. Lett.*, 2011, **501**, 358–363.

63 R. Biswas, A. R. Das, T. Pradhan, D. Touraud, W. Kunz and S. Mahiuddin, *J. Phys. Chem. B*, 2008, **112**, 6620–6628.

64 M.-L. Horng, J. A. Gardecki and M. Maroncelli, *J. Phys. Chem. A*, 1997, **101**, 1030–1047.

65 S. Koley, H. Kaur and S. Ghosh, *Phys. Chem. Chem. Phys.*, 2014, **16**, 22352–22363.

66 K. Mukherjee, S. Das, E. Tarif, A. Barman and R. Biswas, *J. Chem. Phys.*, 2018, **149**, 124501.

67 E. Tarif, K. Mukherjee, A. Barman and R. Biswas, *J. Chem. Sci.*, 2019, **131**, 1–12.

68 I. Płowaś-Korus and R. Buchner, *Phys. Chem. Chem. Phys.*, 2019, **21**, 24061–24069.

69 D. Maji and R. Biswas, *J. Chem. Phys.*, 2023, **158**, 174503.

70 M. L. Horng, J. A. Gardecki, A. Papazyan and M. Maroncelli, *J. Phys. Chem.*, 1995, **99**, 17311–17337.

71 E. Tarif, J. Mondal and R. Biswas, *J. Mol. Liq.*, 2020, **303**, 112451.

72 S. Dinda, A. Sil, A. Das, E. Tarif and R. Biswas, *J. Mol. Liq.*, 2022, **349**, 118126.

73 E. Tarif, J. Mondal and R. Biswas, *J. Mol. Liq.*, 2020, **303**, 112451.

74 M. D. Ediger, *Annu. Rev. Phys. Chem.*, 2000, **51**, 99–128.

75 J. R. Lakowicz, Ed., *Principles of Fluorescence Spectroscopy*, Springer US, Boston, 2006.

76 N. Das, T. Khan, N. Subba and P. Sen, *Phys. Chem. Chem. Phys.*, 2021, **23**, 9337–9346.

Chapter 7

Detection of Ultrafast Solvent Dynamics Employing a Streak Camera

7.1 Introduction

Solvation dynamics is a fundamental process in chemistry[1,2] and biology[3,4], and critically influences solution phase chemical reactions[5,6] and biological functions.[2,7–9] Understanding solvation dynamics requires the ability to capture ultrafast events occurring on sub-picosecond timescale, which can be achieved by employing ultrafast spectroscopic detection technique such as fluorescence up-conversion while performing time-resolved fluorescence Stokes shift measurements. Streak camera-based detection provides another powerful way for studying ultrafast events, [10–16] and has enabled researchers to capture dynamic processes taking place on sub-picosecond timescale.[17]

EG is one of the most widely used solvents because of several interesting physicochemical proerties[18] that include high boiling point, low toxicity, and ability to dissolve a wide range of solutes[19], and biomolecules such as proteins and nucleic acids[20–22] EG has also found industrial applications as antifreeze medium,[23,24] coolant[25,26] and solvents for paints and coating.[27,28] Glycerol is widely used as a cryoprotectant[29–32] and a protein stabilizer. [33–35] The cryoprotection arises from inhibiting the formation of ice crystals and subsequently protecting the cells from damage. Glycerol has found applications in cosmetic, pharmaceutical, and food production industries [36] as well.

C153, regarded as a gold standard fluorescent probe, has been widely employed in the study of solvation dynamics of common dipolar solvents,[37] binary mixtures,[38,39] confined systems,[40–42] ionic and neutral deep eutectics[43,44] ionic liquids,[45–47] and proteins. [48] Interestingly, ultrafast dynamic Stokes shift measurements of C153 via streak camera-based detection system has not been conducted yet, although fluorescence up-conversion, a popular technique for capturing sub-picosecond solvent response, has repeatedly used this gold standard solvation probe. Note the dipole moment of C153 in its ground (S_0) electronic state is ~6.6 D[49] and, depending on solvents,[50] ~14 -16 D in the first excited electronic state (S_1).

DMASBT is a heterocyclic organic dye that has several applications, including as an organic light-emitting diode, a laser dye, and a fluorescent labelling agent[51]. It is also known to be nongenotoxic and may be used as a drug molecule due to the presence of its benzothiazole ring[52]. In fluorescence studies, DMASBT is particularly important due to its sensitivity to both solvent polarity and viscosity. Unlike other fluorescent molecules such as coumarins and molecular rotors, emission intensity and wavelength of DMASBT are affected by both solvent polarity and viscosity[53]. This unique characteristic makes it a potential candidate as a sensitive biosensor[54]. Structural nature of DMASBT also allows it to act as a molecular probe to study biological functions and biomimicking systems[54]. In particular, DMASBT has been found to act as a surface probe to monitor the premicellar aggregation and phase change during the process[55]. It also induces the formation of nanotubular suprastructures by cyclodextrins[55,56].

Despite DMASBT undergoing an easy photoinduced trans-cis isomerization process, the lifetime of cis isomer is only about ~1 ps and has a negligible contribution to the emission spectrum under steady-state conditions. The similarity between the absorption and emission transition moments in a variety of solvents suggests that the absorption and emission processes involve the same two electronic states (S0 ↔ S1) in them.[57] These previous observations make DMASBT a probe to be studied in solvation dynamics. The ground state and the excited state dipole moments reported as 4.5 D and 10.2 D respectively[57]. Moreover, the relatively shorter excited state lifetime of DMASBT provides an opportunity to probe the importance of the slow diffusive solvent modes in governing the solvation response at long time. However, to the best of our knowledge, there has been no study yet that employed DMASBT as a solvation probe. We present here such a study where DMASBT and C153 have been used as solvation probes in order to highlight the importance of the slow diffusive solvent modes for complete measurements of polar solvation response in two polar solvents of differing viscosities, glycerol and EG. Chemical structures of these probes and solvents are shown in Scheme 1.

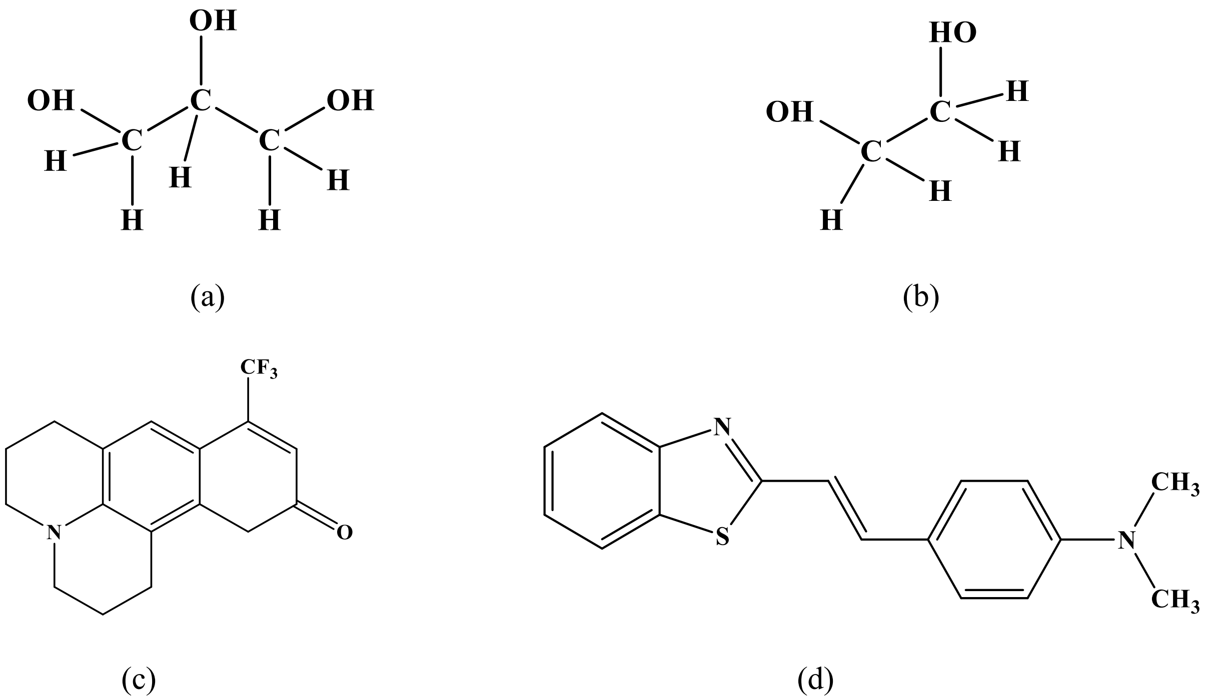

(a) (b)

(c) (d)

Scheme 1. Chemical structures of (a) glycerol, (b) ethylene glycol, (c) coumarin 153, and (d) trans-2-[4-(dimethylamino)styryl] benzothiazole.

7.2 Experimental Methods

7.2.1 Chemicals and Samples Preparation

Laser grade Coumarin 153 (C153) and trans-2-[4-(dimethylamino)styryl] benzothiazole (DMASBT) were used without further purification. Both of these chemicals were purchased from Sigma Aldrich. Glycerol (≥99%, Sigma-Aldrich) and anhydrous ethylene glycol (≥99.8%, Sigma-Aldrich) were also used without any further purification. The concentration of both C153 and DMASBT in the solution was kept approximately 10^{-6} M for all the experiments performed in this study.

7.2.2 Absorption and Steady-State Fluorescence Emission Data Collection and Analysis

The study employed UV-Visible spectrophotometer (UV-2600, Shimadzu) and fluorimeter (Fluorolog, Jobin-Yvon, Horiba) connected with a Peltier-temperature controller to collect steady-state absorption and emission data, respectively. The solvent blank spectra were subtracted from the probe spectra and converted appropriately from linear wavelength to linear frequency domain prior to analysis for frequency determination and other spectral properties[37].

7.2.3 Data Collection and Two Dimensional Streak Camera (2DSC) Measurement Protocol

For ultrafast detection of the solvent response, the relevant time-resolved fluorescence spectra were collected by using a streak camera (Optoscope SC-10) in this experiment. A spectrograph (HRS-300SS, Princeton instruments) with a 300 mm path length and grating constant of 300 grooves/mm and central wavelength fixed at the peak wavelength of fluorescence emission spectrum of the solute probe dissolved in the solvent under investigation was used in combination with the streak camera. The excitation light was generated from a Ti:Sapphire laser (Mai Tai HP-1040S, Spectra physics). The laser pulse had a pulse width of 100 fs and a repetition rate of 80 MHz, and the frequency-doubled light at 440 nm was generated by a BBO crystal from an 880 nm laser pulse. The sample was placed in a 1 cm path length quartz cuvette, and the excitation was focused onto the sample after passing through a 440 nm interference filter. The emitted fluorescence was collected at a right angle with respect to the excitation and was then focused by two lenses onto the entrance slit of the monochromator with a slit width of 10 μm and a height of 4 mm. The fluorescence was then passed through a bandpass filter of 471 nm to eliminate scattering, and the fluorescence data were collected at the magic angle (54.7°) polarization. The whole fluorescence emission was diffracted in the spectrograph with central wavelength fixed at the emission peak maximum of each system with a spectral resolution of 0.09 nm. The wavelength-dispersed fluorescence was then focused onto the entrance of the streak camera. The streak camera system was operated in the photon counting mode with a 1392 (time) × 1040 (wavelength) pixel 2D image. One pixel in the time axis corresponds to 206.7 fs, and one pixel in the wavelength axis corresponds to 1.4 Å. The instrument response function (IRF) of the streak camera using scattering particle in water was recorded to be ~2.1 ps (FWHM of the collected spectrum). All images were collected in 1000 acquisitions, keeping the MCP gain at 800 V and delay at 32.5% with a sweep speed of 15 ps/mm. All the steady-state and time-resolved measurements were performed at 20 ± 2 °C. To obtain the time-resolved fluorescence spectra (TRES) at the desired delay times from the streak image, the wavelength-time 2D fluorescence profile obtained were divided into required time intervals (see **Figure 7.A.1** in Appendix 7.A), and corresponding TRES were generated by summing up the data along the time axis. Zero time was chosen from the streak image from where the fluorescence decay started (indicated in **Figure 7.A.1**). The TRES were taken at an interval of 207 fs (1 pixel) from 0 to 2 ps, after that 1034 fs (5 pixels) interval up to 20–30 ps, and then in the interval of 4.961 ps (24 pixels) to 60–70 ps and the rest in 10 ps interval (48 pixels). This scheme of time division was altered to suit different systems under study. After obtaining the TRES spectra, they were fitted with a log-normal line shape function. All the analyses were performed in the wavenumber plane. The peak frequency was obtained from each TRES and was then used to obtain the spectral response function. The spectral response function was calculated as follows[37]

$$S(t) = \frac{\nu(t)-\nu(\infty)}{\nu(0)-\nu(\infty)} \qquad (7.1)$$

Eq. 7.1 represents the time dependent relaxation of the solvation energy associated with the excited dipolar solute in the solvent, where ν(x) represents the frequency at time 0, t, and ∞. Magic angle intensity decay at the peak wavelength of the steady state of the dissolved probe in the solvent was collected to calculate the lifetime of the probes in the system[58].

A detailed discussion of streak camera operation procedure can be found in Chapter 2.

7.2.4 Time Correlated Single Photon Counting (TCSPC) Measurements and Analysis

TCSPC technique was employed to capture the relatively slower diffusive component of the solvent dynamics. The set-up (LifeSpec-ps, Edinburgh Instruments, U.K.) used was fitted with an LED that produced excitation light of wavelength of 409 nm.[58,59] Full-width half-maximum (FWHM) of the instrument response function was ~90 ps. To perform dynamic Stokes shift analysis, 15-16 fluorescent decays (at the magic angle) were collected at uniformly spaced wavelengths throughout the steady-state emission spectrum of the dissolved solute (probes) in the solvents. The time-resolved emission spectra (TRES) were regenerated following the established protocol[37,60].

After obtaining the time dependent frequencies, ($\nu(t)$), from the TCSPC data, they were appropriately combined with those accessed via the streak camera measurements in order to generate the full solvent response function, $S(t)$, defined by Eq. 7.1. This is how the detection of the polar solvation dynamics in glycerol and EG were maximized in the present study.

7.3 Results and Discussion

7.3.1 Steady State Absorption and Emission Spectral Features: Solvent Reorganization Energies for C153 and DMASBT

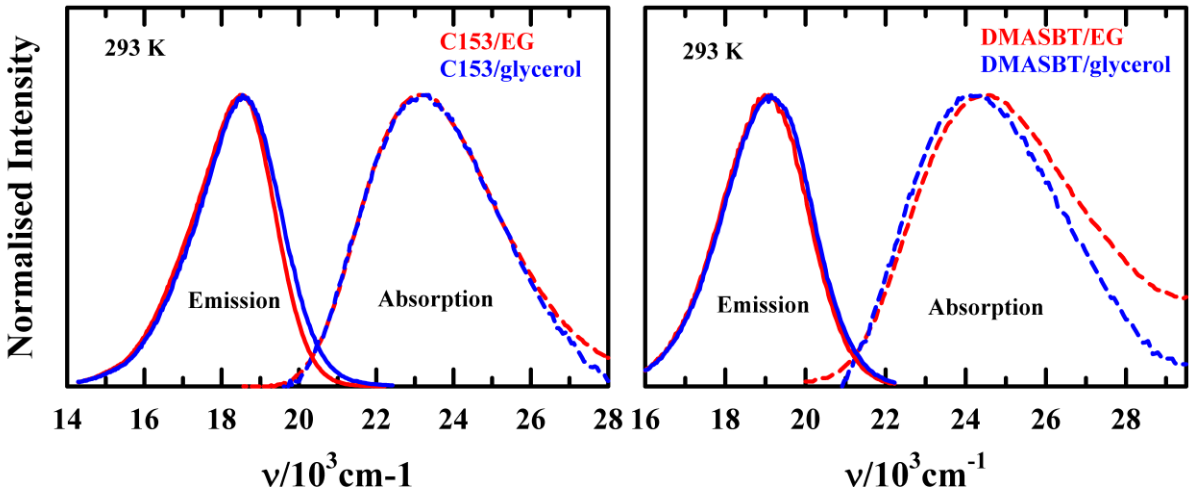

Figure 7.1. Steady-state absorption and emission spectra of C153 (left panel), and DMASBT (right panel) in EG and glycerol at 293K. All representations are colour-coded.

Steady state UV-VIS absorption and fluorescence emission spectra of C153 and DMASBT in EG and glycerol at 293K are shown in **Figure 7.1**. Clearly, no significant solvent dependence is visible in these spectra. This is not surprising because the static dielectric constants (ε_0) of glycerol and EG are nearly equal, suggesting that the solvent reorganization energies,[61] $\Delta\lambda_{sol} \approx \frac{1}{2}\Delta\Delta\nu$, with $\Delta\Delta\nu = [\nu^{abs.} - \nu^{em.}]^{polar} - [\nu^{abs.} - \nu^{em.}]^{nonpolar}$, in these two solvents should be very similar in magnitudes. This is indeed the case as the data summarized in **Table 7.A.1** and **Table 7.A.2** (Appendix 7.A) indicate, where a difference of ~300 cm^{-1} between them determined employing C153 can be accounted for by the error associated with the spectral measurements and the tiny difference between the solvent refractive indices. Note that we have used hexane as the nonpolar reference solvent in which the Stokes shift, $\Delta\nu^{nonpolar} = [\nu^{abs.} - \nu^{em.}]^{nonpolar}$, arises solely from the electronic part of the solvent polarization (through the solvent refractive index, n) because $\varepsilon_0 \approx n^2$ for hexane. **Figure 7.A.2** (Appendix 7.A) provides the steady state UV-VIS absorption and fluorescence emission spectra of C153 and DMASBT in these two solvents. These findings are consistent with previous studies that reported solvent polarity dependence of reorganization energy for different dipolar fluorescent probes.[57,62–64] For DMASBT, however, the difference in $\Delta\Delta\nu$ between these two solvents is

>500 cm^{-1}, and this manifests the simultaneous impact of the relatively shorter lifetime of DMASBT and higher viscosity of glycerol.

7.3.2 Average Fluorescence Lifetime Measurements: TCSPC and Streak Camera Data

The fluorescence lifetime decays of C153 and DMASBT in glycerol and EG measured via the TCSPC set-up (resolution ~90 ps) are displayed in **Figure 7.2**. Except for C153 in glycerol, a considerable portion of the faster decay in each of the cases is missing. This lacuna has been partly removed by the streak camera based detection system that provides a temporal resolution < 2 ps and proper estimates for $\langle\tau_{fl}\rangle$ made.

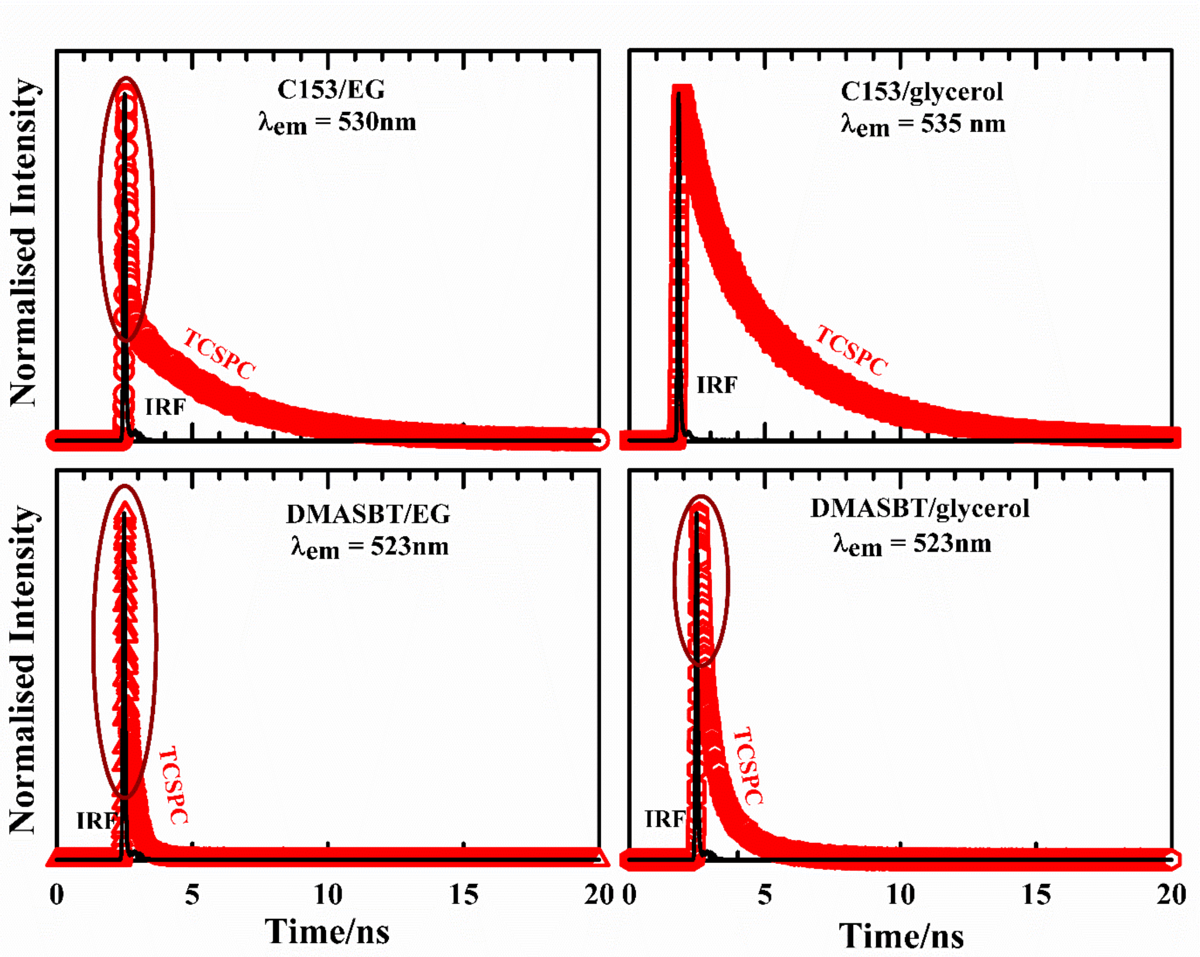

Figure 7.2. TCSPC data for fluorescence lifetime decays of C153 and DMASBT in EG and glycerol at 293 K. Photon counting were done at the respective peak wavelengths of the fluorescence emission spectra of these solute probes in EG and glycerol.

We next collected streak images for C153 and DMASBT in EG via the spectrograph with central wavelength fixed at 490 nm and 523 nm, respectively. In normal solvents, $\langle\tau_{fl}\rangle$ for C153 is ~4-5 ns at its emission peak maximum, whereas for DMASBT in low-viscous solvents [37,57] $\langle\tau_{fl}\rangle$ < 100 ps. Considering the maximum temporal detection range of our streak camera based detection system being 287 ps, we appropriately combined the streak camera data with those from TCSPC measurements for proper estimation of $\langle\tau_{fl}\rangle$ for C153 and DMASBT in these two solvents. Note here that the lifetime decay of DMASBT in EG is totally captured within the available detection time window of the streak camera, while the data stitching was necessary for other cases. These are shown below in **Figure 7.3** along with the corresponding multi-exponential fits. **Table 7.1** summarizes the fit parameters and the estimated $\langle\tau_{fl}\rangle$ values, While **Figure 7.A.3** (Appendix 7.A) represents the quality of fits obtained while describing the combined data via the fit function chosen.

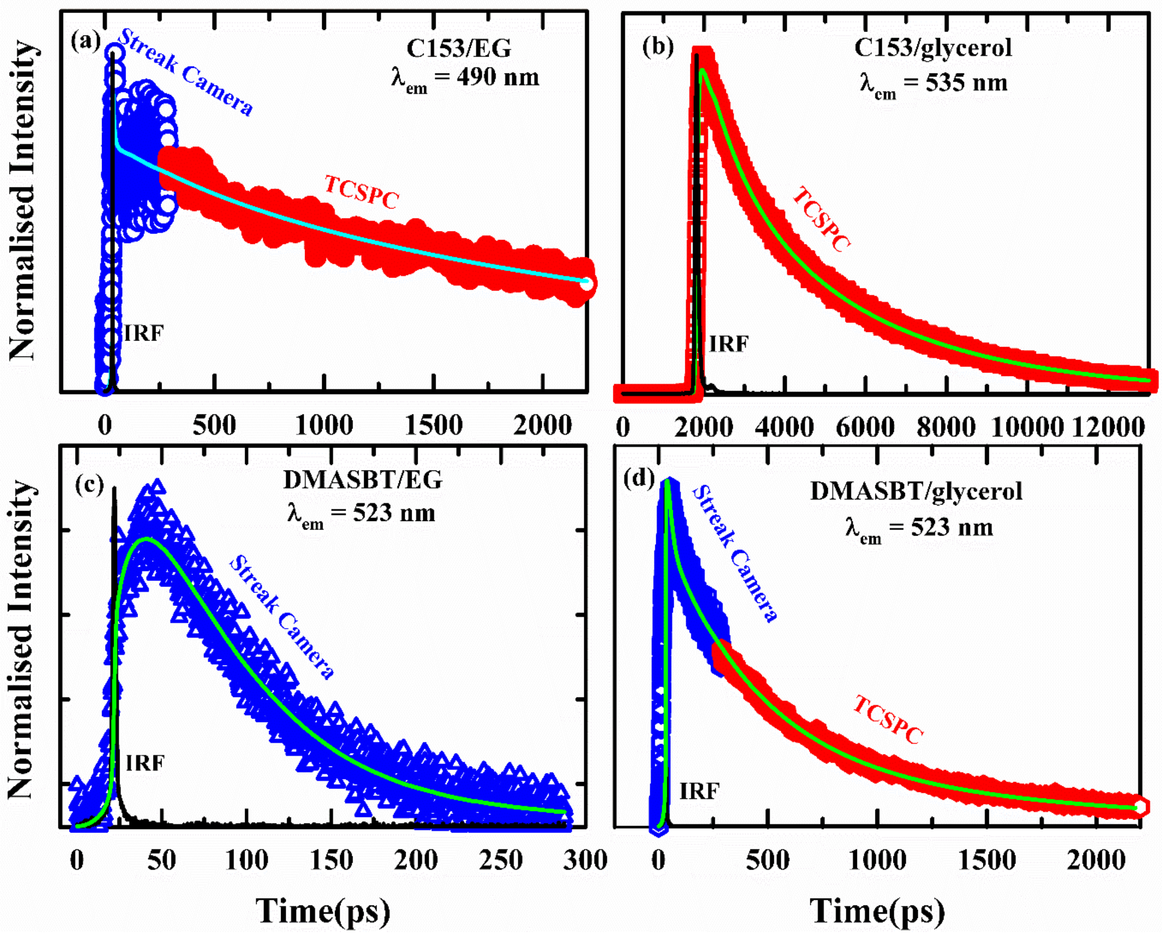

Figure 7.3. Combined (streak camera and TCSPC) lifetime decay data for C153 and DMASBT in EG and glycerol. Data from streak camera are represented by blue, while those from TCSPC denoted by red. Solid lines passing through the data represent the multi-exponential fits.

Table 7.1. Multi-exponential fit parameters associated with the fluorescence lifetime decays of C153 and DMASBT in EG and glycerol at 293 K. Data in parentheses are taken from literature for comparison.

Solute	Solvent	a_1	τ_1(ps)	a_2	τ_2(ps)	a_3	τ_3(ps)	$\langle\tau_{fl}\rangle$(ps)
C153	EG	0.08	30	0.18	563	0.74	3572	2694
	Gly	0.07	400	0.32	1000	0.61	3845	2744
DMASBT	EG	-0.36	20	0.64	64	-	-	121 (184)
	Gly	0.30	20	0.55 (0.32)	419 (257)	0.15 (0.68)	1583 (1100)	473 (880)

*Negative sign indicates the rise portion in lifetime decay of DMASBT in EG at 293 K.

Note that the $\langle\tau_{fl}\rangle$ values of C153 in EG and glycerol are very similar to each other, reflecting the insensitivity of $\langle\tau_{fl}\rangle$ to the medium viscosity. For DMASBT, however, this is not the case as the $\langle\tau_{fl}\rangle$ values suggest a significant viscosity dependence. As already discussed, this viscosity dependence arises from the photo-induced trans→cis isomerization of DMASBT producing the non-fluorescent cis conformer. A bi-exponential fit to the lifetime decay of DMASBT in EG produced a significant negative component with a time constant of 20 ps, suggesting a rise part in the fluorescence intensity decay, followed by a dominating decay component (~65%) with a time constant of 64 ps. The rise component may be a result of the probe rotation and vibrational relaxation of the dissolved probe. This is a proposition and requires independent experimental confirmation. The $\langle\tau_{fl}\rangle$ was calculated to be 121 ps and correlates well with a previous report ($\langle\tau_{fl}\rangle$ =184 ps)[57] via TCSPC measurements (temporal resolution ~25 ps). Subsequently, we estimated $\langle\tau_{fl}\rangle$ of DMASBT in a more viscous solvent, glycerol (η= 1489 cP at 293K)[65] than EG (η= 19.1 cP at 295K[66]). Bi-exponential fit parameters for lifetime intensity decay of DMASBT in glycerol reported in the literature[54] are shown in parentheses of **Table 7.1** for a comparison. Note that these data are from TCSPC measurements[54] performed with a temporal resolution ~50ps at 298K and collected at the red end emission wavelength, λ_{em} = 550 nm.

7.3.3 Solvation Dynamics

For complete measurements of the solvation dynamics via following the time dependent Stokes shift, we combined streak camera measurements with those from TCSPC. The streak image of C153 and DMASBT in EG and glycerol are shown below in **Figure. 7.4**.

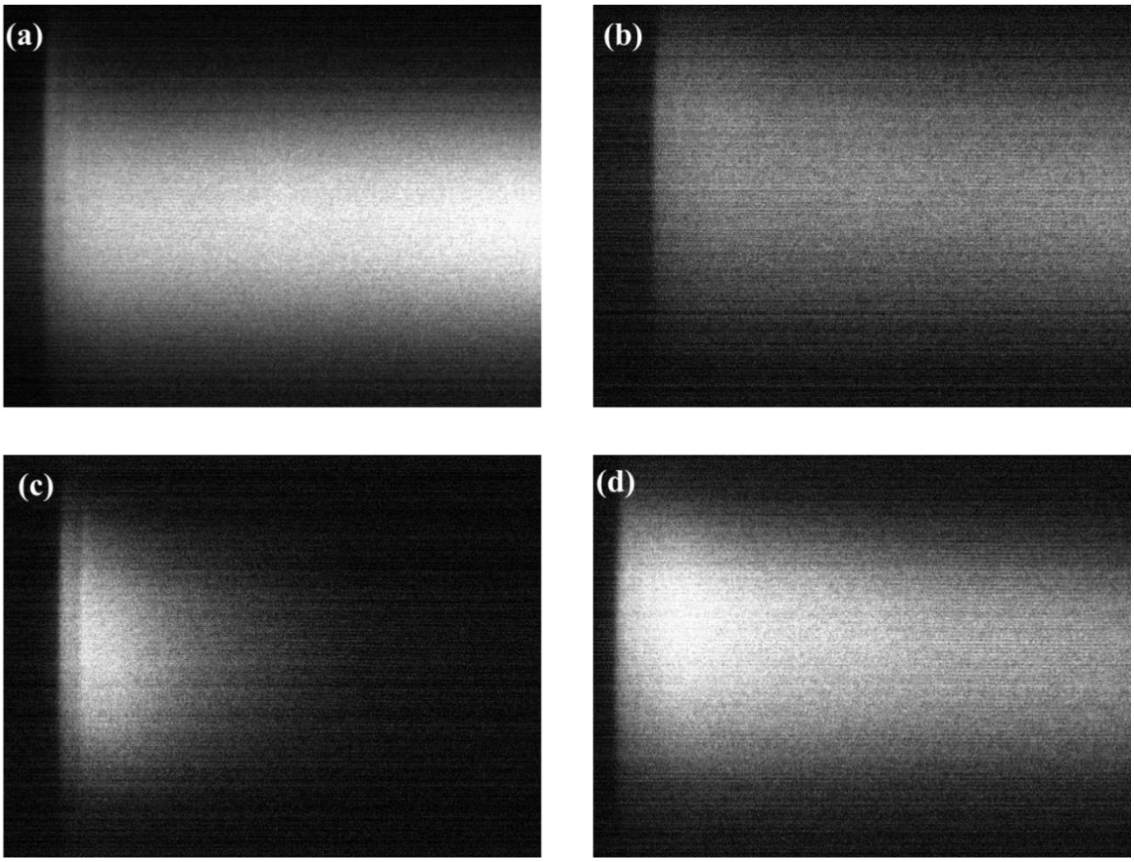

Figure 7.4. Two-dimensional streak camera image of (a) C153 in EG, (b) C153 in glycerol, (c) DMASBT in EG, and (d) DMASBT in glycerol at 293 K. Horizontal axis represents time evolution of the fluorescence intensity, while the perpendicular axis denotes spatial variation (wavelength) of the fluorescence emission at a given time.

To analyse the data, we extracted the time-resolved emission spectra (TRES) from the streak images and fitted each spectrum with a log-normal line shape function. As mentioned before, all of the analyses were performed after appropriately converting the wavelength data to the frequency plane. The time-evolution of the TRES for C153 and DMASBT in EG and glycerol are shown in **Figure 7.5** at three representative times. Note the high viscosity of glycerol allows DMASBT to probe solvent polarization density fluctuations even at t~ 250 ps, while this is limited to ~50 ps for EG. C153, in contrast, can probe successfully the solvent fluctuations both in EG and glycerol. Therefore, it is the rapidity of the solvent density fluctuations that dictates the solvent fluctuation timescales being probed by C153 in EG and glycerol, while it is the average lifetime of DMASBT that limits its application for a broad variety of solvents.

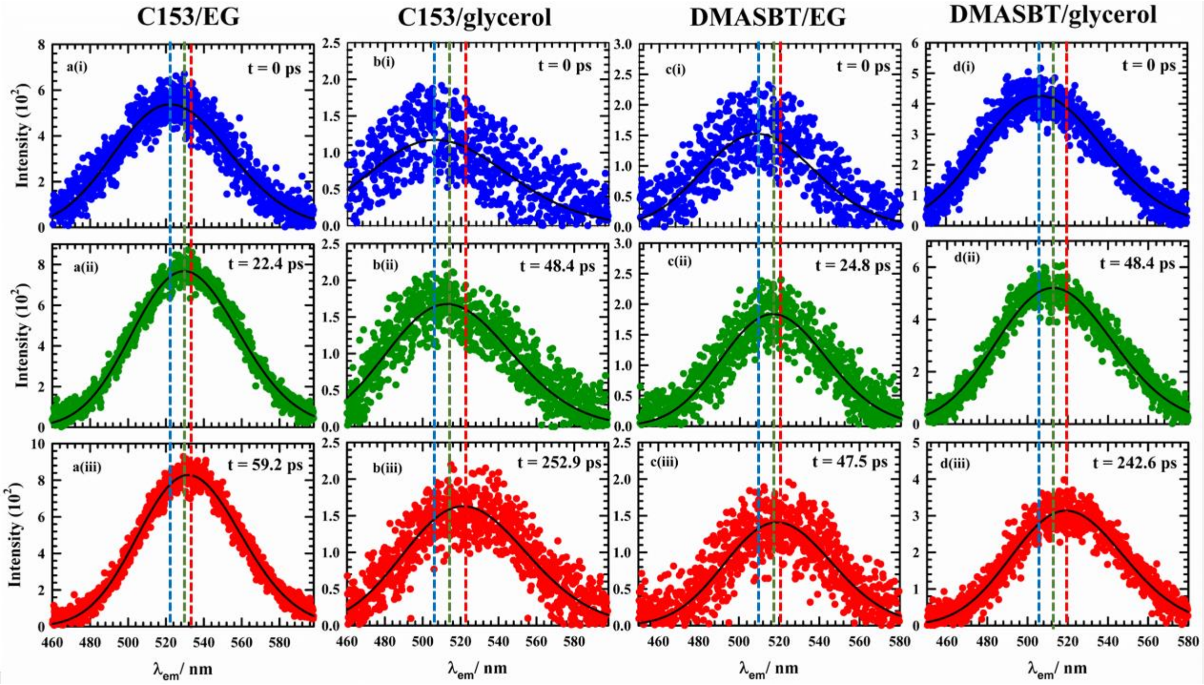

Figure 7.5. Representative TRES from the streak camera data (a) C153 in EG, (b) C153 in glycerol, (c) DMASBT in EG, and (d) DMASBT in glycerol. T = 293 K. The solid lines going through the data represent log normal fit to the data points. The vertical dashed lines indicate spectral shift with time.

The peak frequencies of these TRES were then used to obtain the spectral response function, $S(t)$, defined by Eq. 7.1. The time-integration of these $S(t)$ decays, which was found to be multi-exponential for each of these solute/solvent combinations, then produced the average solvation times, $\langle\tau_s\rangle = \int_0^\infty dt\, S(t) = \int_0^\infty dt\, \sum_i a_i \exp[-t/\tau_i]$, with a_i and τ_i being respectively the amplitudes and time constants associated with the decay components, and $\sum_i a_i = 1$.

7.3.4 Polar Solvation Dynamics Employing C153 and DMASBT: Probe Solute Dependence

We extracted the TRES of C153 in EG and glycerol was obtained by combining the streak images with the TCSPC data, while TRES of DMASBT were accessed only from the streak camera images. The upper panels of **Figure 7.6** shows the TRES of C153 in both the solvents along with the steady-state emission and the lower panels show the corresponding DMASBT data. The magnitudes of the total fluorescence spectral shifts or dynamic Stokes shifts, $\Delta\nu^t = \nu(t = 0) - \nu(t = \infty)$, observed in the present measurements are shown in **Table 7.2**. The estimated $\Delta\nu^t$ for these systems by applying the Fee-Maroncelli[67] method are also shown in the same table. Clearly, a large portion of the $\Delta\nu^t$ has been missed even when the TCSPC data were combined with those from streak camera. This underlines the inherent ultrafast character of the polar solvent dynamics in these poly-hydroxy alcohols.

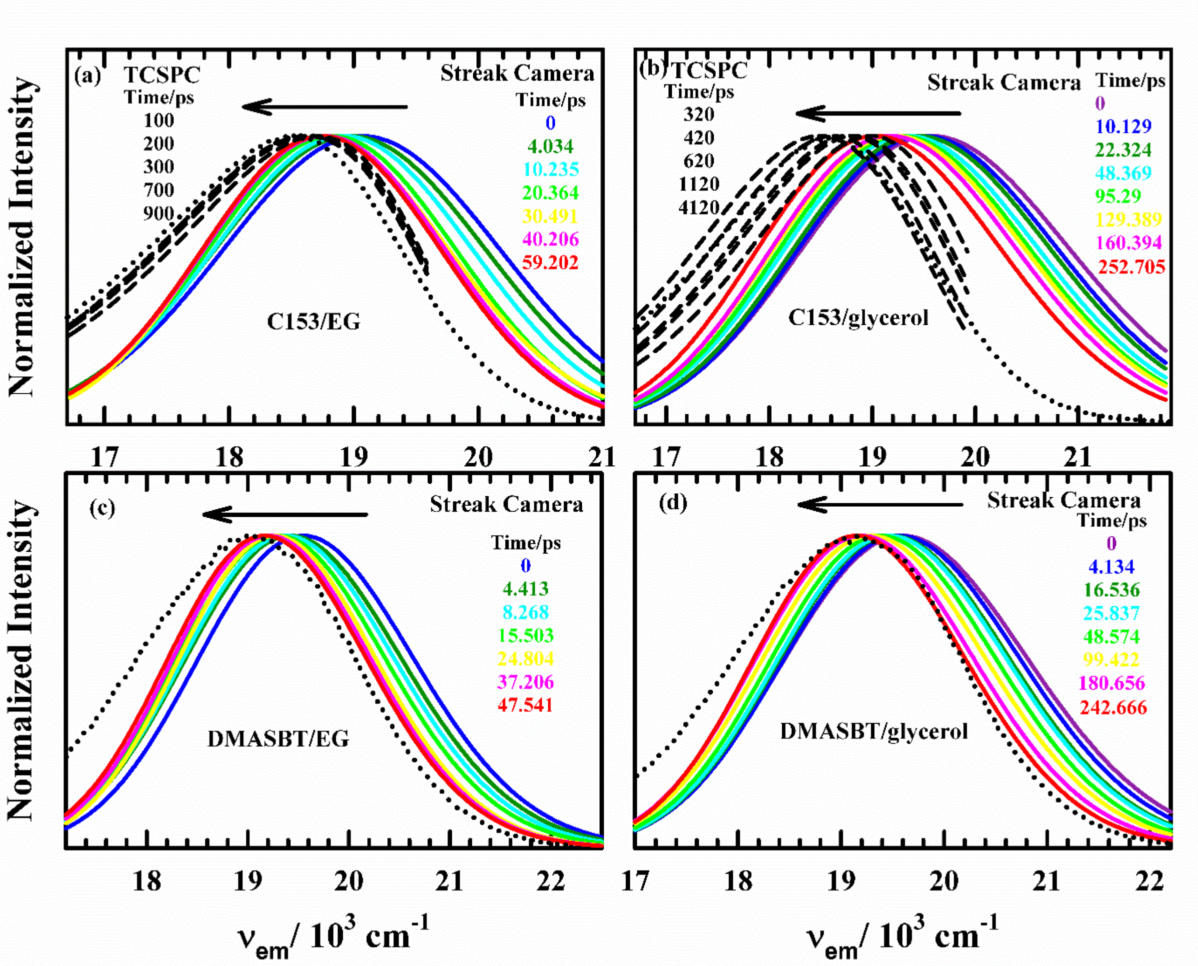

Figure 7.6. Representative time resolved emission spectra (TRES) of (a) C153 in EG, (b) C153 in glycerol, (c) DMASBT in EG, and (d) DMASBT in glycerol at 293 K. The steady state emission spectra of these solutes in ethylene and glycerol are shown by dotted lines in these panels. All representations are colour-coded.

Table 7.2. Magnitudes of estimated ($\Delta\nu_{est}$), and observed ($\Delta\nu_{Obs.}$) dynamic Stokes shift, and the corresponding missing percentages for C153 and DMASBT in EG and glycerol at 293 K. $\Delta\nu_{Obs.}^{2DSC}$and $\Delta\nu_{Obs.}^{TCSPC}$ denote dynamic shifts detected by the streak camera and TCSPC measurements, respectively. $\Delta\nu_{Obs.}^{Total} = \Delta\nu_{Obs.}^{2DSC} + \Delta\nu_{Obs.}^{TCSPC}$. % missed was calculated using total spectral shift ($\Delta\nu_{Obs.}^{Total}$) taking into account.

System	$\Delta\nu_{est}$(cm^{-1})	$\Delta\nu_{Obs.}^{2DSC}$ (cm^{-1})	$\Delta\nu_{Obs.}^{TCSPC}$(cm^{-1})	$\Delta\nu_{Obs.}^{Total}$(cm^{-1})	% missed
C153 in EG	1298	352	276	628	52
C153 in glycerol	1234	519	561	1080	12
DMASBT in EG	1783	362	-	362	80
DMASBT in glycerol	1327	468	-	468	65

The solvent response functions, $S(t)$, measured by C153 and DMASBT are shown in **Figure 7.7**. For C153 in EG, a sum of two exponentials was found to be sufficient to describe the measured $S(t)$, whereas a sum of four exponentials was needed to fit the $S(t)$ measured with C153 in glycerol. When we obtained the solvation response function solely from the streak camera data, a sum of three exponentials provided the best fit. The fitting parameters for all of the cases are summarized in **Table 7.3**.

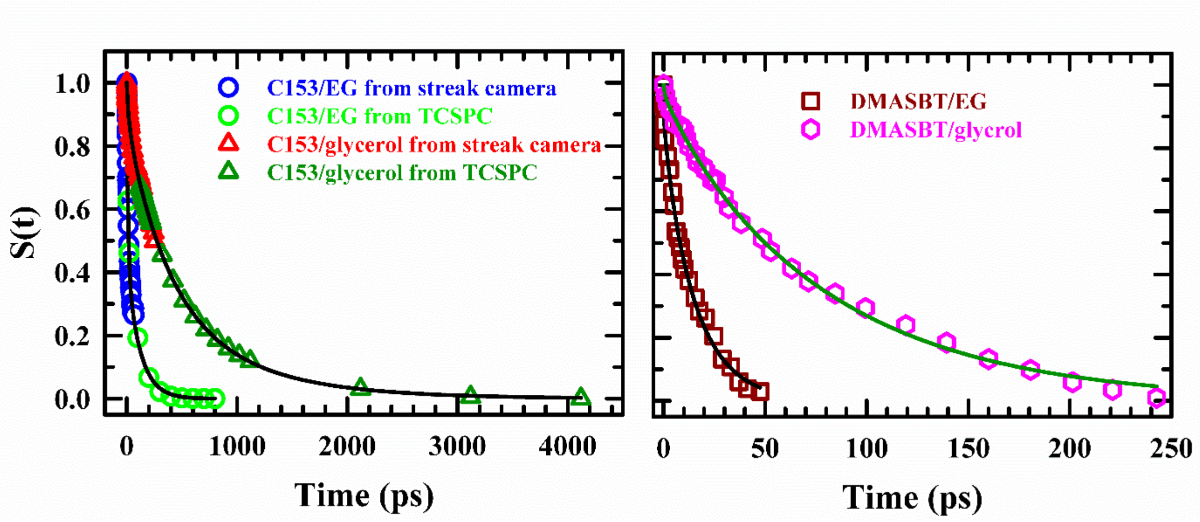

Figure 7.7. Solvation response functions, S(t), probed by C153 (left panel) in EG and glycerol measured by combining streak camera data with those from TCSPC at 293 K. S(t) for DMASBT (right panel) in these two solvents have been calculated from the streak camera

images only. Symbols represent the experimental data, while the solid lines through them denote multi-exponential fits.

Table 7.3. Multi-exponential fit parameters for $S(t)$ decays measured employing C153 and DMASBT in EG and glycerol at 293 K.

Solute	Solvent	a_1	τ_1(ps)	a_2	τ_2(ps)	a_3	τ_3(ps)	a_4	τ_4(ps)	$\langle\tau_s\rangle$(ps)
C153	EG			0.15	4.75	0.85	16.61			14.83
	EG*	0.05	5	0.52	12.2	0.43	117.6	-	-	57.2
	Gly	0.04	1.2	0.09	28.09	0.87	476.2			416.87
	Gly*	0.04	1.2	0.08	28.09	0.54	357.1	0.34	833	478.35
DMASBT	EG	0.11	0.226	0.08	3.6	0.81	16.05			13.31
	Gly	0.03	0.4	0.05	13.94	0.92	81.3			75.5

*Combine multi-exponential fit of C153 in EG and glycerol from streak camera and TCSPC data analysis at 293 K

The time constants summarized in **Table 7.3** clearly demonstrates that our streak camera based detection system can capture the rapid sub-picosecond solvation timescales in these polyhydroxy alcohols where the collective intermolecular H-bond network fluctuations are expected to produce significant ultrafast solvent response.[37,68] Interestingly, the 100 ps timescale in EG is realized only when TCSPC data for C153 were combined with the corresponding streak camera measurements. For glycerol, however, the average solvation times ($\langle\tau_s\rangle$) did not differ greatly upon combining data from these two techniques, although an extra solvation component with ~1ns timescale became visible when TCSPC data were stitched together. For EG, streak camera data provide very similar $\langle\tau_s\rangle$ values for dynamic Stokes shift measurements employing C153 and DMASBT, although the short-time dynamics reported by DMASBT is ultrafast (~200 fs) and larger in magnitude. Considering the fast rise observed for DMASBT/EG magic angle fluorescence intensity decay (see **Table 7.1**), this ultrafast timescale may not be solely connected to the polar solvation response. The longer timescales, however, are similar to those measured with C153 and can be regarded as polar solvation timescales. Note here that previous fluorescence up-conversion measurements for C153 in EG employing a temporal resolution of ~180 fs reported similar average solvation timescale as found in the present streak camera measurements.[37]

For glycerol, DMASBT fails completely to detect the slowest solvation timescale reported by C153. This is a direct consequence of much shorter $\langle\tau_{fl}\rangle$ for DMASBT than C153. This observation, therefore, limits the wide application of DMASBT as a solvation probe, particularly for slow viscous solvent systems. These results also show that probe solute dependence of polar solvation timescales may also occur from $\langle \tau_{fl} \rangle$ even if one employs detection techniques to capture both the initial fast response and the slow diffusive dynamics at later times.

7.4 Conclusion

In conclusion, our study has provided insight into the Stokes shift dynamics of two molecules in two polar protic solvents with different viscosities. The use of a combination of TCSPC technique and a 2DSC allowed us to capture a significant portion of the fast component of the total polar solvent response in EG and glycerol. Our findings revealed that the average fluorescence lifetime, in addition to temporal resolution and time window, is a controlling factor for measurements of the complete solvation response in slow viscous solvents. The probe solute dependence, which is not otherwise expected for polar solvation response because of the overwhelming dominance of the longer-ranged collective polarization density fluctuations, may therefore occur from the inherent excited state character of solutes employed for solvation measurements.

Appendix 7.A

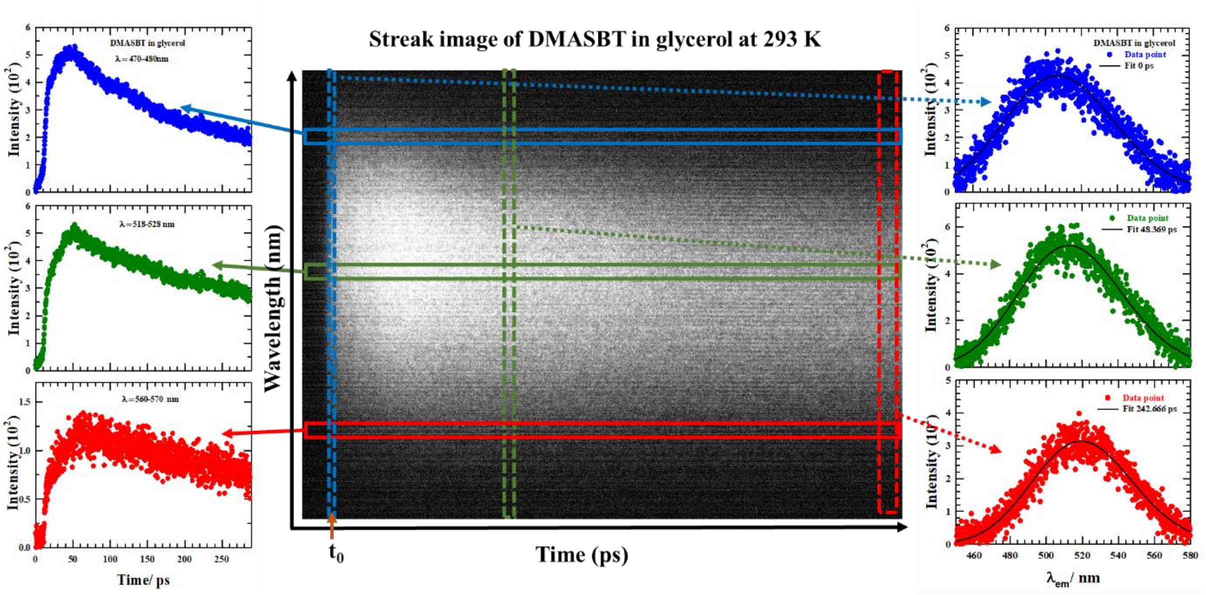

Figure 7.A.1. Streak image of DMASBT in glycerol. Horizontal line represents the time axis and vertical line is wavelength axis. The coloured stripes represent the blue end, emission peak wavelength and the red end emission region in the 2DSC image respectively. t_0 represents the initial time or zero time from where the emission decay starts and the time value increases along the positive x- axis.

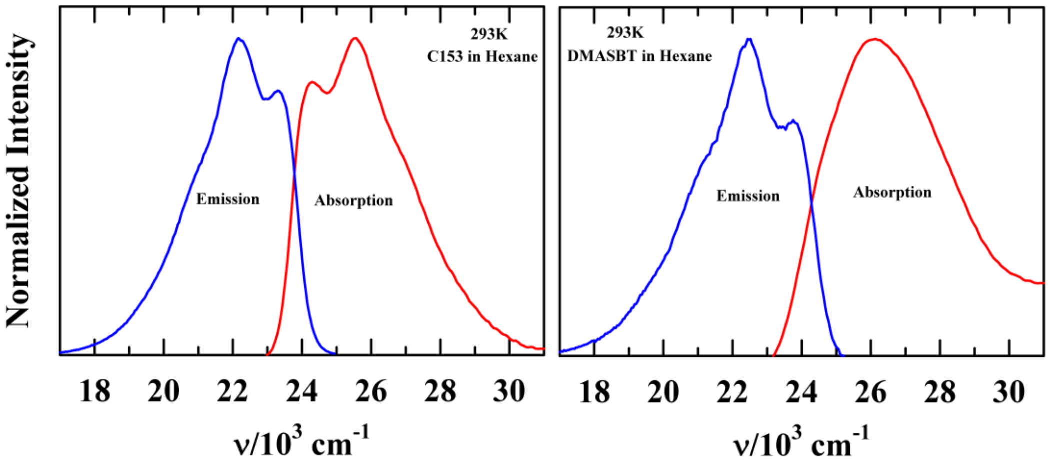

Figure 7.A.2. Steady state UV-VIS absorption and fluorescence emission spectra of C153 (left panel) and DMASBT (right panel) in the nonpolar solvent hexane at 293K. All representations are colour coded.

Table 7.A.1. Steady state spectral characteristics of C153 and DMASBT in hexane at 293K. In order to compare our findings, we have included values from the literature[37,57] in parentheses.

Absorption						Emission				
Solute	FPK[a] (cm^{-1})	1st Mom. Freq. (cm^{-1})	Avg.[b] Freq (cm^{-1})	Peak[c] Avg. (cm^{-1})	FWHM[d] (cm^{-1})	FPK (cm^{-1})	1st Mom. Freq. (cm^{-1})	Avg. Freq (cm^{-1})	Peak Avg. (cm^{-1})	FWHM (cm^{-1})
C153	25548	25911	25552 (25670)	25670	3644	22193	21948	22265 (22230)	22135	3154
DMASBT	26102	26883 (27130)	26475	26487	4316	22479	22113 (21870)	22488	22360	3553

[a] FPK is the peak frequency obtained from fit from the top 50% of the spectra taking two inverted parabolas.
[b] Avg. Freq. is the average of the frequencies at two half maxima points.
[c] Peak Avg. is the arithmetic mean of FPK, 1st Mom. Freq., and Avg. Freq.
[d] FWHM represents full width at half maximum of the spectra.

Table 7.A.2. Reorganization energy, $\frac{1}{2}\Delta\Delta\nu = \frac{1}{2}[\nu^{abs.} - \nu^{em.}]^{polar} - [\nu^{abs.} - \nu^{em.}]^{hexane}$ for C153 and DMASBT in EG and glycerol.

Frequency	$\Delta\nu_{HEX}^{C153}$ (cm^{-1})	$\Delta\nu_{EG}^{C153}$ (cm^{-1})	$\Delta\nu_{GLY}^{C153}$ (cm^{-1})	$\Delta\Delta\nu$(EG) (cm^{-1})	$\Delta\Delta\nu$(GLY) (cm^{-1})
FPK	3355	5033	4537	1678	1182
1st Mom. Freq	3963	5523	5121	1560	1158
Avg. Freq.	3287	5155	5015	1868	1728
Peak avg.	3535	5160	4891	1625	1356
	$\Delta\nu_{HEX}^{DMASBT}$ (cm^{-1})	$\Delta\nu_{EG}^{DMASBT}$ (cm^{-1})	$\Delta\nu_{GLY}^{DMASBT}$ (cm^{-1})	$\Delta\Delta\nu$(EG) (cm^{-1})	$\Delta\Delta\nu$(GLY) (cm^{-1})
FPK	3623	5446	4990	1823	1367
1st Mom. Freq	4770	6477	5863	1707	1093
Avg. Freq.	3987	6038	5489	2051	1502
Peak avg.	4127	5987	5447	1860	1320

‘GLY’ denotes glycerol, ‘HEX’ represents hexane

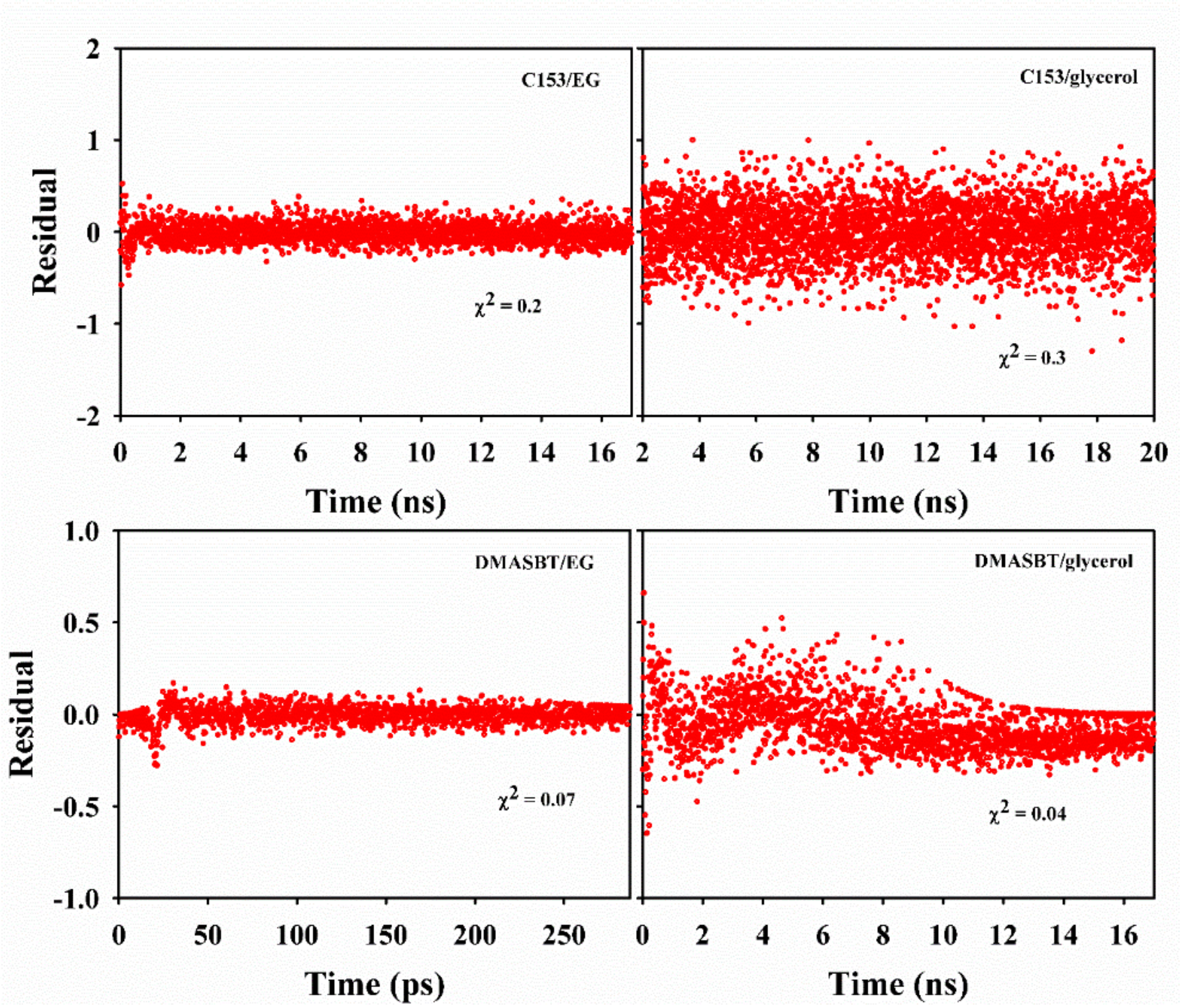

Figure 7.A.3. Residuals of fittings for C153 (upper panel) and DMASBT (lower panel) in the two solvents ethylene glycol and glycerol has been depicted. Note the experimental temperature is 293K.

References

1. R. Jimenez, G. R. Fleming, P. V. Kumar and M. Maroncelli, *Nature*, 1994, **369**, 471–473.
2. N. Nandi, K. Bhattacharyya and B. Bagchi, *Chem. Rev.*, 2000, **100**, 2013–2045.
3. O. Dopfer and M. Fujii, *Chem. Rev.*, 2016, **116**, 5432–5463.
4. D. K. Sasmal, S. Ghosh, A. K. Das and K. Bhattacharyya, *Langmuir*, 2013, **29**, 2289–2298.
5. J. T. Hynes, H. J. Kim, J. R. Mathis and J. J. i Timoneda, *J. Mol. Liq.*, 1993, **57**, 53–73.
6. G. Van Der Zwan and J. T. Hynes*, J. Chem. Phys.*, 1998, **78**, 4174.
7. S. K. Pal and A. H. Zewail, *Chem. Rev.*, 2004, **104**, 2099–2123.
8. S. Bandyopadhyay, S. Chakraborty, S. Balasubramanian and B. Bagchi, *J. Am. Chem. Soc.*, 2005, **127**, 4071–4075.
9. S. Pal, P. K. Maiti, B. Bagchi and J. T. Hynes, *J. Phys. Chem. B.*, 2006, **110**, 26396–26402.
10. Y. Tamoto, H. Segawa and H. Shirota, *Langmuir*, 2005, **21**, 3757–3764.
11. I. H. M. Van Stokkum, B. Van Oort, F. Van Mourik, B. Gobets and H. Van Amerongen, in Biophysical Techniques in Photosynthesis, Springer, Dordrecht, Netherlands, 2008, vol. II.
12. A. K. Shaw, R. Sarkar, D. Banerjee, S. Hintschich, A. Monkman and S. K. Pal, *J. Photochem. Photobiol. A: Chem.*, 2007, **185**, 76–85.
13. Y. F. Zhao, G. Y. Gao, S. F. Wang and W. J. Jin, *J. Porphyr. Phthalocyanines*, 2013, **17**, 367–375.
14. S. Saha, P. K. Mandal and A. Samanta, *Phys. Chem. Chem. Phys.*, 2004, **6**, 3106–3110.
15. A. Jha, K. Ishii, J. B. Udgaonkar, T. Tahara and G. Krishnamoorthy, *Biochemistry*, 2010, **50**, 397–408.
16. S. G. Su and J. D. Simon, *J. Phys. Chem.,* 1987, **91,** 2693.
17. G. A. Naylor, K. Scheidt, J. Larsson, M. Wulff and J. M. Filhol, *Meas. Sci. Technol.*, 2001, **12**, 1858.
18. H. Yue, Y. Zhao, X. Ma and J. Gong, *Chem. Soc. Rev.*, 2012, **41**, 4218–4244.
19. R. K. Ibrahim, M. Hayyan, M. A. AlSaadi, S. Ibrahim, A. Hayyan and M. A. Hashim, *J. Mol. Liq.*, 2019, **276**, 794–800.
20. J. Hašek, *Z. Kristallogr. Suppl.*, 2006, **23**, 613–618.
21. L. L. Y. Lee and J. C. Lee, *Biochemistry*, 1987, **26**, 7813–7819.

22. J. Courtois, E. Byström and K. Irgum, *Polymer*, 2006, **47**, 2603–2611.
23. A. D. WALDER and C. K. G. TYLER, *Anaesthesia*, 1994, **49**, 964–967.
24. D. B. Thomas, *Entomol. News*, 2008, **119**, 361–365.
25. M. R. Islam, B. Shabani and G. Rosengarten, *Energy Procedia*, 2017, **110**, 101–108.
26. K. S. Suganthi, V. Leela Vinodhan and K. S. Rajan, *Appl. Energy*, 2014, **135**, 548–559.
27. K. D. Weiss, *Prog. Polym. Sci.*, 1997, **22**, 203–245.
28. T. Learner, *The Conservator*, 2010, **24**, 96–103.
29. J. Junaedi, J. Junaedi, R. I. Arifiantini, C. Sumantri and A. Gunawan, Chalaza *J. Animal Husbandry*, 2016, **1**, 6–13.
30. B. T. Storey, E. E. Noiles and K. A. *Thompson, Cryobiology*, 1998, **37**, 46–58.
31. W. J. Armitage and C. J. Hunt, *Cryobiology*, 1982, **19**, 110–117.
32. M. A. Alvarenga, F. O. Papa, F. C. Landim-Alvarenga and A. S. L. Medeiros, *Anim. Reprod. Sci.*, 2005, **89**, 105–113.
33. V. Vagenende, M. G. S. Yap and B. L. Trout, *Biochemistry*, 2009, **48**, 11084–11096.
34. K. Gekko and S. N. Timasheff, *Biochemistry*, 1981, **20**, 4667–4676.
35. R. Sousa, *Acta. Cryst.*, 1995, **51**, 271–277.
36. N. Izyan, W. Azelee, A. Nor, M. Ramli, N. Hasmaliana, A. Manas, N. Salamun, R. C. Man and H. El Enshasy, *Int. J. Sci. Technol. Res.*, 2019, **8**, 553–558.
37. M. L. Horng, J. A. Gardecki, A. Papazyan and M. Maroncelli, *J. Phys. Chem.*, 1995, **99**, 17311–17337.
38. X. X. Zhang, M. Liang, J. Hunger, R. Buchner and M. Maroncelli, *J. Phys. Chem. B.*, 2013, **117**, 15356–15368.
39. S. Daschakraborty and R. Biswas, *J. Phys. Chem. B.*, 2014, **118**, 1327–1339.
40. A. Datta, D. Mandal, S. K. Pal and K. Bhattacharyya, *J. Phys. Chem. B.*, 1997, **101**, 10221–10225.
41. K. Sahu, S. K. Mondal, S. Ghosh and K. Bhattacharyya, *Bull. Chem. Soc. Jpn.*, 2007, **80**, 1033–1043.
42. B. Guchhait, R. Biswas and P. K. Ghorai, *J. Phys. Chem. B.*, 2013, **117**, 3345–3361.
43. E. Tarif, J. Mondal and R. Biswas, *J. Phys. Chem. B.*, 2019, **123**, 9378–9387.
44. B. Guchhait, S. Das, S. Daschakraborty and R. Biswas, *J. Chem. Phys.*, 2014, **140** 104514.
45. R. Karmakar and A. Samanta, *J. Phys. Chem. A*, 2002, **106**, 4447–4452.
46. S. Arzhantsev, N. Ito, M. Heitz and M. Maroncelli, *Chem. Phys. Lett.*, 2003, **381**, 278–286.

47. A. Samanta, *J. Phys. Chem. Lett.*, 2010, **1**, 1557–1562.
48. P. Dutta, P. Sen, A. Halder, S. Mukherjee, S. Sen and K. Bhattacharyya, *Chem. Phys. Lett.*, 2003, **377**, 229–235.
49. C. R. Moylan, *J. Phys. Chem* 1994, **98**, 13513.
50. W. Baumann and Z. Nagy, *Pure & Appl. Chem.*, 1993, **65**, 1729–1732.
51. T. Deligeorgiev, A. Vasilev, S. Kaloyanova and J. J. Vaquero, *Color. Technol.*, 2010, **126**, 55–80.
52. H. Li, C. Y. Ung, C. W. Yap, Y. Xue, Z. R. Li, Z. W. Cao and Y. Z. *Chen, Chem. Res. Toxicol.*, 2005, **18**, 1071–1080.
53. S. K. Saha, P. Purkayastha and A. B. Das, *J. Photochem. Photobiol. A: Chem.*, 2008, **195**, 368–377.
54. S. K. Saha, P. Purkayastha, A. B. Das and S. Dhara, *J. Photochem. Photobiol. A: Chem.*, 2008, **199**, 179–187.
55. S. S. Jaffer, M. Sowmiya, S. K. Saha and P. Purkayastha, *J. Colloid Interface Sci.*, 2008, **325**, 236–242.
56. S. S. Jaffer, S. K. Saha and P. Purkayastha, *J. Colloid Interface Sci.*, 2009, **337**, 294–299.
57. M. Kondo, X. Li and M. Maroncelli, *J. Phys. Chem. B*, 2013, **117**, 12224–12233.
58. T. Pradhan, H. Al, R. Gazi, B. Guchhait and R. Biswas, *J. Chem. Sci*, 2012, **124**, 355–373.
59. R. Biswas, A. R. Das, T. Pradhan, D. Touraud, W. Kunz and S. Mahiuddin, *J. Phys. Chem. B*, 2005, **119**, 6620.
60. N. Sarma, J. M. Borah, S. Mahiuddin, H. Al, R. Gazi, B. Guchhait and R. Biswas, *J. Phys. Chem. B*, 2011, **115**, 9040–9049.
61. R. Biswas, J. E. Lewis and M. Maroncelli, *Chem. Phys. Lett.*, 1999, **310**, 485–494.
62. S. Dinda, A. Sil, A. Das, E. Tarif and R. Biswas, *J. Mol. Liq.,* 2022, **349,** 118126.
63. A. Das and R. Biswas, *J. Phys. Chem. B,* 2015, **119**, 10102.
64. K. Kumbhakar, E. Tarif, K. Mukherjee and R. Biswas, *J. Mol. Liq.*, 2019, **290**, 111225.
65. A. G. M. Ferreira, A. P. V. Egas, I. M. A. Fonseca, A. C. Costa, D. C. Abreu and L. Q. Lobo, *J. Chem. Thermodyn.*, 2017, **113**, 162–182.
66. T. Sun and A. S. Teja, *J. Chem. Eng. Data.*, 2002, **48**, 198–202.
67. R. S. Fee and M. Maroncelli, *Chem. Phys.*, 1994, **183**, 235–247.
68. B. Bagchi and R. Biswas, *Adv. Chem. Phys., Bd*, 1999, **109**, 207–433.

Chapter 8

Concluding Remarks and Future Problems

8.1 Concluding Remarks

In this thesis, we delved into the understanding the interaction and relaxation dynamics of wide variety of room temperature biodegradable eutectic solvents that includes ionic DES, naturally abundant DES (NADES), therapeutic DES (THEDES), and low viscosity green solvents via utilizing dielectric relaxation (DR), time resolved fluorescence (TRF), and other experimental methods and computer simulation where necessary. Our investigation into a NADES composed of betaine urea and water elucidated the multi-step relaxation mechanism through molecular dynamics simulations, highlighting the role of collective reorientation and structural hydrogen bond relaxation. Additionally, our exploration of ionic DESs, particularly the impact of substituting Na^+ for K^+, revealed changes in viscosity decoupling, glass transition temperature, and fragility, providing crucial information for industrial applications. Furthermore, the development of a THEDES comprising aspirin and menthol significantly enhanced the solubility of aspirin, with preliminary structural and dynamic characterization revealing temporal heterogeneity and extensive intermolecular hydrogen bond formation. We also addressed the challenge of high viscosity in chemical reactions by designing a low-viscosity molten mixture, demonstrating its excellent solvent properties despite slower dynamics compared to water. Moreover, our investigation into the ultrafast solvation of glycerol and ethylene glycol using combining streak camera and time-correlated single photon counting (TCSPC) has provided detailed insights into solvation dynamics. Additionally, our study on concentration-dependent hyaluronic acid (HA) aggregation in aqueous environments has revealed critical concentration thresholds and biphasic water dynamics near the aggregation point, offering valuable knowledge for understanding organ dysfunction related to HA aggregation.

As we have provided conclusions at the end of every chapter, so we have not repeated them here again in detail.

8.2 Future Problems

8.2.1 Hz-GHz Dielectric Relaxation of (glucose+urea+water) DES: Molecular Insight via Computer Simulations

We prepared a NADES comprising biocompatible components: glucose, urea, and water, in a molar ratio of 6:4:1 and we investigated the interactions and dynamics via utilizing time resolved fluorescence spectroscopy.[1] Due to presence of highly H-bonded and complex interactions, their dynamics span the nanosecond to picosecond range. To comprehensively probe the interaction and dynamics of the system, we propose employing dielectric relaxation spectroscopy (DRS) across a frequency range of 20 Hz to 50 GHz. This approach offers a level-free measurement, enabling direct exploration of the medium inherent dynamics. Additionally, molecular simulations can provide insights into the individual contributions of each component to the observed DRS dynamics.

The structural aspect of the system can be investigated using small-angle X-ray scattering. These results can be supplemented by simulated structure factor calculations, allowing for a detailed analysis of each constituent's contribution.

8.2.2 Permeation Study of Aspirin of (Aspirin+Menthol) DES via Lipid Membrane

In Chapter 3, we detailed the preparation of a new therapeutic deep eutectic solvent (THEDES) composed of aspirin and menthol in molar ratio 1:4, aimed at enhancing the solubility of aspirin, an anti-inflammatory drug known for its poor water solubility.[2,3] Through a combination of fluorescence spectroscopy and molecular simulations, we explored the interactions, dynamics, and microstructure of this solvent-drug system.

Our future research endeavours focus on investigating the permeability of aspirin molecules through lipid membranes. Utilizing fluorescence spectroscopy alongside complementary techniques, we aim to gain insights into the intricate process of aspirin permeation. In particular, molecular dynamics simulations will play a crucial role in providing a detailed characterization of the free energy surface and diffusion coefficients along the permeation pathway.[4,5] By precisely mapping out these molecular properties, we can predict aspirin permeability through lipid membranes and elucidate the underlying molecular mechanisms driving this process.

8.2.3 Effect of Alkyl Chain Length of DESs Composed of Proline and Carboxylic Acids via Dielectric Relaxation Spectroscopy

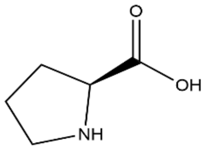

Proline

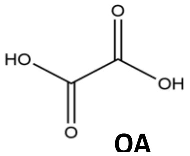

OA

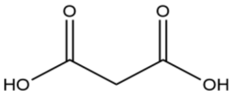

MA

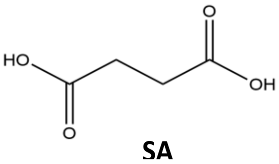

SA

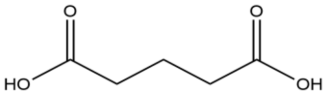

GA

Proline can form DESs with a wide range of carboxylic acids featuring varying carbon chain lengths. Our objective is to prepare these DESs, utilizing proline as the hydrogen-bond donor and oxalic acid (OA), malonic acid (MA), succinic acid (SA), and glutaric acid (GA) as the hydrogen-bond acceptors. The DESs will form at different temperature and composition for each acid pair.[6]

Our investigation will focus on dielectric relaxation studies spanning the frequency window from Hz to GHz. The dynamics of such complex systems span from nanoseconds to picoseconds, making this frequency range crucial for understanding their behaviour. Additionally, we will explore the effect of alkyl chain length on the dielectric relaxation dynamics as well as their static dielectric constants.

Furthermore, molecular dynamics simulations will be conducted to analyze the impact of alkyl chain length on H-bond formation and how structural relaxation of H-bond relaxation contributes to the measured dielectric relaxation dynamics. In addition, simulated dielectric relaxation may also shed light on the self and cross-molecular interactions within these DESs.

References

1 E. Tarif, J. Mondal and R. Biswas, *J. Phys. Chem. B.*, 2019, **123**, 9378–9387.

2 K. Florey, in *Analytical Profiles of Drug Substances*, Academic Press, 1979, vol. 8, pp. 1–46.

3 D. J. Bjorkman, *Am. J. Med.*, 1998, **105**, 8S-12S.

4 A. R. C. Duarte, A. S. D. Ferreira, S. Barreiros, E. Cabrita, R. L. Reis and A. Paiva, *Eur. J. Pharm. Biopharm.*, 2017, **114**, 296–304.

5 M. Orsi, W. E. Sanderson and J. W. Essex, *J. Phys. Chem. B*, 2009, **113**, 12019–12029.

6 L. Hao, M. Wang, W. Shan, C. Deng, W. Ren, Z. Shi and H. Lü, *J. Hazard. Mater.*, 2017, **339**, 216–222.

Addendum I

Dynamical Transformation of Water During Sol-Gel Transition in Aqueous Solutions of Hyaluronic Acid: Probed via Dielectric Relaxation Spectroscopy

Ad.1.1 Introduction

Hyaluronic acid (HA) plays a crucial role in biological processes, affecting how cells function and maintaining tissue integrity. Its presence spans across diverse organs [1–3] such as the lungs, kidney, brain, muscle, and liver, where its aggregation and subsequent formation of high-viscosity stiff material have been implicated in the pathology of organ dysfunction and fibrosis.[4,5] Amidst its multifaceted roles, involvement of HA in the extracellular matrix (ECM) of organs emerges as a crucial regulator of cellular behaviours, including growth, migration, and differentiation.[6] The effects of HA aggregation vary depending on the molecular weights (MW) of the aggregated structures, leading to different biological outcomes.[7] Notably, high MW HA polymer ($\geq 10^6$ Da) has been identified as a key contributor to gel formation, thereby elevating the risk of tissue-stiffness mediated fibrosis. [4,8,9]

Two primary methods of crosslinking are employed for HA-hydrogel synthesis: physical and chemical. Physical crosslinking can be induced through agitation, changes in pressure, or temperature, while chemical crosslinking involves the addition of foreign crosslinkers to the hydrogel scaffold. Although chemical crosslinkers enhance the physical strength and biodegradability time of the hydrogel,[10] they may also elevate its toxicity level.[11] Fortunately, HA exhibits the remarkable capability to form hydrogels through both physical and chemical crosslinking mechanisms, offering a versatile platform for biomedical applications. [11–14]

In light of these findings, the imperative to trace the critical threshold concentration that induce the sol-gel transition of high MW HA polymer in aqueous solutions becomes evident. This explanation is essential for understanding how the aggregation of HA contributes to health issues and for developing treatments to improve organ function and reduce fibrosis.

Although structure, physical properties and dynamics of HA-based hydrogel were studied with or without crosslinker at high HA concentration ($\geq 1\%$) or low water containing system[12,13,15–

[24], a systematically concentration dependent study and thereby finding the critical concentration of HA in sol→gel formation of HA-water mixture is utmost important. Following that we have investigated HA concentration dependent sol-gel transition and dynamics of bound water from sol to gel via dielectric relaxation spectroscopy (DRS), and differential scanning calorimetry (DSC). HA concentration dependence static dielectric constant (ε_s) in these systems show a sol-gel transition is occurred in between 0.5 % to 0.75 % HA containing mixture. DC conductivity observed due to mobility of sodium cation also indicate sol-gel phage transition in the same concentration range (0.5 % to 0.75 %) in HA-water mixtures. Earlier studies of hyaluronate/water mixtures have been showed that, gel formation was observed at 3 % HA-water mixture when annealing was performed from 60 °C to 15 °C.[12] But this work not investigated less than 1% HA mixtures. In our investigation, sol-gel transition occurred in between 0.5 % to 0.75 % HA-water mixtures. Only liquid gel was formed up to 1% HA concentration in water and after that concentration, it transforms soft transformable sticky gel which is shown in sol-gel picture presentation section. In some earlier studies DRS measurements have been performed in HA-water hydrogel with higher HA concentration up to frequency coverage 10 MHz. High frequency DRS measurement from 200 MHz to 50 GHz in sol to gel HA-water mixtures is missing in these mixtures. In this light we explore free and bound water relaxation in high frequency regime via DRS measurement. In addition, DSC measurement was revealed a clear signature of bound water and effect of HA concentration on water freezing.

Ad.1.2 Experimental Details

Ad.1.2.1 Sample Preparation

Hyaluronic acid (HA) sodium salt, sourced from Streptococcus equi, was acquired from Sigma-Aldrich, alongside water for the experiment. The chemical structure of HA is illustrated in **Scheme Ad.1.1.**

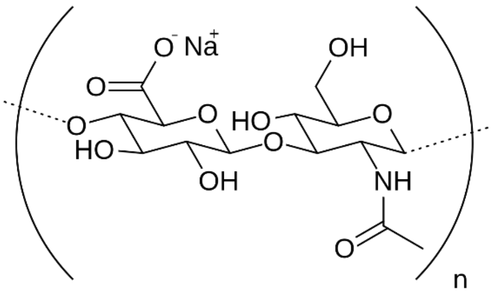

Scheme Ad.1.1. Chemical structure of Hyaluronic acid sodium salt (HA)

To prepare the samples, the required quantities of HA and water were carefully weighed into a glass container. A series of aqueous solutions of HA were prepared, varying in weight percentage (wt%) of HA: 0, 0.15, 0.3, 0.5, 0.65, 0.75, 1, 1.5, and 2. These solutions were thoroughly mixed by shaking them in a shaker incubator at ~250 rpm for ~1 hour. Subsequently, the samples underwent ultrasonic sonication for approximately 5 minutes to remove any air bubbles. All experimental procedures were conducted at ~293 K, and the prepared samples were left overnight to ensure complete dissolution and the sol or gel was prepared. A visual representation of the samples after preparation can be found in **Figure Ad.1.A.1** of the Appendix Ad.1.A.

Ad.1.2.2 DR Measurement Details

Dielectric relaxation (DR) measures the microscopic electric polarization of a system when subjected to a time-varying external field $\vec{E}(t)$. Studied in the frequency domain (ν), it reveals molecular-level phenomena.[25,26] As a result, the frequency-dependent complex relative permittivity $\varepsilon^*(\nu)$ is derived which is expressed as,[27]

$$\varepsilon^*(\nu) = \varepsilon'(\nu) - \left[i\varepsilon''(\nu) + \frac{i\sigma}{2\pi\epsilon_0\nu}\right]. \qquad \text{(Ad.1.1)}$$

Where ν $(\frac{\omega}{2\pi})$ is the linear frequency, σ is the dc conductivity of the system and ϵ_0 is the free space permittivity. ε' and ε'' are relative permittivity and loss component of the complex spectrum respectively.

DR of liquid system were recorded using two different dielectric set-ups. For low frequency measurement we used the E4990A impedance analyzer coupled with liquid test fixture 16452A covering frequency range from 20 Hz to 10 MHz. Short compensation, air capacitance measurement and followed by capacitance of liquid material measurement were performed to get the complex DR spectra. A PNA-L network analyzer N5235B with open ended coaxial probe kit N1501A was employed to record the DR spectra in frequency window 200 MHz to 50 GHz. Calibration of the instrument was performed by measuring air, shorting block and water as open, short, load circuit respectively. More details about these measurement techniques are available in chapter 2 and the following references.[27–29]

Ad.1.2.3 Data Analysis

Experimentally obtained complex DR data were fitted with a sum of Havriliak-Negami (HN) equation[27,30]

$$\varepsilon^*(\nu) = \varepsilon_\infty + \sum_j \frac{\Delta\varepsilon_j}{\left(1+\left(i2\pi\nu\tau_j\right)^{1-\alpha_j}\right)^{\beta_j}} \qquad \text{(Ad.1.2)}$$

where $0 \leq \alpha_j < 1$ and $0 < \beta_j \leq 1$. Here ε_∞ is the permittivity at infinite frequency regime where $\varepsilon_\infty \approx n_D^2$. Note that from Debye model[31], dielectric relaxation described as $\alpha_j = 0$ and $\beta_j = 1$, whereas $\alpha_j = 0, 0 < \beta_j \leq 1$ describes Cole-Davidson (CD) model[32,33] and $0 \leq \alpha_j < 1$, $\beta_j = 1$ describes the Cole-Cole model[34], respectively. The relaxation parameters were generated by simultaneously fitting $\varepsilon'(\nu)$ and $\varepsilon''(\nu)$ by using non-linear least square fitting method. The fit quality was resolved by inspect both the "goodness-of-fit" parameter (χ^2) and residual. The expression of (χ^2) defined as[28]

$$\chi^2 = \frac{1}{2m-l} \sum_{i=1}^{m} \left[\left(\frac{\delta\varepsilon_i'}{\sigma\varepsilon_i'}\right)^2 + \left(\frac{\delta\varepsilon_i''}{\sigma\varepsilon_i''}\right)^2 \right]. \qquad \text{(Ad.1.3)}$$

Where m, l, $\delta\varepsilon_i$ and $\sigma\varepsilon_i$ are denotes data triples, number of adjustable parameters, residual and standard deviation of the individual data point respectively. For the current measurement two-Debye fitting model best fitted the experimental DR spectra.

Ad.1.2.4 Differential Scanning Calorimetric (DSC) Measurements

To explore HA concentration dependence melting temperature (T_m) in HA-water mixtures, the differential scanning calorimetry (DSC) (DSC, TA Instruments Q200) measurements were carried out. All DSC measurements were conducted within a temperature window of -50 to 30 °C, with a constant heating rate of 5 °C/min. The samples were completely airtight sealed in an aluminium pan by sealing with aluminium cap (40 µl, Tzero, TA Instruments).

Ad.1.2.5 Conductivity of Aqueous HA Sol or Gel

The frequency dependent conductivity of the HA solution is shown in **Figure Ad.1.A.2** of the Appendix Ad.1.A. The conductivity was measured using an impedance analyser working in parallel plate capacitor mechanism in the frequency range from 20 Hz to 10 MHz. The electrical conductivity of HA solution is represented as a combination of frequency independent dc conductivity part and a strongly frequency dependent ac conductivity part. Typical frequency dependent conductivity spectra show three distinguished regions i) low frequency dispersion due to polarization, ii) intermediate frequency plateau region and iii) high frequency dispersion region.[35–37] The low frequency dispersion region is described by the polarization of electrode in the low frequency region. As the frequency decreases, more charges accumulate to the electrodes hence reduction in conductivity occur. In the intermediate region here in KHz to MHz region in the figure the conductivity is independent of frequency. Here an intermediate plateau region is formed which is dc conductivity.

Ad.1.3 Results and Discussion

Ad.1.3.1 Static Dielectric Constant: Indication of Sol→Gel Formation

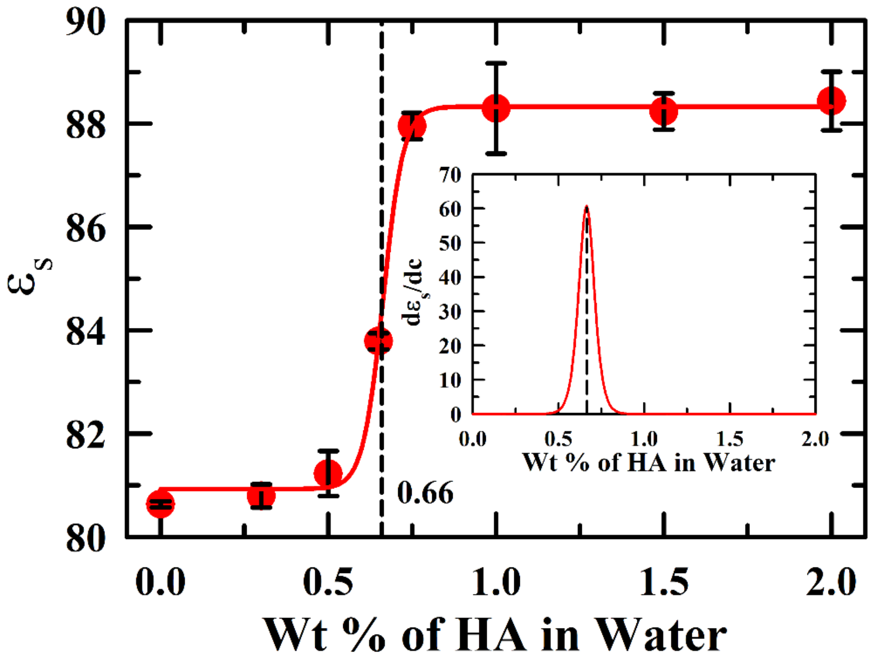

Figure Ad.1.1 HA concentration (0 to 2 wt%) dependent static dielectric constant (ε_S) of HA-water mixture at 293 K. Inset shows the transition of ε_S occurring around 0.66 wt% HA via derivative plot of ε_S with respect to concentration.

Given the predominantly water-dominated environment (98-100 wt%), DR measurements were conducted across the Hz to GHz frequency range. These measurements serve a dual purpose: firstly, to ascertain the static dielectric constant of the medium, and secondly, to directly explore environment relaxation dynamics and the impact of aggregation on water relaxation. Static dielectric (ε_s) constant of HA-water mixtures were taken at 5 MHz from the low frequency DR measurements are shown in **Figure Ad.1.1**. The ε_s of HA-water mixture increases from pure water to 0.75 wt% HA concentration. In between 0.75 to 2 wt% HA concentration, no significant change is observed in the measured ε_s. This indicates that sol→gel transition also has impact on ε_s. The question arises here: why ε_s in these systems increase with HA concentrations. **Scheme Ad.1.1** showed that HA monomers have multiple polar groups, like $-\mathrm{OH}$, $-\mathrm{COO}^-$ and $-\mathrm{NH(CO)OH}$ in their backbone and these polar groups have fixed dipole moment vector. Consequently, HA polymer has permanent effective dipole moment that is coming from vector summation of all the dipoles of polar groups. Note that ε_s of a system at temperature T and volume V can be expressed by following equation[38,39] $\varepsilon_s = 1 + \langle M\rangle_{eff}/3\varepsilon_0 V k_B T$, where ε_0 and k_B are vacuum permittivity and the Boltzmann constant, respectively. $\langle M\rangle_{eff}$ is total effective dipole moment defined as $\langle M\rangle_{eff} = \langle M^2\rangle - \langle M\rangle^2$. Above relation shows that the ε_s is directly proportional to total effective dipole moment ($\langle M\rangle_{eff}$), which is coming from HA molecule, water and their cross terms.[40,41] Because of the polar nature of the HA molecule, dipole moment contribution from HA and its cross correlation with water increase the ε_s of these systems with increasing HA concentrations. This type of anomalous dielectric increment has been also observed in aqueous protein solutions.[40,41] But increase of ε_s is prominent from 0.5 to 0.75 wt % HA. This result suggests that enhancement of ε_s mainly coming from dipole moment contribution of HA molecules which transformed from disordered to ordered polymer backbone arrangement due to sol→gel transformation. HA concentration dependent ε_s was fitted with sigmoidal equation $y = y_0 + a/\left(1 + exp((x - x_0)/b)\right)$ where a is $\varepsilon_s(max) - \varepsilon_s(initial)$, b is constant it depends on concentration of mixtures and x_0 is position of maximum slop change in sigmoidal curve. Its corresponding peaks of derivative presented by dashed line in inset **Figure Ad.1.1**. This indicates that a sol→gel transition is observed around 0.66 wt% HA.

Ad.1.3.2 Conductivity Measurements and Indication of Sol→Gel Formation

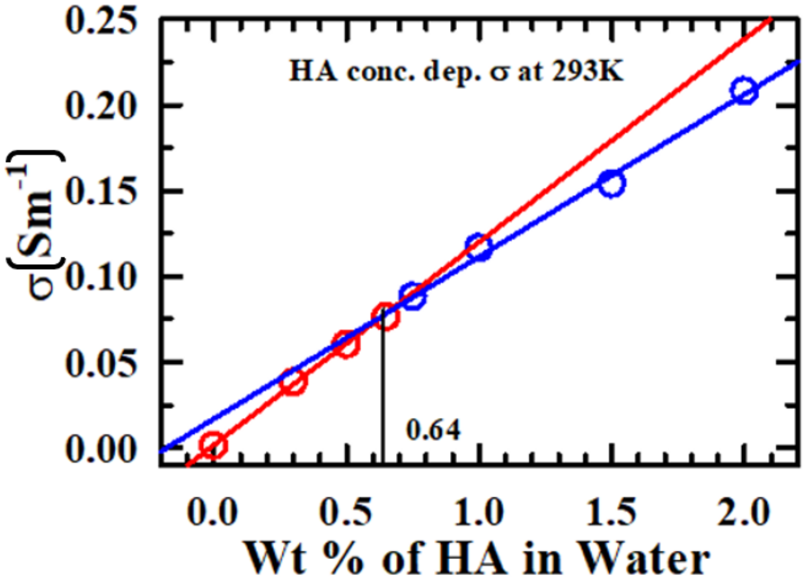

Figure Ad.1.2. conductivity (σ) in aqueous HA mixtures at 293K. Note that σ is calculated from DR measurements at 5 MHz frequency where frequency dependence conductivity become plateau (see Figure Ad.1.A.2). Red and blue colour circle in figure denotes the 0 to 0.65 wt.% and 0.75 to 2 wt.% HA in water respectively. Solid lines passing through the experimental data represent respective linear fits. All representations are colour-coded.

Figure Ad.1.2 represents sol-gel transition features of aqueous HA solutions observed from conductivity (σ) measurement. Note that the σ values were taken from frequency dependent DR at 5 MHz where frequency dependent conductivity spectra get plateau (see **Figure Ad.1.A.2** of Appendix Ad.1.A). In our system as we added more and more HA to water, we have seen a gradual increase of conductivity of the medium. The conductivity ranges from 0.04 S/m^2 to 0.2 S/m^2 as we go from 0.3% HA to 2% HA. We have plotted the conductivity with respect to HA concentration. We fitted the conductivity with simple straight line. While fitting we have found we need two distinct straight line having different slope is better fitted the experimental observation. After fitting with two different straight line, we have found an inflection point at around 0.63% HA concentration. So, we can say the conductivity below 0.63% HA is behaving differently with respect to conductivity above 0.63% HA. This observation supports our previous experimental finding that the sol to gel transition is occurring around 0.65% HA concentration. It can be seen from **Figure Ad.1.2** that in sol phase the slope is greater than in gel phase. This is because when gel matrix is formed, the mobility of the sodium ion is hampered or decreased or retarded compared to the ion mobility in sol phase.

Ad.1.3.3 Experimental DR Spectra: Detection of Slow Water

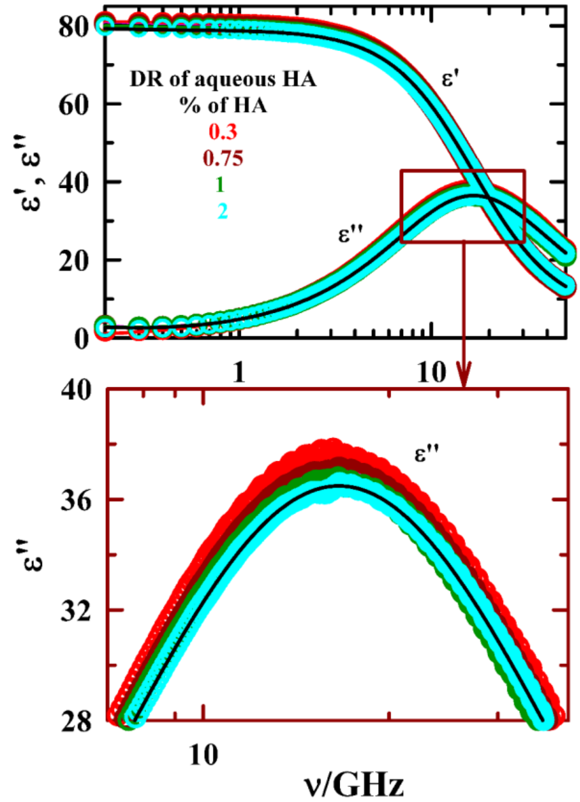

Figure Ad.1.3. HA concentration dependence real (ε') and imaginary (ε'') component of complex DRS data of aqueous HA mixtures in frequency regime $0.2 \leq \nu/\mathrm{GHz} \leq 50$ at 293 K, (upper panel) and the peak maxima of ε'' that zoom from the upper panel (lower panel). The line passing through the experimental data point express two Debye (2D) fitting model. All presentations are color-coded.

Figure Ad.1.3 represents the frequency dependent dielectric relaxation spectra of the aqueous HA solution at 293 K with few concentrations of HA ranging from 0.3 to 2 wt% HA. For all cases bimodal relaxation characteristic dictated by 2-Debye model fitting to experimental data and the fitting parameters along with average DR time ($\langle\tau_{DR}\rangle$) are tabulated in **Table Ad.1.1**. The figure shows that with increasing HA wt% there is a visible change in both real and imaginary parts of the DR spectra. We have thoroughly investigated the finding via plotting various DR parameters with respect to concentration obtained from **Table Ad.1.1** and see the effect of HA concentration dependence sol→gel transition.

Table Ad.1.1. HA concentration dependent 2-Debye fit parameters of experimentally measured DR spectra (frequency window: 200 MHz to 50 GHz) in aqueous HA mixtures at 293K.[a] Debye fit parameter of pure water from DRS measurement also shown in same table.

Conc.	ε_s	$\Delta\varepsilon_1$	$\tau_1(ps)$	$\Delta\varepsilon_2$	$\tau_2(ps)$	ε_∞	n_D	$\varepsilon_\infty - n_D^2$	$\langle\tau_{av}\rangle(ps)$
0%	80.7	-	-	74.7	10	6.0	1.332	4.225	10
0.3%	81	0.4 (1)[b]	316	75 (99)	10	5.6	1.333	3.823	14
0.5%	82.5	2.4 (3)	1996	74.2 (97)	10	5.9	1.333	4.123	70
0.65%	84.5	5.0 (6)	2650	73.3 (95)	10	6.1	1.333	4.323	181
0.75%	88	8.2 (10)	2987	74 (90)	10	5.8	1.333	4.023	308
1.0%	89	9.4 (11)	3562	73.3 (89)	10	6.3	1.334	4.520	400
1.5%	88.5	8.82 (11)	3880	73.45 (89)	10	6.2	1.335	4.418	435
2.0%	89	9.41 (11)	4182	73.42 (89)	10	6.0	1.335	4.217	468

a) Individual amplitudes and time constants can be reproduced within ±5% of the reported values. *b*) Number in parenthesis indicates dispersion amplitude of a given DR dispersion step in percentage.

Figure Ad.1.4 shows concentration dependent $\langle\tau_{DR}\rangle$ time. This depicts that $\langle\tau_{DR}\rangle$ increases with increasing HA concentrations. The increment of $\langle\tau_{DR}\rangle$ in these systems is sigmoidal in nature similar to ε_s. Black dashed line indicates the peak position of first derivative (shown in inset of **Figure Ad.1.4.**) of sigmoidal fit of $\langle\tau_{DR}\rangle$ data. This revealed that sol→gel transition occurs at 0.66 wt.% HA concentration in water as shown earlier in case of ε_s.

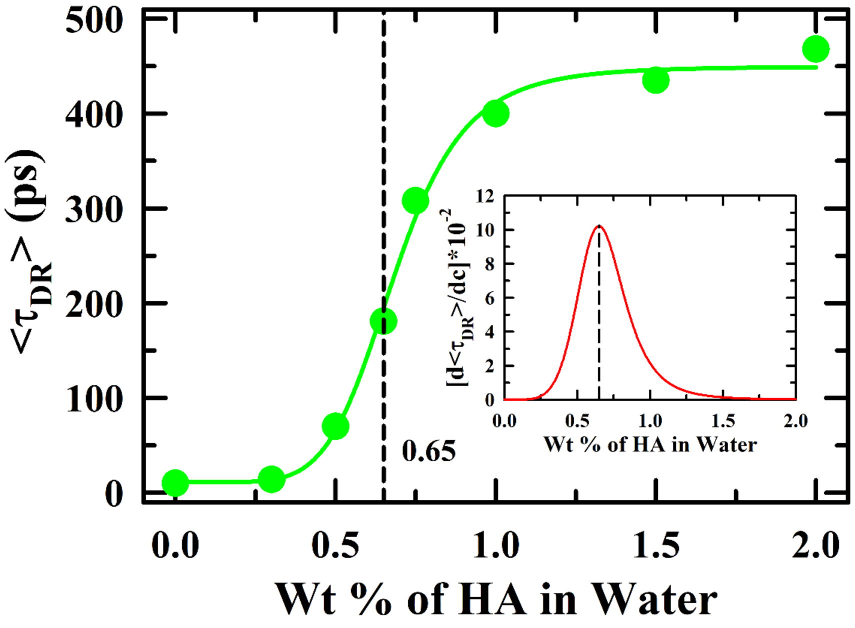

Figure Ad.1.4. HA concentration dependent average DR time ($\langle\tau_{DR}\rangle$), its sigmoidal fitting and first order derivative of sigmoidal fitting curve (in inset) in aqueous HA mixtures at 293 K.

Figure Ad.1.A.3 (Appendix Ad.1.A) depicts the concentration dependent deconvoluted spectra of imaginary (ε'') component of complex DR data in aqueous HA mixtures with two different DR time contributions. This figure clearly indicates the amplitudes of the two different time scales. Figure shows that DR time scale τ_1 posses the dominant contribution while the amplitude of slower relaxation time, τ_2, gradually increases with HA concentration and at the highest HA concentration the value is nearly 10%. In the next section we have plotted the time scales and their associated amplitude in a different plot and analysed the effect of sol→gel transition on DR time scales and amplitudes.

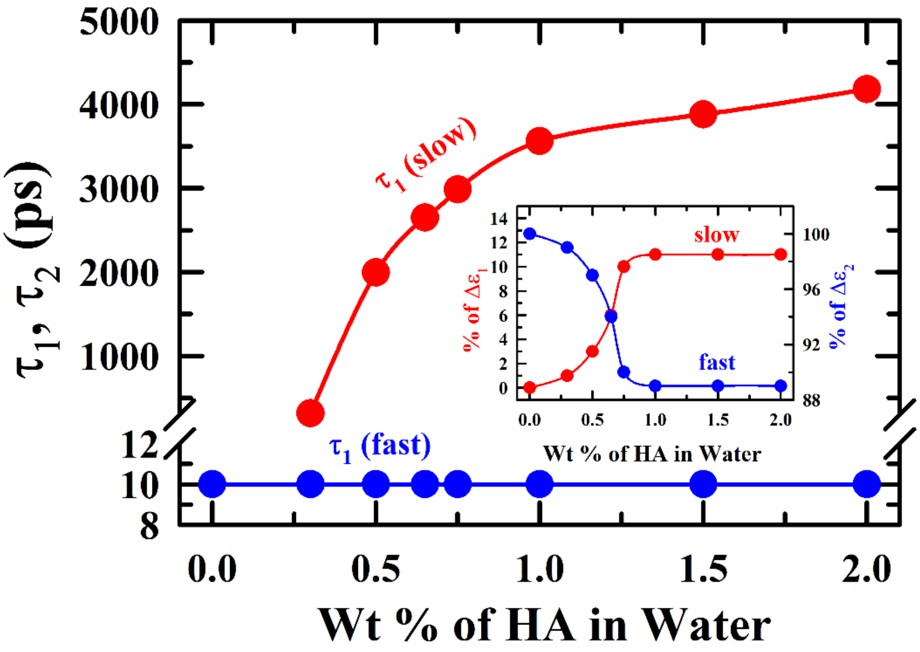

Figure Ad.1.5. HA concentration dependence DR times (τ_1 and τ_2) and its corresponding amplitudes ($\Delta\varepsilon_1$ and $\Delta\varepsilon_2$ in percentage shown in inset of Figure Ad.1.4) in aqueous HA mixtures at 293 K.

Figure Ad.1.5 represents the two DR times and their amplitudes (inset panel) in these sol-gel systems. The relatively faster DR timescale (τ_2) which is originating from the relaxation from bulk water[42,43]. Note that, with increasing HA concentration, the faster DR time scale (τ_2~ 10 ps at 293 K) remains constant while its amplitude decreases up to a certain concentration of HA (1 wt%) and then it gets saturated. The transition has been occurred in between 0.5% HA to 0.75%HA, where the sol to gel transition is occurred. As the HA concentration increases the bulk water concentration gradually decreases and the fast time scale contribution is progressively replaced by slower relaxation time scale. The slower DR time (τ_1) detecting in these aqueous HA sol-gel systems, increases from sub-nanosecond to a few nanoseconds with HA wt%. Amplitude of the slower dispersion is gradually increasing with HA concentration of 0 to 1 wt% and then it saturates. The above result suggests that with increasing HA concentration, some portion bulk water may transform into dynamically slow water which are engaging for hydration of polar group in HA.[44–48] This type of bimodal relaxation has been seen in dielectric relaxation of aqueous protein solution.[41,44,45]

Ad.1.3.4 DSC Measurements: Identifying the Presence of Slow Water

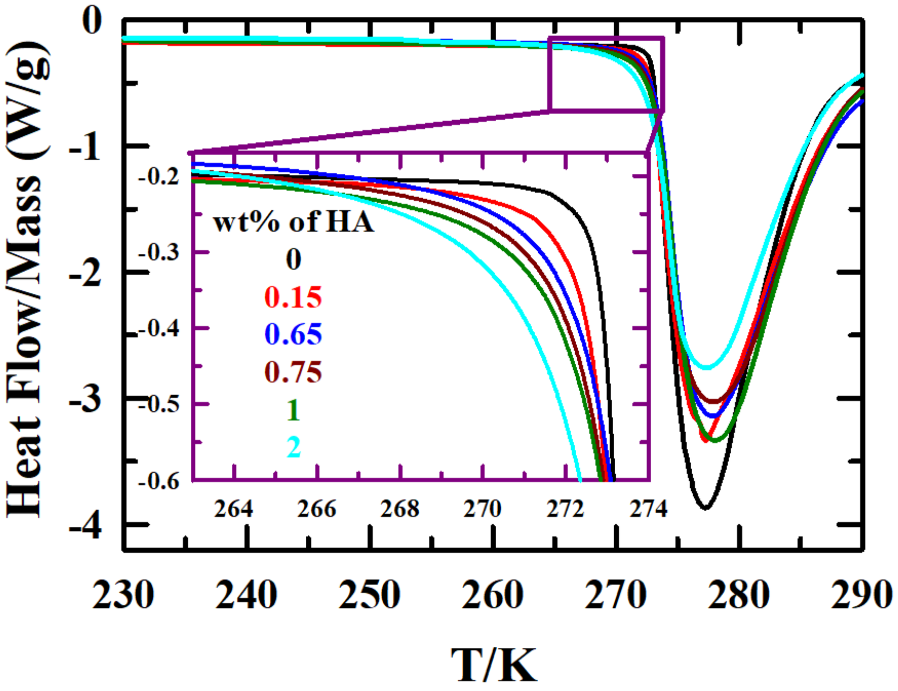

Figure Ad.1.6. Concentration dependent DSC thermogram in aqueous HA sol-gel mixtures. The sub-zero features are shown in inset of the Figure.

Further dynamically slower water is examined via DSC measurements. The HA concentration dependent DSC thermograms for aqueous HA sol-gel systems are shown in **Figure Ad.1.6**. Note that the composition dependent peak area is decreased with addition of HA in water. This indicates that population of bulk water decreases with increasing HA concentration. Interestingly, inset of **Figure Ad.1.6** clearly indicate that melting initialization gradually shifted towards sub-zero temperature with HA concentrations. This indicates a signature of freezable but dynamically slow water associated to polymer hydration[47] and confirmed the conjecture of dynamically slow water molecules in these sol-gel systems, previously observed in our DRS measurements.

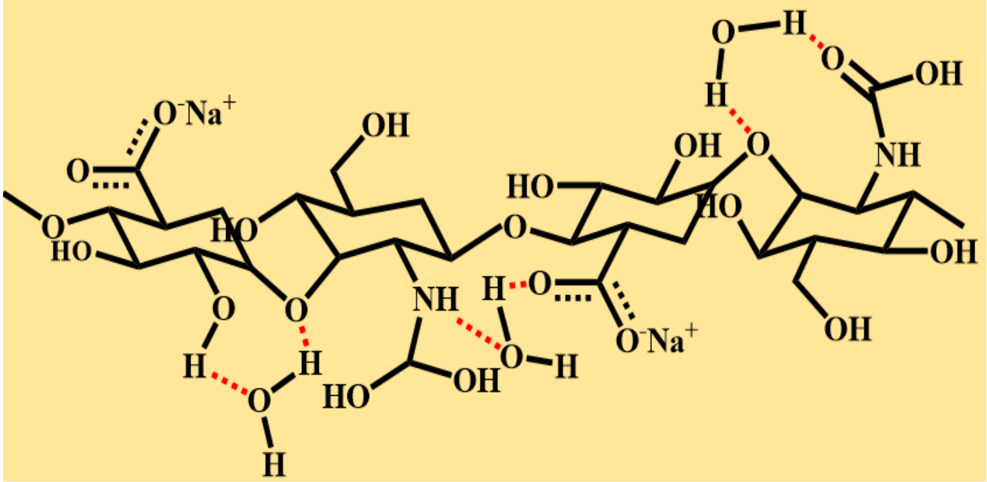

Figure Ad.1.7. Schematic presentation of dynamically slow water in aqueous HA mixture, where H-bond between water and polymer represents by red dashed line.

Figure Ad.1.7 represent an artistic view of hydration water of HA polymer chains participating in formation of hydrogen bond with $-\mathrm{OH}/-\mathrm{COO}^{-}/-\mathrm{NH(CO)OH}$ groups. We believe in post gel formation stage, due to the limitation of interaction sites occupied by dynamically slow water get saturated. Morphological study using cryo-SEM will be a good experiment to uncover the 3D gel structure of HA-water sol-gel system. Change in fluorescence intensity with HA concentration using a viscosity sensing probe such as Thioflavin-T (ThT) may indicate the critical concentration for sol→gel transition and complement the finding using DRS and DSC measurements.

Appendix Ad.1.A

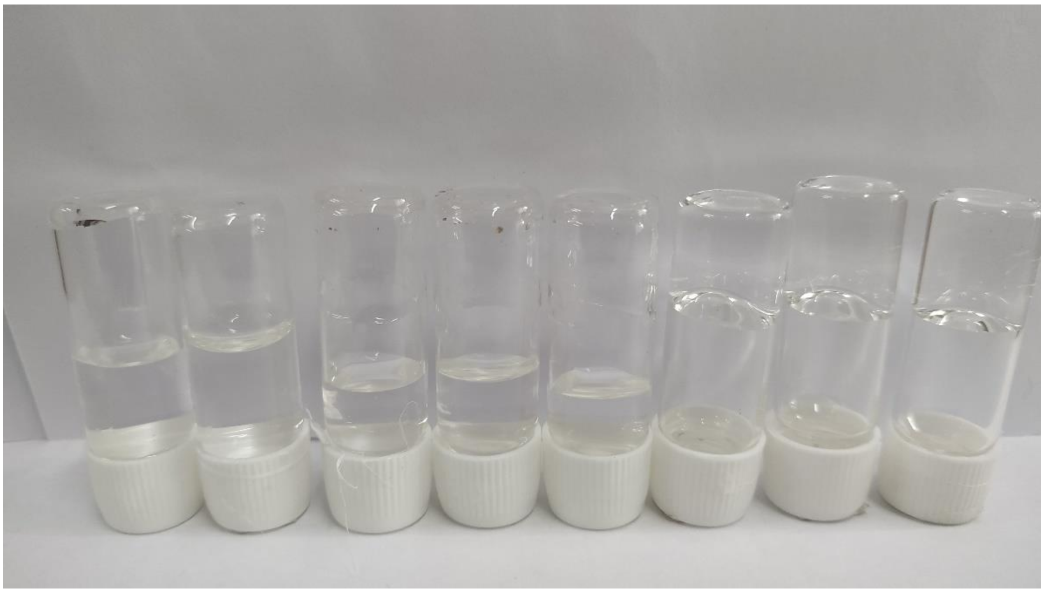

Figure Ad.1.A.1. HA-water mixtures at various concentration ($0 \leq HA\ wt\% \leq 2$) after sample preparation.

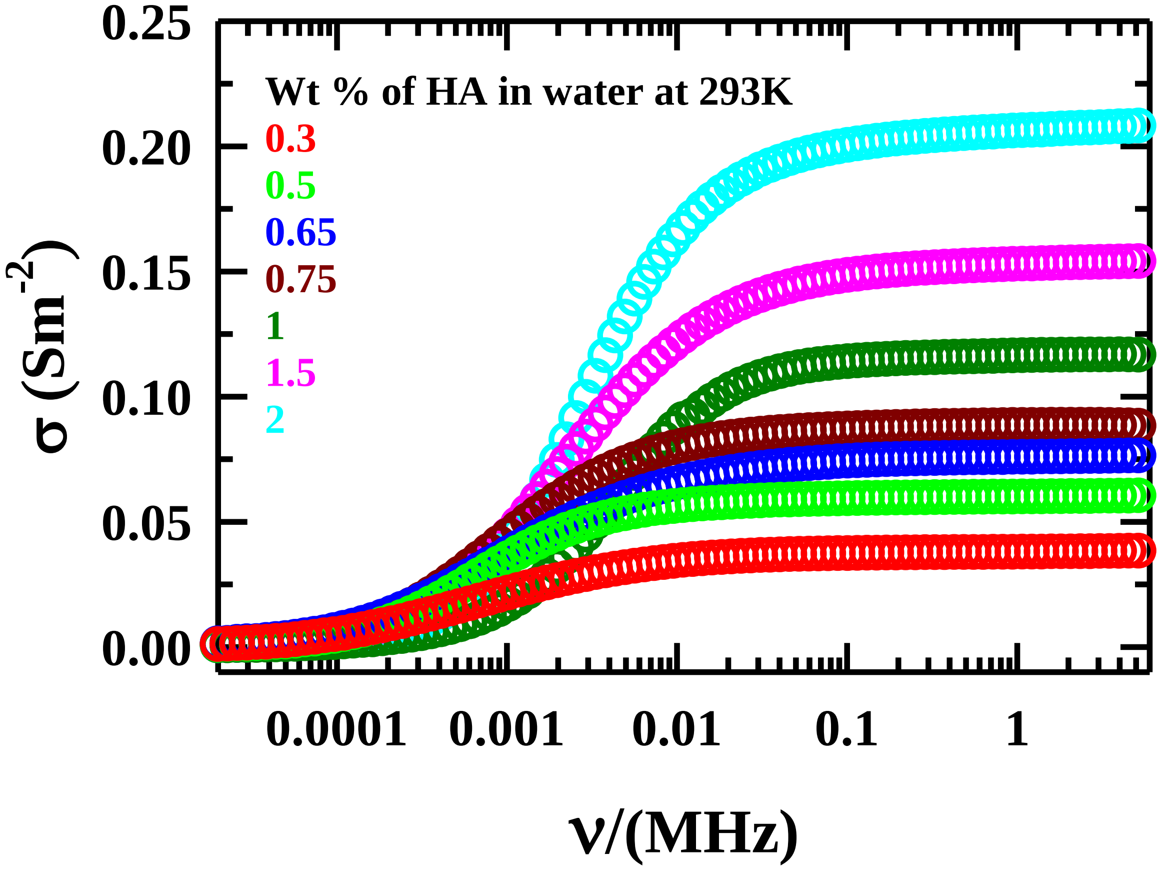

Figure Ad.1.A.2. Frequency dependence conductivity (σ) in HA-water mixtures from low frequency DRS (20 Hz to 5 MHz) measurements. All presentations are color-coded.

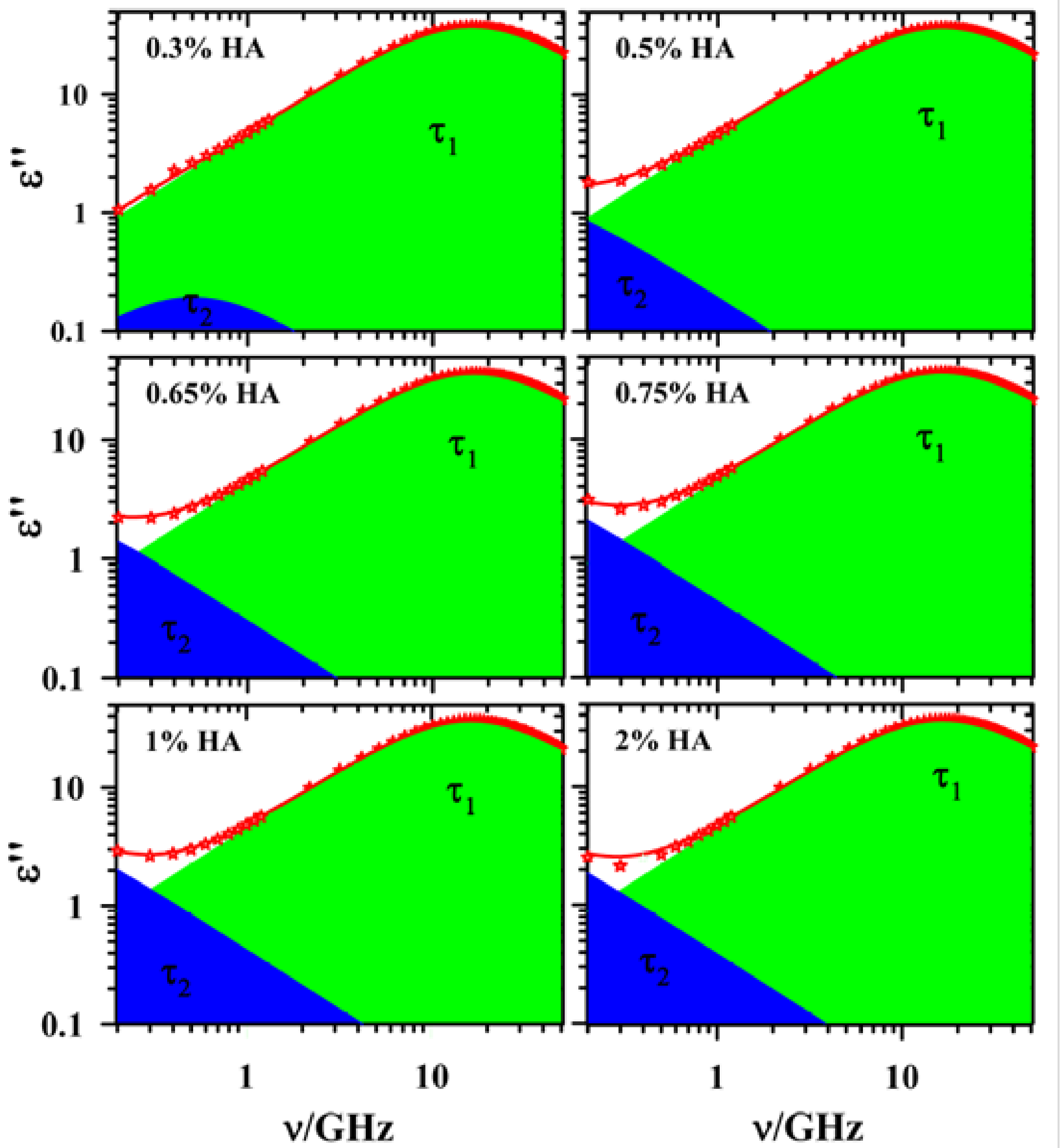

Figure Ad.1.A.3. HA concentration dependence deconvoluted imaginary (ε'') DR spectra with respect to DR times (τ_1 and τ_2) and its corresponding amplitudes ($\Delta\varepsilon_1$ and $\Delta\varepsilon_2$) in the frequency window $0.2 \leq \nu/\mathrm{GHz} \leq 50$ in aqueous HA mixtures at 293K.

References

1 J. R. E. Fraser, T. C. Laurent and U. B. G. Laurent, *J. Intern. Med.*, 1997, **242**, 27–33.

2 M. N. Collins and C. Birkinshaw, *Carbohydr. Polym.*, 2013, **92**, 1262–1279.

3 A. Mero and M. Campisi, *Polymers*, 2014, **6**, 346–369.

4 A. Stecco, M. Cowman, N. Pirri, P. Raghavan and C. Pirri, *Bioengineering*, 2022, **9**, 159.

5 P. G. Pavan, A. Stecco, R. Stern and C. Stecco, *Curr. Pain Headache Rep.*, 2014, **18**, 1–8.

6 M. Hemshekhar, R. M. Thushara, S. Chandranayaka, L. S. Sherman, K. Kemparaju and K. S. Girish, *Int. J. Biol. Macromol.*, 2016, **86**, 917–928.

7 A. G. Tavianatou, I. Caon, M. Franchi, Z. Piperigkou, D. Galesso and N. K. Karamanos, *FEBS J.*, 2019, **286**, 2883–2908.

8 A. M. Handorf, Y. Zhou, M. A. Halanski and W. J. Li, *Organogenesis*, 2015, **11**, 1–15.

9 N. L. Spartano, J. A. Augustine, W. K. Lefferts, W. E. Hughes, J. Garay Redmond, E. D. Martin, J. T. Kuvin, B. B. Gump and K. S. Heffernan, *Curr. Biomark. Find.*, 2014, 23.

10 H. J. Chung and T. G. Park, *Nano Today*, 2009, **4**, 429–437.

11 X. Xu, A. K. Jha, D. A. Harrington, M. C. Farach-Carson and X. Jia, *Soft Matter*, 2012, **8**, 3280–3294.

12 J. Fujiwara, M. Takahashi, T. Hatakeyama and H. Hatakeyama, *Polym. Int.*, 2000, **49**, 1604–1608.

13 A. Panagopoulou, J. V. Molina, A. Kyritsis, M. M. Pradas, A. V. Lluch, G. G. Ferrer and P. Pissis, *Food Biophys.*, 2013, **8**, 192–202.

14 J. M. Silva Garcia, A. Panitch and S. Calve, *Acta Biomater.*, 2019, **84**, 169–179.

15 A. Jacobson, M. Rahmanian, K. Rubin and P. Heldin, *Int. J. Cancer*, 2002, **102**, 212–219.

16 B. P. Toole, *Nat. Rev. Cancer*, 2004, **4**, 528–539.

17 T. C. Flynn, D. H. Thompson, S. H. Hyun and D. J. Howell, *Dermatol. Surg.*, 2015, **41**, S143–S152.

18 T. Vuletić, S. Dolanski Babić, T. Ivek, D. Grgičin, S. Tomić and R. Podgornik, *Phys. Rev. E*, 2010, **82**, 011922.

19 S. Kripotou, K. Zafeiris, M. Culebras-Martínez, G. Gallego Ferrer and A. Kyritsis, *Eur. Phys. J. E*, 2019, **42**, 1–18.

20 B. J. Kong, A. Kim and S. N. Park, *Carbohydr. Polym.*, 2016, **147**, 473–481.

21 R. Barbucci, R. Rappuoli, A. Borzacchiello and L. Ambrosio, *J. Biomater. Sci. Polym. Ed.*, 2012, **11**, 383–399.

22 I. Jacoboni, U. Valdrè, G. Mori, D. Quaglino and I. Pasquali-Ronchetti, *J. Struct. Biol.*, 1999, **126**, 52–58.

23 Y. Luo, K. R. Kirker and G. D. Prestwich, *J. Control. Release*, 2000, **69**, 169–184.

24 B. Tavsanli and O. Okay, *Carbohydr. Polym.*, 2020, **229**, 115458.

25 U. Kaatze and K. Giese, *J. Phys. E*, 1980, 13, 133–141.

26 R. Buchner, *Pure Appl. Chem.*, 2008, **80**, 1239–1252.

27 C. J. F. ; B. P. Böttcher, *Theory of electric polarization*, Elsevier, Amsterdam, Netherlands, 1978, vol. 2.

28 P. R. ; R. D. K. Bevington, *Data reduction and error analysis*, McGraw-Hill, New York, 2003.

29 A. Schönhals and F. Kremer, *Theory of Dielectric Relaxation*, Springer Berlin Heidelberg, 2003.

30 S. Havriliak and S. Negami, *Polymer*, 1967, **8**, 161–210.

31 P. J. W. Debye, *Polar Molecules*, Chemical Catalog Company, Incorporated, 1929.

32 D. W. Davidson and R. H. Cole, *J. Chem. Phys.*, 1950, 18, 1417.

33 D. W. Davidson and R. H. Cole, *J. Chem. Phys.*, 1951, **19**, 1484–1490.

34 K. S. Cole and R. H. Cole, *J. Chem. Phys.*, 1941, **9**, 341–351.

35 L. L. Hench and J. K. West, *Principles of electronic ceramics*, Wiley, New York, 1990.

36 A. K. Jonscher, *Thin Solid Films*, 1976, **36**, 1–20.

37 C. T. Moynihan, L. P. Boesch and N. L. Laberge, *Phys. Chem. Glasses*, 1973, **14**, 122–125.

38 M. Neumann, *Mol. Phys.*, 1983, **50**, 841–858.

39 H. Froehlich, *Theory of Dielectrics*, Oxford University Press, New York, 1958.

40 N. Nandi and B. Bagchi, *J. Phys. Chem. A*, 1998, **102**, 8217–8221.

41 E. H. Grant, B. G. R. Mitton, G. P. South and R. J. Sheppard, *Biochem J*, 1974, **139**, 375–380.

42 T. Sato and R. Buchner, *J. Phys. Chem. A*, 2004, **108**, 5007–5015.

43 K. Mukherjee, A. Barman and R. Biswas, *J. Mol. Liq.*, 2016, **222**, 495–502.

44 N. Nandi and B. Bagchi, *J. Phys. Chem. B*, 1997, **101**, 10954–10961.

45 N. Nandi, K. Bhattacharyya and B. Bagchi, *Chem. Rev.*, 2000, **100**, 2013–2045.

46 S. Schrödle, R. Buchner and W. Kunz, *J. Phys. Chem. B*, 2004, **108**, 6281–6287.

47 K. Mukherjee, A. Barman and R. Biswas, *J. Chem.Phys.*, 2019, **151**, 184901.

48 F. Heatley and J. E. Scott, *Biochem J.*, 1988, **254**, 489.